CERN-LHCC-2004-025
ALICE-TDR-011
10 September 2004

A L I C E

Technical Design Report

on

Forward Detectors:

FMD, T0 and V0

Cover design by CERN Desktop Publishing Service
Model of T0 and FMD, prototype V0, and overall layout. Printed at CERN

September 2004

ISBN 2-9083-229-0

ALICE Collaboration

Alessandria, Italy, Facoltà di Scienze dell'Università:
P. Cortese, G. Dellacasa, L. Ramello and M. Sitta.

Aligarh, India, Physics Department, Aligarh Muslim University:
N. Ahmad, S. Ahmad, T. Ahmad, W. Bari, M. Irfan and M. Zafar.

Athens, Greece, University of Athens, Physics Department:
A. Belogianni, P. Christakoglou, P. Ganoti, A. Petridis, F. Roukoutakis, M. Spyropoulou-Stassinaki and M. Vassiliou.

Bari, Italy, Dipartimento di Fisica dell'Università and Sezione INFN:
G. Bruno, M. Caselle, G. De Cataldo, D. Di Bari, D. Elia, A. Franco, R.A. Fini, B. Ghidini, V. Lenti, V. Manzari, A. Mastroserio, F. Minafra, E. Nappi, F. Navach, C. Pastore, F. Posa, R. Santoro, I. Sgura, A. Tauro and G. Volpe.

Bari, Italy, Politecnico and Sezione INFN:
F. Corsi, D. De Venuto, U. Fratino and C. Marzocca.

Beijing, China, China Institute of Atomic Energy:
X. Li, Z. Liu, S. Lu, Z. Lu, Q. Meng, B. Sa, J. Yuan, J. Zhou and S. Zhou.

Bergen, Norway, Department of Physics, University of Bergen:
A. Klovning, J. Nystrand, B. Pommeresche, D. Röhrich, K. Ullaland, A.S. Vestbø and Z. Yin.

Bergen, Norway, Bergen University College, Faculty of Engineering:
J. Alme, T. Alt, K. F. Hetland, H. Helstrup, J.A. Lien and M. Richter.

Bhubaneswar, India, Institute of Physics:
R.K. Choudhury, A.K. Dubey, D.P. Mahapatra, D. Mishra, S.C. Phatak and R. Sahoo.

Birmingham, United Kingdom, School of Physics and Space Research, University of Birmingham:
D. Evans, G.T. Jones, P. Jovanović, A. Jusko, J.B. Kinson, R. Lietava and O. Villalobos Baillie.

Bologna, Italy, Dipartimento di Fisica dell'Università and Sezione INFN:
A. Alici, F. Anselmo, P. Antonioli, S. Arcelli, G. Bari, M. Basile, L. Bellagamba, D. Boscherini, A. Bruni, G. Bruni, G. Cara Romeo, L. Cifarelli, F. Cindolo, M. Corradi, D. Falchieri, A. Gabrielli, E. Gandolfi, P. Giusti, D. Hatzifotiadou, G. Laurenti, M.L. Luvisetto, A. Margotti, M. Masetti, S. Morozov, R. Nania, F. Noferini, P. Otiougova, F. Palmonari, A. Pesci, F. Pierella, A. Polini, G. Sartorelli, E. Scapparone, G. Scioli, G.P. Vacca, G. Valenti, G. Venturi, M.C.S. Williams and A. Zichichi.

Bratislava, Slovakia, Comenius University, Faculty of Mathematics, Physics and Informatics:
V. Černý, R. Janik, S. Kapusta, L. Lúčan, M. Pikna, J. Pišút, N. Pišútová, B. Sitár, P. Strmeň, I. Szarka and M. Zagiba.

Bucharest, Romania, National Institute for Physics and Nuclear Engineering:
C. Aiftimiei, V. Catanescu, M. Duma, C.I. Legrand, D. Moisa, M. Petrovici and G. Stoicea.

Budapest, Hungary, KFKI Research Institute for Particle and Nuclear Physics, Hungarian Academy of Sciences:
E. Dénes, B. Eged, Z. Fodor, T. Kiss, G. Pálla, J. Sulyán and J. Zimányi.

Cagliari, Italy, Dipartimento di Fisica dell'Università and Sezione INFN:
S. Basciu, C. Cicalo, A. De Falco, M. Floris, M.P. Macciotta-Serpi, G. Puddu, S. Serci, E. Siddi, L. Tocco and G. Usai.

Catania, Italy, Dipartimento di Fisica dell'Università and Sezione INFN:
A. Badalà, R. Barbera, G. Lo Re, A. Palmeri, G.S. Pappalardo, A. Pulvirenti and F. Riggi.

CERN, Switzerland, European Organization for Nuclear Research:
Y. Andres, G. Anelli, I. Augustin, A. Augustinus, J. Baechler, P. Barberis, J.A. Belikov[1)], L. Betev, A. Boccardi, A. Braem, R. Brun, M. Burns, P. Buncic, I. Cali[3)], R. Campagnolo, M. Campbell, F. Carena, W. Carena, F. Carminati, N. Carrer, S. Chapeland, C. Cheshkov, P. Chochula, P. Christianssen, J. Conrad, J. Cruz de Sousa Barbosa[5)], M. Davenport, G. de Cataldo, J. de Groot, A. Di Mauro, R. Divià, C. Engster, S. Evrard, C. Fabjan, D. Favretto, L. Feng[6)], P. Foka, F. Formenti, U. Fuchs E. Futó[7)], A. Gallas-Torreira, A. Gheata, C. Gonzalez-Gutierrez, C. Gregory, M. Hoch, H. Hoedelmoser, P. Hristov, M. Ivanov, L. Jirden, A. Junique, W. Klempt, A. Kluge, T. Kuhr, L. Leistam, C. Lourenço, I. Makhlyeva, J.-C. Marin, P. Martinengo, A. Masoni[10)], M. Mast, D. Meunier-Picard, T. Meyer, M. Morel, A. Morsch, B. Mota, H. Muller, L. Musa, P. Nilsson, D. Nouais, F. Osmic, D. Perini, F. Piuz, S. Popescu, F. Rademakers, J.-P. Revol, P. Riedler, W. Riegler, E. Rosso, K. Šafařík, J.-C. Santiard, K. Schossmaier, J. Schukraft, Y. Schutz[11)], E. Schyns, P. Skowronski[12)], C. Soos[7)], G. Stefanini, R. Stock[3)], D. Swoboda, P. Szymanski, H. Taureg, M. Tavlet, P. Tissot-Daguette, P. Vande Vyvre, C. Van-Der-Vlugt, J.-P. Vanuxem and A. Vascotto.

Chandigarh, India, Physics Department, Panjab University:
M.M. Aggarwal, A.K. Bhati, A. Kumar, M. Sharma and G. Sood.

Clermont-Ferrand, France, Laboratoire de Physique Corpusculaire (LPC), IN2P3-CNRS and Université Blaise Pascal:
A. Baldit, V. Barret, N. Bastid, G. Blanchard, J. Castor, P. Crochet, F. Daudon, A. Devaux, P. Dupieux, P. Force, B. Forestier, F. Guerin, C. Insa, F. Jouve, J. Lecoq, F. Manso, P. Rosnet, L. Royer, P. Saturnini, G. Savinel and F. Yermia.

Columbus, U.S.A., Department of Physics, Ohio State University:
T.J. Humanic, I.V. Kotov, M. Lisa, B.S. Nilsen and D. Truesdale.

Columbus, U.S.A., Ohio Supercomputer Centre:
D. Johnson.

Copenhagen, Denmark, Niels Bohr Institute:
I. Bearden, H. Bøggild, C.H. Christensen, J.J. Gaardhøje and B.S. Nielsen.

Cracow, Poland, Henryk Niewodniczanski Institute of Nuclear Physics, High Energy Physics Department:
J. Bartke, E. Gładysz-Dziaduś, E. Kornas, A. Rybicki and A. Wroblewski[13)].

Darmstadt, Germany, Gesellschaft für Schwerionenforschung (GSI):
A. Andronic[14)], D. Antonczyk, H. Appelshäuser, E. Badura, E. Berdermann, P. Braun-Munzinger, O. Busch, M. Ciobanu[14)], H.W. Daues, P. Foka[15)], U. Frankenfeld, C. Garabatos, H. Gutbrod, C. Lippman, P. Malzacher, A. Marin, D. Miśkowiec, S. Radomski, H. Sako, A. Sandoval, H.R. Schmidt, K. Schwarz, S. Sedykh, R.S. Simon, H. Stelzer, G. Tziledakis and D. Vranic.

Darmstadt, Germany, Institut für Kernphysik, Technische Universität:
A. Förster, H. Oeschler and F. Uhlig.

Frankfurt, Germany, Institut für Kernphysik, Johann Wolfgang Goethe-Universität:
J. Berger, A. Billmeier, C. Blume, T. Dietel, D. Flierl, M. Gaździcki, Th. Kolleger, S. Lange, C. Loizides, R. Renfordt and H. Ströbele.

Gatchina, Russia, St. Petersburg Nuclear Physics Institute:
Ya. Berdnikov, V. Evseev, V. Ivanov, A. Khanzadeev, N. Miftakhov, V. Nikulin, V. Poliakov, V. Riabov, E. Rostchine, V. Ryazanov, V. Samsonov, O. Tarasenkova, V. Tarakanov and M. Zhalov.

Havana, Cuba, Centro de Aplicaciones Technlógicas y Desarrollo Nuclear (CEADEN):
E. Lopez Torres, A. Abrahantes Quintana and R. Diaz Valdes.

Heidelberg, Germany, Kirchhoff Institute for Physics:
V. Angelov, M. Gutfleisch, V. Lindenstruth, R. Panse, C. Reichling, R. Schneider, T. Steinbeck H. Tilsner and A. Wiebalck.

Heidelberg, Germany, Physikalisches Institut, Ruprecht-Karls Universität:
C. Adler, D. Emschermann, S. Freuen, P. Glässel, N. Herrmann, Th. Lehmann, W. Ludolphs, T. Mahmoud, J. Milosevic, K. Oyama, I. Rusanov, R. Schicker, P. Shukla, H.C. Soltveit, J. Stachel, M. Stockmeier, B. Vulpescu, B. Windelband and S. Yurevich.

Helsinki and Jyväskylä, Finland, Department of Physics, University of Jyväskylä and Helsinki Institute of Physics:
J. Äysto, M. Bondila, S. Yamaletdinov, V. Lyapin, T. Malkiewicz, M. Oinonen, V. Ruuskanen, H. Seppänen and W. Trzaska.

Jaipur, India, Physics Department, University of Rajasthan:
S. Bhardwaj, R. Raniwala and S. Raniwala.

Jammu, India, Physics Department, Jammu University:
S.K. Badyal, A. Bhasin, A. Gupta, V.K. Gupta, S. Mahajan, L.K. Mangotra, B.V.K.S. Potukuchi and S.S. Sambyal.

JINR, Russia, Joint Institute for Nuclear Research:
P.G. Akichine, V.A. Arefiev, Ts. Baatar[16)], B.V. Batiounia, G.S. Chabratova, V.F. Chepurnov, S.A. Chernenko, V.K. Dodokhov, L.G. Efimov, O.V. Fateev, T. Grigalashvili[17)], M. Haiduc[18)], D. Hasegan[18)], V.G. Kadychevsky, E.K. Koshurnikov, V. Kuznetsov[19)], V.L. Lioubochits, V.I. Lobanov, A.I. Malakhov, L.V. Malinina, M. Nioradze[20)], P.V. Nomokonov, Y.A. Panebrattsev, V.N. Penev, V.G. Pismennaya, I. Roufanov, V. Shestakov[19)], A.I. Shklovskaya, P. Smykov, M.K. Suleimanov, Y. Tevzadze[20)], R. Togoo[16)], A.S. Vodopianov, V.I. Yurevich, Y.V. Zanevsky, S.A. Zaporojets and A.I. Zinchenko.

Karlsruhe, Germany, Institut für Prozessdatenverarbeitung und Elektronik (IPE)[*)]:
T. Blank and H. Gemmeke.

Kharkov, Ukraine, National Scientific Centre, Kharkov Institute of Physics and Technology:
G.L. Bochek, A.N. Dovbnya, V.I. Kulibaba, N.I. Maslov, S.V. Naumov, V.D. Ovchinnik, S.M. Potin and A.F. Starodubtsev.

Kharkov, Ukraine, Scientific and Technological Research Institute of Instrument Engineering:
V.N. Borshchov, O. Chykalov, L. Kaurova, S.K. Kiprich, L. Klymova, O.M. Listratenko,
N. Mykhaylova, M. Protsenko, O. Reznik and V.E. Starkov.

Kiev, Ukraine, Department of High Energy Density Physics, Bogolyubov Institute for Theoretical Physics, National Academy of Sciences of Ukraine:
O. Borysov, Y. Martynov, S. Molodtsov, O. Sokolov, Y. Sinyukov and G. Zinovjev.

Kolkata, India, Saha Institute of Nuclear Physics:
P. Bhattacharya, S. Bose, S. Chattopadhyay, N. Majumdar, S. Mukhopadhyay, A. Sanyal, S. Sarkar,
P. Sen, S.K. Sen, B.C. Sinha and T. Sinha.

Kolkata, India, Variable Energy Cyclotron Centre:
Z. Ahammed, P. Bhaskar, S. Chattopadhyay, D. Das, S. Das, M.R. Dutta Majumdar, M.S. Ganti,
P. Ghosh, B. Mohanty, B.K. Nandi, T.K. Nayak, P.K. Netrakanti, S. Pal, R.N. Singaraju, B. Sinha,
M.D. Trivedi and Y.P. Viyogi.

Košice, Slovakia, Institute of Experimental Physics, Slovak Academy of Sciences and Faculty of Science, P.J. Šafárik University:
J. Bán, M. Bombara, S. Fedor, M. Hnatič, I. Králik, A. Kravčáková, F. Kriváň, M. Krivda,
G. Martinská, B. Pastirčák, L. Šándor, J. Urbán, S. Vokál and J. Vrláková.

Legnaro, Italy, Laboratori Nazionali di Legnaro:
M. Cinausero, E. Fioretto, G. Prete, R.A. Ricci and L. Vannucci.

Lisbon, Portugal, Departamento de Física, Instituto Superior Técnico:
P. Branco, R. Carvalho, J. Seixas and R. Vilela Mendes.

Lund, Sweden, Division of Cosmic and Subatomic Physics, University of Lund:
H.-A. Gustafsson, A. Oskarsson, L. Osterman, I. Otterlund and E.A. Stenlund.

Lyon, France, Institut de Physique Nucléaire de Lyon (IPNL), IN2P3-CNRS and Université Claude Bernard Lyon-I:
M. Chartoire, B. Cheynis, C. Combaret, L. Ducroux, D. Essertaize, J.Y. Grossiord, A. Guichard, J.-C. Ianigro, G. Maurelli, M. Miguet, P. Pillot, B. Rapp, R. Tieulent, W. Tromeur, S. Vanzetto, Y. Zoccarato.

Mexico City and Merida, Mexico, Centro de Investigacion y de Estudios Avanzados del IPN, Universidad Nacional Autonoma de Mexico, Instituto de Ciencias Nucleares, Instituto de Fisica:
J.R. Alfaro Molina, A. Ayala, A. Becerril, E. Belmont Moreno, J.G. Contreras, E. Cuautle,
J.C. D'Olivo, V. Grabski, G. Herrera Corral, M. Linares, M.I. Martinez, A. Martinez Davalos,
A. Menchaca-Rocha, L.M. Montano Zetina, L. Nellen, G. Paic[21)], J. Solano and S. Vergara.

Moscow, Russia, Institute for Nuclear Research, Academy of Science:
V.A. Feshchenko, M.B. Golubeva, V.G. Gorlychev, F.F. Guber, O.V. Karavichev, T.L. Karavicheva,
E.V. Karpechev, A.B. Kurepin, A.I. Maevskaia, V.V. Marin, I.A. Pshenichnov, V.I. Razin, A.I. Reshetin,
K.A. Shileev and N.S. Topilskaya.

Moscow, Russia, Institute for Theoretical and Experimental Physics:
A.N. Akindinov, V. Golovine, A.B. Kaidalov, M.M. Kats, I.T. Kiselev, S.M. Kisselev, E. Lioublev,
M. Martemianov, A.N. Martemiyanov, P.A. Polozov, V.S. Serov, A.V. Smirnitski, M.M. Tchoumakov,
I.A. Vetlitski, K.G. Volochine, L.S. Vorobiev and B.V. Zagreev.

Moscow, Russia, Russian Research Center Kurchatov Institute :
D. Aleksandrov, V. Antonenko, S. Beliaev, S. Fokine, M. Ippolitov, K. Karadjev, A. Kazantsev, V. Lebedev, V.I. Manko, N. Mishustin, T. Moukhanova, A. Nianine, S. Nikolaev, S. Nikouline, O. Patarakine, D. Peressounko, I. Sibiriak, A. Tsvetkov, A. Vasiliev, A. Vinogradov and I. Yushmanov.

Moscow, Russia, Moscow Engineering Physics Institute:
V.A. Grigoriev, V.A. Kaplin and V.A. Loginov.

Münster, Germany, Institut für Kernphysik, Westfälische Wilhelms Universität:
C. Baumann, D. Bucher, R. Glasow, H. Gottschlag, N. Heine, M. Hoppe, K. Reygers, R. Santo, W. Verhoeven, J. Wessels, A. Wilk and O. Zaudtke.

Nantes, France, Laboratoire de Physique Subatomique et des Technologies Associées (SUBATECH), Ecole des Mines de Nantes, IN2P3-CNRS and Université de Nantes:
L. Aphecetche, A. Boucham, K. Boudjemline, G. Conesa-Balbestre, J.P. Cussonneau, H. Delagrange, M. Dialinas, C. Finck, B. Erazmus, M. Germain, P. Lautridou, F. Lefèvre, L. Luquin, L. Martin, G. Martinez, O. Ravel, C. Roy and A. Tournaire.

Novosibirsk, Russia, Budker Institute for Nuclear Physics:
A.R. Frolov and I.N. Pestov.

Oak Ridge, U.S.A., Oak Ridge National Laboratory:
T. Awes.

Omaha, U.S.A., Creighton University:
M. Cherney and M. Swanger.

Orsay, France, Institut de Physique Nucléaire (IPNO), IN2P3-CNRS and Université de Paris-Sud:
V. Chambert, C. Coardos, M.P. Comets, P. Courtat, B. Espagnon, I. Hřivnáčová, R. Kunne, Y. Le Bornec, J. Peyré, J. Pouthas, S. Rousseau, C. Suire and N. Willis.

Oslo, Norway, Department of Physics, University of Oslo:
L. Bravina, G. Løvhøiden, B. Skaali, T.S. Tveter, T. Vik, J.C. Wikne and D. Wormald.

Padua, Italy, Dipartimento di Fisica dell'Università and Sezione INFN:
F. Antinori, A. Dainese, D. Fabris, M. Lunardon, M. Morando, S. Moretto, A. Pepato, E. Quercigh, F. Scarlassara, G. Segato, F. Soramel[22)], R. Turrisi and G. Viesti.

Prague, Czech Republic, Institute of Physics, Academy of Science:
A. Beitlerova, J. Mareš, E. Mihoková, M. Nikl, K. Píška, K. Polák and P. Závada.

Prague, Czech Republic, Technical University:
V. Petráček.

Protvino, Russia, Institute for High Energy Physics:
M.Yu. Bogolyubsky, G.I. Britvitch, G.V. Khaoustov, I.V. Kharlov, N.G. Minaev, V.S. Petrov, B.V. Polichtchouk, S.A. Sadovsky, P.A. Semenov, A.S. Soloviev, P.V. Stolpovsky and V.A. Victorov.

Puebla, Mexico, Benemerita Universidad Autonoma de Puebla, Centro de Investigacion y de Estudios Avanzados:
A. Fernandez Tellez, E. Gamez Flores, R. Lopez, S. Roman, M.A. Vargas and A. Zepeda.

Řež u Prahy, Czech Republic, Academy of Sciences of Czech Republic, Nuclear Physics Institute:
D. Adamová, S. Kouchpil, V. Kouchpil, A. Kugler, M. Šumbera, P. Tlustý and V. Wagner.

Rome, Italy, Dipartimento di Fisica dell'Università 'La Sapienza' and Sezione INFN:
S. Di Liberto, M.A. Mazzoni, F. Meddi and G.M. Urciuoli.

Rondebosch, South Africa, University of Cape Town, Department of Physics:
B. Becker, J.W.A. Cleymans, G. de Vaux, R.W. Fearick, A. Szostok and Z. Vilakazi.

Saclay, France, Centre d'Études Nucléaires, DAPNIA:
M. Anfreville, A. Baldisseri, H. Borel, D. Cacaut, E. Dumonteil, R. Durand, P. De Girolamo, J. Gosset, P. Hardy, V. Hennion, S. Herlant, F. Orsini, Y. Pénichot, H. Pereira, S. Salasca, F.M. Staley and M. Usseglio.

Salerno, Italy, Dipartimento di Fisica 'E.R.Caianiello' dell'Universitá and Sezione INFN:
A. De Caro, S. De Pasquale, A. Di Bartolomeo, M. Fusco Girard, G. Grella, M. Guida, G. Romano, S. Sellitto and T. Virgili.

Sarov, Russia, Russian Federal Nuclear Center (VNIIEF):
V. Basmanov, D. Budnikov, V. Demanov, V. Ianowski, R. Ilkaev, L. Ilkaeva, A. Ivanov, A. Khlebnikov, A. Kouryakin, S. Nazarenko, V. Pavlov, S. Philchagin, V. Punin, S. Poutevskoi, I. Selin, I. Vinogradov, S. Zhelezov and A. Zhitnik.

Split, Croatia, Technical University of Split, Faculty of Electrical Engineering, Mechanical Engineering and Naval Architecture (FESB):
S. Gotovac, E. Mudnic and L. Vidak.

St. Petersburg, Russia, V. Fock Institute for Physics of St. Petersburg State University :
M.A. Braun, G.A. Feofilov, S.N. Igolkin, A.A. Kolojvari, V.P. Kondratiev, P.A. Otyugova, O.I. Stolyarov, T.A. Toulina, F.A. Tsimbal, F.F. Valiev, V.V. Vechernin and L.I. Vinogradov.

Strasbourg, France, Institut de Recherches Subatomiques (IReS), IN2P3-CNRS and Université Louis Pasteur:
J. Baudot, D. Bonnet, J.P. Coffin, C. Kuhn, J. Lutz and R. Vernet.

Trieste, Italy, Dipartimento di Fisica dell'Università and Sezione INFN:
V. Bonvicini, L. Bosisio, M. Bregant, P. Camerini, F. Faleschini, E. Fragiacomo, N. Grion, R. Grosso, G.V. Margagliotti, A. Penzo, S. Piano, I. Rachevskaya, A. Rachevski, R. Rui and A. Vacchi.

Turin, Italy, Dipartimenti di Fisica dell'Università and Sezione INFN:
B. Alessandro, R. Arnaldi, G. Batigne, S. Beolé, P. Cerello, E. Chiavassa, E. Crescio, N. De Marco, A. Ferretti, M. Gallio, L. Gaudichet, P. Giubellino, R. Guernane, M. Idzik, P. Innocenti, A. Marzari-Chiesa, M. Masera, M. Monteno, A. Musso, D. Nouais, C. Oppedisano, A. Piccotti, F. Prino, L. Riccati, E. Scomparin, F. Tosello, E. Vercellin, A. Werbrouck and R. Wheadon.

Utrecht, The Netherlands, Subatomic Physics Department, Utrecht University and National Institute for Nuclear and High Energy Physics (NIKHEF):
M. Botje, J.J.F. Buskop, A.P. De Haas, R. Kamermans, P.G. Kuijer, G. Nooren, C.J. Oskamp, Th. Peitzmann, E. Simili, R. Snellings, A.N. Sokolov, A. Van Den Brink and N. Van Eijndhoven.

Wako-shi, Japan, Institute of Research, RIKEN[*)]:
H. En'yo, K. Fujiwara, J. Heuser, H. Kano, T. Kawasaki H. Onishi, A. Taketani and M. Tanaka.

Warsaw, Poland, Soltan Institute for Nuclear Studies:
A. Deloff, T. Dobrowolski, K. Karpio, M. Kozlowski, H. Malinowski, K. Redlich[23)], T. Siemiarczuk, G. Stefanek[24)], L. Tykarski and G. Wilk.

Warsaw, Poland, University of Technology, Faculty of Physics:
Z. Chajecki, M. Janik, A. Kisiel, T.J. Pawlak, W.S. Peryt, J. Pluta, M. Slodkowski and T. Traczyk.

Worms, Germany, University of Applied Sciences Worms, ZTT[*)]:
E.S. Conner and R. Keidel

Wuhan, China, Institute of Particle Physics, Huazhong Normal University:
X. Cai, F. Liu, F.M. Liu, H. Liu, Y. Liu, W.Y. Qian, X.R. Wang, T. Wu, C.B. Yang, H.Y. Yang Z.B. Yin, D.C. Zhou and D.M. Zhou.

Yerevan, Armenia, Yerevan Physics Institute:
M. Atayan, A. Grigoryan, S. Grigoryan, H. Gulkanyan, A. Hayrapetyan, A. Harutyunyan, V. Kakoyan, M. Poghosyan and R. Shahoyan.

Zagreb, Croatia, Ruder Bošković Institute:
T. Anticic, K. Kadija and T. Susa.

[*)] Associate member.
[1)] On leave from JINR, Dubna, Russia.
[2)] On leave from Frankfurt, Institut für Kernphysik, Johann Wolfgang Goethe-Universität, Germany.
[3)] On leave from Università del Piemonte Orientale, Alessandria, Italy.
[4)] On leave from University of Istanbul, Instabul, Turkey.
[5)] On leave from Instituto Superior Técnico, Lisbon, Portugal.
[6)] On leave from China Institute of Atomic Energy, Beijing, China.
[7)] On leave from Budapest University, Budapest, Hungary.
[8)] On leave from Universidad de Cantabria, Santander, Spain.
[9)] On leave from Henryk Niewodniczanski Institute of Nuclear Physics, High Energy Physics Department, Cracow, Poland.
[10)] On leave from Dipartimento di Fisica dell'Università and Sezione INFN, Cagliari, Italy.
[11)] On leave from Laboratoire de Physique Subatomique et des Technologies Associées (SUBATECH), Ecole des Mines de Nantes, IN2P3-CNRS and Université de Nantes, Nantes, France.
[12)] On leave from University of Technology, Faculty of Physics, Warsaw, Poland.
[13)] Cracow Technical University, Cracow, Poland.
[14)] On leave from National Institute for Physics and Nuclear Engineering, Bucharest, Romania.
[15)] Also at CERN, Geneva, Switzerland.
[16)] Institute of Physics and Technology, Mongolian Academy of Sciences, Ulaanbaatar, Mongolia.
[17)] Institute of Physics, Georgian Academy of Sciences, Tbilisi, Georgia.
[18)] Institute of Space Sciences, Bucharest, Romania.
[19)] Research Centre for Applied Nuclear Physics (RCANP), Dubna, Russia.
[20)] High Energy Physics Institute, Tbilisi State University, Tbilisi, Georgia.
[21)] Department of Physics, Ohio State University, Columbus, U.S.A.
[22)] Universitá degli Studi, Udine, Italy.
[23)] Physics Faculty, University of Bielefeld, Belfield, Germany and University of Wroclaw, Wroclaw, Poland.
[24)] Institute of Physics, Swietokrzyska Academy, Kielce, Poland.

Acknowledgements

The Collaboration wishes to thank all the administrative and technical staff involved in the preparation of this Technical Design Report and in particular: the CERN Desktop Publishing Service; the CERN Photo Service; and the CERN print shop.

The help and advice of A. Denisov and S. White in the design of the V0A is gratefully acknowledged.

The Forward Detector projects would like to give special thanks to Y. Foka for her efforts, A. Gheata for helping us out in a tight spot, and E. Rosso for writing the integration chapter.

Contents

List of Figures

List of Tables

1 Introduction

The forward detector considered in the present document comprises:

- T0 — two arrays of Cherenkov radiators.
- V0 — two rings of plastic scintillators.
- FMD — five rings of silicon strip detectors.

The initial concept of ALICE as defined in the Technical Proposal [1] mentions a set of Micro–Channel Plate (MCP) detectors as the preferred solution to providing the Level 0 trigger and multiplicity information in the forward/backward regions ($|\eta| > 1.5$). The MCP option would have been a novel and elegant way to build a forward detector system, but it was realized that it would have required substantial funds and a major R&D effort and that, the desired functionality could be achieved with existing and proved technologies based on Cherenkov radiators, scintillators, and Si-strip detectors. This led to the division into the T0, the V0 and the FMD, for convenience named the Forward Detectors (FWD). These systems provide different functionalities, but also to some extent functional overlap and complementarity, which is considered an advantage for ALICE.

Since then, work on the three sub-detectors has proceeded independently, although on issues such as integration, electronics, simulations, etc. there has always been good co-operation between the relevant detectors. Therefore, recognizing the common roots and the physical proximity of the modules and anticipating even closer collaboration in the future, it was decided to submit a joint Technical Design Report on the Forward Detectors (FMD, T0 and V0 TDR).

Figure 1.1 shows schematically the location and layout of the Forward Detectors together with the Inner Tracking System and beam pipe. A detailed vertical cut of the same area is shown in a scaled technical drawing in Fig. 1.2.

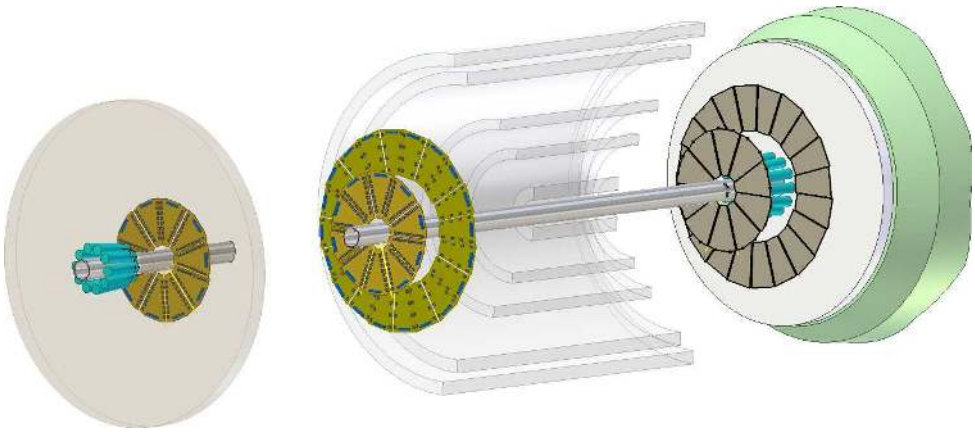

Figure 1.1: Schematic of the placement of T0, V0 and FMD on both sides of the interaction point of ALICE. The five layers of ITS are sketched in the central region.

All three detector systems are located at small radial distances from the beam line. The systems consist of detectors located on both sides (labelled ‘A’ towards RB24, and labelled ‘C’ towards RB26) of the interaction point (IP) and at various distances from the IP. Each system builds on a small number detector assemblies for maximum modularity, ease of manufacture, and reduction of cost. The pseudorapidity coverage of the three detectors is listed in Table 1.1.

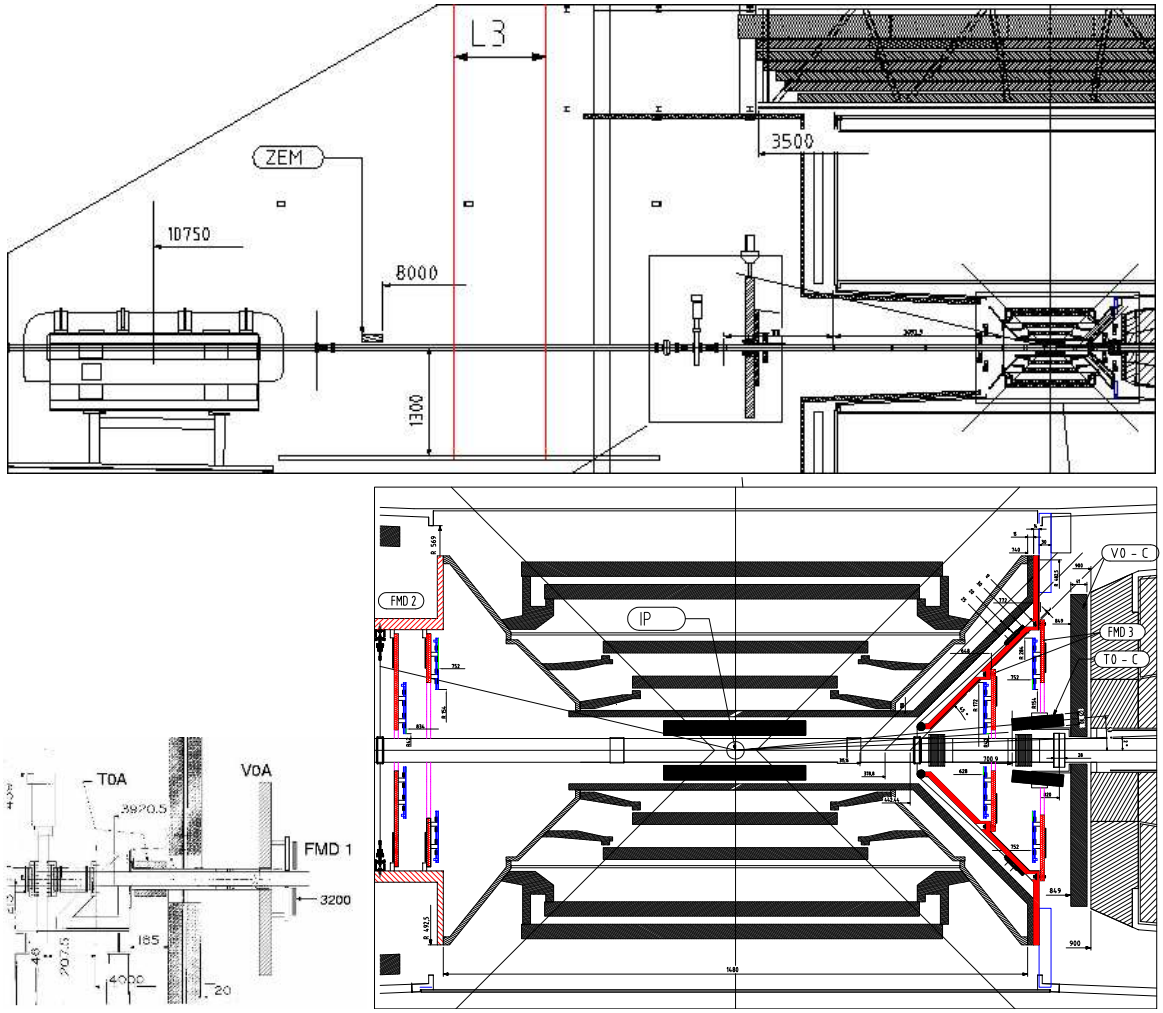

Figure 1.2: Plane view of T0, V0 and FMD together with the ITS and surrounding detector systems in the inner parts of ALICE.

Table 1.1: Overview of pseudorapidity covered by the three forward detectors.

Detector	η_{min}/η_{max}	
	A side (RB24)	C side (RB26)
T0	4.5 / 5.0	-3.3 / -2.9
V0	2.8 / 5.1	-3.7 / -1.7
FMD	1.7 / 5.0	-3.4 / -1.7

Throughout this document, the coordinate system and definitions laid out in Ref. [2] will be used. The right–handed Cartesian system has its origin at the IP and the z axis is parallel to the main beam direction with positive z in the direction of RB24 of the LHC machine (opposite the muon absorber). The x points towards the LHC centre, and the azimuthal angle ϕ and polar angle θ are defined according to the usual conventions. Each side of the experiment from the IP is called A and C, also known as RB24 and RB26, respectively. Figure 1.3 summarizes these conventions. Due to the recent ALICE-wide decision to change the direction of the z axis, z and derived quantities (e.g. pseudorapidity η) are not necessarily consistent with previous ALICE TDRs [3, 4, 5, 6, 7, 8, 9, 10, 11, 12, 13]

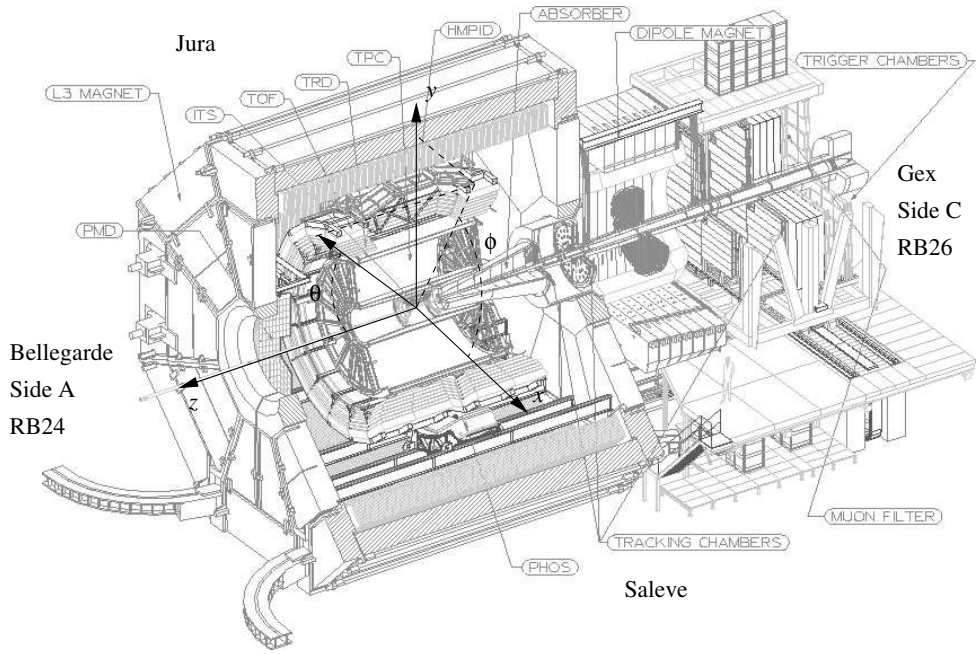

Figure 1.3: Definition of the ALICE coordinate system axes, polar angles and detector sides taken from Ref. [2]

In the following we briefly outline the main physics functionality associated with each of the considered systems.

1.1 The T0 detector

The T0 detector consists of 2 arrays of PMTs equipped with Cherenkov radiators. The arrays are on the opposite sides of the Interaction Point (IP). The main task of T0 is to supply fast timing signals which will be used in the L0 trigger for ALICE, to provide a wake-up call for TRD and to deliver collision time reference for Time-of-Flight (TOF) detector. T0 covers pseudorapidity range of $-3.3 < \eta < -2.9$ and $4.5 < \eta < 5$. The time resolution of T0 is better than 50 ps (σ). The triggering efficiency varies from about 50% for pp collisions up to 100% for A–A collisions. The main trigger signal will be T0-vertex confirming the location of the IP within the pre-defined limits with accuracy of better than 1.5 cm. For A–A collisions, T0 will also give fast evaluation of the multiplicity using a pre-programmed 3-grade scale (minimum bias, central and semi-central).

1.2 The V0 detector

The V0 system consists of 2 disks of modestly segmented (8 segments) plastic scintillator tiles read out by optical fibres. The pseudorapidity coverage of the V0 system is approximately equal to that of the FMD, providing redundancy, although the segmentation is much smaller so the mean number of hits per

detector segment is much higher. The main functionality of the V0 system is to provide the on–line L0 centrality trigger for ALICE by setting a threshold on deposited energy, and to provide a background rejection capability for the di–muon arm. An additional function is to contribute to the rejection of asymmetric beam–gas events, although the modest timing performance of this detector (≈ 0.6 ns) does not yield precise vertex or event timing information.

1.3 The FMD detector

The FMD consists of 51,200 silicon strip channels distributed over 5 ring counters of two types which have 20 and 40 sectors each in azimuthal angle, respectively. The main function of the FMD system is to provide (off–line) precise charged particle multiplicity information in the pseudorapidity range $-3.4 < \eta < -1.7$ and $1.7 < \eta < 5.0$. The read–out time for the system ($\approx 13\mu$s) only allows it to participate in the ALICE trigger hierarchy at L2 and above.

Together with the pixel system of the ITS, the FMD will provide charged particle multiplicity distributions for all collision types in the range $-3.4 < \eta < 5.0$. Small overlaps between the various rings and with the ITS inner pixel layer provide redundancy and important checks of analysis procedures. The maximum mean number of hits for very central Pb–Pb collisions will be less than 3 charged particles per strip. The FMD will also allow the study of multiplicity fluctuations on an event by event basis and enable flow analysis (relying on the azimuthal segmentation).

2 The T0 Detector

2.1 Naming Convention

Practically all the drawings of the ALICE detectors, starting from the early conceptual studies pre-dating the first ALICE Technical Proposal [1] until the most recent ALICE internal notes, show the detector from the same side: the muon absorber is depicted on the right-hand side of the figure (see Fig. 1.3). This resulted in widespread reference to the side occupied by the muon absorber (RB26) as the RIGHT side. Consequently the opposite side (RB24) became the LEFT. The orientation of the z-axis followed the usual convention (from left to right), pointing from the interaction point to the absorber. A change of convention occurred in 2003 [2, 3]. According to the new convention the z-axis now runs in the opposite direction (right to left on all depiction of ALICE) and A, B and C are to be used to indicate detector sides. Table 2.1 clarifies the naming convention change. As far as pseudorapidity is concerned, only the absolute value $|\eta|$ will be used. This will avoid any potential problems in cross-reference to previous publications.

Table 2.1: Conversion between the old and new naming conventions for T0 detector components.

Location	Old Name	New Name
RB24 *(opposite the muon absorber)*	**T0-Left**	**T0-A**
RB26 *(on the side of the muon absorber)*	**T0-Right**	**T0-C**

2.2 Physics Objectives

The T0 detector is required to fulfil the following functions:

1. To supply main signals to the ALICE L0 trigger.
2. To deliver an early (prior to the L0 trigger) “wake–up” trigger to the TRD.
3. To give a start signal with good time resolution for the Time–of–Flight (TOF) particle identification system in ALICE.

The trigger functions requested from T0 are as follows:

- to measure the approximate vertex position;
- to give a rough estimate of event multiplicity;
- to inform that at least one of the arms of the T0 detector has registered a valid pulse.

The first trigger function is crucial for discriminating against beam–gas interactions. With 50 ps time resolution one should obtain ± 1.5 cm accuracy in vertex determination. If the vertex position falls within the pre–defined values, an L0 trigger signal called *T0–vertex* will be produced.

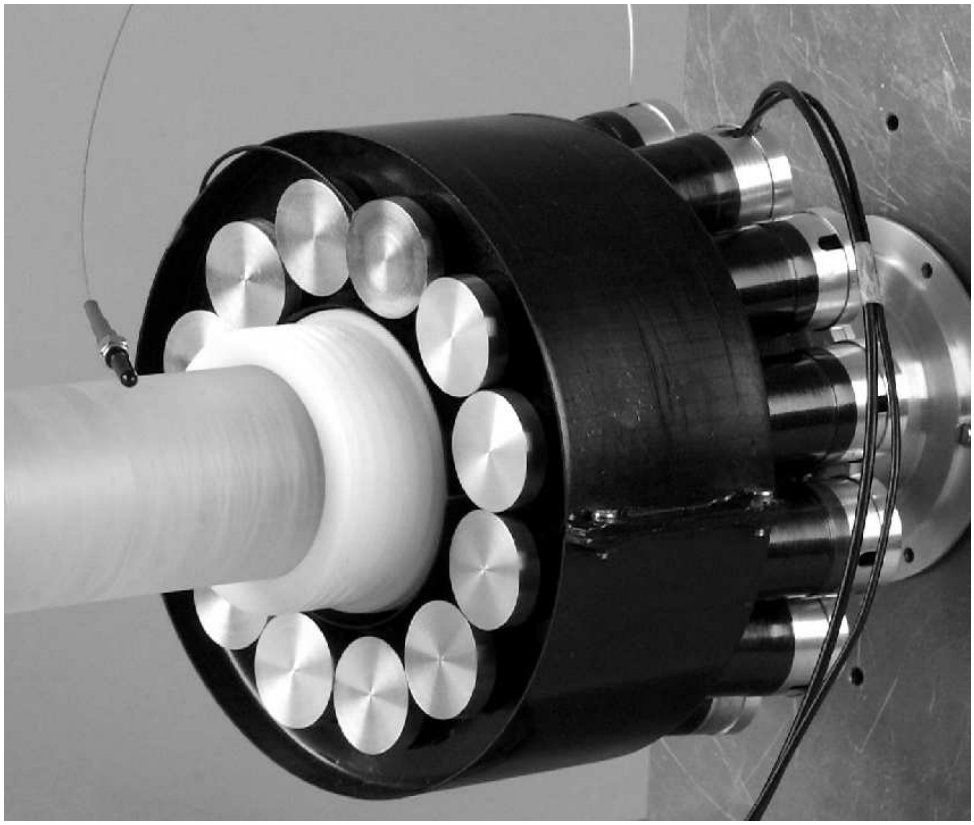

Figure 2.1: Photography of the prototype of T0-C.

The second feature (multiplicity determination) will be an important back–up option for V0 that covers a considerably larger pseudorapidity range. For T0, the covered pseudorapidity range is $2.9 < |\eta| < 3.3$ on the RB26 and $4.5 < |\eta| < 5$ on the RB24. The measured multiplicity will be compared to 2 pre–set values to generate one of the three possible trigger signals: *T0(minimum bias)*, *T0(semi–central)*, or *T0(central)*, corresponding to low, intermediate, and high multiplicities. There will be only two threshold values because the minimum bias signal is identical to *T0–vertex* (sufficient multiplicity to have triggered both halves of the T0 detector). Since the T0 detector generates the earliest L0 trigger signals, all these signals should be strictly generated on–line without the possibility of any off–line corrections.

The early wake–up signal to the Transition Radiation Detector also must be strictly produced on–line. The full list of trigger signals delivered by T0 is listed in Table 2.2.

The T0 detector is the only ALICE sub–detector capable of delivering a high–precision start signal for the TOF detector. This T0 signal must correspond to the real time of the collision (plus a fixed time delay) and be independent of the position of the vertex. The required precision of the T0 signal must be better or at least equal to that of the TOF detector ($\sigma = 50\,\text{ps}$). Generating the T0 start will not be done by any other detector in ALICE so the quality of the T0 time resolution will directly influence the quality of TOF identification. In favourable cases, mostly for HI collisions, one may expect some further improvement of T0 time resolution in off–line analysis. For that purpose it is important to read out and store the time and amplitude of each PMT of the T0 array (see the prototype of T0-C in Fig. 2.1).

2.3 Design Considerations

The requirement to generate the *T0–vertex* pulse for the ALICE trigger and to give an on–line position–independent T0–start signal implies a two–arm design with detectors on each side of the interaction

Table 2.2: List of trigger signals delivered by the T0 detector to the Central Trigger Processor (CTP) and the Transition Radiation Detector (TRD).

Trigger signal	**Purpose**	**Adjustable parameters**[1]
T0–vertex	*Beam gas suppression*; Will also serve as *minimum bias*; *Can not* be used to study *beam gas interactions* because Cherenkov detectors are direction sensitive.	*Two programmable thresholds* defining the upper and lower limit for the acceptable time difference in arrival time between T0-C and T0-A. The maximum acceptable range is about ± 80 cm.
T0-C(T0-Right)	Useless as stand–alone. To be combined with V0	None
T0-A(T0-Left)	Useless as stand–alone. To be combined with V0	None
T0 semi–central	*Semi–central collisions* (back–up for V0)	*One:* threshold level
T0–central	*Central collisions* (back–up for V0)	*One:* threshold level
TRD wake–up	*Wake–up call*	*None* (There will be 24 delays and 24 thresholds to be adjusted jointly by the T0 and TRD group using laser calibration before each run.)

point. The presence of the muon absorber on the RB26 side of ALICE reduces the available space in that area to a small volume around the beam pipe, to be shared by T0, V0 and FMD. The distance from the interaction point is less than 1 m and there will be no access to that area unless the entire central part of ALICE is disassembled. All in all, only a small detector system could be considered: it must be based on well–tested and reliable technology, capable of maintenance–free operation for at least 10 years.

The total dead time of the detector, including pulse generation and processing, should be less than the bunch–crossing period in pp collisions, that is, less than 25 ns. The detector must tolerate operation inside the L3 magnet in a magnetic field of strength up to 0.5 T.

The list of design considerations can be summarised as follows:

- detectors on both sides of the interaction point
- compact design
- time resolution of about 50 ps;
- high efficiency;
- total dead time of less than 25 ns;
- operation in a magnetic field of up to 0.5 T;
- radiation tolerance up to 500 krad;
- reasonable multiplicity resolution for charged particles;
- high reliability;
- maintenance–free operation.

2.4 T0 Detector Overview

All in all, three different techniques were considered and tested for the T0 detector design: microchannel plate detectors (MCP), resistive plate chambers (RPC) and Cherenkov radiators optically coupled to photo–multiplier tubes (PMT). The most ambitious and challenging of the tested alternatives was based on MCP [4, 5]. If such a detector operates properly and if it covers sufficient pseudorapidity range it will work not only as T0 but also as V0 and FMD. In other words, it will combine the functions of all 3 forward detectors in one. Unfortunately MCP technology is also the most expensive, requires operation in good vacuum and has not been used before in any similar applications. Therefore, considering the available time, manpower and resources as well as proven performance, the ALICE collaboration approved in spring 2001 the PMT solution as the baseline for the T0 detector.

2.4.1 Detector Module Design

Once the PMT technology was chosen, remaining issues included the right tubes, selection of Cherenkov radiators and design the electronics. In this we could learn from the experience of the PHENIX experiment at RHIC, where a very similar detector, based on quartz radiators and Hamamatsu fine–mesh phototubes, has been built and is operated by the Hiroshima group [6]. This group, using 1.6 GeV/c negative pions, has demonstrated a time resolution of 50 ps after off–line pulse shape correction. A 100 ps resolution was obtained without any off–line correction with a simple leading–edge discriminator.

2.4.2 Photomultiplier Tube (PMT)

Currently there are only two manufacturers in the world producing PMTs capable of operation in a magnetic field and fulfilling T0 specifications. The tubes are *R5506* from the Japanese company Hamamatsu (PHENIX's choice) and *FEU–187* from the Russian firm Electron. Both products are fine–mesh phototubes with good timing properties, UV entrance windows, which can operate in the axial magnetic field of 0.5 T.

In a series of extensive tests we have verified that the differences in performance between the R5506 and the FEU–187 are negligible, while the spread in key characteristic parameters of units delivered by the manufacturer in the same batch are very big. For instance, Hamamatsu's catalogue quotes anode sensitivity of 40 μA/Lm, but the actual value can be anywhere from 5 to 300. To produce a detector array giving 50 ps time resolution for any combination of the firing PMTs, they must all match closely. Ordering closely matched tubes sharply increases the price and requires good – preferably direct – contact with the producer, so that user can verify the units selected. Since we have no access to the Hamamatsu plant, but we do have good contacts with Electron, we decided to use FEU–187 (presented in Fig. 2.2).

The additional factor in support of our choice was the price (even an unselected R5506 is twice as expensive as FEU–187). As a precaution the tubes in our design will be interchangeable. This means that if the need arises the change from FEU–187 to R5506 will be possible with only minimal modifications.

2.4.3 Cherenkov Radiator

It is uncertain whether a fast scintillator will survive 10 years of operation under LHC conditions, since most organic materials quickly lose transparency, especially at short wavelengths when they are exposed to high radiation doses. For these reasons we have opted for Cherenkov detectors with fused quartz radiators. Quartz is known to be radiation hard and is transparent to UV. The other advantage of the Cherenkov option is a very fast light emission in comparison with other fast scintillators.

The length of the quartz radiator was estimated based on the assumption that the PMT will respond to the 200-550 nm band of the Cherenkov light emission spectrum — see Fig. 2.3.

Figure 2.2: FEU–187. The outside diameter of the photomultiplier tube is 30 mm.

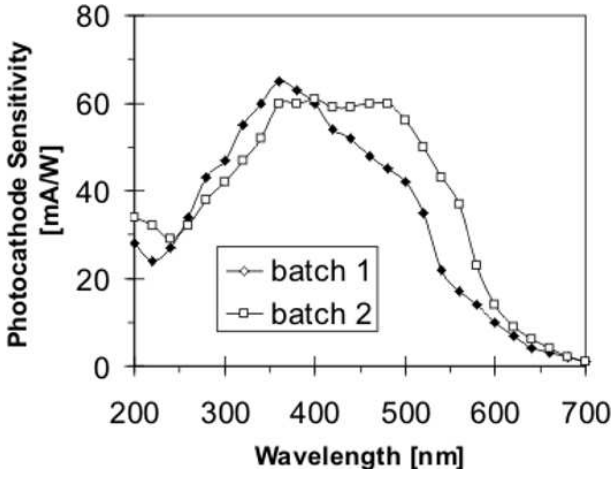

Figure 2.3: Photocathode sensitivity measured for two different production batches of FEU–187 photomultiplier tube.

The average number of emitted photons per 1 cm of radiator is given by the expression:

$$N_{ph} = 2\pi\alpha\,(1/\lambda_2 - 1/\lambda_1)\sin^2\Theta\,. \tag{2.1}$$

For fused quartz the refraction index is $n = 1.458$, yielding $\cos\Theta = 1/n = 0.686$, $\sin^2\Theta = 0.53$. Hence the average number of photons per 1 cm length will be about 770, 440 and 250 for the wavelength bands 200-550 nm, 300-550 nm, and 350-550 nm, respectively. With these values, assuming an average quantum efficiency of the photocathode equal to 15%, we estimate 112, 66, and 38 emitted photons for the corresponding wavelength bands for a 1 cm long radiator. To triple the number of photons one needs a 3 cm long quartz radiator. According to the actual experimental data given in [6], Hamamatsu R5505 with a conventional borosilicate glass entrance window (spectral sensitivity 300-550 nm) or R5506 with a UV glass entrance window (spectral sensitivity 200-550 nm) should give enough photoelectrons to achieve a 50 ps time resolution for the very short and well–focused Cherenkov light emission. We have verified this with our own measurements of the time resolution and dynamic range of the three types of PMTs: Hamamatsu R3432–01 (which is quite similar to R5505), Hamamatsu R5506 and FEU–187.

All tests and calculations indicate that a 3 cm long quartz is a good choice for the Cherenkov radiators of the ALICE T0 detector.

2.4.4 Location and Size of the Two T0 Arrays

To measure the exact time of an event and the vertex position along the z–axis, the T0 detector should consist of two arrays of Cherenkov counters with the IP in–between. On the muon absorber side (RB26) the distance of the array from the IP is limited by the position of the absorber nose. The distance from the IP to T0-C is 70 cm – as close as possible to the absorber. On the opposite side (RB24) the distance from T0-A to the IP is about 3.6 m. T0-C covers the pseudorapidity range $2.9 < |\eta| < 3.3$, and T0-A of $4.5 < |\eta| < 5$. The chosen location of the two T0 arrays inside ALICE is shown schematically in Fig. 2.4.

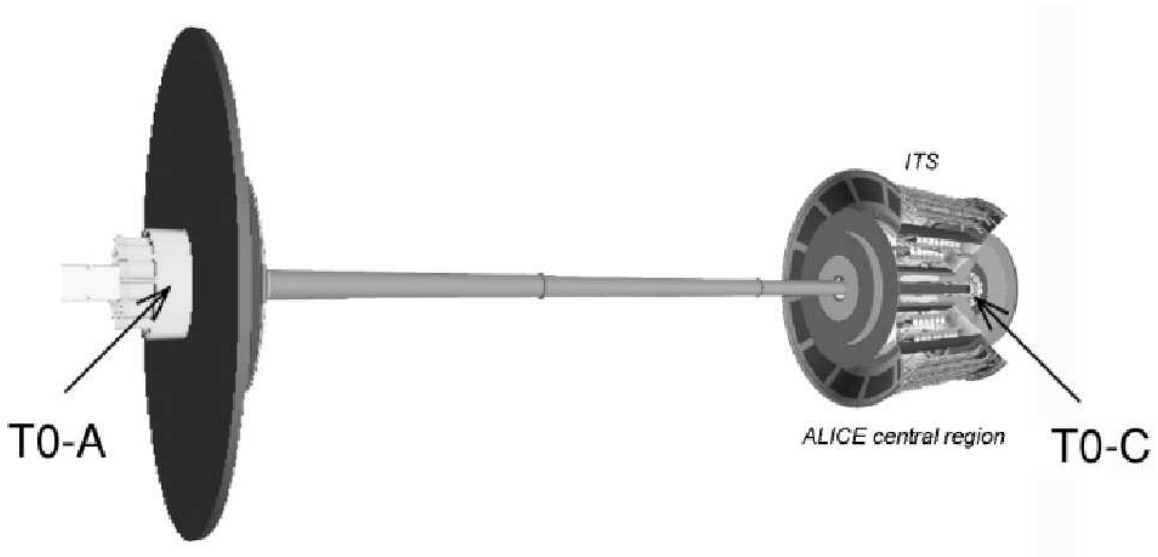

Figure 2.4: Position of the T0 detector inside ALICE.

We have made Monte Carlo simulations of the efficiency and background conditions for this geometry using the latest version of PYTHIA [6.125]. We have included Cherenkov light emission and light collection processes in the simulation procedure. Figure 2.5 shows the resulting track multiplicity for charged particles and gammas for simulated pp collisions (light grey). The y–axis shows the number of generated PYTHIA events for the given multiplicity in the range $|\eta| < 10$. If in the simulated event at least one track produced at least one photon reaching the photo cathode of a PMT in the studied array,

we considered it as registered (hit) and the event was plotted in black. T0-C hits are shown in Fig. 2.5 (top), T0-A in Fig. 2.5 (bottom), and coincidence hits from the same event in both arrays are shown in Fig. 2.6.

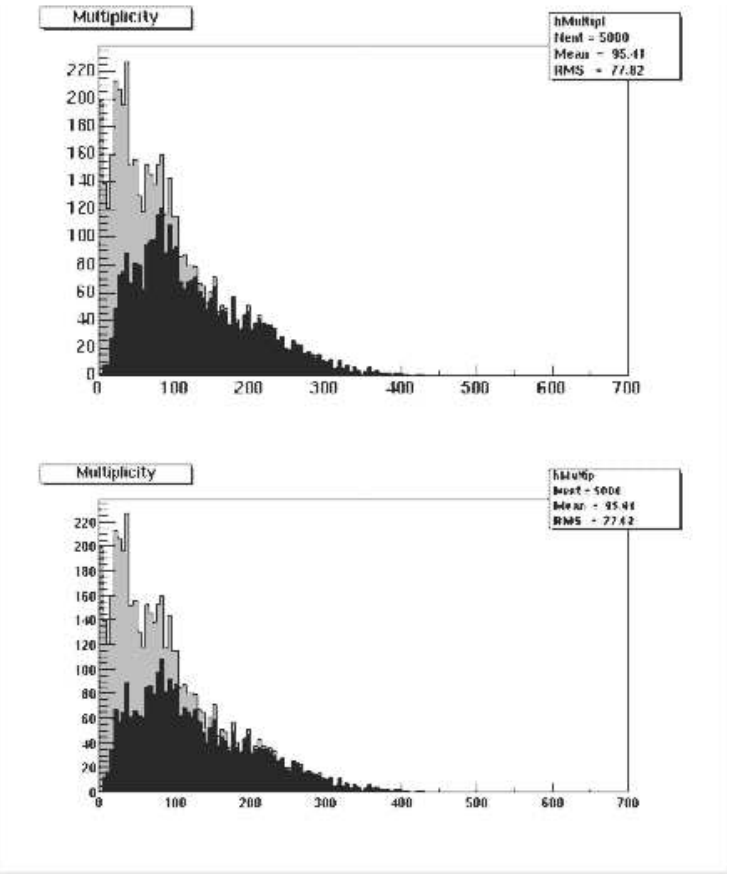

Figure 2.5: Total track multiplicity distribution of charged and neutral particles given by PYTHIA 6.125. Light grey: all events, black: those registered by T0-C (top), by the T0-A (bottom).

One can see that efficiency increases rapidly with the multiplicity of events. It becomes quite satisfactory already at $M > 100$. The combined geometrical efficiency for all processes included in PYTHIA and estimated from these distributions is about 64% for T0-C, 59 % for T0-A, and 45% for the coincidence of both arrays. The actual efficiencies should, in fact, be slightly higher (67%, 60% and 48%) due to photon conversion into electrons in the beam pipe and other material between the IP and the Cherenkov radiators. In heavy–ion collisions, with the exception of extremely peripheral collisions, the efficiency of T0 is always 100%.

The simulations were made assuming that the diameter of the Cherenkov radiators matches that of the outside diameter of the PMT (3 cm for FEU–187). By reducing the diameter one reduces the efficiency correspondingly, but gains slightly in the time resolution. This is because the active area of the photocathode is only 20 mm in diameter. At the moment 30 mm is still the base line for the radiator diameter but there are now good arguments for reduceing it to 20 mm (see Section 2.9.2).

Initially two design options were considered for the T0 array: a smaller version, with just 12 detectors in each array forming a single layer of PM tubes wrapped around the beam pipe, and a version with 24 detectors arranged in 2 layers. Due to the space constraints on the muon absorber side the smaller version was chosen. In fact simulations indicate that, unlike on the RB24 side, the second layer on the RB26 would not considerably improve efficiency as it would already be too far away ($|\eta| < 2.9$). The described calculations were made for the adopted version ($12 + 12$).

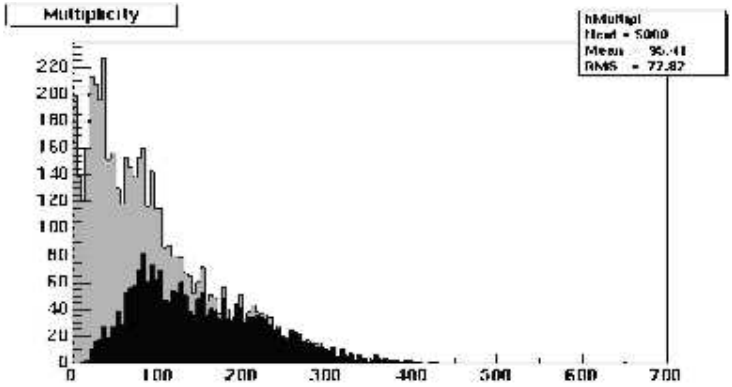

Figure 2.6: Total track multiplicity distribution of charged and neutral particles given by PYTHIA [6.125]. Light gray: all events, black: those registered by both arrays in coincidence.

2.4.5 Laser Calibration System (LCS)

The goal of the LCS is to tune the T0 electronics and monitor the performance of the detector before and during the ALICE experiments. For that reason it is necessary to provide simultaneous light pulses with adjustable amplitudes for all 24 PMTs of the T0 detector. It is highly desirable that the amplitudes of the laser pulses at the input of each PMT cover the full dynamic range of the detector and that the wavelength is well within the sensitivity range of the photocathode. Regrettably, the latter requirement excludes red lasers, which are widely used for instance in telecommunication, and therefore have a very broad range of relatively inexpensive accessories. We have only been able to find one laser that matched our specifications and price range. It is Picosecond Injection Laser PIL040G 408 nm (Fig. 2.7). The maximum power of this laser is close to the limit of that required by our application, therefore it is essential to minimize signal loss along the optical wire and couplings. It is also important that the timing characteristics of the laser pulse should be preserved on the way to the PMT. Otherwise it would be impossible to tune the arrays to better than 50 ps accuracy.

Figure 2.7: PIL040G 408 nm laser.

Tests made with the laser and 20 m long multi–mode optical fibre indicate that the LCS concept sketched in Fig. 2.8 is sound and can be used for T0 calibration. The achieved time resolution for different light outputs is plotted in Fig. 2.9. For the test a manual attenuator was used. In the actual set-up it will be replaced by a computer controlled attenuator (for instance Digital Variable Attenuator `DA--100--3S--830--9/125--M--3`) [12]. The attenuated signal will then be split into 24 identical

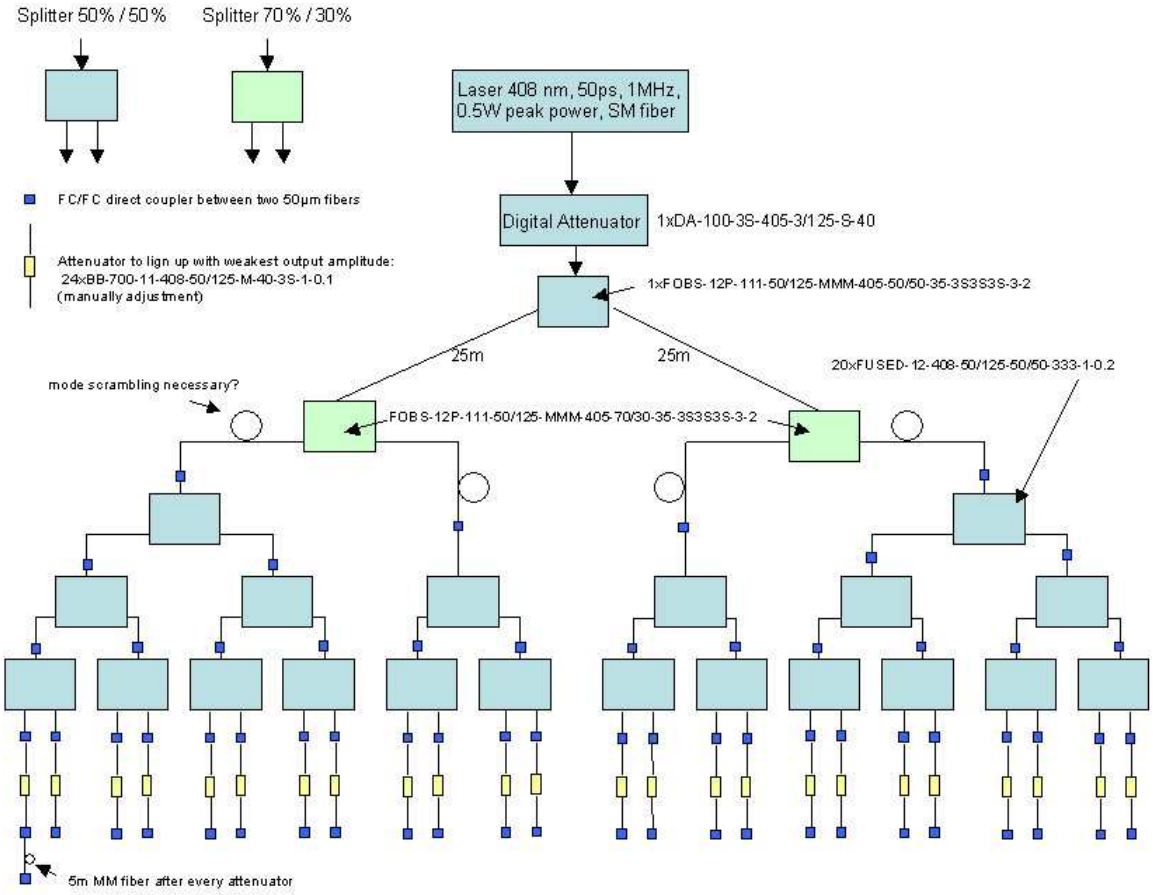

Figure 2.8: Current conceptual drawing of LCS.

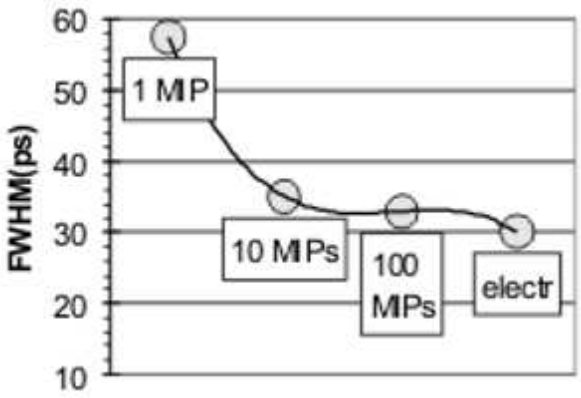

Figure 2.9: Time resolution measured with laser amplitudes corresponding to 1, 10 and 100 MIP. The laser pulse was delivered over 20 m of multi–mode optical fibre. The resolution coming from the electronic noise is also plotted.

pulses and delivered to 24 PMT arrays, about 25 m from the laser. The PMTs will be divided into 2 groups of 12 PMTs and placed in different locations. Each PMT will be equipped with a short (1 m) optical fibre. One end of this fibre will have a standard connector to couple to the 25 m fibre coming from the laser. The other end will be permanently attached to the PMT assembly in such a way as to illuminate the photocathode of the PMT. The design of this part is not yet fixed but most probably it will be just a cut and polished end of the fibre shining directly on the quartz surface in front of the PMT.

2.4.6 PMT Operation Voltages

All the tests have confirmed that FEU–187 can provide very good time resolution in a wide range of bias voltages and magnetic fields (Figures 2.10 and 2.11). Naturally, increasing HV bias rapidly increases pulse amplitude at the output (by up to 3 orders of magnitude) and changes the relative pulse delay by several nanoseconds. Therefore selection of the optimum HV has a big impact on detector performance and must be made with care. Even a slight change of HV bias necessitates retuning of all delays and thresholds, affecting the efficiency and often also the time resolution.

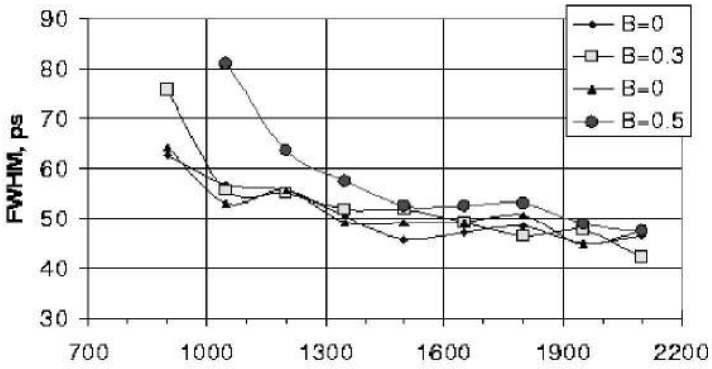

Figure 2.10: Dependency of time resolution on HV bias (V) as a function of external magnetic field strength ($B = 0.3$ and 0.5 T). To demonstrate the consistency of the results two measurements at $B = 0$ T are shown.

Since most of the events in pp and Pb–Pb collisions will be minimum bias events, it makes sense to operate in both types of runs at the same PMT HV. Running at the same voltage is also beneficial for normalization of the results.

While 1 MIP performance is very important, the most interesting heavy–ion events are expected to produce up to 100 MIP signals. This is the main reason why we need signal processing with a sufficiently wide dynamic range to handle all the cases between 1 and 100 MIP. A PMT can produce a maximum signal amplitude of about 5 V. Assuming the linear characteristic of a PMT and taking 5 V for a 100 MIPs signal one obtains the average amplitude of 50 mV for a 1 MIP signal. Due to statistics the amplitude distribution for a 1 MIP particle is very broad, so to get a reasonable efficiency the electronics threshold has to be set at about 1/3 of the average amplitude, i.e. at about 15 mV. These values (15 mV and 5 V) translate to 1:333 dynamic range. Adding a small safety margin the required dynamic range for pulse processing is therefore 1:500. We have shown that it is possible to cope with such dynamic range with a single CFD unit but as a further precaution we shall also amplify the PMT pulses with two different amplification coefficients (1 and 20).

The next important consequence of the 1–100 MIP range is the need to use relatively low HV bias values (about 1000 V) to avoid the distortion of large pulses. We have tested to ensure that even at such low voltages the time resolution remains quite good at 1 MIP and improves with the increase of the light emitted. Keeping the HV bias low we did not encounter pulse saturation up to the 100 MIP level.

To guarantee longevity of the PMT the average anode current (not to be confused with HV divider, which current is larger by nearly 3 orders of magnitude) should be kept below 1 μA even if short bursts of

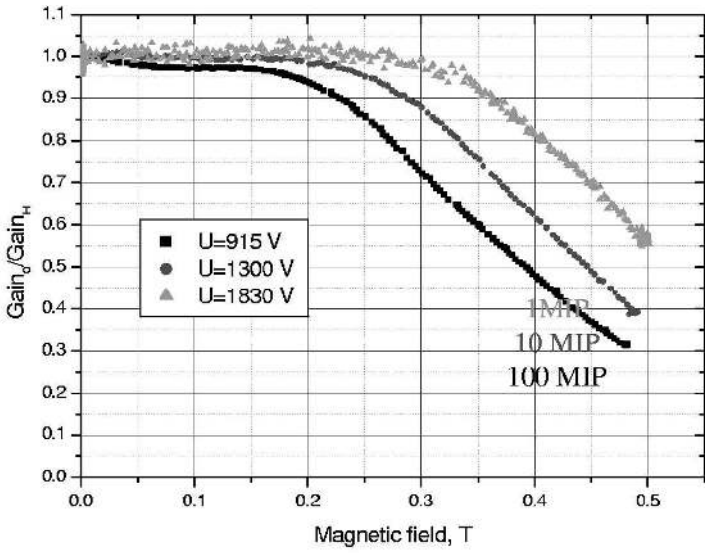

Figure 2.11: Relative PMT gain loss in the magnetic field. The shown measurements were made at 3 different HV bias values and at 3 amplitude settings corresponding to 1, 10, and 100 MIP.

up to 10 μA are acceptable. According to our estimates this condition will be fulfilled with the proposed operation voltage giving 50 mV pulses for 1 MIP. In the calculations we have used nominal luminosities with occupancies and multiplicities generated by PYTHIA and HIJING. If ageing nevertheless takes place it is known from the manufacturer that it will lead to a slow decrease of the gain. This effect is relatively easy to compensate for by increasing the operating voltage. It is also known that after turning HV off for a longer period the PMT partially recovers; its gain factor slowly comes back.

2.4.7 Mechanical Support

A 1:1 mechanical model of T0-C has been build, tested and fully integrated into the central and forward detectors mock–up. The entire support structure (see Fig. 2.12) is made of carbon fibre and other lightweight components. It will be fixed to the muon absorber prior to the installation of V0 and FMD. All the services will be supplied via the dedicated duct (Fig. 2.14) placed on the 12–hour position of the absorber (Fig. 2.13). This location was chosen to minimize the cable length to the TRD "wake-up" box.

2.5 Gain and Time Properties of Fine–Mesh PMTs

The initial studies of the timing properties of fine–mesh phototubes as well as their behaviour in the magnetic field were undertaken in collaboration with Rice University group (USA) and PNPI group (St. Petersburg) for the STAR TOF system [7, 8]. The PMTs under study were Hamamatsu models R5505, and R3432–01, and the Russian FEU–527 produced by the Moscow *MELZ* enterprise in cooperation with the St. Petersburg *Electron* enterprise. Later *Electron* started to produce the same PMTs under the name FEU–187. In 2002 the measurements were repeated at PNPI by the MEPHI group for the latest samples: Hamamatsu R5506 (2 pieces), R3432–01(1 piece) and FEU–187 (similar to FEU–527; 8 pieces). In these measurements light emitting diode was used to imitate a scintillation pulse. We studied the gain behavior at different HV values resulting in a wide dynamic range of the output signals. Typical results of these measurements for FEU–187 are given in Fig. 2.15.

The behavior of the gain in a magnetic field at nominal values of HV does not differ from those obtained for R5505 and FEU–527. At lower voltages the gain falls somewhat faster with the increase of magnetic field compared with nominal high voltage. For all samples we measured the gain in the

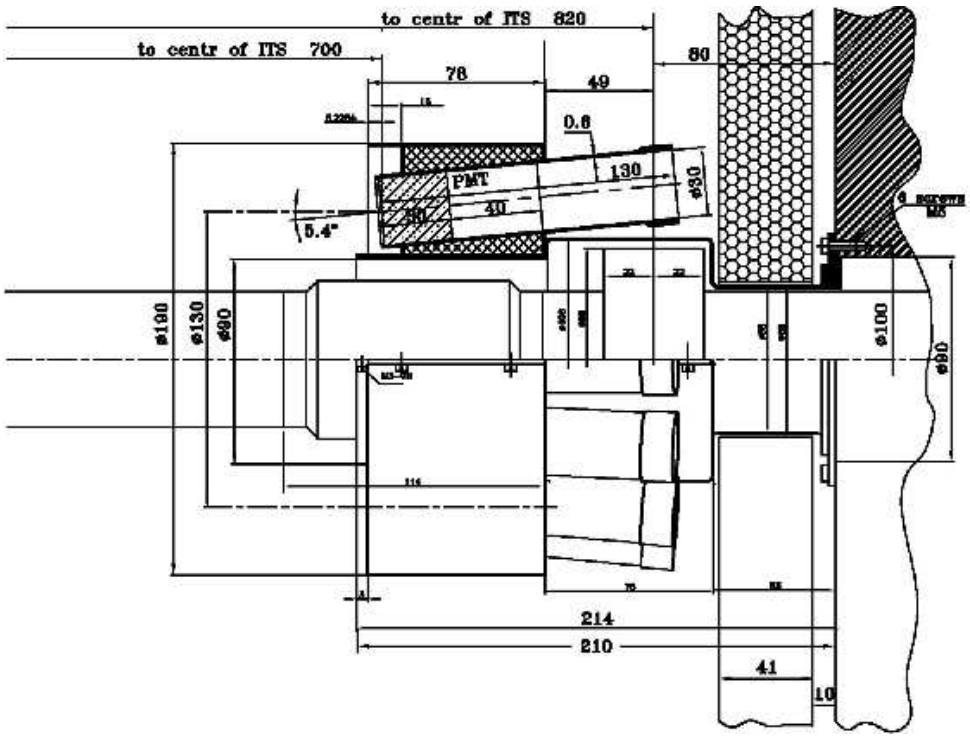

Figure 2.12: Layout of the T0 support on the muon absorber side.

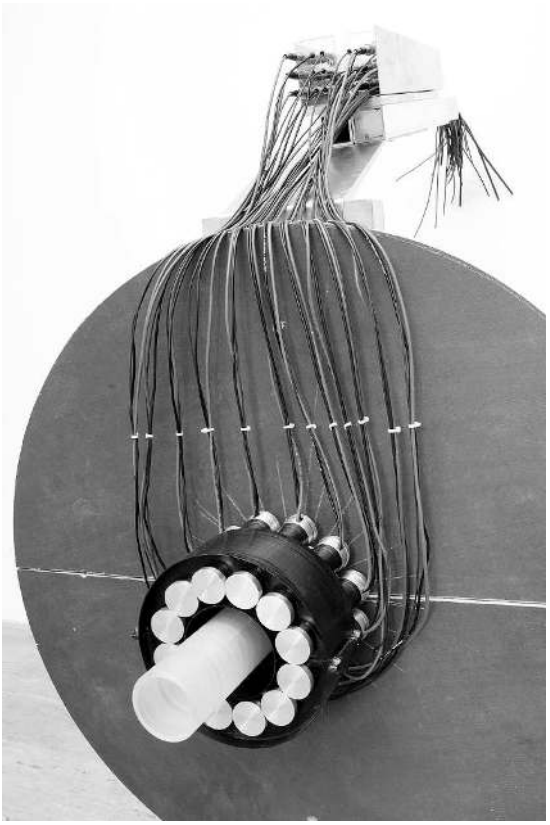

Figure 2.13: Integration test. The plywood structure mocks the muon absorber and the tube, the beam pipe. All cables are fed to patchpanels located in the 12 o'clock duct.

Figure 2.14: T0 patch panels inside the duct on the top of the muon absorber.

magnetic field at voltages corresponding to 100, 10 and 1 % of the nominal gain. Our conclusions are as follows:

1. The differences between the samples are not large.

2. The gain difference for different samples can be easily compensated by changing HV bias.

3. All studied PMTs could operate in magnetic field in a wide dynamic range (1:100).

In order to measure the time characteristics of the tested PMTs at conditions close to those in the Cherenkov detector we have used a pulsed laser (70 ps FWHM). Two types of measurement were made with the laser. In the first run we changed the intensity of the laser pulse and monitored the time resolution and the amplitude. The results are shown in Fig. 2.16.

As expected, the time resolution initially improves with the increase of the light flux and then levels off. At the fluxes expected from the Cherenkov radiator the resolution should stay below 50 ps. Also the flux–amplitude characteristic is good.

In the second run the number of photoelectrons was fixed at about 120–140 and the time resolution and the amplitude were measured as a function of the applied HV. The results of this run are given in Fig. 2.17.

One can see that the time resolution of the fine–mesh PMT FEU–187 remains below 40 ps in a broad dynamic range (at least 1:120) of the output amplitudes. A small decrease in the time resolution at low amplitudes is caused by the increase in electronic jitter [9].

2.5.1 Routine PMT Tests in Magnetic Field

Good test results with selected PMT units cannot guarantee the proper behaviour of the entire production batch. To be sure of that each PMT has to be thoroughly tested in magnetic field. Since each PMT is slightly different, the full set of performance curves at various field and HV settings will be taken

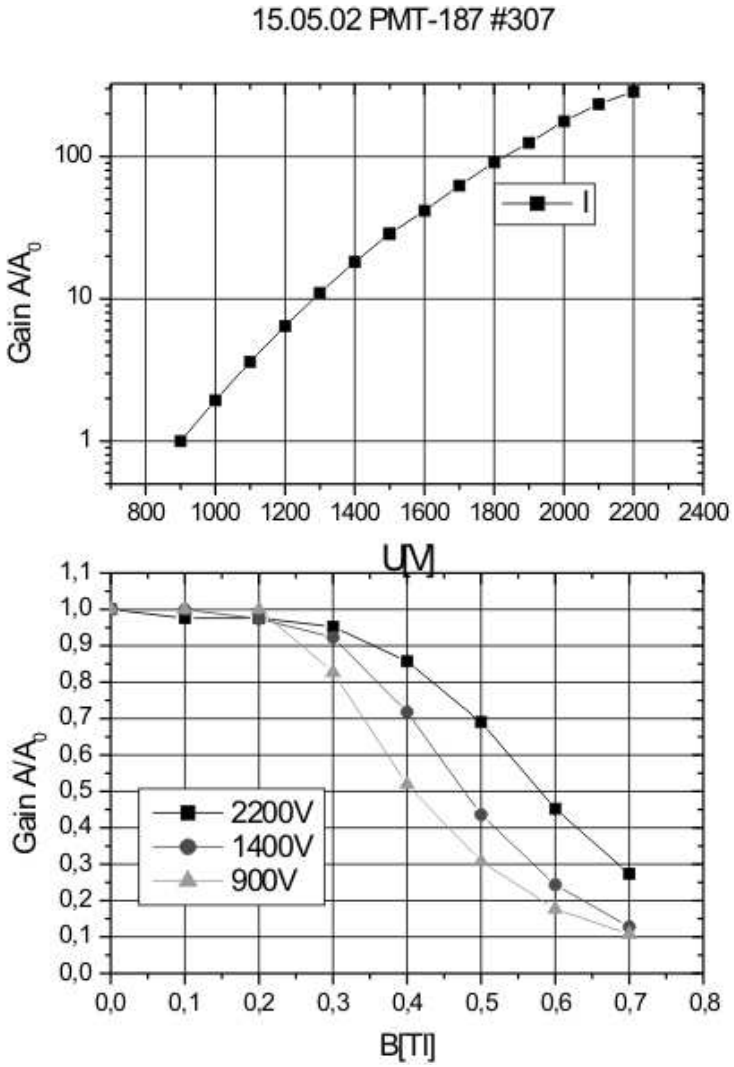

Figure 2.15: Typical characteristics of FEU–187: gain versus high voltage (at 0.5 T magnetic field) and relative gain versus magnetic field at different high voltages.

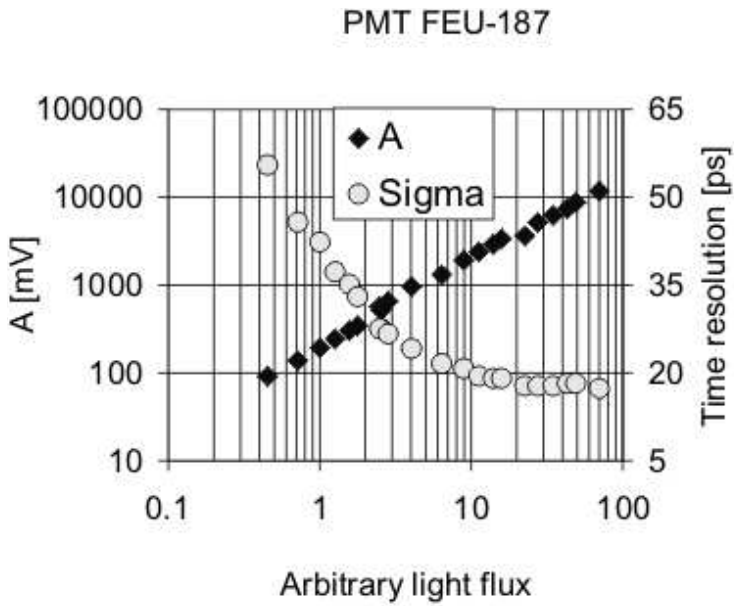

Figure 2.16: Gain and time resolution versus high voltage for typical FEU–187. Arbitrary light flux equal to unity corresponds to approximately 100 photoelectrons.

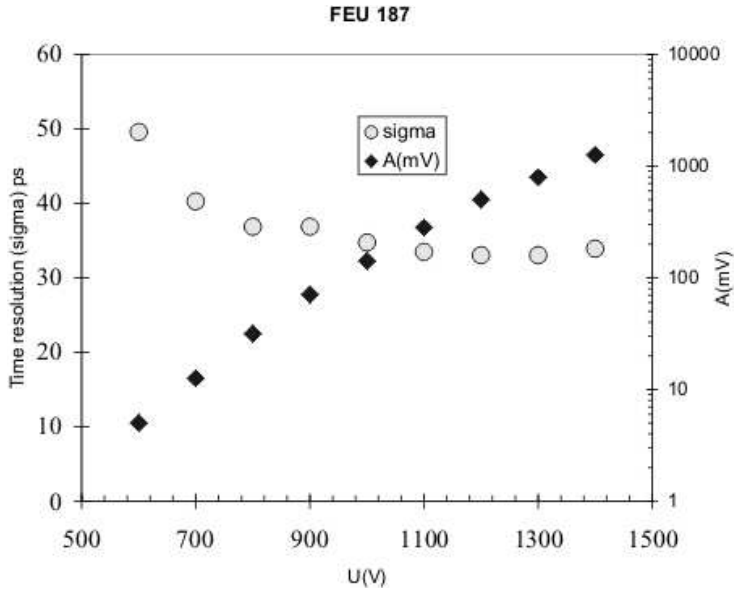

Figure 2.17: Time resolution and amplitudes of the output signal of PMT FEU–187 as functions of high voltage at a fixed light flux equal approximately to 120–140 photoelectrons (1 MIP).

and stored in the detector database. To do that a small air-cooled magnet was designed and constructed (Fig. 2.18). It provides uniform magnetic field of up to 0.5 T inside a volume large enough to accommodate one T0 detector unit. PMT tests with this magnet will be periodically repeated to monitor the performance stability of the T0 modules.

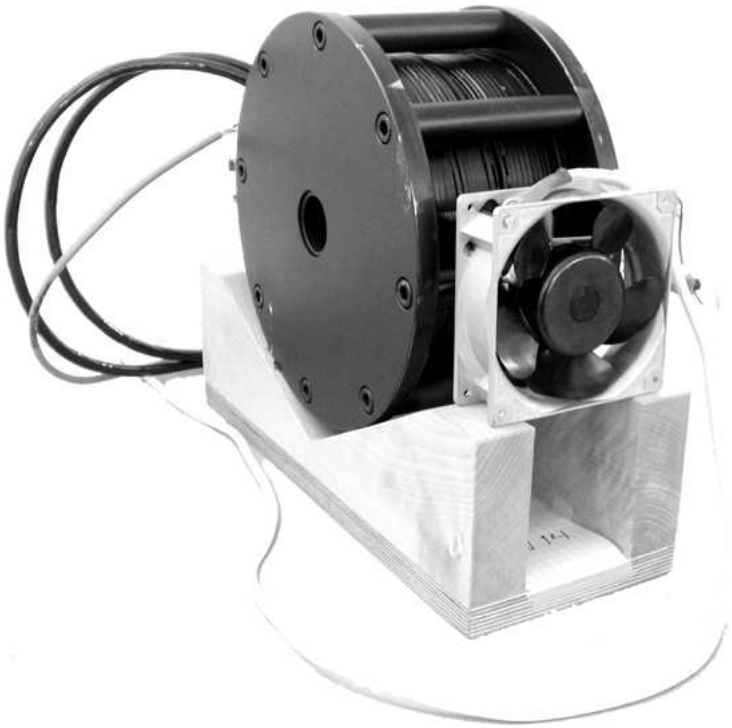

Figure 2.18: A small, air-cooled magnet for testing PM tubes in up to 0.5 T magnetic field.

2.6 Initial Beam Tests of Detector Prototypes

In our R&D studies we have tested different Cherenkov counter option, varying the types of PMTs and radiators. Scintillation counters based on the BC–408 scintillator have also been tested [9, 11, 10].

2.6.1 Experimental Setup

For the first tests we used the mixed ITEP pion/proton beam and the experimental setup of the ALICE ITEP group. This setup was also used in the ITEP studies of the timing properties of RPCs for the ALICE TOF detector. The schematic diagram of the test beam setup is shown in Fig. 2.19.

The test beam facility includes several detectors. S1 and S2 are two identical scintillation counters working as START. Each consists of a PMT XP7229 and BC 408 scintillator $2 \times 2 \times 2.5$ cm. The S3 scintillator, located at a flight distance of 10 m from the START, allows the separation of pions from protons ($p = 1.28\,\mathrm{GeV/c}$) with nearly 100% efficiency. Scintillators F1 and F2 form a cross, defining the beam profile to 0.8×0.8 cm. There were also additional scintillation counters S4 and L1 intended for coincidence operation with other counters if needed. The time resolution of each counter was typically about 50 ps. It was continuously monitored during the run.

The investigated Cherenkov detector (CHD) was about 2 m downstream from S1. The signals from S1, and S2 were fed to a constant fraction discriminator inputs, whereas the signals from CHD were fed to a fast leading edge discriminator with a 60 mV threshold. All TDC channels had an identical 50 ps/channel resolution. A 1024 channel QDC was used to measure the amplitude distributions of the CHD signals. All measurements were made at 1.28 GeV/c for both pions and protons.

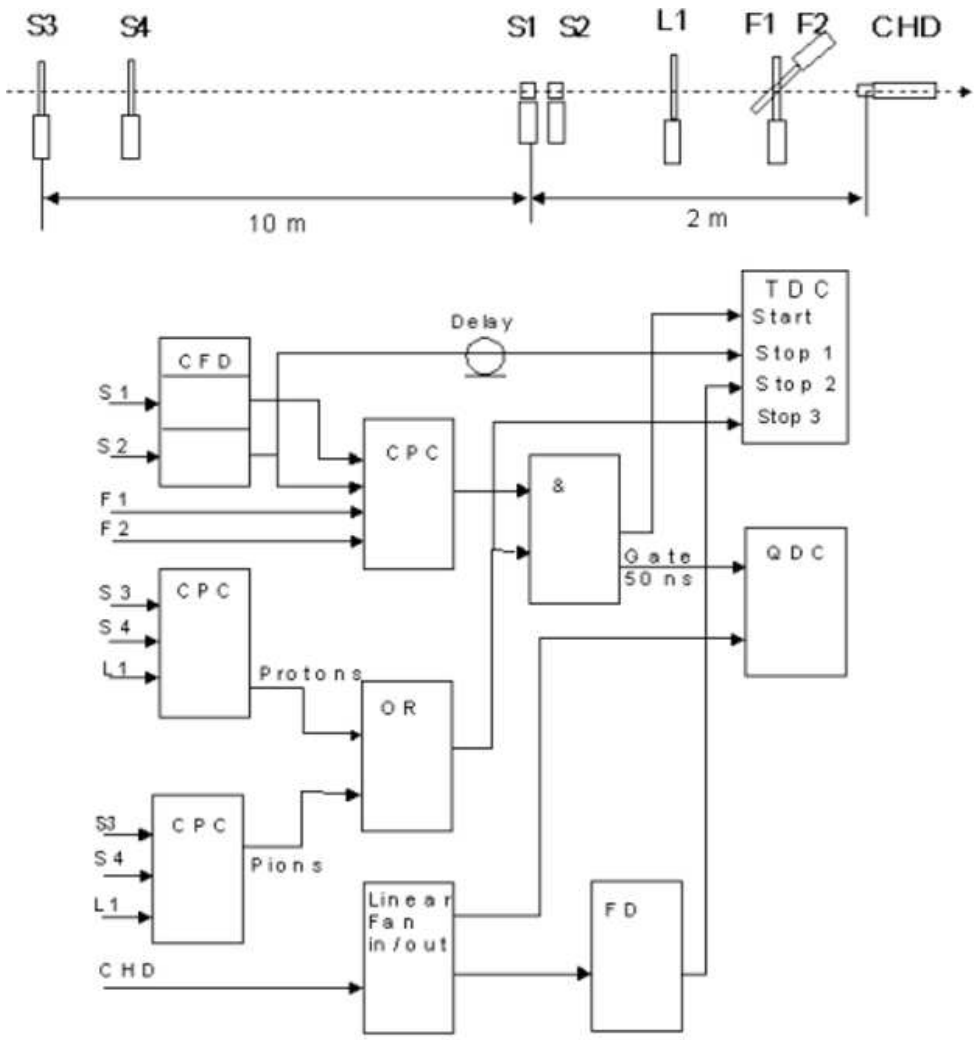

CPC- coincidence / priority circuit
FD - fast leading edge discriminator
CFD - constant fraction discriminator
S1,S2 - scintillation START detectors
S3 - scintillation counter
F1,F2 - Scintillation counters, limiting the beam cross-section to 0.8 cm × 0.8 cm
S4,L1 - beam coincidence counters
CHD - Cherenkov detector

Figure 2.19: Test beam layout.

2.6.2 Experimental Results

We have compared the time resolution of scintillation and Cherenkov detectors using different radiator types and shapes. The scintillation detector used the same PMT but used BC–408 in place of a Cherenkov radiator. The studied radiators included:

1. A cylindrical quartz radiator 26 mm in diameter and 30 mm long.
2. A similar quartz radiator but with a thin Al cover to provide mirror reflection with 98 % efficiency.
3. A Lucite (Plexiglas) radiator of rectangular shape $18 \times 18 \times 30\,\mathrm{mm}^3$.

Among the studied PMTs were Hamamatsu R3432–01 (26 mm diameter) and a Russian fine–mesh PMT FEU–187 (30 mm in diameter). We also used a 20 mm thick BC–408 scintillator with a diameter matching that of the PMT (26 mm and 30 mm correspondingly). A fast leading edge discriminator was used in all runs, and we applied an off–line correction in order to obtain the final time resolution values of each different type of detector.

All our measurements were made at two geometries of the beam: a limited rectangular cross–section beam $0.8 \times 0.8\,\mathrm{cm}^2$ defined by the F1 and F2 counters, and a broad beam illuminating the whole detector. The amplitude distributions of the PMT output signals differed significantly for these two geometries. In the first case all radiator types produced a single–peak Gaussian distribution. In the second case the amplitude distribution consisted of two peaks (Fig. 2.20).

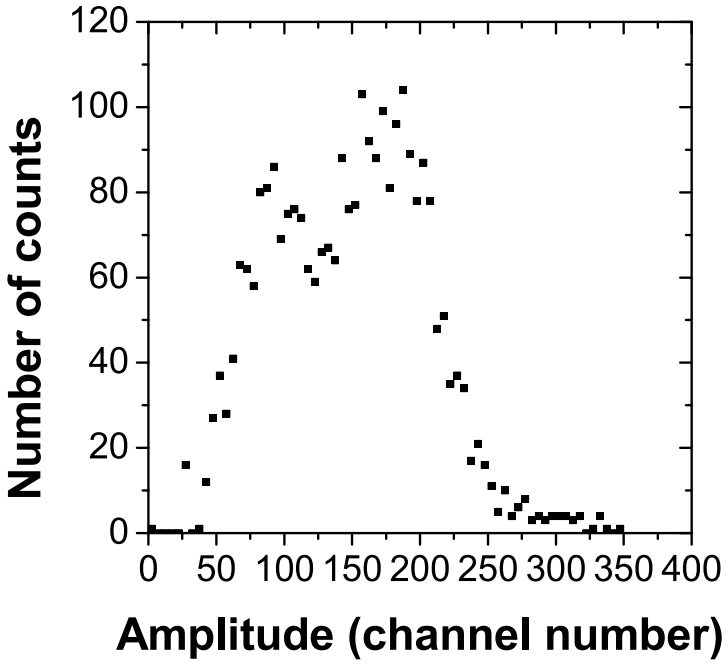

Figure 2.20: Amplitude distribution of PMT output signals for "broad" beam geometry for pions 1.28 GeV/c (cylindrical quartz Cherenkov radiator).

The right–hand part (high–amplitude) of the double peak coincides roughly with the position of the single peak registered with the limited beam. The left–hand bump is at half the amplitude value. A similar amplitude distribution for the broad beam geometry was obtained by the Hiroshima group in the PHENIX experiment [6]. Monte Carlo simulations explain this doubling effect quite well, as will be shown in the next section.

A summary of our results is collected in Table 2.3 and Table 2.4. It is clear that Cherenkov counters give better performance than the BC–408 scintillator. As far as time resolution is concerned both Lucite

and quartz radiators are acceptable. The advantage of a Lucite radiator is a smaller radiation length. The radiation length of Lucite is $X0 = 34.4\,\text{cm}$, whereas for quartz $X0 = 11.7\,\text{cm}$. A 3 cm quartz radiator makes about $0.25X0$ as compared to $0.1X0$ for 3 cm of Lucite. However, the radiation stability of Lucite is only 100 krad, which is substantially less than the expected cumulative dose for the T0 detector. This was the main reason for choosing quartz radiators.

Table 2.3: Typical time resolution values obtained with different PMTs, radiators and scintillators.

Beam geometry PMT	**Radiator/scintillator**	**Time resolution**
R3432–01	Quartz diam 26×30 mm	40 ps
FEU–187	Quartz diam 26×30 mm	42 ps
R3432–01	BC–408, diam 26×20 mm (with a diffuse reflection)	57 ps
FEU–187	BC–408, diam 30×20 mm (with a diffuse reflection)	55 ps
R3432–01	Aluminized quartz diam 26×30 mm	48 ps
Broad–beam geometry		
R3432–01	Quartz diam 26×30 mm	55 ps
FEU–187	Quartz diam 26×30 mm	57 ps
R3432–01	BC–408, diam 26×20 mm (with a diffuse reflection)	80 ps
FEU–187	BC–408, diam 30×20 mm (with a diffuse reflection)	89 ps
R3432–01	Aluminized quartz diam. 26×30 mm	54 ps
R3432–01	Plexiglas radiator $18 \times 18 \times 30$ mm	45 ps

Table 2.4: Results from ITEP accelerator, pions 1.28 GeV/c, March 2, 2002. Broad–beam geometry. Both Lucite and quartz radiators were 30 mm long and their diameter was matched to that of the PMT (26 mm for Hamamatsu and 30 mm for FEU–187)

Run No.	**Type of PMT**	**Type of radiator**	**Time resolution, ps**
3	Hamamatsu R3432–01	Quartz	53
3	Hamamatsu R3432–01	Lucite	50
7	Hamamatsu R3432–01	Lucite	54
8	Hamamatsu R3432–01	Lucite	56
9	Hamamatsu R5506	Quartz	59
10	Hamamatsu R5506	Lucite	75
11	FEU–187	Quartz	55
12	FEU–187	Quartz	58
13	FEU–187	Quartz	52
14	FEU–187	Quartz	42

2.7 Monte Carlo Simulations

Adequate description of the response function of a Cherenkov counter is needed to simulate experimental data and to estimate the influence of the secondaries scattered by surrounding detectors on the performance of the T0 detector. In our first approach we did not use AliROOT because our goal was to compare the results of the simulations with the experimental data obtained in our beam tests. The simulations were based on GEANT 4.2 and confirmed with GEANT 3. We have added own program modules (in C++) describing the conditions of our experiments.

2.7.1 Detector Response Function

We have made simulations of the following beam profiles: narrow, limited ($0.8 \times 0.8\,\mathrm{cm}^2$) beam geometry) and broad beam geometry. In all cases we have assumed fully random, uniform flux of $\beta = 1$ particles flying parallel to the symmetry axis of the Cherenkov counter. The simulations were made for PMT R3432–01 with a quartz radiator 30 mm in diameter, and 30 mm long.

In the narrow beam geometry all particles followed exactly the same path so the light collection efficiency was constant and the PMT output pulse distribution follows the Poisson distribution of photoelectrons emitted from the photocathode. The result of this simulation for particle trajectories on the axis of the counter is shown in Fig. 2.21.

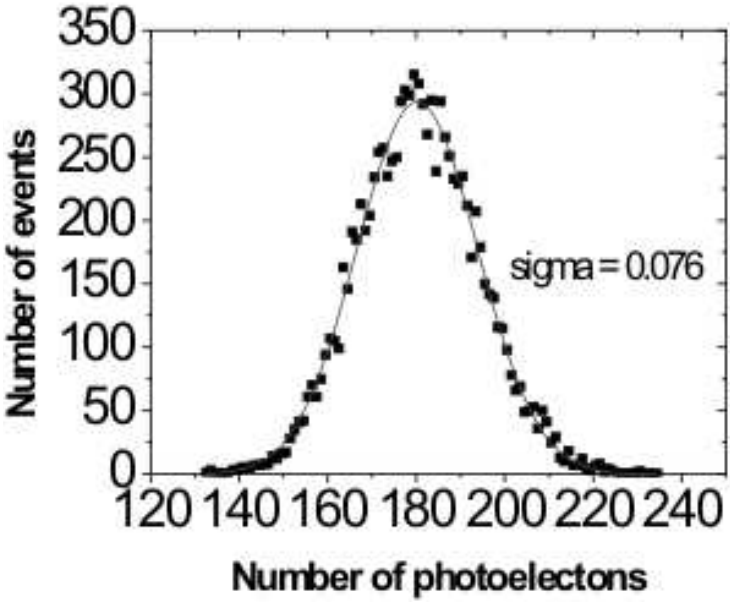

Figure 2.21: Monte Carlo simulations of the number of photoelectrons emitted by particles with $\beta = 1$ traversing the cylindrical quartz Cherenkov radiator along its central axis.

$\langle N \rangle \approx 180$ is the mean number of photoelectrons emitted from the photocathode in response to the Cherenkov light produced in 3 cm of quartz by a relativistic particle. This result is in good agreement with the estimate presented in Section 2.4.3. The value $\eta = 0.15$ was taken as the average of the quantum efficiency of the photocathode in the 300–550 nm wavelength range. The extracted width parameter $\sigma = 0.076$ is consistent with 0.075 calculated placing $\langle N \rangle = 180$ to the formula $\sigma = 1/\sqrt{\langle N \rangle}$.

Since the photocathode of a fine–mesh PMT covers only about 45% of the surface of the entrance window, light collection drops sharply at the edges, as illustrated in Fig. 2.22. This explains the double peak character of the amplitude distribution measured in the broad beam geometry (shown in Fig. 2.20). Figure 2.23 demonstrates the results of Monte Carlo simulations based on the response function of a Cherenkov detector with a cylindrical quartz radiator to the broad beam profile (approximated by realistic two–dimensional Gaussian distribution of the density of the particles in the beam, with $\sigma = 0.85\,\mathrm{cm}$).

In actual ALICE conditions the amplitude distribution of the Cherenkov counters' outputs will be somewhat different from those in Fig. 2.23 because of the changing position of the IP. Gamma rays, originating from the IP and subsequently converting into electron–positron pairs, should also be taken into account. We have done that by implementing into AliROOT subroutines the response function of the Cherenkov counters and generating events with PYTHIA [6.125]. The resulting amplitude distributions for T0-C (0.7 m from the IP, on the muon absorber side) and for T0-A (3.6 m from the vertex on the RB24 side) are given in Fig. 2.24 (without and with the background induced by the beam pipe background).

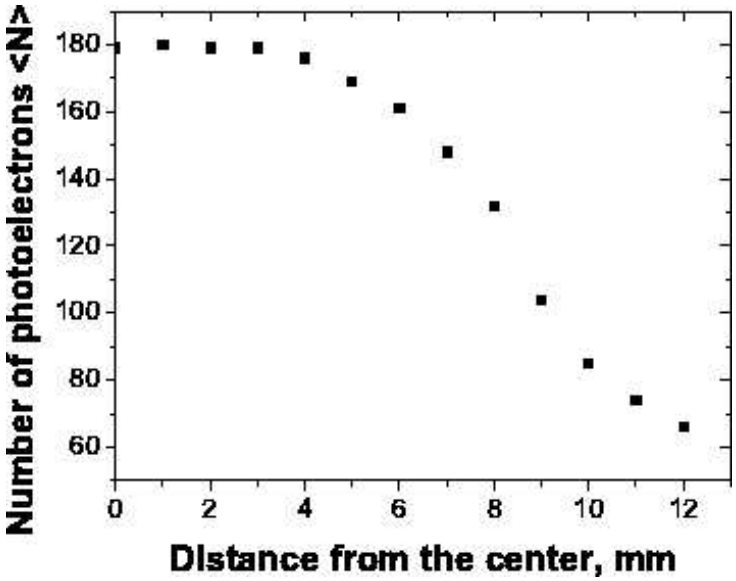

Figure 2.22: Mean number of photoelectrons $\langle N \rangle$ emitted by particles with $\beta = 1$ traversing the cylindrical quartz radiator at different distances from the centre.

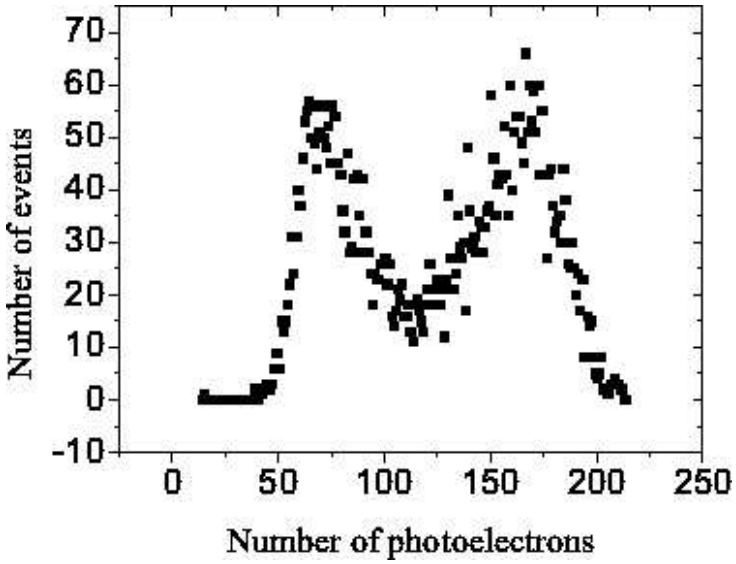

Figure 2.23: Monte Carlo simulations of the number of photoelectrons emitted by particles with $\beta = 1$ in the cylindrical quartz radiator and "broad" beam geometry with "realistic" beam density distribution.

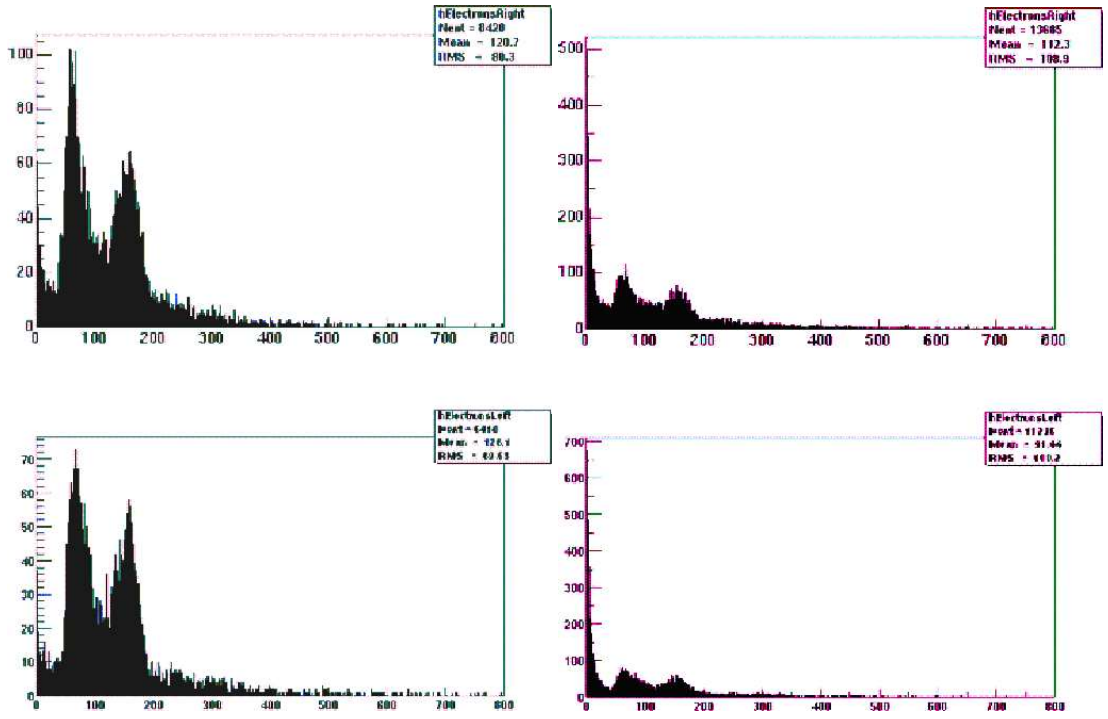

Figure 2.24: Amplitude distributions for the Cherenkov counter in the T0-C (top), and the T0-A (bottom) given by PYTHIA version 6.125. On the left hand side background from the beam pipe is not taken into account, the right hand side does include this background.

2.7.2 T0 Efficiency in pp Collisions

The triggering efficiency of the T0 detector in heavy–ion collisions (due to high multiplicities of produced particles) is nearly 100% and therefore is of no concern at this point. But in pp collisions the involved multiplicities are much smaller and the expected efficiency must be carefully simulated, taking into account not only the response function of the Cherenkov detector but also all the details of geometry, location and thickness of the beam pipe, support structures, etc. In carrying out these simulations we have considered a particle to be registered if the signal from the PMT was larger than 40 photoelectrons. This threshold value was based on our actual experimental data. The background from the interaction of primary particles coming from the IP with the beam pipe was also taken into account. The results of these simulations were shown in Section 2.4.4 (Figures 2.5 and 2.6). Table 2.5 summarizes the calculated efficiencies extracted from the data for all events generated by PYTHIA.

Table 2.5: Calculated efficiencies of the T0 detector for pp collisions

	Right array	**Left array**	**Both arrays in coincidence**
Physical efficiency without beam pipe	62%	58%	43%
Geometrical efficiency without beam pipe	64%	59%	45%
Physical efficiency with beam pipe	67%	60%	48%

The increase of the physical efficiency in the presence of the beam pipe is caused mainly by the conversion of gammas into electrons in the material of the pipe. The efficiencies given in Table 2.5 are averaged over all multiplicities. Efficiency at multiplicities larger than 20 is given in Fig. 2.25.

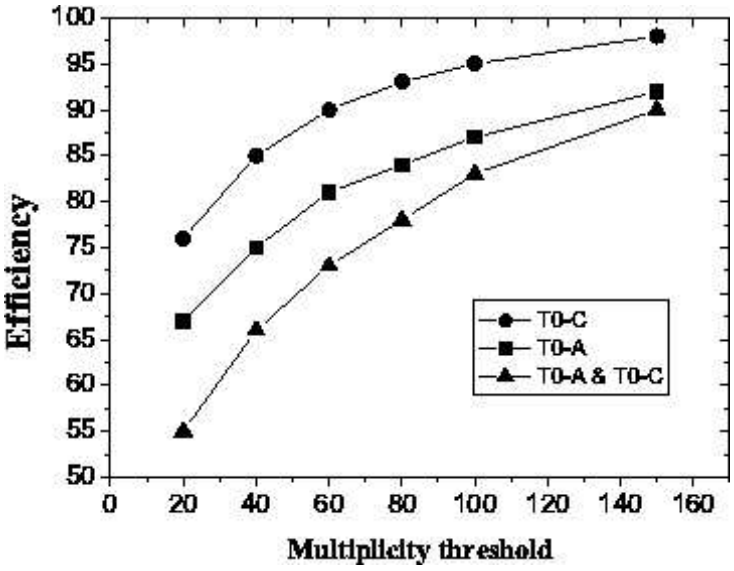

Figure 2.25: Efficiency of registration of pp collisions as function of total multiplicity of events.

At multiplicities $M > 150$ the efficiency of the T0 detector (coincidence of T0-A and T0-C) is already about 90%. It is therefore obvious that for ion–ion collisions the efficiency will be 100%, excepting the ultra–peripheral collisions.

2.7.3 Simulations of Multiplicity Resolution

The T0 detector should generate 3 trigger signals corresponding to the 3 multiplicity levels: minimum–bias, semi–central, and central ion–ion collisions. Such signals could be produced, for instance, by analysing the sum of all PMT pulses with discriminators. Obviously, this procedure will work only in the case of high multiplicities (i.e. for ion–ion collisions). In pp collisions the average occupancy per Cherenkov counter is only about 0.3, making multiplicity determination impossible.

To estimate T0 multiplicity resolution from the sum of PMT signals we have used a simple step–by–step approach. First we estimated multi–particle resolution of a single Cherenkov counter in broad–beam geometry. This can be done in two ways. As the distribution of the particles is random and uniform across the surface of the radiator, one can simply sum the number of photoelectrons for 2 particles, 3 particles, etc. Typical results for this procedure are given in Fig. 2.26. When the number of particles exceeds 3 the photoelectron distribution becomes Gaussian.

The other way is to calculate directly the dispersion $D = \langle n^2 \rangle - \langle n \rangle^2$. For the distribution given in Fig. 2.23 $D = 1936, \sigma_0 = D^{1/2} = 44$ (r.m.s.) and the relative error is $\delta_0 = \sigma_0 / \langle N \rangle = 0.39$ ($\langle N \rangle = 112$). For n particles $\delta_n = \delta_0 / \sqrt{n}$. The results of these calculations are given in Fig. 2.27.

The dashed curve is the function δ_n. The rhombs give the values of deltas obtained from the Gaussian fits of the distributions similar to Fig. 2.26. The solid curve represents the Poisson fluctuations of the number of particles' relative statistical error $\delta = 1/\sqrt{n}$. It is clear that the resolution of a Cherenkov counter for multi–particle events is approximately two times better than the statistical error.

Figure 2.24 characterises the Cherenkov counters' response to the random flux of relativistic particles parallel to the counter axis. Under actual ALICE conditions the angular distribution of particles, gamma ray conversion in the radiator, and the background induced by the beam pipe should also be taken into account. Since full treatment requires a lot of computer time we have settled for simplified approach. To simulate multi–particle resolution of the detector we have used a parametrized HIJING event generator. The multiplicity of events was fixed at a certain value, corresponding to the average number of primary charged particles per Cherenkov counter equal to unity. In the course of simulations (10 000 events)

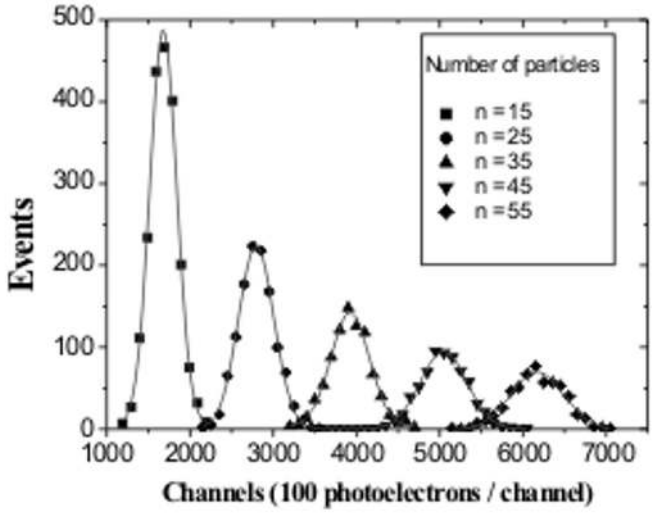

Figure 2.26: Monte Carlo simulations of response functions of a Cherenkov counter for n particles randomly distributed across the surface of the radiator.

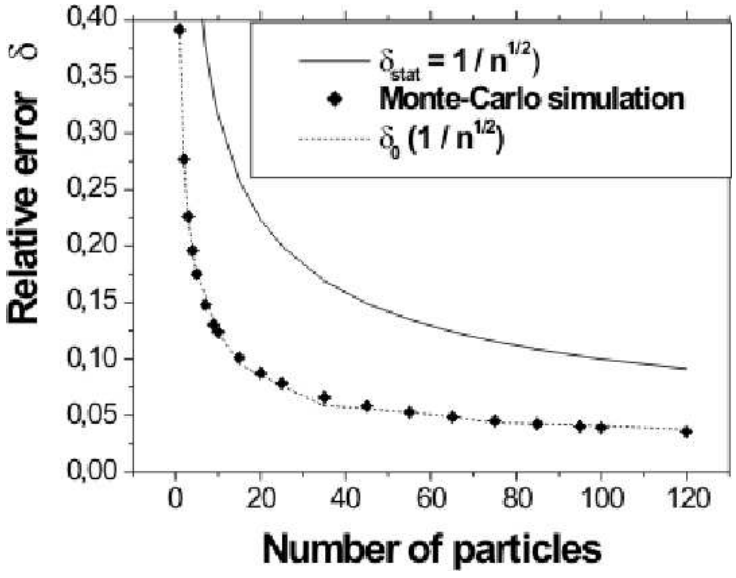

Figure 2.27: Relative statistical errors for the registration of multi–particle events for parallel random charged particles' flux.

we have fixed each amplitude in each Cherenkov counter for each event. The primary gamma–ray conversion in the radiator, as well as the secondary particles (electron–positron pairs and δ-electrons), were also taken into account. The resulting amplitude distribution, averaged over all counters and events, in a single Cherenkov counter is shown in Fig. 2.28. The relative error δ_0 of this distribution is equal to 1.04 (compared to the value 0.39 obtained for the narrow beam geometry hitting the center of the radiator).

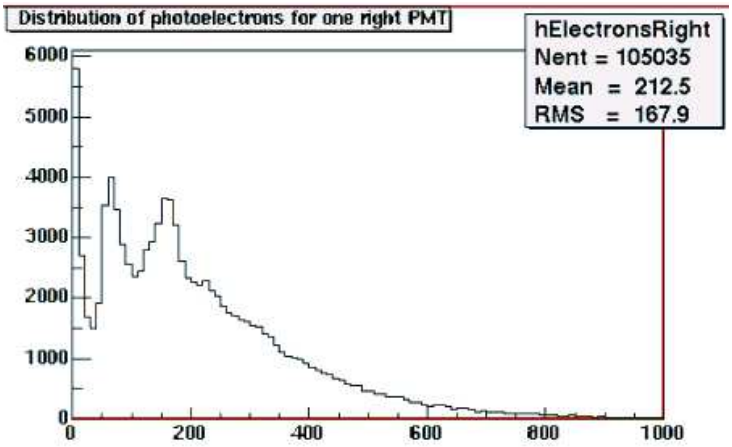

Figure 2.28: Amplitude distribution in one PMT from the (T0-C), averaged over 10 000 HIJING events. Zero amplitudes are excluded from the distribution for reasons of scaling.

The sum of the signals coming from the 12 PMTs of the T0-C and averaged over all events is shown in Fig. 2.29. The shape of this amplitude distribution approaches Gaussian distribution. The relative error δ_0 of the distribution is equal to 0.295, practically equal to that of the distribution for a single PMT divided by $\sqrt{12}$.

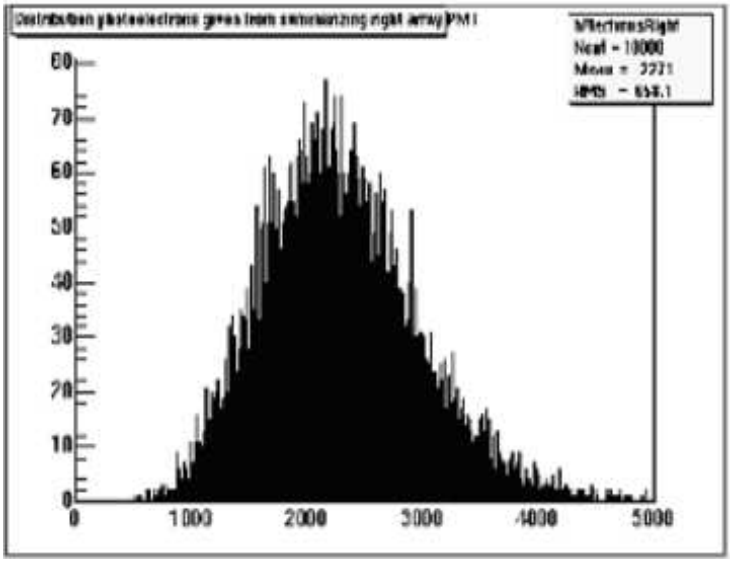

Figure 2.29: Averaged over 10 000 HIJING events, the amplitude distribution of the sum of 12 PMTs' amplitudes in the T0-C.

Note The distributions given in Figures 2.28 and 2.29 include the statistical Poisson distribution of the primaries coming from IP. This Poisson distribution for primary charged particles registered in the T0-C

is shown in Fig. 2.30.

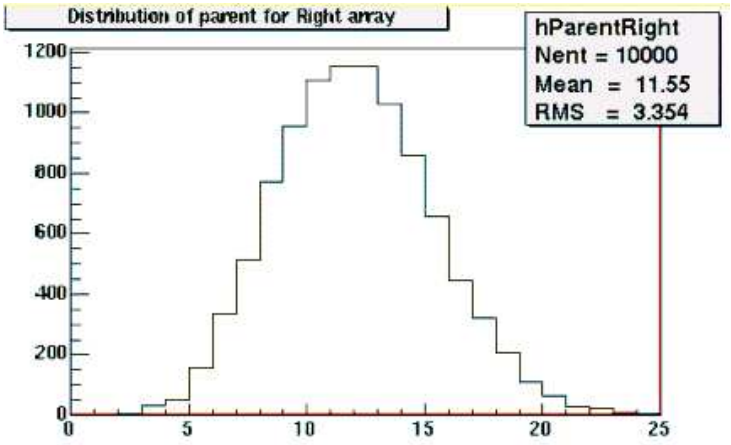

Figure 2.30: Poisson distribution of the number of primary charged particles registered by the T0-C in one HIJING event at fixed multiplicity, corresponding to 1 primary charged particle per Cherenkov counter.

The multi–particle resolution of the array when the average number of primary charged particles per Cherenkov detector is equal to 2, 3, and 4 was obtained by summing the amplitudes for 2, 3 and 4 events.

It is interesting to compare these results with the case when only statistical Poisson fluctuations of the number of primary charged particles are taken into account. Figure 2.31 shows the statistical Poisson fluctuations as a function of the mean number of particles (solid line).

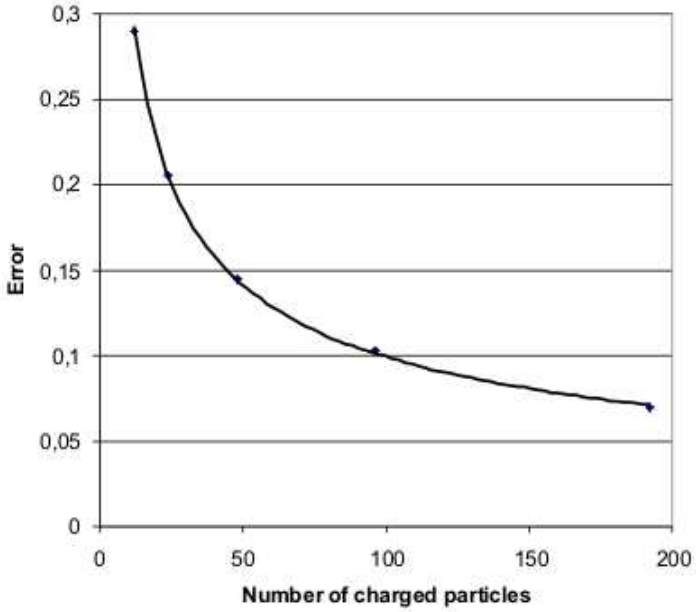

Figure 2.31: Relative statistical errors for the registration of the number of primary charged particles by the T0-A. Solid line – Poisson statistics, rhombs – detector resolution obtained by Monte Carlo simulations.

The rhombs show the statistical errors of charged particle multiplicities defined as above. This coincidence may be explained by taking into account that every Cherenkov counter registers not only primary charged particles but also some primary gammas (which contribute about 20 % of the signals) and charged particles from the beam pipe, the number of which is correlated with the primary statistics. The results of the simulations show, that the actual number of charged and neutral particles registered by each

counter is two times larger than the number of primary charged particles. The same simulations were carried out for the T0-A at a fixed multiplicity corresponding to the mean number of primary charged particles per single Cherenkov counter in the array and being equal to one. The results of the simulations practically coincide with those given in Fig. 2.30 for T0-C.

In conclusion one can say that the multi–particle resolution for primary charged particles of both arrays is determined almost solely by Poisson statistics (statistical error).

2.8 Fast Electronics

The overall diagram of T0 electronics is shown in Fig. 2.32. Signals from each PMT are first sent to the so-called shoeboxes, located some 6 m from the detectors. The main role of the shoeboxes is to split and amplify the signals to generate a wake–up call for the TRD detector. Otherwise no electronics would be required between the PMTs and the main electronics racks of T0 outside the L3 magnet. There the T0 pulses are processed and used to produce the required trigger signals. The time and amplitude information from each PMT will be read out and stored by ALICE DAQ. The T0 readout will be nearly identical to that of the TOF detector. This solution was adopted to cut costs and to guarantee the performance of the T0. Currently TOF is the only ALICE sub-detector that needs non-trigger information from T0.

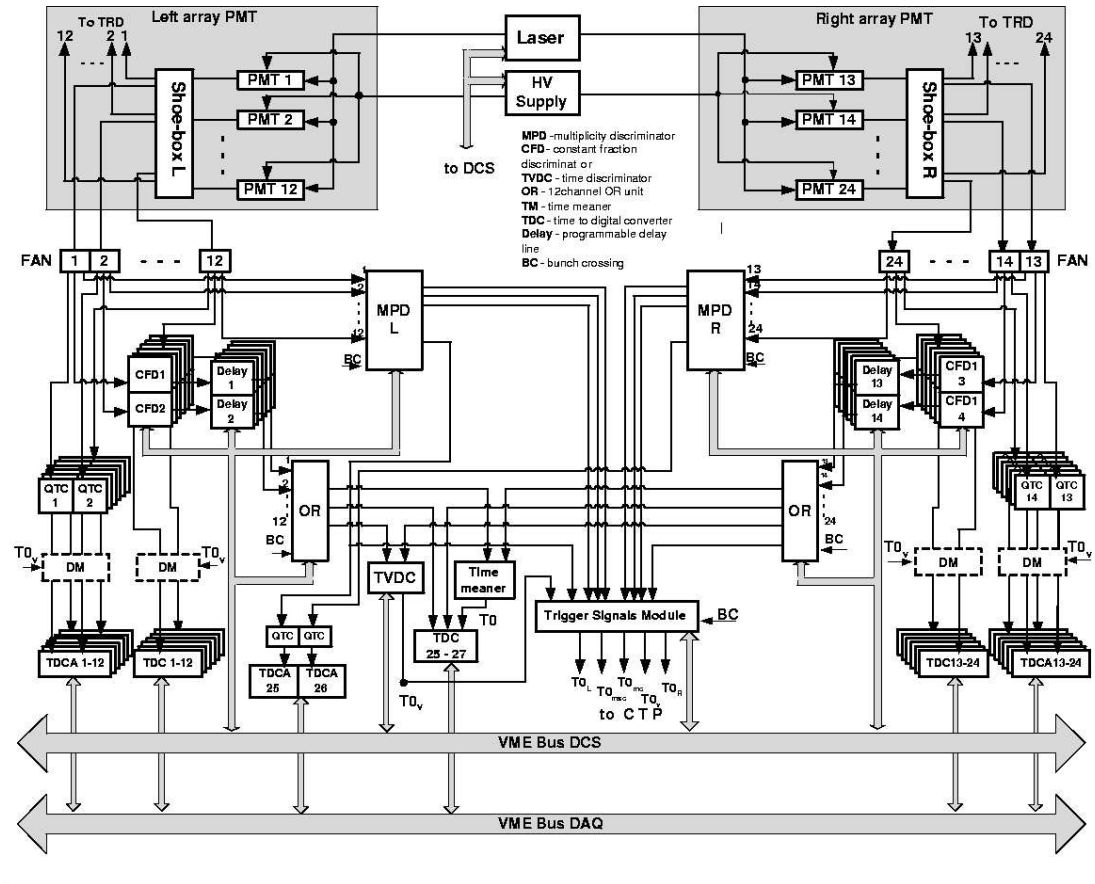

Figure 2.32: T0 fast electronics.

2.8.1 Shoebox with front–end electronics

There will be two separate shoeboxes, one for each arm of the T0 detector. The T0-A shoebox will be a stand-alone unit containing only the electronics for splitting and amplifying the signals. The T0-C

shoebox will be in direct proximity to the TRD wake–up shoebox, where the pulses from all T0 and V0 detector will merge and be processed in a similar fashion.

As discussed in Section 2.4.6 the expected signal amplitude of the input to the shoebox will be from 15 mV up to 5 V. To secure 50 ps time resolution throughout the entire dynamic range it is necessary to preserve as much of the signal's original shape as possible. To prevent the zero level from floating with changing count rate, the ultra–wideband amplifier in the shoebox should be of the direct current type.

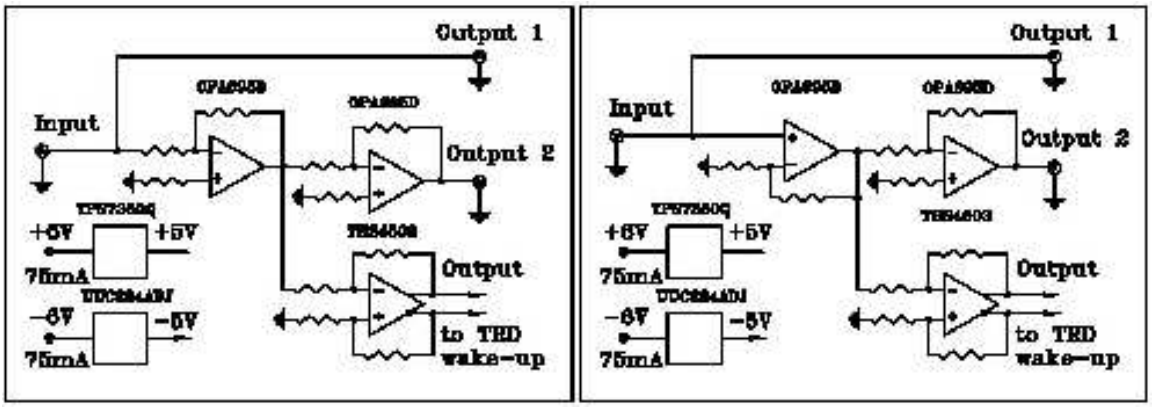

Figure 2.33: Block diagrams of the amplification stage of the shoebox as tested at CERN, 2004 (left), and the improved version (right).

Figure 2.33 shows the "shoebox" used during the June 2004 run and the modified design that will be tried out next. Each channel of the shoebox has one input for PMT pulses and 3 outputs: 1 direct and 2 with gain of about 25. The direct output will go to the wide range CFD (see the next section). In principle, if the CFD works as expected in the full dynamic range, the amplified signal will only be used to improve the accuracy of amplitude digitization. In case of unforeseen problems, the amplified output could also feed to the second CFD working in parallel with the one with the direct signal, allowing for precise off-line corrections.

The TRD wake–up electronics does not need the same time resolution as TOF. Since small time shifts such as those due to saturated pulses are not a problem for the wake–up, and the absence of low amplitude (not amplified) pulses makes the design easier and more tolerant of electronic noise and interference, only the amplified signals will be delivered to the TRD wake–up electronics.

The main construction elements of the shoebox are the OPA695 current-feedback operational amplifier and THS4503 - a wideband, low-distortion fully differential amplifier. Since even these modern operational amplifiers provide the proper bandwidth only for gain below 8, we have had to use a two-stage system, each with gain of about 5. The Printed Circuit Board (PCB) of the prototype was 80 mm $\times$ 75 mm and included two low-dropout voltage regulators providing the amplifier with a clean and stabilised power supply. In the quiescent mode the unit consumes 75 mA from +6 V and from -6 V. At high counting rate the current will increase to 100 mA.

For the next version of the prototype the size of the PCB will be reduced to $50 \times 60\,\mathrm{mm}^2$ and a non-inverting stage will be used to eliminate the passive fan out at the input, which currently gives a slight (50/70) attenuation.

2.8.2 Constant Fraction Discriminator with Wide Dynamic Range

Constant Fraction Discriminators (CFD) are used to determine the arrival time of analogue pulses from fast detectors. As long as the amplitude of the pulse stays within the dynamic range of the CFD, no slewing corrections are needed. The time does not depend on the amplitude of the pulse. A very good CFD, for instance the Phillips Scientific 715 [13] exhibits typical time walk plus slewing of $\pm$75 ps for

amplitudes between threshold and 100 times threshold. As discussed in Section 2.4.6, the dynamic range required in ALICE experiments will be 5 times larger. In principle, off-line slewing corrections are a standard procedure that enables good time resolution even with simpler Leading Edge discriminators (LED). However, considering the need for good on-line performance (trigger) and to stay below the 50 ps range in time resolution, we opted to develop a CFD that will work in a dynamic range of 1:500 (see Fig. 2.34).

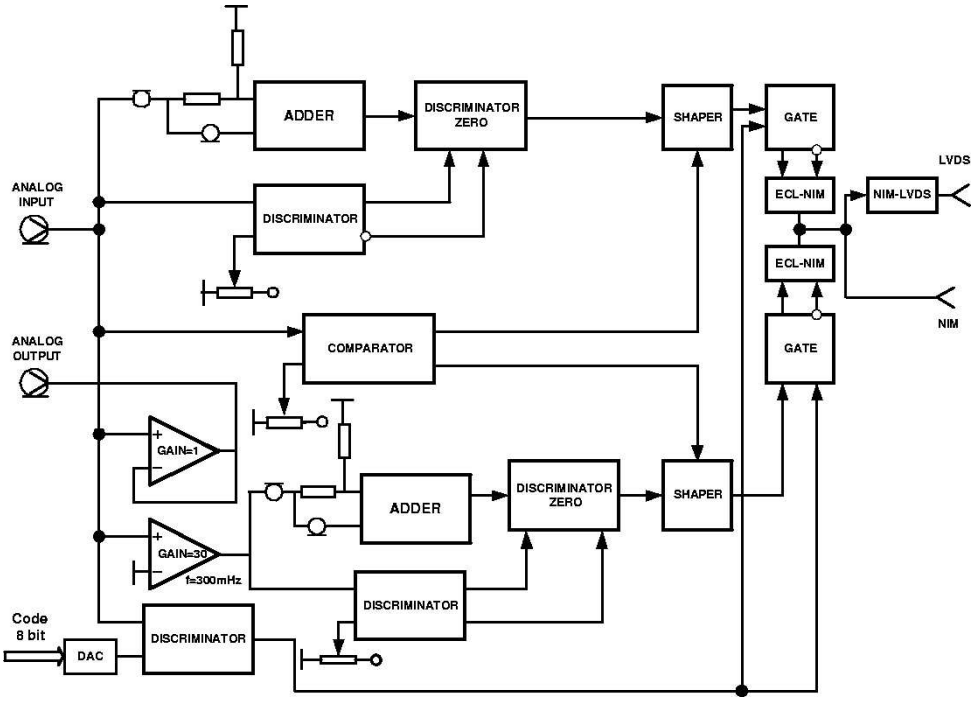

Figure 2.34: Schematic diagram of the prototype of the wide range CFD.

The timing channel of the CFD is implemented according to the traditional scheme, with the detection of zero crossing using an inverted, delayed and attenuated signal. The main difference is in the use of the two signals (amplified and without amplification) instead of just one. In this way our CFD is in fact two CFDs working in parallel and governed by a comparator of output signals. The delay and attenuation values are set by input signal parameters. A lot of attention was paid to the design of the wide-range amplifier. It provides relatively high amplification ($K_{amp} = 22$) while retaining the characteristics of the original input signal. The use of the amplifier is crucial for extracting time signals with low amplitude. On the tested prototype the lowest discrimination level was 4 mV and was restricted only by the noise level of the amplifier stage. The threshold level is set using 8-bit code. The utilization of two channels makes it possible to obtain a timing accuracy of $T = \pm 25$ ps while the input signal ranges from 4 mV to 3 V. The amplitude discriminator commutates the output signals from the first or second timing channels depending on the amplitude of the input signal. The output shapers of the unit generate the signals in NIM and LVDS standards, matching the requirements of the receiving units.

The buffer amplifier incorporated into the tested CFD prototype has gain $K = 1$ and serves as an input signal splitter.

2.8.3 T0 Vertex Unit

Determination of the IP of each collision and comparing it to preset minimum and maximum values is one of the main trigger functions of the T0 detector. The unit intended to perform these operations is the T0 Vertex Unit or TVDC. The main parameters of the TVDC are determined by the expected size of the

interaction area (0.7 m), nominal resolution of the measurements (± 1.5 cm), and the working frequency of the LHC (40 MHz). Accordingly, the TVDC should meet the following requirements:

- time range of ± 2.5 ns(5 ns);
- nominal time resolution of 20 ps (for 8-bit conversion);
- total dead time below 25 ns.

The block diagram of the tested prototype is shown in Fig. 2.35.

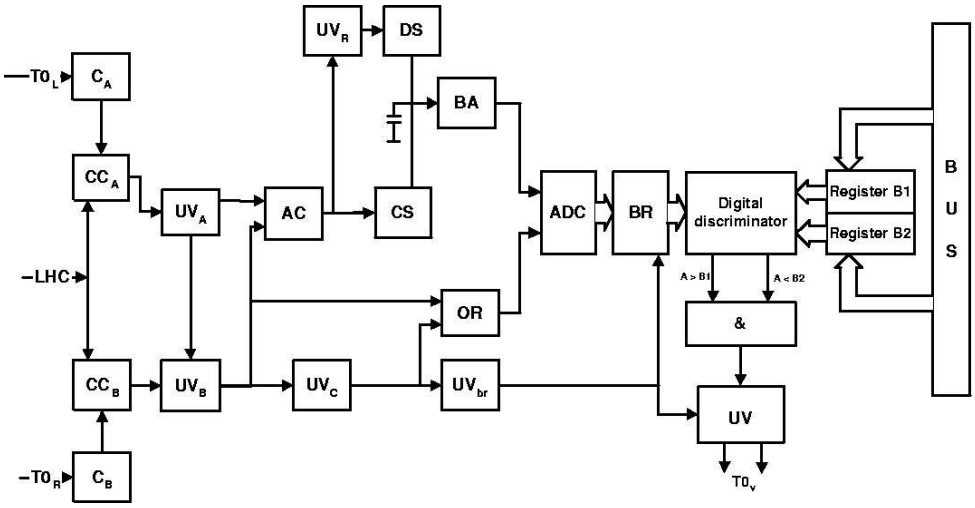

C	= Comparator	BR	= Buffer Register
CC	= Coincidence Circuit	ADC	= Amplitude-Digital Converter
UV	= Univibrator	BA	= Buffer Amplifier
AC	= Anticoincidence Circuit	&	= AND circuit
CS	= Charging current Switch	OR	= OR circuit.
DS	= Discharge Switch		

Figure 2.35: TVDC unit.

The main components of TVDC are the Time to Amplitude Converter (TAC) followed by a flash ADC with digital discriminators for T0 Vertex signal generation. The TAC is designed to generate an output signal only when both input signals come within the allowed time interval (4 ns) and in the presence of the LHC clock signal (or Bunch Crossing signal). The 8–bit flash ADC AD9002 used in the prototype has the encoding frequency 150 MSPS, and 20 ps granularity. The digital comparator K1500CP166 has a delay equal to 3 ns. It generates the T0 Vertex output signal when the code of the flash ADC coincides with one of the preset (allowed) codes of the vertex position. The total dead time of the TVDC unit is, as expected, below 25 ns.

The performance of the first prototype of the T0 Vertex Unit obtained during the July 2003 test run at CERN is shown in Fig. 2.36.

2.8.4 T0 Multiplicity Discriminator

The Multiplicity Discriminator (MPD) generates three logical signals corresponding to the three pre-set levels of desired particle multiplicity. The MPD output goes to Trigger Signal Module (TSM) where all the other T0 trigger signals are converted to the form acceptable by the Central Trigger Processor (CTP). In addition to the trigger function MPD generates analogue sum that will be digitized and stored by ALICE DAQ. The block diagram of the first prototype to be successfully tested at CERN (in June 2004) is shown in Fig. 2.37.

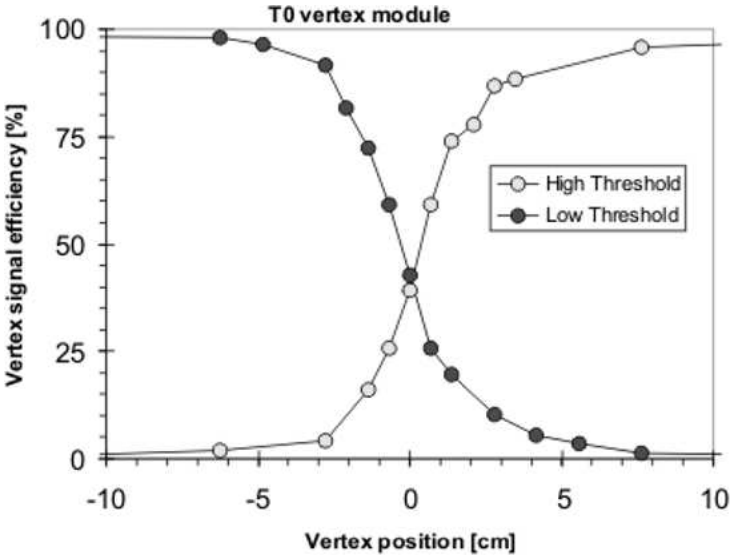

Figure 2.36: Performance of the first prototype T0 Vertex Unit during the July 2003 test experiment using PS beams at CERN.

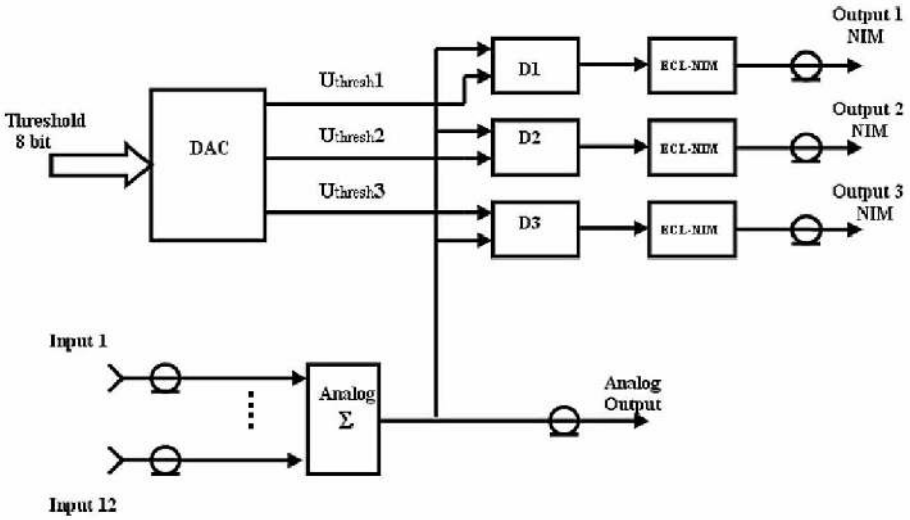

Figure 2.37: Multiplicity Discriminator. DAC stands for Digital to Analogue Converter; D1, D2, D3 indicate Comparators (Discriminators).

The 12 analogue signals originating either from T0-A or from T0-C arrive at the input of an analogue summator (Σ). The summed–up signals than go to the inputs of the three comparators (D1, D2, D3) and one analogue output. The threshold voltages, set with 8-bit resolution, correspond to the low, middle, and high level of multiplicity. These voltages are shaped by the multi-channel Digital to Analogue Converter (DAC) using the digital octal codes written to the RG1- RG3 data registers, allowing for remote control. After additional stretching, the output signals from the comparators come to the outputs of low (Output1), middle (Output2), and high (Output3) levels of multiplicity.

2.8.5 Mean Timer

Just as the time difference between T0-A and T0-C gives vertex position along the z-axis, the average of T0-A and T0-C arrival times cancels this dependence and yields position-independent collision time (plus some fixed delay along the cables, fast electronics, etc.). On-line calculation of the collision time is accomplished by a time-coordinate compensator (Mean Timer) whose schematic diagram is shown in Fig. 2.38. The prototype of the Mean Timer has been tested in in-beam conditions at CERN during the July 2003 run and yielded consistency of about 10 ps of compensation error, as shown in Fig. 2.39. Since the Mean Timer signal (T0) is extracted from two independent pulses, T0 time resolution is better from that of a single detector by about $\sqrt{2}$. The actual results from the 2003 experiment yielded $\sigma_{T0} = 28\,\text{ps}$.

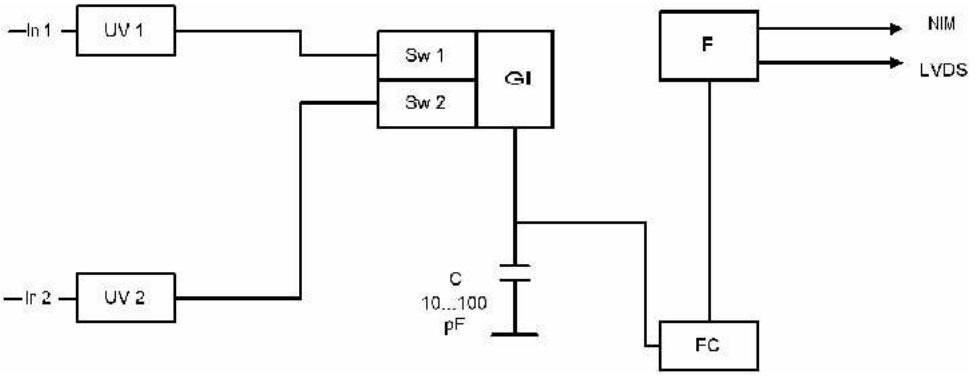

Figure 2.38: Mean Timer. UV1, UV2 are Univibrators (monostable multivibrators); Sw1 and Sw2 indicate switches; GI is a current generator; FC = Fast Comparator; and F is a shaper for forming the output pulses.

2.8.6 Variable Delay Unit

Strict matching of the characteristics of all 24 PMT units forming the T0 detector is simply not possible. As a result each T0 detector tube will operate at a different and individually selected voltage. This alone will cause differences in the arrival times of the signals of up to few ns. To equalize these and comparable differences we have designed the Variable Delay Unit (VDU). Each VDU channel consists of an NIM to ECL converter, an MC100EP195 chip with programmable delay, and an output ECL to NIM converter. A dedicated register connected through an interface with VME is used to record the value of delays. The block diagram of the current prototype VDU is shown in Fig. 2.40.

2.8.7 Charge to Time Converter

T0 will not develop its own readout system but use the one developed for TOF, as explained in the next chapter. The normal procedure to digitize and store the amplitudes of PMT signals would be to use a Charge to Digital Converter (QDC). Although TOF does have provision for a QDC it does not have sufficient resolution to cope with the dynamic range expected from the T0 signals. As the resolution of the TOF TDC is much better it was decided to develop a Charge to Time Converter (QTC) and connect

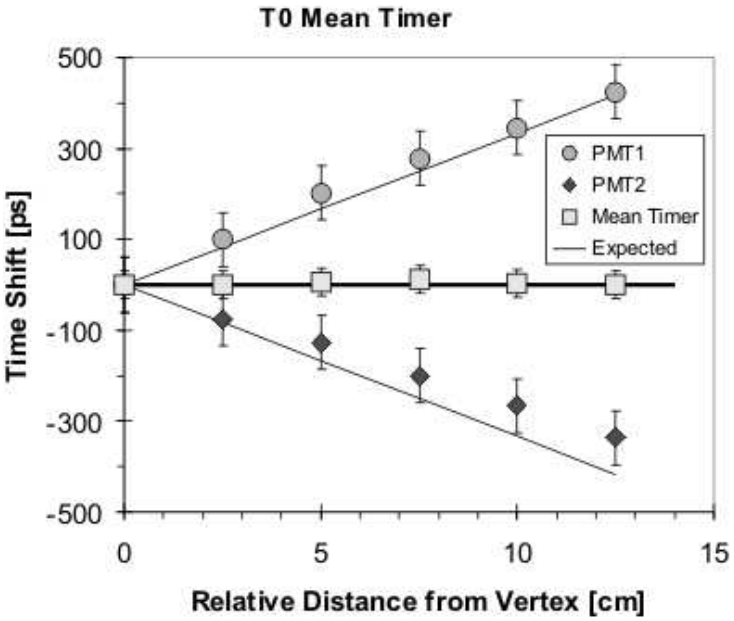

Figure 2.39: Performance of the Mean Timer determined during the July 2003 test run at CERN.

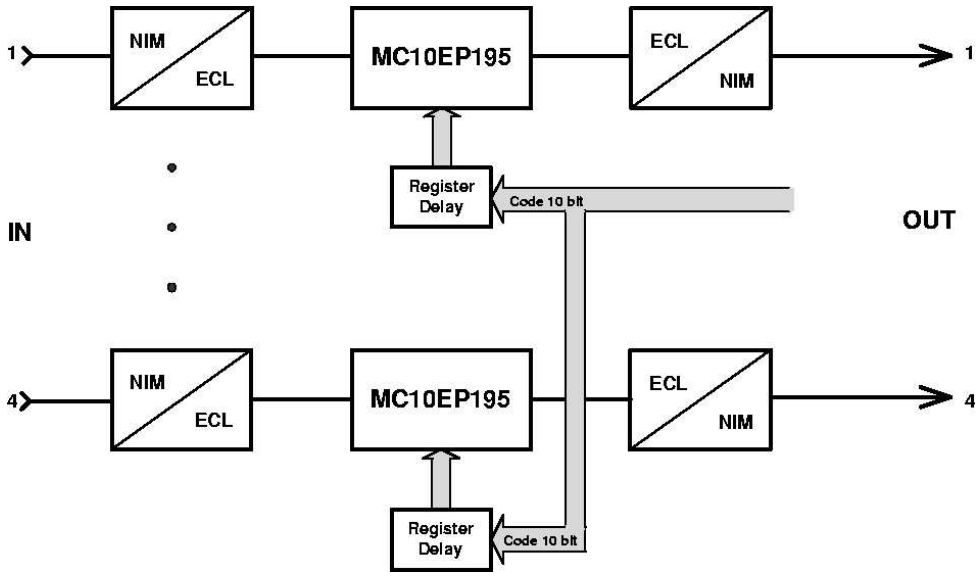

Figure 2.40: Block diagram of prototype VDU.

its output to the TOF TDC for digitization, readout and storage. The same approach is used to digitize the summed amplitude used for multiplicity determination. For unification of the measurements and data transmission to the DAQ, HPTDC converters (designed for other ALICE detectors) are used for final charge-to-code conversion. Thus, the QTC converts the amplitude (charge) to the time delay adequate for coding using an HPTDC converter. The logarithmic characteristic of the converter is necessary due to the wide range in the PMT signal amplitude. From the output of the comparator, the signal goes to the differential circuit (Shaper 1 and 2 in Fig. 2.41), generating pulses bound to the rising and falling edges of the comparator pulse. These pulses go to the ECL-LVDS level converter for shaping into the LVDS format.

The first prototype of the QTC unit was successfully tested during the June 2004 experiment at CERN.

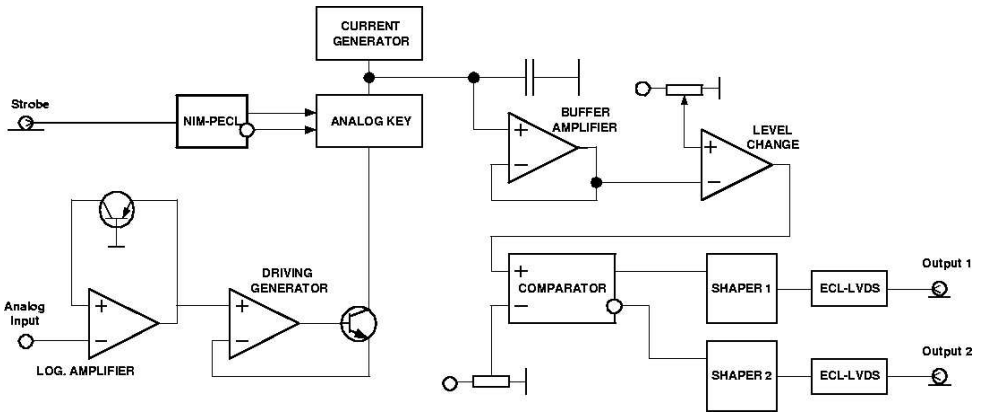

Figure 2.41: Schematic layout of the QTC unit.

2.9 Beam Test of complete T0 system

The beam tests described in Chapter 2.6 were essential to verify the validity of the concept of the detector and to determine the baseline parameters of the main T0 components. Since then progress has been made both in the detector R&D and in the development of the electronics. There have also been important advance in ALICE integration, down to the defining of cables, connectors, etc. With prototypes of all major electronics components, the actual cables, PMTs, and quartz radiators, we have made additional in-beam tests recreating closely the actual ALICE environment. The goal of these tests was to check the detectors and electronics with real signals as opposed to laser and generator pulses in low-noise laboratory conditions and to find out if the baseline parameters (such as the size of the quartz radiators) are indeed the best possible. Two measurements with test beam were held in July 2003 and in June 2004. The first concentrated on the electronics prototypes. During the 2004 session the second generation of prototypes was tested but the main emphasis was on light collection and the pulse shape obtained by various quartz radiators. Otherwise both experiments were very similar so, for the sake of brevity, only the 2004 setup is described.

2.9.1 Experimental Setup

The beam (a mixture of 6 GeV/c negative pions and kaons) that for the purpose of our measurements can be considered as Minimum Ionizing Particles (MIP) as they could easily penetrate all (usually up to four) detectors placed in their path without any nuclear interactions nor appreciable loss of energy. A typical configuration with four T0 detector modules is shown in Fig. 2.42. Usually the first and the last detector worked as triggers while the two middle detectors were investigated. The modules were placed one after

the other and were well aligned with the beam axis. The width of the beam was considerably larger than 3 cm - the diameter of the largest tested detector.

Figure 2.42: Photograph of a typical detector configuration during the 2004 test run at CERN PS. There are four PMT + quartz detector units. Each unit has its own aluminum casting with plastic end cups.

Depending on the need, the individual units could be shifted in respect to each other (to change the relative timing), tilted (to reduce the working area and to check the beam profile) or inverted 180 $^\circ$ to study the pulse from the particles traversing the radiator in the "wrong direction".

Each PMT divider ended with a short pigtail of cables going to a small patch panel on the supporting rail. To reproduce exactly the expected configuration in ALICE the PMT signals were sent from the patch panel to the shoebox prototype (see Fig. 2.43) over a 6 m long cable. From the shoebox the signals were delivered over 25 m long cables to the main electronics rack, just as it will be in the final setup.

2.9.2 Tested Quartz Radiators

The baseline size of the T0 quartz radiator is 30 mm long (see calculations in Section 2.4.3) and 30 mm in diameter. This diameter coincides with the outer diameter of the PM tube (see Fig. 2.2) but is substantially larger than the diameter of the photocathode (20 mm). Larger cross section of the radiator gives a larger solid angle, increasing the overall detection efficiency. In broad beam conditions and assuming perfect electronics the detection probability can be taken as simply proportional to the cross section of the radiator. The price to pay when the diameter of the radiator exceeds that of the photocathode is the deterioration of the shape of the pulse, leading to the loss of time resolution, and decreased efficiency. The best way to verify the results of simulations is to take real measurements. We tested radiators of 3 diameters:

- 30 mm (the current baseline; same as the PMT)
- 20 mm (matching that of the photocathode)
- 26 mm (an arbitrary intermediate value)

The length of all radiators was 30 mm.

Figure 2.43: Photograph of the shoebox prototype (for two input channels) tested at CERN PS in June 2004. The input cables are seen entering from below and the output cables exit from the top. The ribbon cables deliver $\pm 6\,\mathrm{V}$ of power.

Figure 2.44: Test version of the main T0 electronics rack photographed during the 2004 run at CERN.

2.9.3 Time Resolution

The most direct way to determine the time resolution of a detector (σ_{det}) is to use two identical detectors as start and stop and to analyse the collected TOF distribution of mono-energetic particles. Ideally, this would be a Gaussian distribution, therefore:

$$\sigma_{TOF} \approx \frac{\mathrm{FWHM}_{TOF}}{2.35} \tag{2.2}$$

and

$$\sigma_{det} = \frac{\sigma_{TOF}}{\sqrt{2}}\,, \tag{2.3}$$

where TOF stands for Time–Of–Flight, FWHM is full width at half maximum and σ_{det} is the time resolution of the detector (in our case one quartz + PMT Cherenkov module). The ALICE requirement for T0 is

$$\sigma_{det} \leq 50\,\mathrm{ps} \tag{2.4}$$

A typical TOF spectrum obtained during the June 2004 experimental session is shown in Fig. 2.45 and the result for all 3 radiators is summarized in Table 2.6.

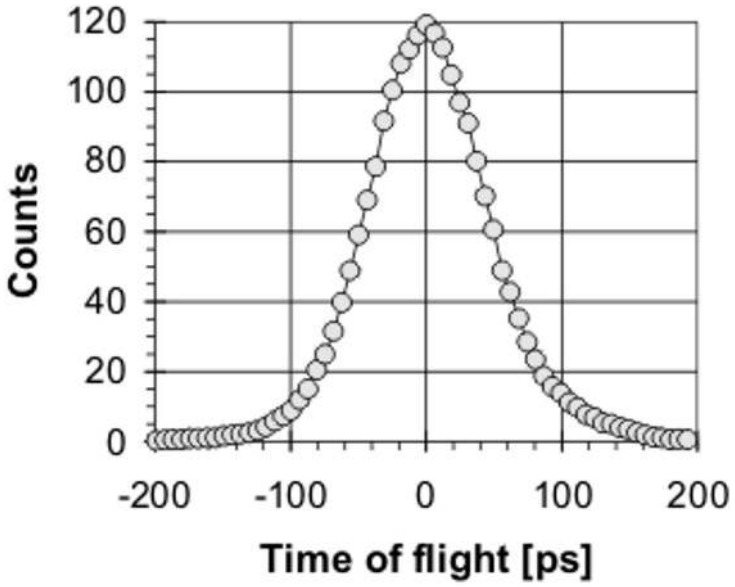

Figure 2.45: Typical TOF spectrum obtained during the 2004 test run at CERN PS. FWHM is 94 ps, which corresponds to $\sigma = 28\,\mathrm{ps}$.

As expected, the best resolution is achieved with the smallest radiator, but even with the current version of the shoebox electronics all results are well within the ALICE specification.

2.9.4 Pulse Shape and Efficiency

Figure 2.46 shows measured amplitudes of the PMT output obtained for 3 different radiator sizes.

The 30 mm diameter radiator produces a broad amplitude spectrum with a characteristic two-hump structure that we have observed before (Fig. 2.20) and is well reproduced by simulations (Fig. 2.23). The lower bump comes from light loss through the area around the photocathode. This gap is smaller for a 26 mm radiator but qualitatively the spectrum is not much different from that of a 30 mm radiator. A great improvement occurs for the smallest radiator i.e., when the diameter does not exceed that of the photocathode. In this case all the light produced inside the volume of the radiator is directed to the

Table 2.6: Dependence of FWHM and time resolution (σ) on the diameter of the Cherenkov radiator. The values in brackets were obtained when the signals were amplified in the shoebox instead of going directly to CFD. Current improvements to the shoebox design should reduce these values, so they are preceded with a less than or equal to sign.

Radiator diameter	**FWHM (TOF)**	**σ (T0detector)**
30 mm	122 ps ($\leq$ 140 ps)	37 ps ($\leq$ 42 ps)
26 mm	112 ps ($\leq$ 128 ps)	34 ps ($\leq$ 39 ps)
20 mm	94 ps ($\leq$ 115 ps)	28 ps ($\leq$ 35 ps)

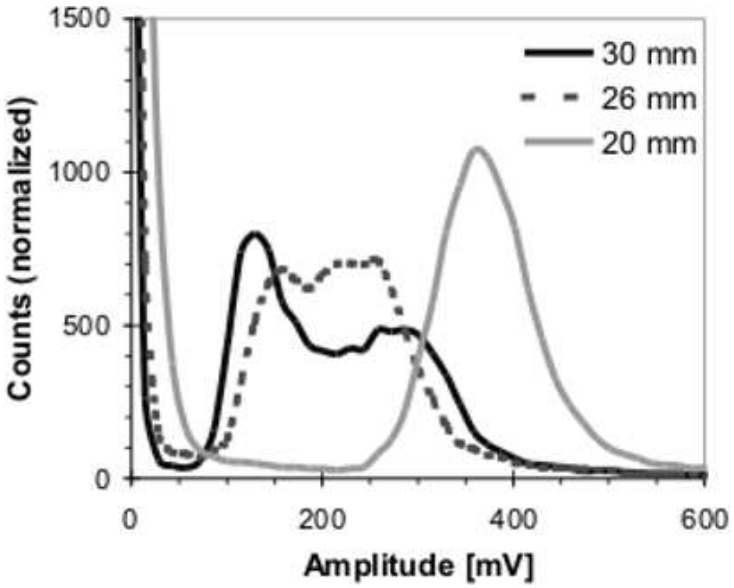

Figure 2.46: Dependence of the light output of a PMT on the diameter of the radiator produced with minimum ionizing particles. 1 MIP results in about 180 photoelectrons ejected from the cathode of the PMT. For easier comparison the spectra were smoothed and their areas normalized.

photocathode. The spectrum shifts up and becomes Gaussian, reflecting the statistical nature of photo conversion. There is a broad and clear area separating the peak from the noise (pedestal) level.

As discussed before, the consequence of the radiator's reduced diameter is the reduction in the covered solid angle (detection efficiency) that is roughly proportional to the second power of the diameter (area). This, however, is true only if the discriminator threshold can be placed at sufficiently low value. A rise in the threshold will lead to loss of efficiency. Figure 2.47 illustrates the dependence of efficiency on the threshold level, calculated using the amplitudes spectra of Fig. 2.46.

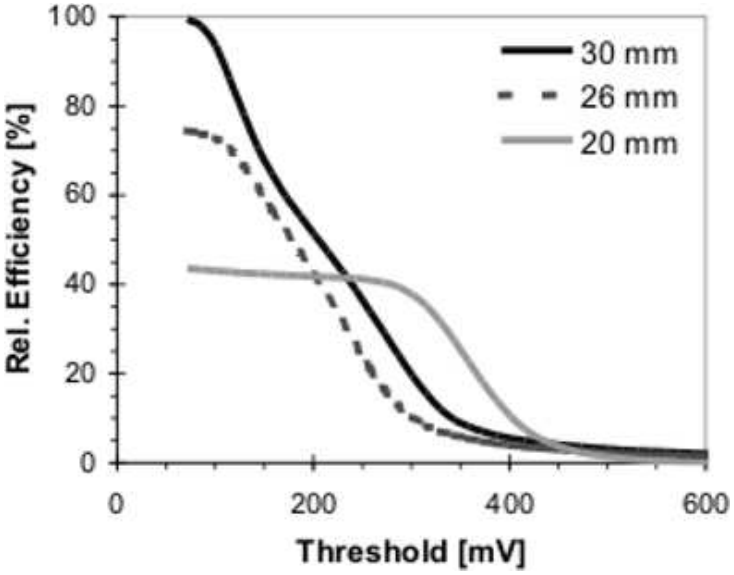

Figure 2.47: Efficiency as a function of the threshold calculated using measured amplitude spectra. 100% was assigned to the 30 mm radiator and the maximum values for the 26 and 20 mm diameter radiators were scaled accordingly.

The steep drop of efficiency for 30 and 26 mm diameter radiators with the increase of the threshold is somewhat disturbing. It means that even if no noise problems prevent the setting of the threshold value sufficiently low, any instability will cause noticeable variations in efficiency. In contrast the characteristics of the 20 mm quartz are excellent with a prominent and broad plateau.

2.9.5 Sensitivity to the Particle Backsplash

Cherenkov radiation is strictly directional but since the polished walls of the quartz radiator work as a mirror, particles travelling in the "wrong" direction will also produce detectable light pulses. This undesirable effect can be partially reduced by covering the front surface of the radiator with a light-absorbing layer, for instance by glueing (to get optical contact) a black paper on top of it. It works well for particles travelling exactly in the opposite direction but those at intermediate angles will inevitably produce some signals. This may not be a problem for T0-C despite being just next to the muon absorber, because the absorber was designed to minimize particle backsplash. This, however, will not be the case for T0-A, which is placed in the proximity of a vacuum pump, valve and support structure. It is therefore important to know what kind of spectra are to be expected from the "wrong" particles. The largest amplitudes from strain particles (the worst-case scenario) arise when they travel in exactly the opposite direction and the front of the radiator is free from optical contact with a light-absorbing material. The results are shown in Fig. 2.48 (26 mm diameter radiator) and Fig. 2.49 (20 mm radiator).

It is reassuring to see that with the 20 mm radiator even the largest signals from strain particle can be effectively (without the loss of pulses from good events) discriminated against by raising the threshold. For 30 and 26 mm radiators this would not be the case.

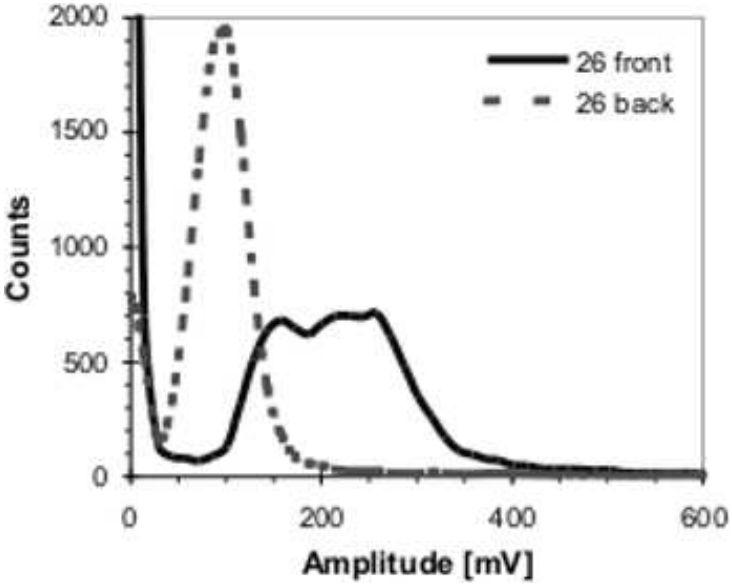

Figure 2.48: Response of the T0 module with 26 mm diameter radiator to MIPs entering directly from the front (solid line) and from the opposite direction (dashed line).

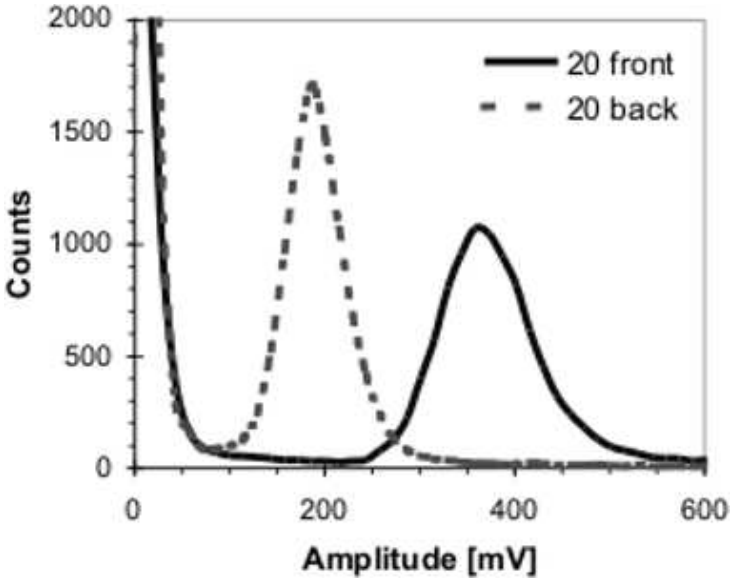

Figure 2.49: Response of the T0 module with 20 mm diameter radiator to MIPs entering directly from the front (solid line) and from the opposite direction (dashed line).

2.9.6 Light Transmission Measurements

The radiators used in our experiments were made at a different time and presumably also from different batches of the quartz material. To check the consistency and quality of production we have made light transmission measurements for each of the tested radiators. The coved wavelength (200–600 nm) matches that of PMT sensitivity. The results are presented in Fig. 2.50. They show that while there are indeed small differences between the samples, the overall quality of quartz radiators is good. The sample with the highest transmission (sample 1) was from the production run of 30 mm diameter radiators.

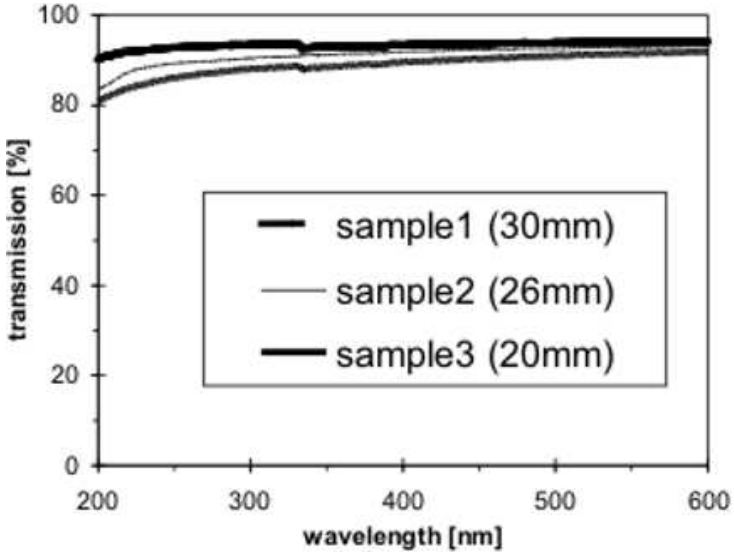

Figure 2.50: Light transmission through 3 cm thick samples of quartz radiators as a function of the wavelength.

2.9.7 Conclusions

The most important conclusion of the beam tests of the complete T0 system is that with the actual cables, connectors and prototypes of the electronics and for all tested radiator types the required time resolution of $\sigma \leq 50$ ps has been achieved.

The tests demonstrated the excellent amplitude spectrum of the 20 mm diameter radiators. It is so much better than the 30 mm radiator that it justifies considering a change in the current baseline. The only drawback would be reduced efficiency in pp collisions. This reduction can however be compensated, if necessary by the doubling the number of T0 modules in the T0-A array, as demonstrated in Table 2.7.

Table 2.7: Simulated efficiency in pp collisions (PYTHIA 6.125; 1000 events) for the baseline configuration (12–12), and for the configuration with 24 detectors on RB24 side (24–12).

Number of detector modules in T0-A	**Number of detector modules in T0-C**	**Efficiency in pp with 30 mm diameter radiators**	**Efficiency in pp with 20 mm diameter radiators**
12	12	53%	36%
24	12	–	49%

2.10 Data Readout

As mentioned in Chapter 2.8, the only ALICE sub-detector requiring non-trigger data from T0 is TOF. TOF needs time and amplitude information from each PMT to make off-line corrections that should further improve the precision and stability in definitions the interaction time. Otherwise, the only reason for storing raw T0 parameters would be for monitoring. Therefore, to cut costs and to guarantee the performance of T0, our readout (see Fig. 2.51) will be nearly identical to that of the TOF detector. For conciseness, only the modifications and changes in the TOF readout will be presented here. Together with arrival times and amplitudes from each PMT a handful of other parameters (vertex, summary amplitudes, etc.) will also be read out and stored by ALICE DAQ in exactly the same fashion. From the point of view of the readout architecture, the T0 detector will be just one more, fully independent, sector of the TOF detector.

The main difference between T0 and TOF pulses (relevant to the readout system) is their dynamic range. To accommodate the larger amplitude range from T0 a QTC + TDC will be used instead of QDC (see Section 2.8.7). A more serious problem is the range of the TDC. The High Performance TDC (HPTDC) developed by TOF has a range of about 200 ns, nearly one order of magnitude more than what is needed by T0. The resolution will be naturally sufficient but there is a problem with the dead time.

There is a small (below a few percent) probability that the same T0 module will produce a pulse in two consecutive bunch crossings. In pp collisions they are separated by just 25 ns. The first pulse will start the HPTDC and block it for the next 200 ns preventing the conversion, readout and storage of the second pulse. Let's further assume that the first signal was just a noise, a strain particle or a cosmic ray while the second come from proper interaction that should be triggered and stored. In this possible but unlikely case the T0 will produce all the correct trigger signals but the data (time and amplitude) from that particular PMT will not be digitised.

There are several ways to handle this problem. The easiest is to simply ignore such events and require the absence of T0 data for at least 200 ns prior to the valid interaction. The only drawback would be a slight (below a few percent) reduction in the data-taking rate. This is the solution that we prefer and consider as the baseline, since it has no consequence for Pb–Pb running and very small effect for pp.

The second solution is to use the the T0 Vertex signal as a strobe for the T0 readout. In this way no reduction in the data-taking rate will take place but the information on the T0 operation in non–trigger conditions will be absent. Such a solution would also require additional delays to the time and amplitude signals in waiting for the production of T0 Vertex. Such delays would slightly worsen signal quality.

Finally, it is possible to solve the problem completely by demultiplexing the signals from each PMT into 16 TDC inputs instead of just one. The prototype of such a demultiplexer has been built and successfully tested (see Fig. 2.52). It may be used as the base for production modules. The biggest disadvantage of the demultiplexer solution is a 16 fold increase in readout electronics. For that reason we consider it only as an upgrade option.

2.10.1 Data Readout Module (DRM)

Each crate will be equipped with a Data Readout Module (DRM) card that will act as the main interface between the Central ALICE DAQ, the CTP and T0 electronics (see Fig. 2.53). The DRM will receive and distribute the 40 MHz clock and the trigger signals (L1 and L2) to the T0–TRMs. The clock will be received through an optical fibre, while the other signals will be derived from a TTCrx. The clock will be distributed to the T0–TRMs via ECL connection. The control signals (L1, L2 accept and L2 reject) will be distributed with an LVDS bus to the T0–TRMs through an external flat cable.

The DRM will read the data from the T0–TRM modules. If an L2 reject is received the corresponding event buffer will be cleared on the T0–TRMs, otherwise, on L2 accept, data will be transferred from all the T0–TRMs to the DRM via the VME64 backplane. This data transfer is performed by the FPGA.

The data will be further processed and encoded by a DSP on board and sent through a standard

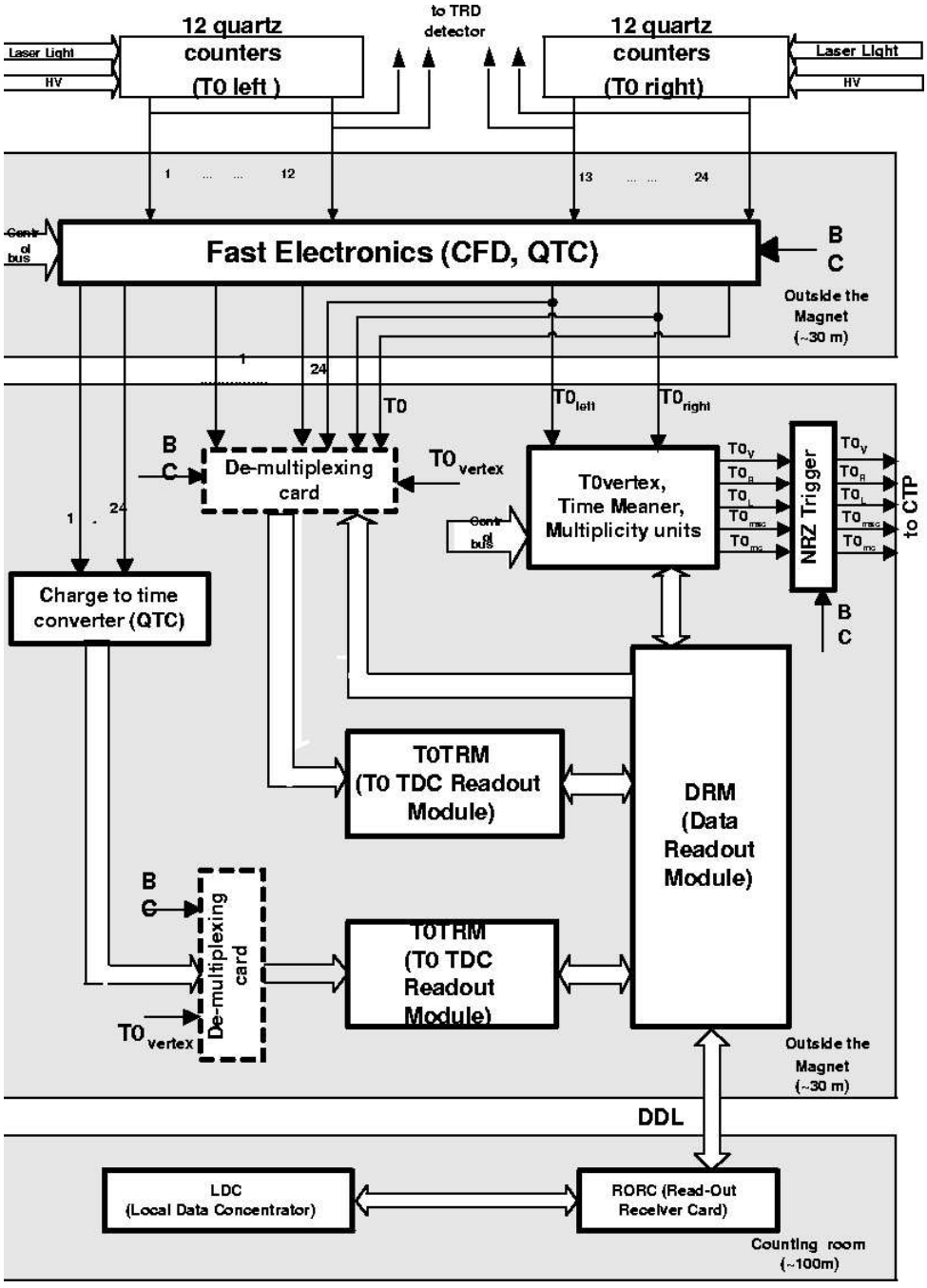

Figure 2.51: Block diagram of T0 readout.

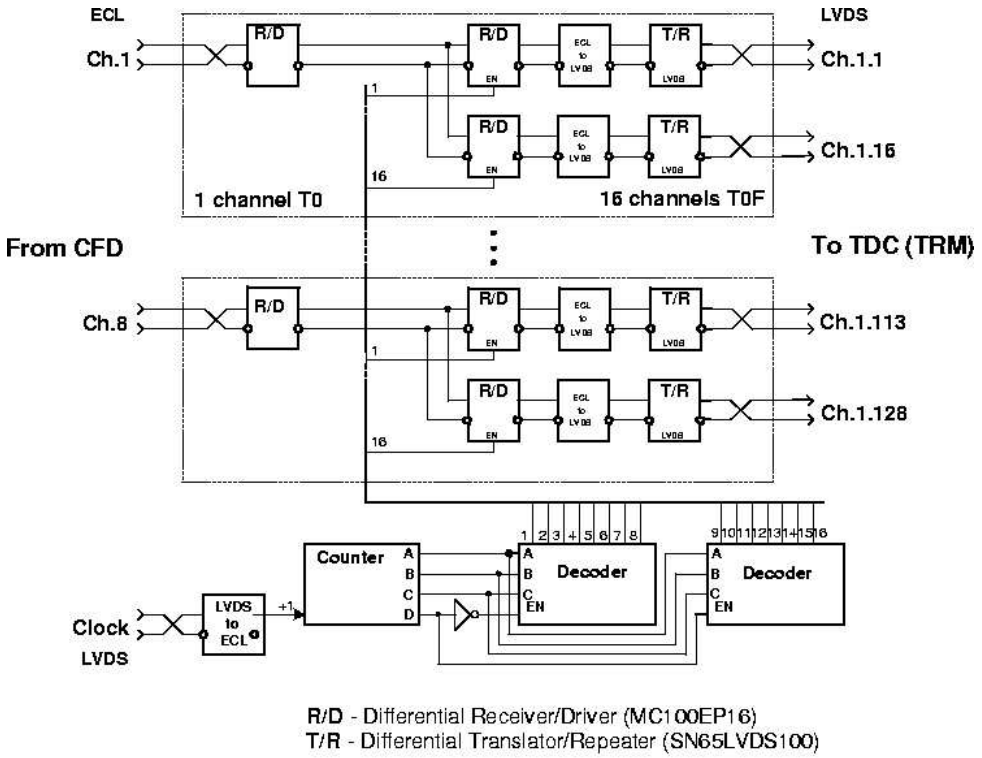

Figure 2.52: Block diagram of the demultiplexer.

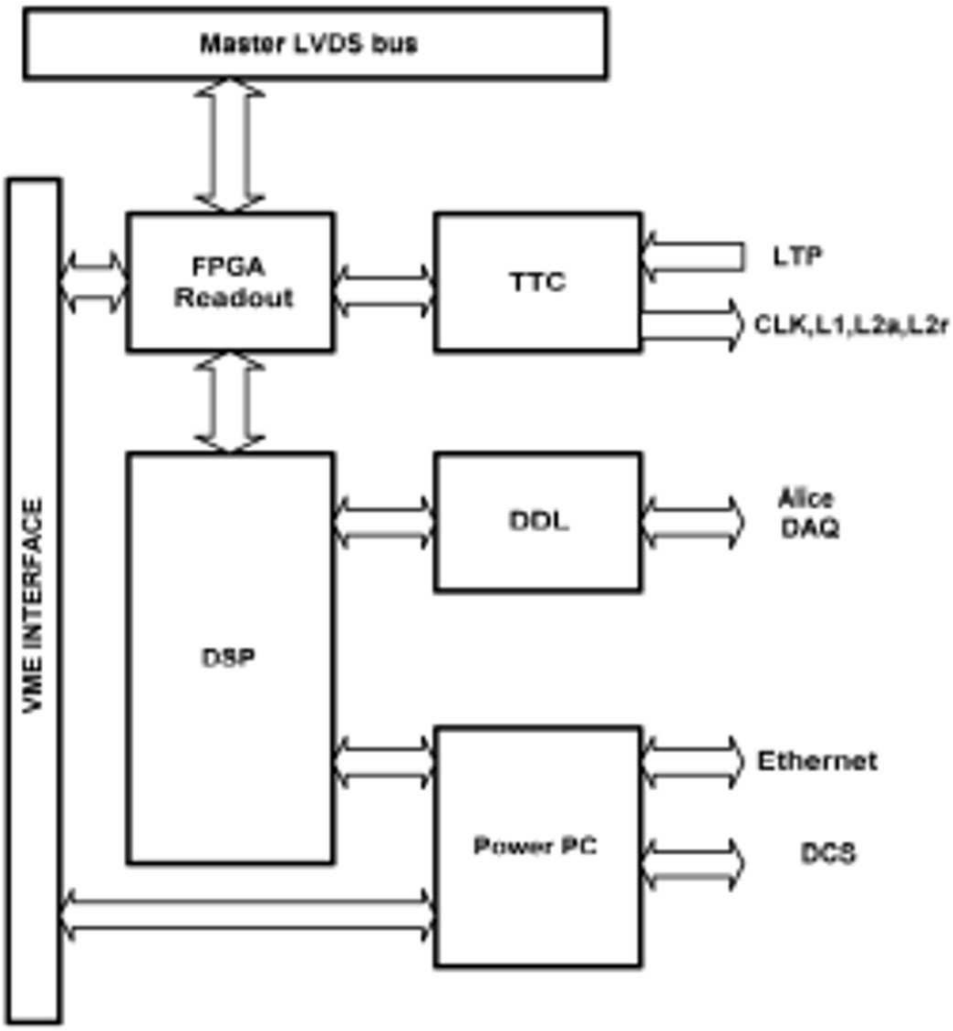

Figure 2.53: T0 Data Readout Module.

ALICE DDL interface to the central DAQ. A power PC will allow monitoring of the data and will host the slow controls of the T0 system (threshold setting, delay setting etc.). All these I/O devices (TTC and DDL interfaces and power PC cards) will be developed as a piggy-back card in standard PMC format applied to a VME card.

2.10.2 TDC Readout Module - TRM unit

An FPGA will perform the readout of the HPTDCs. To ensure high bandwidth the FPGA will act as an external readout controller of two separate chains consisting of 15 HPTDC slaves (in token - base parallel-readout configuration). The use of an Altera APEX family FPGA is foreseen. A Digital Signal Processor (DSP) will control various setup operations (including R-C delay chain calibration) and data packaging. The use of an Analog Devices Shark family DSP is foreseen. Memory (RAM and SRAM) is provided for event buffering and program hosting.

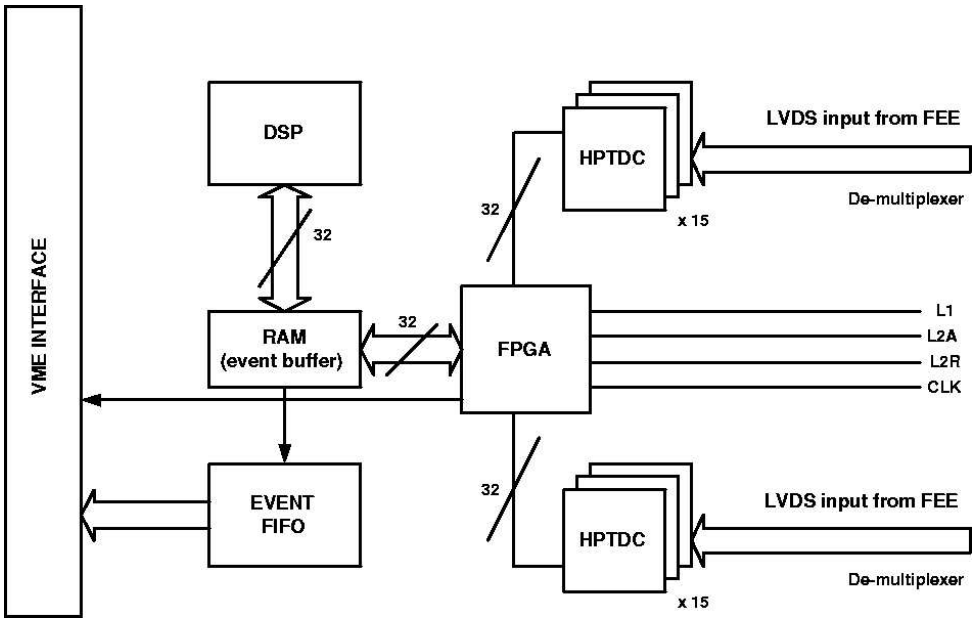

Figure 2.54: TRM unit.

Program loading and general control of the TRM will be managed through a VME interface (see Fig. 2.54). Initialization and setup of the HPTDC chips will be normally performed through the DSP. At reception of an L1 signal from the ALICE Central Trigger Processor (CTP) the HPTDCs will look for hits with a time offset of 6.2 μs, moving then to the internal readout FIFO. This operation does not cause dead time to the acquisition of data by the HPTDC.

2.11 Detector Control System

The T0 detector modules are relatively straightforward, stable, and reliable units making controlling them easier. Standard off-the-shelf products will be used as High Voltage and current monitoring devices. The only problems arise from stray magnetic fields in the vicinity of L3 magnet and elevated radiation levels. This, however, is a common problem for all ALICE detectors and we are simply planning to use one of the standard solutions like the EASY system currently under development by C.A.E.N. There are also several ready-made solutions for the control of electronics. In each T0 channel there are several thresholds, delays, etc. that have to be adjusted prior to and sometimes during the run. T0 Vertex and Multiplicity Units control the main trigger signals and need to be addressed during normal ALICE

operations. Monitoring of all PMT modules will be done with laser pulses during the longer breaks in the beam. This should cause no problems as even the current laser power supply has the provision for remote triggering.

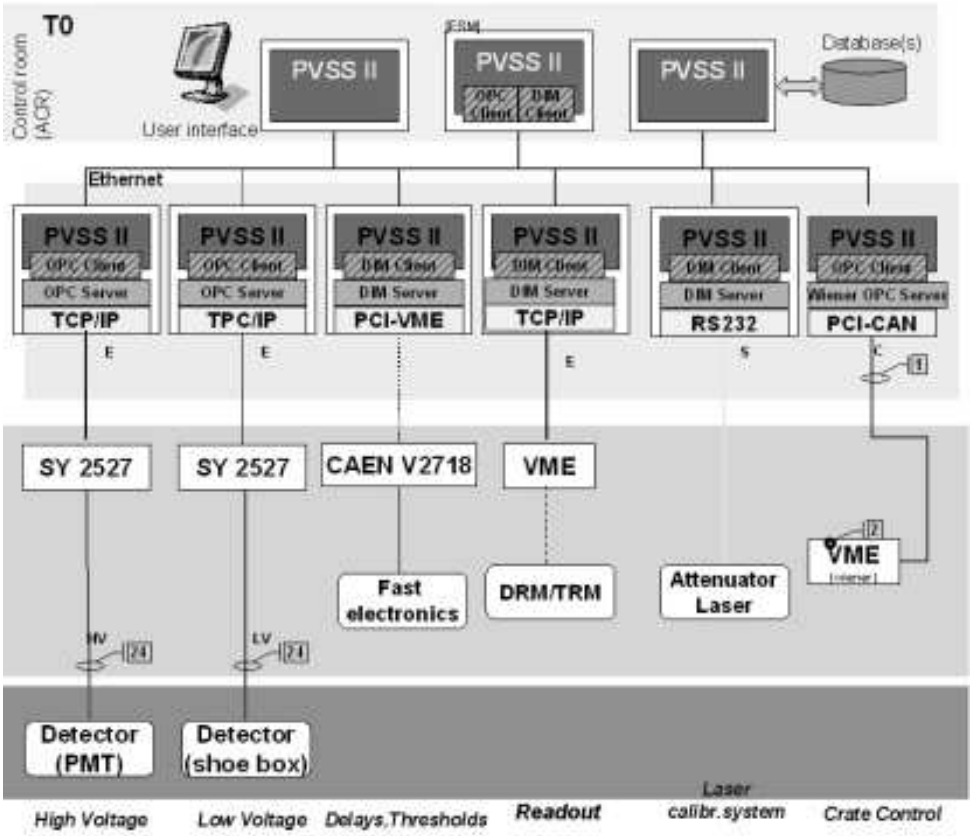

Figure 2.55: Scheme of T0 DCS.

The DCS scheme for the T0 detector is shown in Fig. 2.55. The main sub-systems are high voltage (HV), low voltage (LV), settings threshold and delays, laser control, generator control and T0–TDCs and T0–DRM readout cards. The list of signals to be monitored and controlled for the T0 detector is listed in Table 2.8.

The T0 electronics will be located in two different areas: the shoebox will be placed inside the magnet (these regions can be accessed only during a long shutdown), fast electronics and T0 TDC/TDM cards will be in the crates just outside the L3 and can be accessed even during a short shutdown. The High and Low Voltage to the PMTs and electronics will be provided by a CAEN SY2527 system with high and low voltage boards. A CAEN OPC server will interface the crate with PVSS, through Ethernet.

The connections between the control computer and the VME crates with fast electronics will be based on a CAEN V2718-A2818 VME-PCI optical link bridge. The module V2718 is a 1-unit wide 6U VME master module, which can be interfaced to the CONET (Chainable Optical NETwork) and controlled by a standard PC equipped with the PCI card CAEN module A2818. The T0–TRM and T0–DRM are presently under development by the ALICE TOF group and we shall use their solution.

For fast electronics we shall use standard VME crates. The control and monitoring will be via CANbus and Kvaser CAN interface card. The top-level application will be a SCADA system based on PVSS software that communicates with the hardware via OPC or DIM servers. Support for all equipment will be implemented based on the JCOP framework.

Table 2.8: Main parameters of the Detector Control System for the T0.

Subsystem	location	Controlled parameters	Number	Parameter	Control
Fast electr.	VME	delays Thresholds for CFD Thresholds for T0-v Thresholds for multiplicity trigger	24 24 2 - 3	- voltage voltage - voltage	- W R/W - R/W
T0-TRM	VME crate	same as TOF			
T0-DRM	VME crate	same as TOF			
Low voltage for Shoebox	CAEN 2725	LV supply on/off LV settings and readings safety switch	24 24 1	voltage complex voltage	R/W R/W on/off
HV voltage	-	HV supply on/off HV settings and readings safety switch	24 24 1	voltage complex voltage	R/W R/W on/off
Laser system	-	switch attenuator	1 1	- complex	on/off R/W
Generator	-	switch	1	voltage	on/off

2.12 Organization

2.12.1 Participating Institutes

The main institutes participating in the design, construction and operation of the T0 detector are:

- HIP — University of Jyväskylä, Department of Physics and Helsinki Institute of Physics, Jyväskylä, Finland;
  - Wladyslaw Trzaska (Project Leader)
  - Sergey Iamaletdinov (Graduate Student)
  - Vladimir Lyapin (Shoebox, LCS)
  - Tomasz Malkiewicz (Graduate Student, Database)
- MEPhI - Moscow Engineering Physics Institute, Moscow, Russia
  - Vladislav Grigoriev (Leader of the Russian Team)
  - Vladimir Kaplin (Electronics)
  - Alexandr Karakash (PMT, test measurements)
  - Vitaly Loginov (Electronics)
- INR — Academy of Science, Institute of Nuclear Research, Moscow, Russia
  - Alexei Kurepin (INR Group Leader)
  - Fedor Guber (Mechanics)
  - Tatyana Karavicheva (DCS, readout)
  - Oleg Karavichev (Electronics)

  - Victor Marin (CFD)
  - Alla Mayevskaya (Simulations)
  - Andrei Reshetin (PMT shielding)

- KI — Russian Research Center "Kurchatov Institute", Moscow, Russia
  - Evgeni Meleshko (T0 Vertex, Multiplicity)
  - Anatoly Klimov (Technical Project)

The Greek group from Athens (Marta Spyropoulu-Stasinakhi) has also expressed serious interest in participating in the T0 DAQ. The Greek group would contribute both in terms of manpower and core costs.

2.12.2 Cost Estimate and Resources

During the signing of the Memorandum of Understanding the T0 project as such did not yet exist. It evolved later by dividing the initial FMD into T0, V0 and the current FMD (based on silicon detectors). It is therefore still unclear how much core money can be used by T0. The only currently available cash comes from part of the Finnish Core Contribution. At the start of the project it was 200 kCHF. This was estimated roughly sufficient for the detector modules, mechanics and front-end electronics. By the end of 2004 more than half of that sum will have been spent. To complete the entire project additional funds will be needed. The main uncertainty is the cost of readout modules. They are custom made by the TOF collaboration and do not have a clear price tag. The final price of the High and Low Voltage power supply systems is also unclear. Systems like the new (not yet on the market) C.A.E.N. EASY are expensive but the cost per channel can be substantially reduced if shared with another subdetector. We are exploring such possibilities. All in all the total cost of T0 should be of the order of 400 kCHF.

2.12.3 Commissioning

T0 is a small detector giving some degree of flexibility in defining and meeting internal milestones. There are, however, issues where no delays are permitted. In August 2006 installation of the detectors on RB26 will start and T0-C will be the first detector installed. This is the most important milestone because after the installation T0-C shall remain practically inaccessible until the end of the operation of ALICE (see the chapter on integration). Therefore it is of utmost importance to ensure the quality and reliability of all parts of T0-C. All the other components of T0, even those inside the L3 magnet (T0-A and the shoeboxes) will have reasonable accessibility, allowing for modification and replacement even during short shutdown periods. In light of this perfection of the detector modules is in the highest priority for us until August 2006. By the end of 2005 T0-C and T0-A will be pre-assembled and tested in Finland prior to their shipment to CERN. Once at CERN both T0 arrays will be tested again. The test will be repeated once more after installation.

Naturally, work on electronics, readout and DCS proceeds in parallel. For instance, completion of the shoeboxes is also of high priority as it involves collaboration between several groups (T0, V0, TRD). Right now (August 2004) the prototypes of all major electronics component have been built, fully tested and proven to work well. In principle, we should be ready to change from the prototypes to the production modules. This, however, is unlikely to happen before the end of 2005 as we are also investigating the possibility of finding some common electronics solutions with V0 and further integration with TOF. For instance we are waiting to test the latest version of the NINO chip (developed by TOF). In the event of positive results the use of a joint TOF, V0 and T0 standard would greatly simplify and accelerate our work.

The first batch of the production components for the laser system have already been ordered. One more series of test is foreseen before the full system will be purchased. If no problems arise, the laser calibration system should be complete in time for the pre-shipment tests of T0 at the end of 2005.

2.12.4 Safety Aspects

With the exception of the high voltage (1–2 kV) delivered to each of the 24 PM tubes using standard HV cables and SHV connectors, the T0 detector poses no safety hazards.

3 The V0 Detector

3.1 Objectives

The V0 detector is a small-angle detector consisting of two arrays of scintillator counters (named V0A and V0C) installed on both sides of the ALICE collision vertex (Fig. 1.1 and 1.2). The counters cover the pseudo-rapidity ranges V0A ($2.8 > \eta > 5.1$) and V0C ($-3.7 < \eta < -1.7$) in partial overlap with the FMD acceptance (Fig. 4.1).

This detector system has several functions. It provides minimum-bias (MB) triggers for the central barrel detectors in pp and ion-ion collisions. These triggers will be obtained from a large set of events with different numbers of emitted charged particles (MIPs) crossing the detector, starting from a single one with an as large as possible efficiency. Particles arise not only from initial collisions, but also from a significant background of secondaries produced in the vacuum chamber elements (Section 3.3.1). The resulting efficiency of triggering (Section 3.3.2) and charged-particle multiplicity distributions (Section 3.3.3) are therefore modified as compared to those expected from pure collisions. However, a monotone dependence between the number of impinging particles on the V0 arrays and the number of primary emitted particles remains, serving as an indicator of the centrality of the collision via the multiplicity recorded in the event. The large background due to secondaries complicates the extraction of quantities like multiplicity and/or impact parameter of the collision. Nevertheless, cuts on the signal can be applied to achieve rough centrality triggers. We plan to have two such classes, central and semi-central.

Interactions of protons with the residual gas of the vacuum chamber will generate tracks through the ALICE detectors. A large trigger rate is expected from background in the dimuon spectrometer trigger chambers [1]. The V0 detector, which will be used as a validation tool, should be a very efficient filter in that case [2]. Moreover, this background will also affect the V0 arrays. Background triggers have thus to be disentangled so that the physical minimum-bias triggering rate can be purified. A time resolution of the order of 1 ns provided by the V0 arrays is necessary to get a good rejection efficiency (Section 3.3.4). As a consequence, the luminosity in pp reaction with the V0 can be envisaged and measured with good precision [1] [3].

3.2 General design and requirements

As for the FMD and T0 detectors, the space available for the V0 detector is constrained by the volumes occupied by the central detector systems (TPC, ITS) and the upstream part of the dimuon spectrometer (front absorber). The placement of the V0A and V0C arrays in the central part of ALICE are shown in Fig. 1.2.

The V0A device is installed on the positive z-direction (RB24) at a distance of about 340 cm from the interaction point (IP). The detector is housed in a box made of two identical halves mounted around the beam pipe. The box occupies a volume of 100 cm in diameter and 60 mm in thickness with a central hole of 80 mm in diameter. A cylindrical support, common with the FMD1 counter of the FMD, keeps it vertical. This support, which surrounds the beam pipe and goes across the central part of the PMD system, is fixed to a vacuum valve support set outside the L3 magnet (see Section 5).

The V0C device is installed on the negative z-direction (RB26) along the absorber nose. As for the V0A, it is mounted inside two rigid half-boxes. This device is fixed to the absorber at 900 mm from the IP. It is a disk of 47 mm in thickness, 76 cm in diameter with a central hole of 84 mm in diameter (see Section 5).

The role attributed to this device in ALICE has led to a system of two arrays as large as possible for a good pseudo-rapidity coverage. The segmentation is shown in Fig. 3.1. Each array consists of 32 counters distributed in 4 rings. Each of these rings covers 0.5 - 0.6 unit of pseudo-rapidity (Table 3.1) and is divided in 8 sectors (45°) in azimuth. For the V0C array, elements of rings 3 and 4 are divided into two identical detectors for an optimized signal uniformity and a smaller time fluctuation.

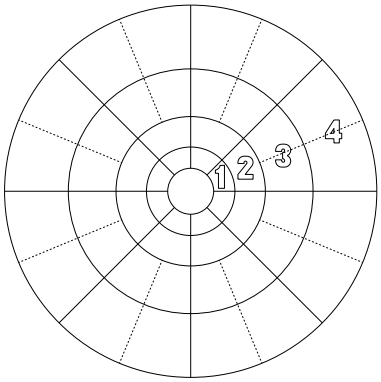

Figure 3.1: Segmentation of the V0A/V0C arrays.

Table 3.1: V0A and V0C arrays. Pseudo-rapidity and angular acceptances (deg.) of the rings.

Ring	**V0A**		**V0C**	
	η_{max}/η_{min}	$\theta_{min}/\theta_{max}$	η_{min}/η_{max}	$\theta_{max}/\theta_{min}$
1	5.1 / 4.5	0.7 / 1.3	-3.7 / -3.2	177.0 / 175.3
2	4.5 / 3.9	1.3 / 2.3	-3.2 / -2.7	175.3 / 172.4
3	3.9 / 3.4	2.3 / 3.8	-2.7 / -2.2	172.4 / 167.5
4	3.4 / 2.8	3.8 / 6.9	-2.2 / -1.7	167.5 / 159.8

For pp reactions, the mean number of charged particles within 0.5 unit of pseudo-rapidity interval (one ring acceptance) is about 10 (20 for the ring 1 of V0C) when secondary contributions are included (Section 3.3.3.1). Each V0 segment is thus mostly hit by only one (two) charged particle(s). Therefore, a very high efficiency for the detection of one MIP is required for a reliable trigger efficiency in this case. The p-gas background influences on MB and dimuon triggers can be identified with a large efficiency if the time resolution of the counters is of the order of or better than 1 ns. In Pb–Pb reactions (Section 3.3.3.2), the number of MIPs within a similar pseudo-rapidity range can reach 4000 (8000 for the V0C ring 1) if secondaries are included. Therefore, each channel has to provide a dynamic range of at least 1 - 500 (1 - 1000) MIPs. The main requirements for each channel are thus:

- a high and uniform light yield from the one minimum-ionization particle (MIP),
- a time resolution better than 1 ns for the MIP,
- a large dynamic range of the Front-End Electronics to accommodate the charged particle multiplicity to be encountered in minimum-bias ion-ion collisions.

Scintillating counters (SC) have been adopted for the arrays. The produced scintillation light is converted by wavelength shifting (WLS) fibres and transported to photomultipliers (PMT) through clear

optical fibres. Similar techniques were used for calorimetry, multiplicity, and time measurements in several other experiments. The present setup is based on some of these works and on specific experimental tests and simulations (see Ref. [4] and references therein).

3.3 Performance simulations

The evaluation of the performance of the V0 detector was made using AliROOT based on GEANT [3]. Minimum-bias pp reactions were simulated at $E_b = 7\,\text{TeV}$ with the generator PYTHIA 6.214 [5]. The corresponding total reaction cross-section is 101 mb. It is the sum of the elastic (22 mb) and inelastic (79 mb) cross-sections. The elastic interactions do not produce particles that interact with the V0 detector, which has a limited coverage at small angles. This component is therefore not included in the present calculations. The Pb–Pb reaction was simulated at 5.5 TeV/nucleon with the generator HIJING [6].

3.3.1 Background from secondaries in pp collisions

The presence of matter (beam pipe, front absorber, FMD, T0, ITS services) in front of the V0 arrays results in an important number of secondaries, which will distort physical information expected from primary charged particles.

Figure 3.2 shows the origin of the charged particles, projected in the *xy* and *zx* planes of ALICE, that contribute to the signals of the V0 arrays, which are exposed to a large quantity of secondary particles (V0C much more than the V0A). The figure shows that they come mainly from the beam pipe and bellows ($0\,\text{cm} > z > -80\,\text{cm}$) and from the flange in front of the detector ($z < -80\,\text{cm}$). The geometry of the setup at the time of the simulation is shown in the same figure. An important change in the beam pipe design would be necessary to drastically reduce the secondary particle contribution.

3.3.2 Trigger efficiency for MB pp physics

The V0 detector will provide the triggering of the largest possible fraction of pp reactions. In this section, we calculate the expected efficiency of the system, taking into account the geometrical coverage given in Table 3.1. Only the inelastic component of the pp cross-section will contribute.

Figure 3.3 (left) shows the multiplicity distribution of the charged particles produced by the inelastic pp interactions over the 4π phase space. The figure also shows the corresponding distributions of events with all ALICE effects (with V0 only) giving at least one charged particle in the V0A array, in the V0C array and in both V0A and V0C arrays, the condition required for a minimum-bias triggering. Trigger efficiencies are about 89% (85%), 87% (84%) and 83% (77%) for the detection of at least one charged particle by V0A, V0C and both V0A and V0C arrays. Thus, the material improves the capability of triggering, especially for events with low outgoing multiplicity.

Triggering with only the left or the right V0 device would have to be interesting in terms of efficiency. About 7 per cent could be gained (Fig. 3.3 (left)). Unfortunately, owing to the large expected background from p-gas interactions (Section 3.3.4), such a trigger configuration is not advantageous. The background from p-gas interactions must be reduced by selecting events with proper time of flight to the two detector arrays. There is a difference of about 6 ns between real pp events and events associated to p-gas interactions. A possible residual pollution of physics data by the background will have to be disentangled off-line. If these polluting events make the acquisition rates prohibitive, a threshold on the minimum number of cells fired in the V0A or (and) V0C array(s) could be required for the filtering of this background.

Figure 3.3 (right) shows the distributions of events as a function of the number of cells (N_{cell}) fired in the V0A, V0C, and both V0A and V0C arrays. We note a large increase of fired cells due to secondaries generated in material in front of the detector. Any cut on N_{cell} would reduce the triggering efficiency of the V0 detector for the smallest multiplicity events.

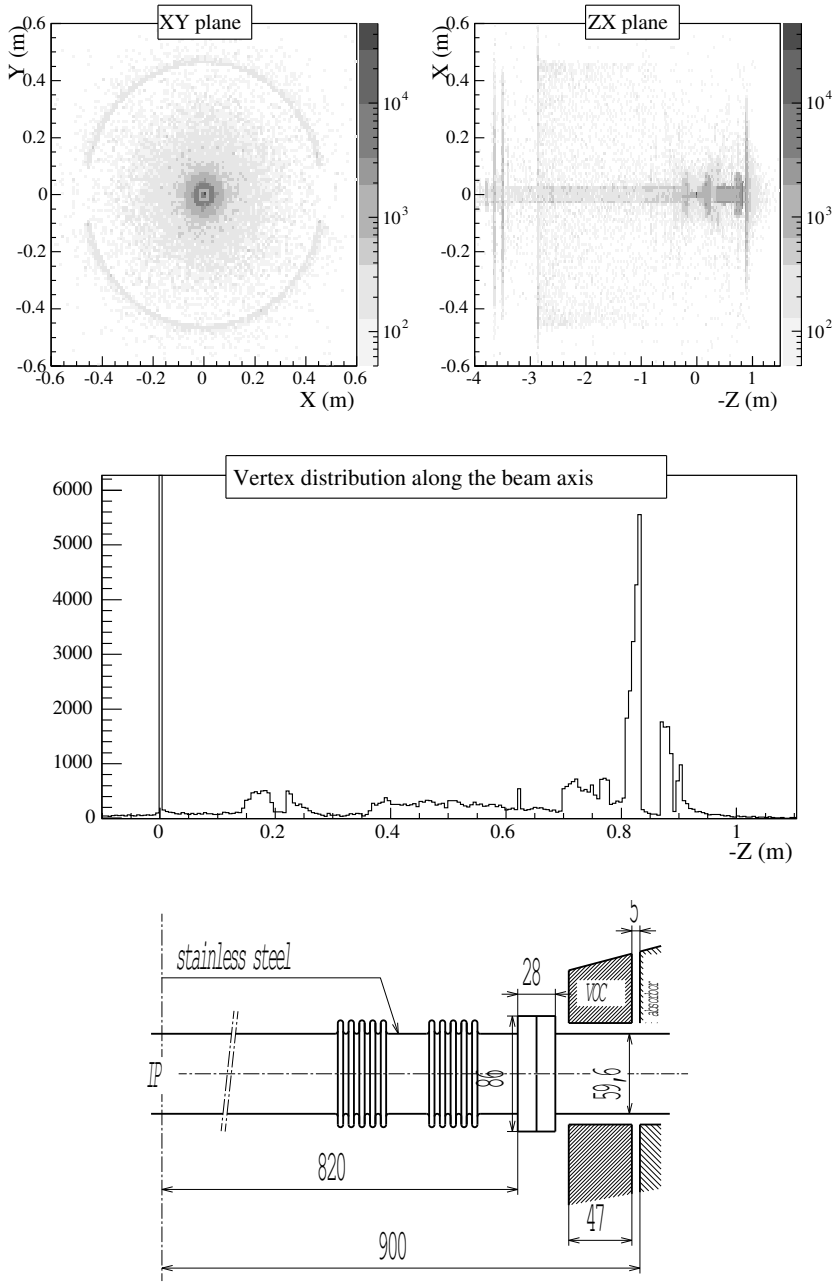

Figure 3.2: Origin of particles detected by the V0 arrays and projected onto the *xy*, *zx* planes, and along the negative beam *z*-direction (top). Geometry of the beam pipe area between the vertex and the V0C array (bottom).

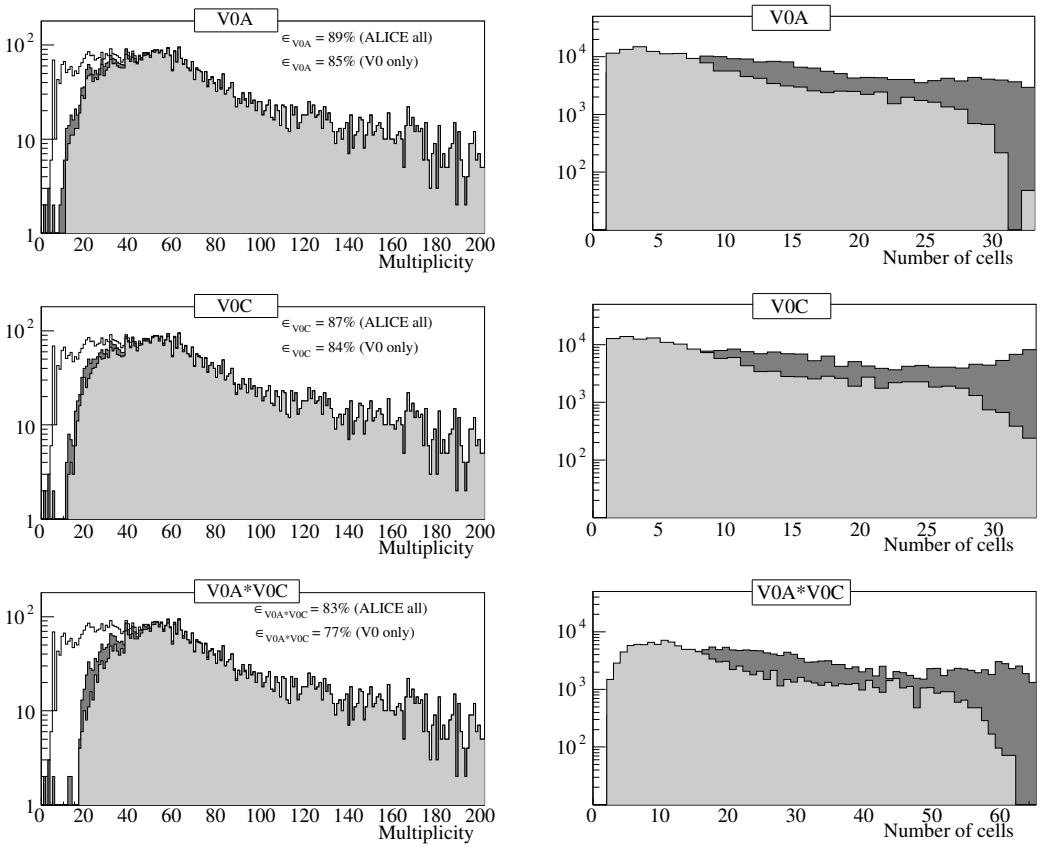

Figure 3.3: V0 triggering efficiencies for pp physics determined by PYTHIA. Transport of particles in vacuum (light grey) and in the ALICE environment (dark grey). Charged-particle multiplicity distribution of events in full space (white) as compared to distributions of events seen by the V0A, the V0C, and both V0A and V0C (left). Distribution of cells fired in the V0A, the V0C, and both the V0A and V0C arrays (right).

In Pb–Pb reactions the efficiency of triggering depends on the required centrality. It is very close to 100% for all but the very peripheral part of the minimum-bias events. Moreover, the contribution of Pb-gas background is expected to be very weak.

3.3.3 Multiplicity distributions in pp and Pb–Pb collisions

3.3.3.1 pp reactions

The multiplicity measurement is not the main aim of the V0 detector. In fact, this detector is not optimized for the individual counting of charged particles. Moreover, the production of many secondaries (Section 3.3.1) will distort physical information about multiplicity.

Figure 3.4 shows the multiplicity distributions in pp reaction as they are detected by each ring of the V0A and V0C arrays. The comparison between results from PYTHIA with particles transported in vacuum and with all the ALICE environment shows the intensity of the background effect and its dependence with the ring number. As expected, ring 1 of V0C is the most affected. The mean numbers of hits are 10 (20) for each ring (ring 1 of V0C). The mean number of MIPs hitting an individual counter of V0C is thus about 1 (2). The corresponding numbers of hits on the V0A individual counters are a little bit smaller.

3.3.3.2 Pb–Pb reaction

The pseudo-rapidity distribution of charged particles in central Pb–Pb collisions ($0 > b > 5$ fm) is given in Fig. 3.5. At $\eta = 0$, $dN/d\eta \approx 3800$. The charged particles emitted inside the acceptance angles of the V0A and V0C rings vary from 1000 to 1600 and from 1400 to 1800, respectively.

The Pb–Pb collisions were simulated using 18 HIJING events with impact parameter varying from 0 to 11.2 fm. The results are given in Fig. 3.6 (top). They show the correlation between the pure (S) and the effective signals (S+N). The background intensity is similar for all the rings of the detector except for ring 1 of V0C where it is two times larger, as observed in pp collisions. A maximum of 4000 (8000) charged particles will fire each ring of the detector (ring 1 of V0C). A MIP dynamics of at least 500 for each channel is proposed to be implemented in the electronics system (Section 3.6).

Finally, the ratio of the integrated S/N values is plotted in Fig. 3.6 (bottom) for each ring. Any improvement of the setup should be explored to increase these values.

3.3.4 p-gas rejection in MB pp physics

A large number of particles are expected to be produced by interactions of accelerated protons with the residual gas in the LHC vacuum chamber. They originate from the ALICE experimental area ('close p-gas', between $+20$ m and -20 m from the IP) and from the LHC ring ('halo'). They were simulated with the HIJING code [1] and with the file established for the LHCb experiment [7], respectively. Their contributions to the V0 signal (V0A and V0C in geometrical coincidence) are 198 kHz and 47 kHz, respectively [1]. The ALICE experiment is expected to run in pp mode with two different luminosities (3×10^{30} and 30 times lower [3]). In the high-luminosity case, the interaction rate will be 200 kHz, of the same order of magnitude as the beam-gas. In the case of the low-luminosity running, the rate of beam-gas events will be many times superior since the proton beams will have an unchanged intensity in the accelerator.

The V0 detector should be able to discriminate p-gas and pp events by measuring the time-of-flight difference between the V0A and V0C arrays [8]. This time difference was estimated in both pp and p-gas events by taking into account the time given by the first hit in V0A and V0C. We generated pp minimum-bias collisions with a Gaussian vertex smearing (σ_z = 5.3 cm). For p-gas events we used the generated events as described above. For each counter channel, we applied a Gaussian time smearing of $\sigma_{time} = 1$ ns according to the V0 scintillator time resolution requirement. We show in Fig. 3.7 (left)

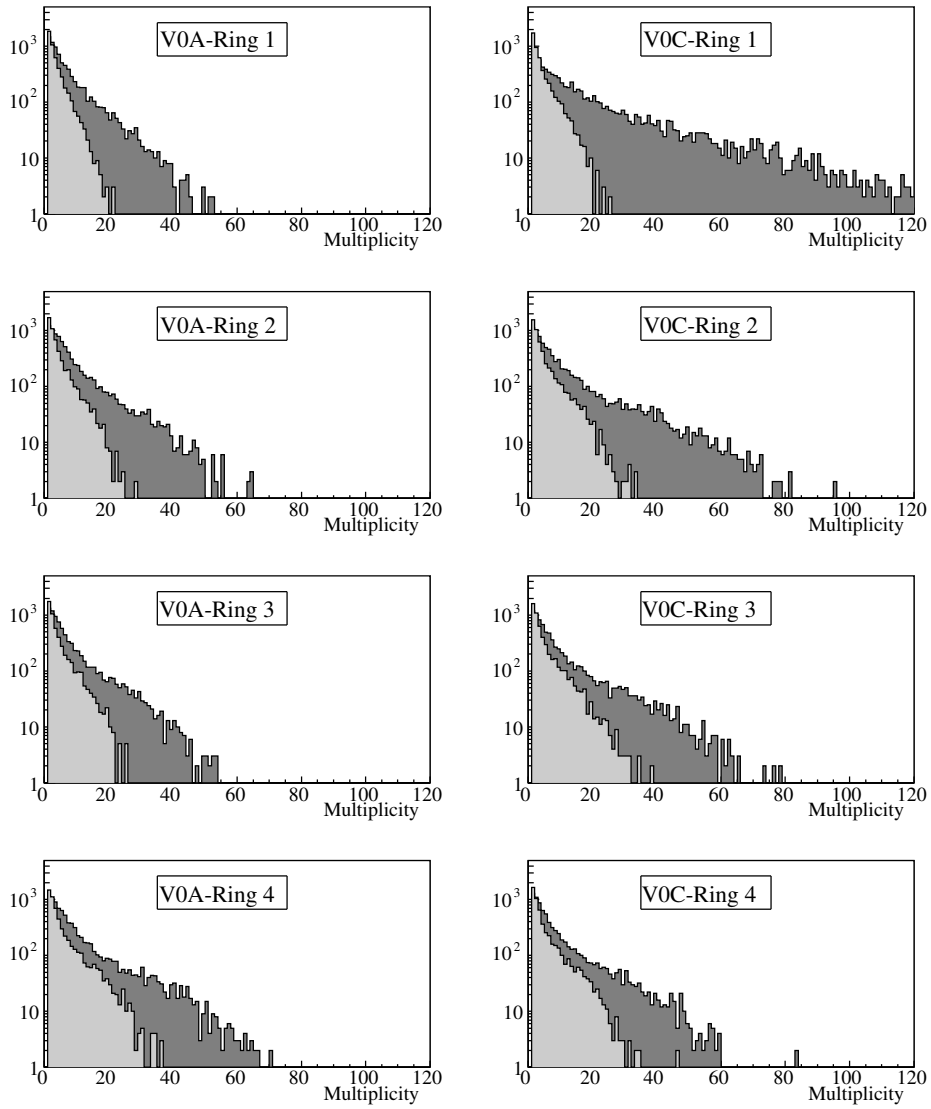

Figure 3.4: Charged-particle multiplicity distributions in pp reaction through each ring of the V0A and V0C arrays as given by 7820 PYTHIA inelastic events after transport of particles in vacuum (light grey) and in the ALICE environment (dark grey).

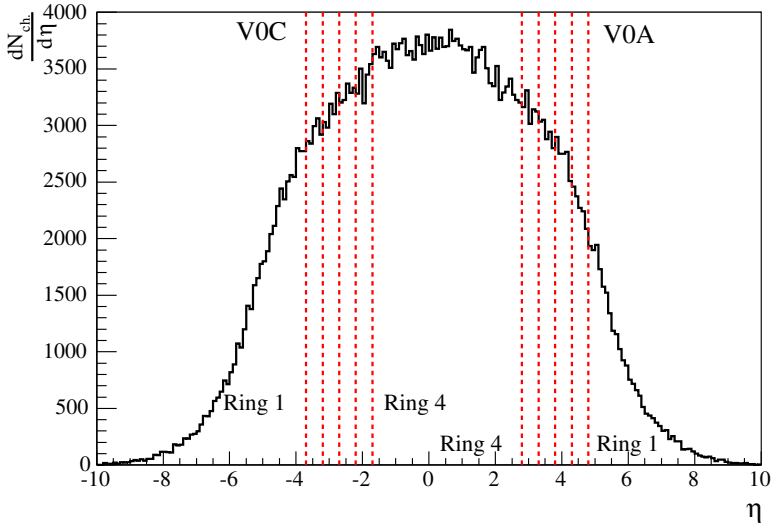

Figure 3.5: Pseudo-rapidity distribution of charged particles calculated with HIJING for central Pb–Pb collisions ($0 > b > 5\ fm$).

the time-of-flight difference as a function of the multiplicity per event [1]. Two clusters appear. The first belongs to p-gas events and is centred at about 14 ns. It originates from the 'halo' at low multiplicity and from the 'close' p-gas at high multiplicity. The second one comes from pp events at about 8 ns. Its multiplicity distribution is centred at around 20.

The Fig. 3.7 (right) gives the projection on the time axis of the previous distribution. The figure shows the performance of the V0 detector for separating the p-gas events from the real pp events. A cut at 11 ns allows 99% of the background triggers to be rejected and the collection of 98% of the 83% of inelastic pp events providing triggers (Section 3.3.2)

3.4 The V0 arrays

3.4.1 R&D

Tests were carried out to determine the light yield and the time resolution from several samples of counters made of scintillator coupled with WLS fibres. A test bench was used to record data from cosmic rays and beam particles. It is described in Ref. [1]. Initial measurements obtained with several assemblies of scintillating elements are presented in Ref. [4]. These results allowed preliminary options of scintillating material, assembling geometry and method, surface treatment, etc. to be chosen so that a maximum of light yield at the end of the fibres for an optimized time resolution can be achieved.

Two different couplings (design 1 and 2) of the scintillator piece with the WLS fibres were finally tested. Each design and its resulting performance are given in the next two sections.

3.4.1.1 Design 1 and performance

For the V0A array which will have 32 cells as shown in Fig. 3.1 except for the fact that rings 3 and 4 will not be subdivided, the 45° slices will be independent while the ring subdivision within a slice will be done by using the 'megatile' construction method developed and used in Refs. [9] and [10].

In the 'megatile' technique a large piece of scintillator is machined with a router plane most of the way through its depth in order to separate one sector from the rest, in this case the ring boundaries in

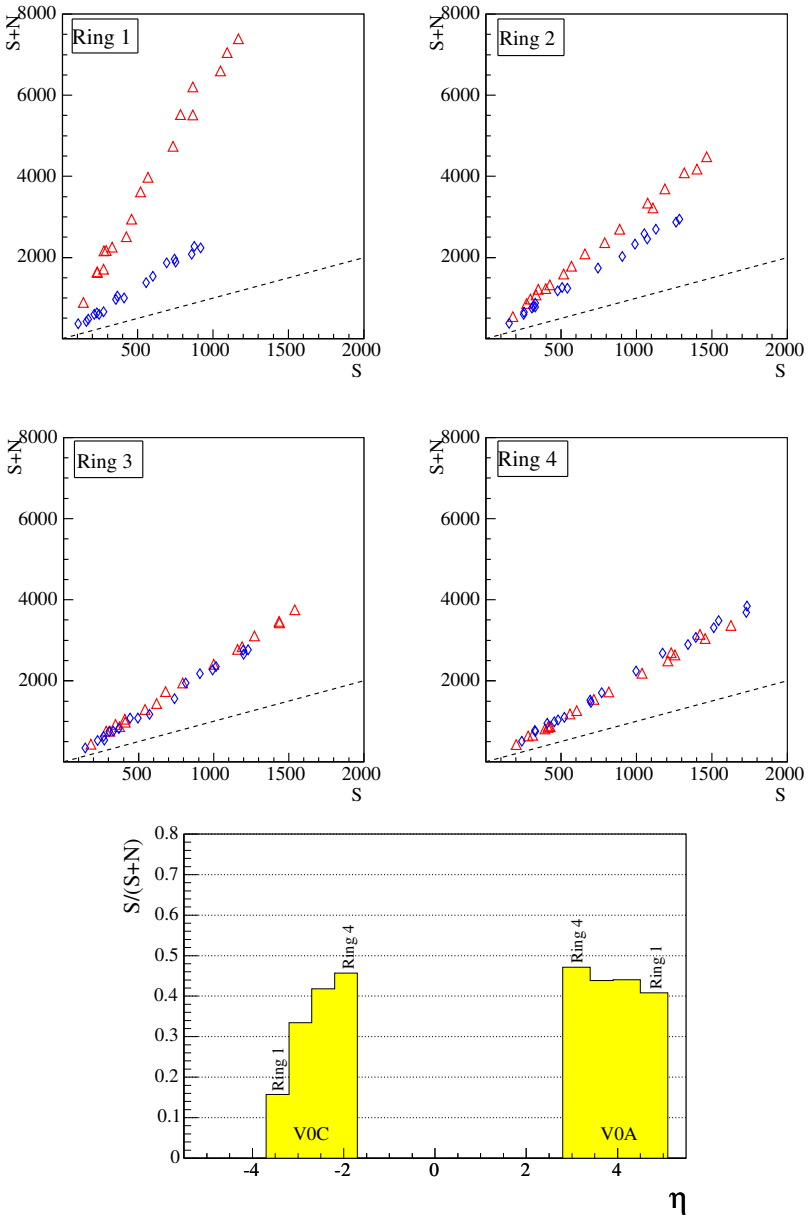

Figure 3.6: Charged particle multiplicity distributions in Pb–Pb reactions in each ring of the V0A (circle) and V0C (triangle) arrays as given by 18 HIJING events. Pure signal (S along x-axis) as a function of effective signal (S+N along y-axis). A perfect setup (N = 0) is represented by the dotted line (top). Signal over Background (S/N) ratio as a function of the pseudo-rapidity range covered by the rings (bottom).

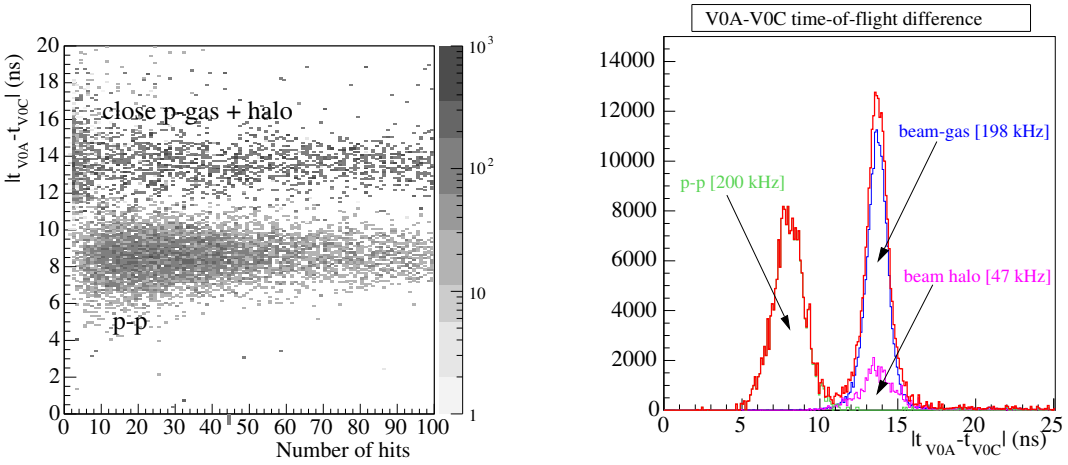

Figure 3.7: Time difference between V0A and V0C arrays as a function of (left) and integrated on (right) the multiplicity per event for pp minimum-bias collision and p-gas interaction.

a slice. The grooves are filled with TiO_2 loaded epoxy to provide optical insulation from the adjoining sectors, and reflection of light into the cell, as well as to restore the mechanical strength. The outer surfaces of the slice will be wrapped with an efficient reflector, in our case Teflon tape. In order to collect the light within each detection cell, parallel grooves 3 mm deep are machined on each face of the cell with a pitch of 10 mm. The grooves will be filled with wavelength shifting optical fibres. These fibres run radially towards the outer edge of the megatile where they are coupled to clear fibres using optical connectors.

The proposed materials to fulfil the required performance are:

- 2 cm thick scintillator Bicron BC404,
- 1 mm diameter WLS Bicron BC9929AMC,
- 1.1 mm diameter clear fibre Bicron BCF98MC.

In the preliminary design we have been using 10 mm BC404 and 1 m clear fibre that were fused to the WLS ones. However, the fusing of fibres would not be practical in the ALICE environment. Our tests with beams at the CERN PS and with cosmic rays indicate that the performance i.e. the number of photoelectrons ($N_{p.e.}$) detected and the time resolution depend crucially on the reflective layer on the scintillator. Comparing Tyvek, aluminium foil and Teflon tape we found that the latter gave the best results.

Time resolution vs $N_{p.e.}$

Minimum-ionized particles were used to establish the dependence of the time resolution on the number of photoelectrons detected with an XP2020 photomultiplier. Using the fact that the charge collected by the PMT is distributed over a large range according to a Landau distribution, we have divided the charged spectrum in 5 bins and have for each bin the corresponding time distribution. Using that information we have obtained the plot of ($N_{p.e.}$) vs the time resolution σ_t as shown in Fig. 3.8. The resulting points can be very well fitted with a curve given by $\sigma_t = 3.4/\sqrt{N_{p.e.}}$.

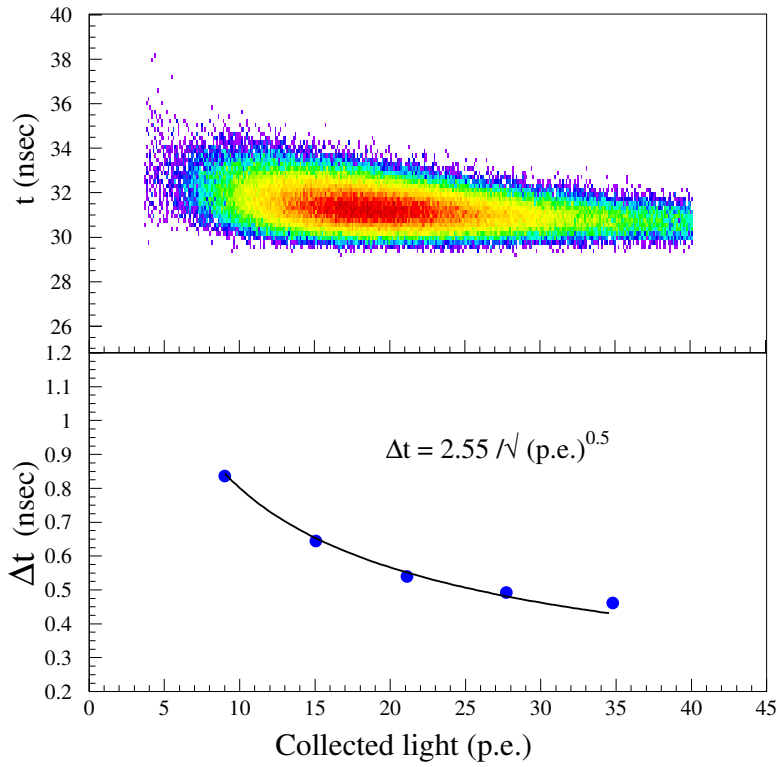

Figure 3.8: The time resolution extracted from a single run. The upper part shows the 2-dimensional plot of the number of photoelectrons vs the time of arrival of the pulse. The lower part shows the extracted time resolution for individual bins shown by black bars in the upper part. The points can be very well fitted by $\sigma_{time} = 2.55/\sqrt{N_{p.e.}}$.

The WLS fibres

During the tests we have used mostly BC9929A single clad WLS fibres. However, we have also tested Bicron BCF92MC WLS fibres. These latter were found to be inferior in light yield by about 20% compared to the BCF92. We are currently testing the performance of a batch of BC9929AMC and the first measurements on a test bench with a blue diode indicate a light yield about 50% superior to the BCF92MC one.

Clear fibres

Since σ_t depends strongly on ($N_{p.e.}$) we have measured the attenuation length of the clear fibre. To carry out the measurement, a WLS was fused to a clear fibre. The WLS was stimulated with a blue LED and the light transmitted at the end of the clear fibre was measured with a photodiode. We found that for a combination BFC92/BFC98 the attenuation length is 8.5 m while for a combination Y11/BCF98 the attenuation length is 7.5 m.

General performance

Prototypes similar to the final configuration (30° slices) of each one of the rings have been tested, the results obtained can be summarized in the following way:

- clear fibres longer than 5 m will not allow a resolution σ_t better than 1 ns,
- after 3 m of clear fibre and optical connector we obtained a light collection of 29 p.e. with a time resolution of 490 ps (after jitter time correction).

3.4.1.2 Design 2 and performance

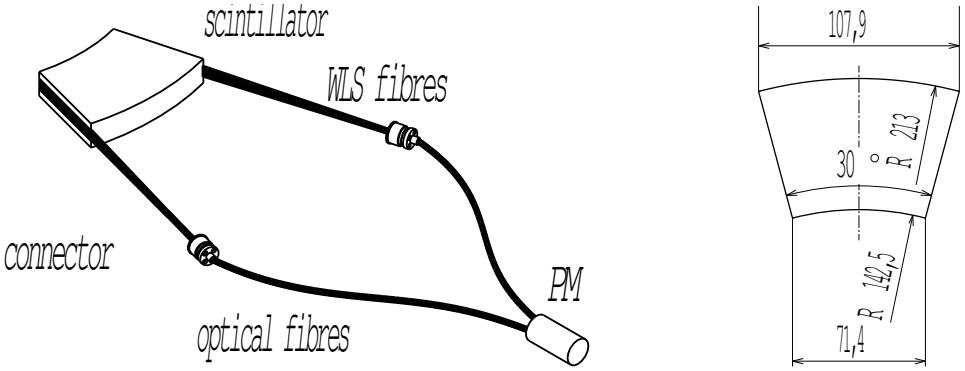

Figure 3.9: Single counter with the fibres embedded along the two radial edges of the scintillator counter (left). Dimensions of the scintillator block used for the tests (right).

The counter corresponding to this design was manufactured from a single scintillator piece, part of a V0 sector, coupled with two layers of WLS fibres glued along its two radial edges as shown in Fig. 3.9 where the dimensions are also given. The components used for these measurements were as follows:

- 2 cm thick scintillator BC408 or BC404 from Bicron [11],
- 1.0 mm diameter WLS fibres Y11 (double cladding) from Kuraray [12] or BCF9929A (single cladding or double cladding) from Bicron,

- 1.1 mm diameter optical fibres BCF98 (d.c.) from Bicron,
- connector for nine passages to transmit the light from the WLS to the optical fibres,
- Teflon film as envelop of the scintillator piece and the WLS fibres,
- aluminium coating as reflector at the end of the WLS fibres, opposite to the PMT,
- BC600 optical cement for embedding the WLS fibre layers in the scintillator block,
- BC630 silicone optical grease for an optimization of the light transmission from WLS to optical fibres.

Minimum-ionizing particles (MIP) were used to evaluate the performances of the counter. In Fig. 3.10, the time resolution is plotted as a function of the light yield for two types of components which are listed above, BC408/Y11 (d.c.) and BC408/BCF9929A (s.c.). These systems were measured with several lengths of optical fibre BCF98 (d.c.), from 1 to 16 m.

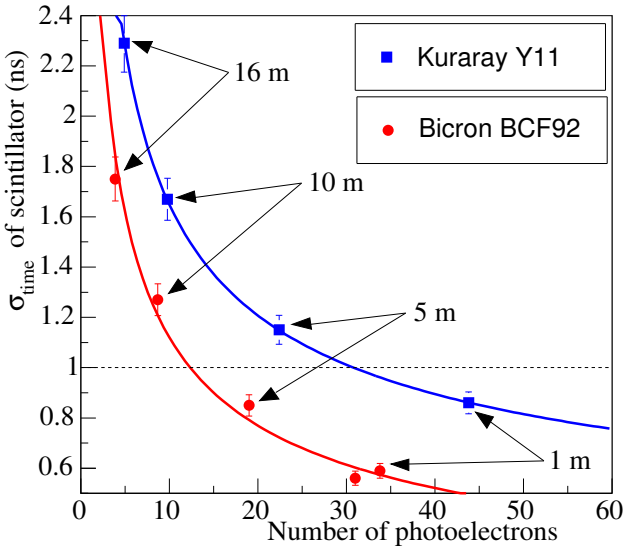

Figure 3.10: Time resolution as a function of light yield measured at the end of an optical fibre beam of several lengths (1, 5, 10 and 16 m) and for a few types of scintillator/WLS fibre coupling (see Fig. 3.9).

The following observations can be extracted from the results:

- The BCF9929A (s.c.) fibre is less efficient than the Y11 (d.c.) fibre as far as the light yield is concerned. Nevertheless, owing to its short decay time (2.5 ns) it provides a better time resolution than the Y11 (d.c.) fibre (decay time of 7 ns).
- For a given combination of materials, the time resolution varies like $1/\sqrt{N_{p.e.}}$. A time resolution of 0.6, 0.8, 1.3, 1.7 ns and 0.9, 1.1, 1.6, 2.3 ns can be achieved at the end of 1, 5, 10 and 16 m of optical fibres with the counter made of BC408/BCF9929A (s.c.) and BC408/Y11 (d.c.), respectively. The time resolution of 1 ns from the MIP can be achieved only if the transport distance is shorter than 5 m and 1 m respectively. This observation shows clearly the necessity of installing photomultipliers inside the L3 magnet at a distance shorter than or equal to 5 m.

These results will be improved if special care is taken in the choice of counter components. For exemple, the association of BC404 with BCF9929A (d.c.) should provide a larger light yield and a better time resolution at the end of the optical fibre beams. This improvement can be anticipated because of a better matching between the wavelength of the maximum emission light of the scintillator (408 nm for the BC404, 425 nm for the BC408) and the wavelength of the maximum absorption light of the WLS fibre (410 nm for the BCF9929A fibre). Moreover, the trapping efficiency of the double cladding fibre is a factor ≈1.7 [11] larger than the one provided by single cladding fibre. These combined effects should make the light yield collected at the end of the optical fibre larger by a factor 1.5 - 2. This expectation will be checked by special measurements.

These results and the previous one will be used to select the best system as regards the time resolution performance. The location of the photomultipliers allows optical fibre lengths shorter than 3 m and 5 m for the V0A and V0C arrays respectively. A time resolution of at least 0.6 ns could be reached.

We have checked [1] that the light yield does not depend significantly on the size of the scintillator blocks which compose the V0 arrays. On the contrary, the smaller the counter, the better the time resolution. The present tests were carried out with scintillator blocks representative of the largest counters of the arrays. Hence, the time resolutions which are given here are representative of the ones expected with the final geometry. We have measured that the adopted geometrical design (Fig. 3.9) provides an homogeneous light yield (within ±5%) across the entire surface of the scintillator. We measured that the efficiency for detecting the MIP was independent of the WLS fibre type. We have verified that no scintillation light is emitted by the WLS fibres when crossed by charged particles. Concerning the possible detection of Cerenkov light produced inside the optical fibres, we can make the following remarks: this light is emitted in the UV wavelength range inside plastic fibres, a very absorbant material, and on a cone surface with a half opening angle of about 40°. Therefore, the light produced in the fibres close to the counters (far from the PMT) will be very much attenuated when reaching the PMT. The light produced in fibres installed along a direction close to that of the particles (proximity of the PMTs) cannot be guided owing to its emitted direction which make its trapping difficult within the ≈25° acceptance angle of the fibres. As a consequence, no significant light yield should be collected due to direct impact of particles on the clear fibre beams. Tests will be carried out to verify this assertion. In conclusion, the choice of the counter elements seems to provide robust characteristics which suit well the needs of the V0 detector.

3.4.2 The V0A and V0C array designs

As shown in the two sections above, both designs give about the same integrated results (25 - 30 p.e./MIP, $\sigma_{time} \approx 600$ ps) if ever a common scintillating material type is adopted. Tests in progress are dedicated to that standardization.

Design 1 (each face of the tiles is read with array of WLS fibres) provides, relatively to the particle track segment within the scintillator, a similar geometrical network of fibres, whatever the position of the particle impact on the counter. This arrangement minimises the time fluctuation of the light signal. It is therefore the appropriate choice for large detector tiles. This design also is very well adapted to the space available on the A-side to integrate the transition needed from counter edges to clear fibres. As a consequence, design 1 was adopted for the realization of the V0A array installed in the RB24 side of ALICE. On the C-side (RB26), the tight space in radial and longitudinal directions only allows design 2 (each tile is read by WLS fibres at their radial edges) for the construction of the V0C array. It is the only one which permits the clear fibre bundles to be connected within the short existing radial distance. Moreover, the thickness of the overall V0C device (47 mm) suits well the reduced longitudinal space between the front absorber and the FMD/T0 detectors.

Finally, the Mexico group will build the V0A array according to design 1, the Lyon group the V0C array according to design 2.

3.4.3 V0A assembly

The V0A detector will be assembled following design 1. The eight slices will be constructed following the megatile technique described previously. The groove shape (key hole type) is such that the WLS fibres will be kept in place without the need of glue (Fig. 3.11). Each one of the WLS fibres will be cut at the outer edge of the megatile slice. At that point they will be joined to clear fibres by an optical connector. For each slice a single optical connector will joint the WLS fibres and the clear fibres (Fig. 3.12). The embedded end of the WLS fibres will be polished and aluminized. The number of fibres will vary proportionally to the size of the cell. The clear fibres (3 m long) will be bunched and brought to the PMT which will be placed in the plane of the scintillator disk. The housing of the counter will provide optical tightness and mechanical support for the optical connector.

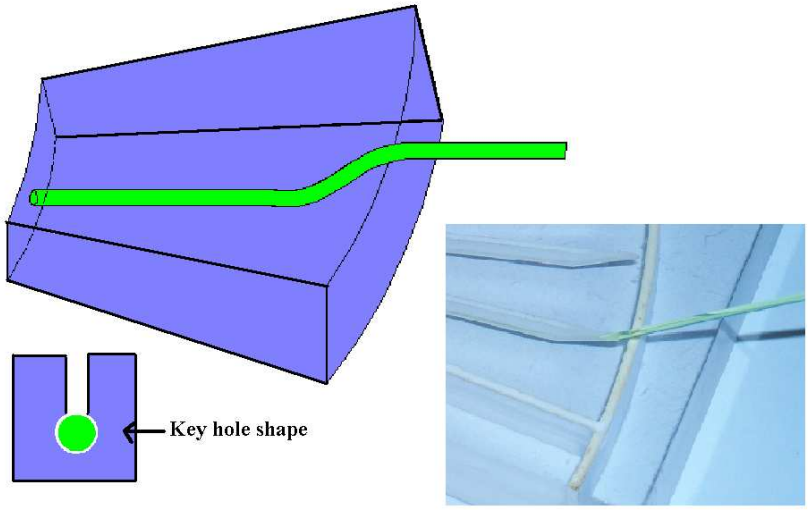

Figure 3.11: The main elements of the V0A design are shown. The upper left shows the way the WLS fibre is sunk into the scintillator to avoid small radii of curvature, while the lower left shows the keyhole design of the groove that keeps the fibre in place. The figure on the right shows the grooves in the scintillator on one face.

3.4.4 V0C assembly

All individual counters are assembled in the same way following design 2. Figure 3.13 (left) shows the different elements in the elementary channel.

The 2 cm scintillator is machined following the dimensions associated to the ring number (Fig. 3.14). A recess of 9 mm in width and 1 mm in depth is made along the radial sides of the block to be used to accommodate the nine WLS fibres. The fibres are preliminarily cut with the help of an assembling gauge and polished on one end. Their lengths are about 335, 309, 263 and 187 mm for elements of rings 1, 2, 3 and 4 respectively. The polished end is coated with aluminium. The other end is embedded in the connector (Fig. 3.13 (right)), and the side is polished. The layers of nine fibres are fixed with BC600 optical glue within the recess. Finally, scintillator and fibres are wrapped in a Teflon strip. The light is thus trapped inside the scintillator and the fibres are protected against mechanical damage.

Optical fibres to be used for the light transport to the PMT are cut at the same length. They are gathered in bunches of nine to constitute a bundle. Each bundle is protected by a black PVC sheath of 5/6 mm in internal/external diameter. The connector (Fig. 3.13 (right)) is mounted on one end for the link to the WLS fibres. The nine fibres are then assembled on the opposite side and inserted into a

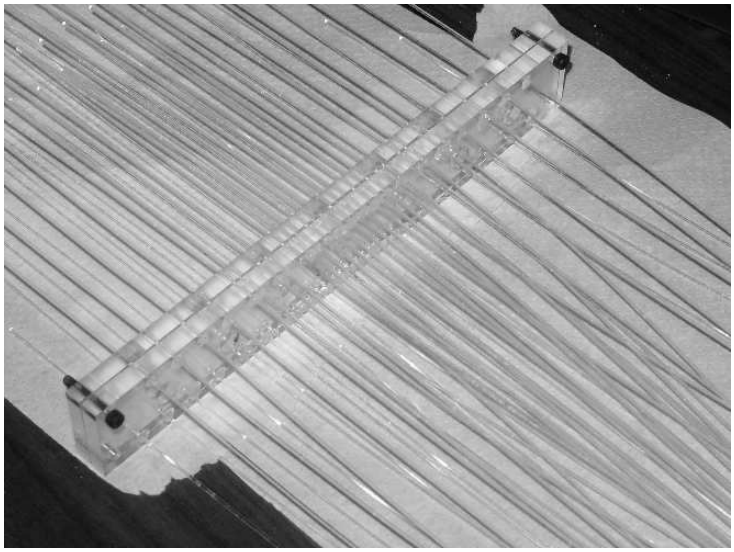

(a)

(b)

Figure 3.12: (a) The optical connector between the WLS fibres and the clear fibres. The WLS fibres, protruding towards the upper left part of the figure are shown before being inserted into the scintillator. The clear fibres are running towards the lower right side of the figure. (b) The three bundles, from the three rings of the prototype are connected to the photomultipliers via the cylindrical connectors. The number of fibres in each connector depends on the size of the respective ring.

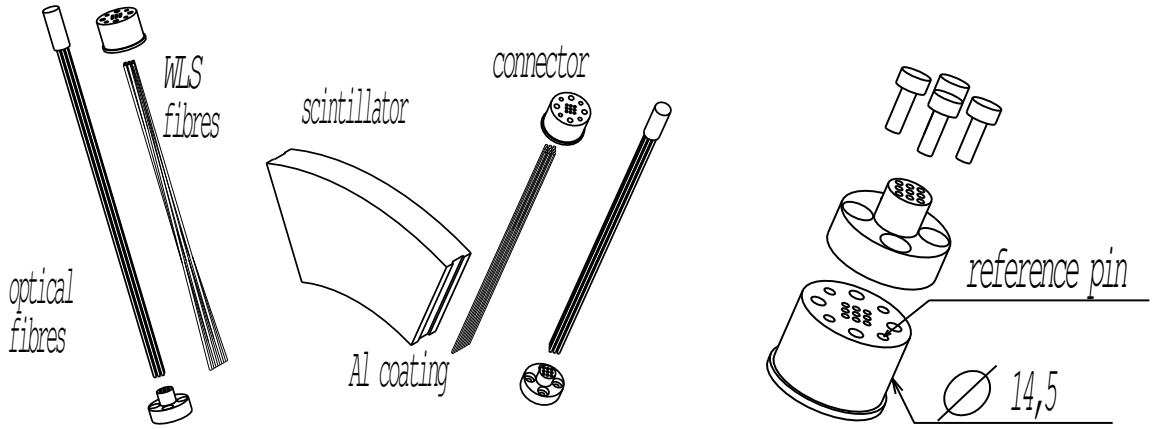

Figure 3.13: Elements for the mounting of the individual V0C counters (left). Connector (right).

plastic cylinder of 5 mm in external diameter. It is used to assure optical contact with the photomultiplier cathode. Finally both ends are polished.

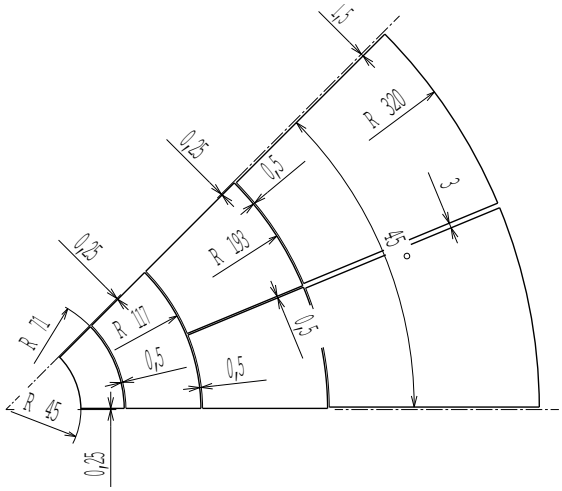

Figure 3.14: Sector of the V0C array. Actual dimensions of the counters taking into account the constraints for their installation.

The sector of the array consist of six counters as shown in Fig. 3.14. Each channel of rings 3 and 4 is made of two identical counters in order to reduce their transverse dimensions and thus to minimize the degradation of the time resolution. The drawing also shows the Teflon strip thickness. The dead surface represents about 2.5% of the array area.

The eight sectors of counters are mounted inside a box made of two identical parts (Fig. 3.15). This box consists of 3 mm carbon fibre plates assembled with glue. The external side is a 16 segment polygon. The part of the connectors attached to the WLS fibres are fixed with glue across these faces. Cut views along directions at 22.5°, 11.25° and 0° relatively to an inter-sector direction are shown in Fig. 3.16. Rings 3 and 4 are set on the bottom of the box. Wedges are glued between elements of ring 4 to prevent any rotation of the pieces. Rings 1 and 2 are raised by 20 and 10 mm from the bottom. The recess for layers of fibres is shifted by 5 mm towards the top of scintillators. The dead zones between the segments are thus minimized. Each sector is maintained in vertical position by a foam of Rohacel glued on the bottom below rings 1 and 2 and under the cover above rings 3 and 4. Finally, two plastic pieces are

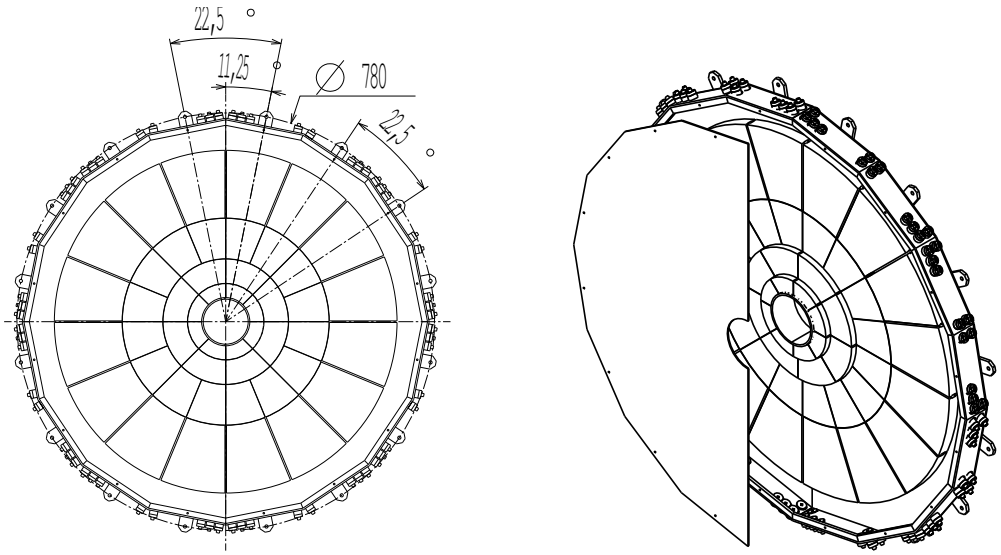

Figure 3.15: Views of the V0C array mounted in its box.

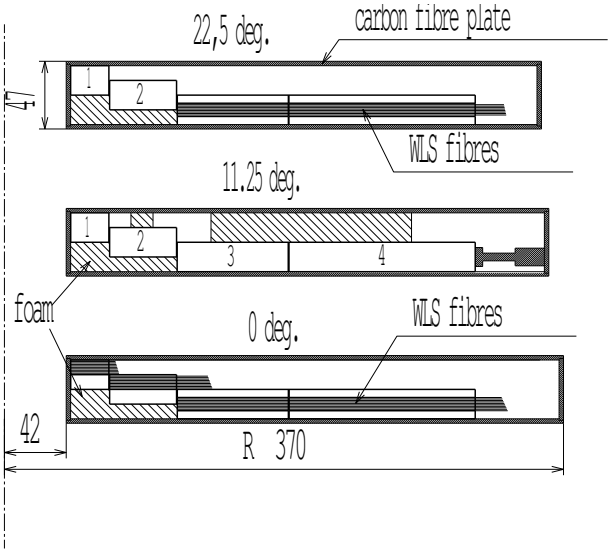

Figure 3.16: Three cut views along the directions at 22.5°, 11.25° and 0° relative to an inter-sector radius of the V0C array.

in extension between the ring 4 segments and the internal face of the box to maintain the sector in the horizontal direction.

3.5 Light pulse treatment

The aim of the light pulse treatment is to supply the V0 Front-End Electronics (and the TDR wake-up electronics) circuits with signal so that:

- minimum-bias triggers from the MIP can be provided with a large efficiency in pp and Pb–Pb collisions,
- the large dynamics of the light signal encountered in the Pb–Pb collision can be transmitted with a minimum of distortion.

A MIP detection efficiency of about 98% is obtained if the electronics system can react starting from its most probable light signal minus twice the rms (σ_{MIP}) of the distribution. The low edge of the signal range will thus be the light corresponding to the MIP$-2\sigma_{MIP}$. Each cell of the V0 will have to detect up to 500 MIPs (Section 3.3.3.2) in Pb–Pb collision. The high edge of the signal range will thus correspond to 500 MIPs. As $\sigma_{MIP} \approx MIP/4$ [2] in the conditions of the tests, the full signal dynamics will have to approach 1000.

In this section, we present the work carried out to choose the photomultiplier. Then, we try to define what will be the first stage of the electronics circuit feeding the Front-End Electronics system as described in Section 3.6.

3.5.1 Photomultiplier

Photomultipliers will be used to amplify the signal. They will be installed inside the magnetic field volume of the L3 magnet. Thus only mesh tubes can be chosen. There are a few such tubes proposed by two companies, Hamamatsu from Japan and Electron from Russia. The description and characteristics of some of them are given in Table 3.2.

Table 3.2: Characteristics of some mesh tubes candidates for equiping the V0 detector.

	PMT4	PMT3	PMT2	PMT1
PMT	**FEU-187**	**R5505-70**	**R5946-70SEL**	**R7761-70**
HV divider	**Tveng(035)**	**H6152-70**	**E6113-03**	**H8409-70**
Tube diam./length (mm)	32/65	25/40	38/50	39/50
Number of stages	15	15	16	19
HVmax	2300	2300	2300	2300
Gain^{HVmax}		10^6	2.5 10^6	7. 10^7
Gain^{2000V} at 0 T/0.5 T	2. 10^5/1.6 10^5	5. 10^5/2.3 10^5	10^6/4.3 10^5	10^7/3. 10^6
Rise/transit time (ns)	1.5/6	1.5/5.6	1.9/7.2	2.6/7.5
Dark current (max) (nA)	20	30	30	100
Pulse linearity (2%) (mA)		180	360	500

In order to select a PMT well adapted to the V0 counter performances (number of p.e. and time resolution from the MIP, dynamics of the signal, etc.) special tests were and are being carried out with green LED light, particles from the PS accelerator, and cosmic MIPs. In the latter case, a scintillator mounted according to design 2 and with dimensions given in Fig. 3.9 was used. Five metres of clear fibres were connected to the WLS fibres which allowed a light yield of about 20 p.e. and a time resolution close to 800 ps (Fig. 3.10). In those measurements, the XP2020 with a bialkali cathode was used.

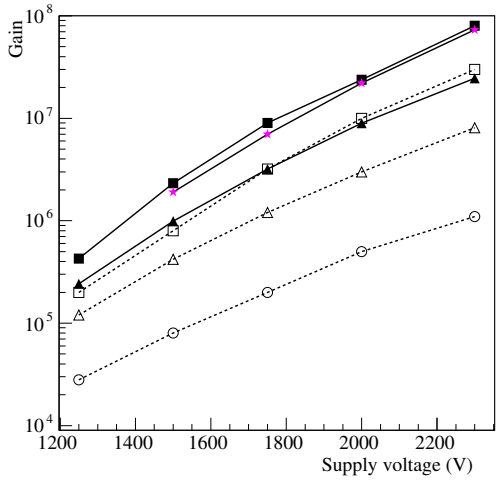

Figure 3.17: Gain distributions as a function of HV applied to PMT1 (square and star), PMT2 (triangle) and PMT3 (circle). Full symbols are from present measurements, stars from measurements by the constructor, empty symbols are from catalogues.

As shown in Table 3.2, there are bialkali cathode mesh PMTs with 19 (PMT1), 16 (PMT2) and 15 (PMT3 and PMT4) dynodes, the two last being in fact very similar. A large spectrum of gain can thus be expected. The gain distribution of some of them (PMT1 and PMT2) was measured with the cosmic MIPs as a function of the HV value. Results are shown in Fig. 3.17 and compared to corresponding distributions measured by the constructor for PMT1 and given by the constructor's catalog for PMT1, PMT2 and PMT3. The results of the measurements with PMT1 are similar, but a factor 2 larger than the distribution given in the catalog. The gain curve of PMT2 is three times larger than that of the catalog. Concerning PMT3, the gain given in the catalog is still lower by a factor of about 10 as compared to the PMT2 gain curve. We think that PMT4, which was chosen for the T0 detector and which we could not test in time, has a gain no larger than that of PMT3.

The charge provided by the MIP (q) measured at the maximum of the distribution by PMT1 and PMT2 is given in Fig. 3.18 (left) as a function of the applied HV. The values cover the ranges 1.3 - 247 pC and 0.9 - 77 pC between 1250 V and 2300 V for PMT1 and PMT2, respectively. The charge distribution obtained with PMT1 at 1250 V is shown in Fig. 3.18 (right). The MIP distribution centred at $q = 1.3$ pC has a r.m.s. value (defined by the distribution at smaller q) of $\sigma_q = \sigma_{MIP} = 0.33$ pC. The electronics noise gives $q = 0$ pC with $\sigma_q = 0.17$ pC. We thus observe that the 1.3 pC is at $3.8\sigma_q$ above the pedestal, which makes possible the discrimination of the MIP signal at the level of the MIP$-2\sigma_{MIP}$ value. Obviously, this figure shows a limit of the possible adjustment. In fact, we need to apply a HV of at least 1250 V and 1350 V to PMT1 and PMT2 respectively. If we refer to the catalog curves we need to apply at least 1400, 1600 and 2000 V to PMT1, PMT2 and PMT3 (PMT4) tubes respectively.

The value of the MIP light obtained by test results (Section 3.4.1.1) and expected by tests in progress (Section 3.4.1.2) cannot be larger than a factor 1.5 - 2 as compared to the present light yield which is 20 p.e. Moreover, the attenuation of the signal due to the magnetic field effect (0.5 T) is of the order of

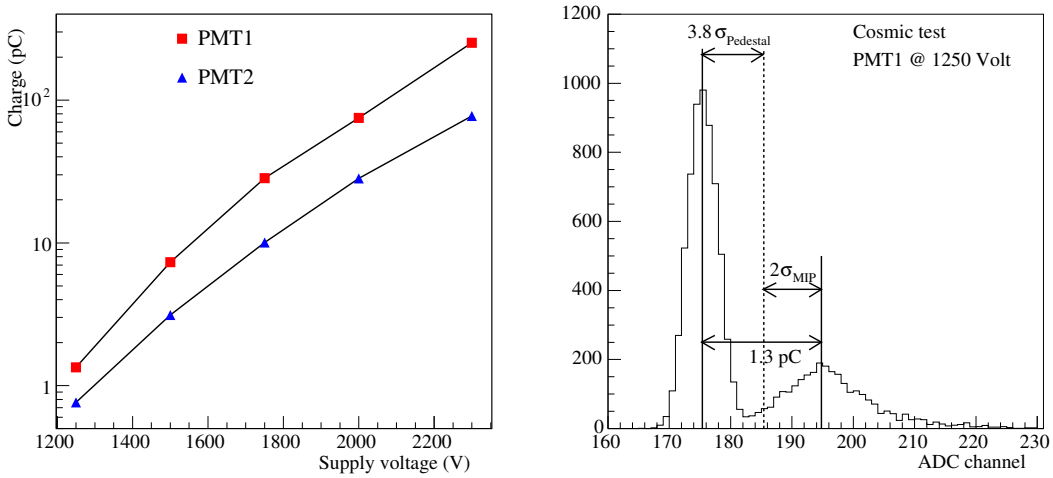

Figure 3.18: Charge delivered by PMT1 (square) and PMT2 (triangle) as a function of the HV value from the cosmic MIP providing about 20 p.e. (left). Distribution of cosmic events as recorded by a QDC (0.07 pC per channel) electronics module (right).

60%. The resulting effect can be compensated by increasing the HV value. PMT3 and PMT4 would see their HV value increased to about 2300 V. This large value is not recommended to guarantee the longevity of these tubes and does not offer any safety margin for adjustment. As a consequence, the 15-dynode PMT3 and PMT4 cannot be adopted for the V0 detector due to their too low amplification. PMT1 and PMT2 clearly offer the possibility of such an increase. The 16-dynode PMT2 could be retained with an optimal working HV value of about 1700 V. Finally, the 19-dynode PMT1 could also be adopted by working at about 1500 V if its performances are not degraded at such low HV working conditions.

Measurements of the time resolution provided by the cosmic MIP were carried out with PMT1 and PMT2 as a function of the HV value. The results are given in Fig. 3.19 (left). The time resolution is degraded when the HV of the PMTs is decreased. That is due to the threshold discriminator used to define the time. The smaller the signal, the larger the time fluctuation of the pulse at a low fixed threshold level. A threshold of about 10 mV was adopted for these measurements. Similar measurements (threshold fixed at 65 mV) were obtained from a pulse signal amplified by a factor 10. The results are plotted in the same figure. They show a clear improvement of the resolution for each value of the HV. An illustration of this effect is given in Fig. 3.19 (right). It shows results obtained with a 2 GeV/c PS beam. The signal provided by PMT2 is amplified by a factor 10, then transmitted to the electronics system through a 25 m cable, length representative of the final distance between the V0 detector and the Front-End Electronics. The time resolution is plotted as a function of the discrimination threshold applied to the signal. Results are shown for three HV values, 1300 V, 1400 V, and 1500 V providing a signal amplitude of 32 mV, 61 mV, and 89 mV, respectively. Above a minimum threshold, the nominal time resolution of 800 ns (Fig. 3.10) is again measured. Moreover, this resolution can be reached at a threshold value corresponding to the MIP$-2\sigma_{MIP}$ amplitude. In the present measurement, 1400 V or 1500 V applied to PMT2 can provide this performance, while 1300 V is too low. Therefore, an amplification of the pulse at the output of the PMT allows one to get rid of the degradation of the time resolution due to a possible low applied HV value.

In conclusion, the 15-dynode PMT3 and PMT4 have a too low gain to be adopted for the V0 detector. On the contrary, the 19/16-dynode PMT1/PMT2 seem to be a good option. Complementary tests are being carried out in order to make a final choice.

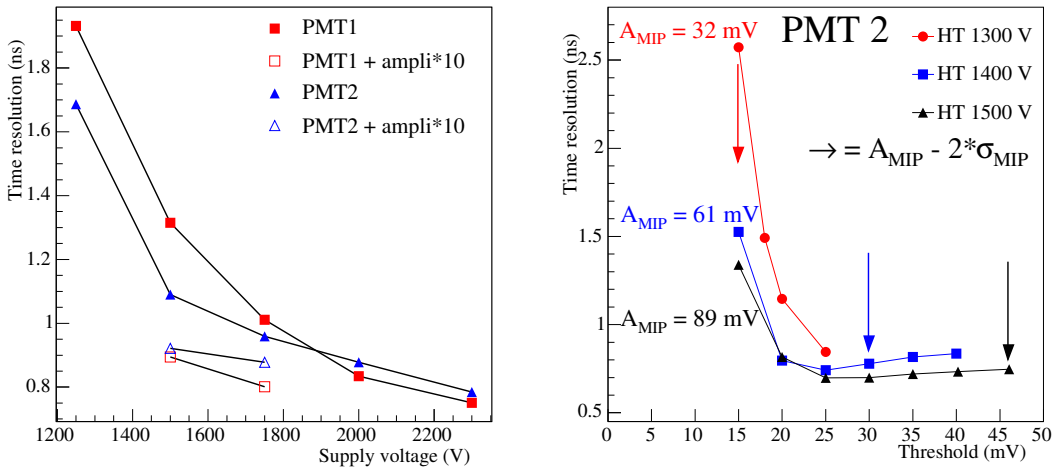

Figure 3.19: Time resolution of PMT1 (square) and PMT2 (triangle) as a function of the HV value from the cosmic MIP providing about 20 p.e. Full symbols are results at the PMT output, empty symbols after signal amplified by a factor 10 (left). Time-resolution of PMT2 as a function of the discrimination threshold applied to the signal after an amplification factor of 10 and a 25 m cable, and for three HV values (right).

3.5.2 First stage of the electronics circuit

The charge of the MIP was 1.3 pC (minimum charge to be detected: 0.65 pC) with PMT1 at 1250 V and PMT2 at 1350 V. Taking into account the pulse width of 10 ns (FWHM), the MIP corresponds to a signal amplitude of 6.5 mV (minimum amplitude to be detected: 3.25 mV) at the output of the PMT terminated in a pure resistance of 50 Ω. The dynamics of 1000 required in Pb–Pb collisions leads to a maximum signal of 650 pC or 3.25 V.

The signal provided by each V0 channel is sent to a threshold discriminator for TRD wake-up generation. This treatment is carried out close to the PMTs, at a distance of a few metres. The signal is also sent to another discriminator (or possibly the NINO circuit [14]) for the generation of the V0 triggers and to an integrator for the measurement of its surface (charge). This treatment is carried out far from the PMTs, at about 25 m (the signal attenuation of 13% at the end of the cable can be compensated by a slight increase of the PMT HV). This double utilization dictates the generation of two parallel signals from a fast initial amplifier situated just at the output of the PMT.

The signal (dynamics of 0.65 pC to 650 pC or 3.25 mV to 3.25 V at the PMT output), after its initial amplification at the PMT output, will have to be adjusted in a second step according to the input characteristics of the discriminators (low minimum threshold and full input dynamics) or the NINO circuit. This last one requires a maximum signal of 1.5 pC and allows one to adjust a minimum-bias threshold up to 5 fC. These specifications do not fit a priori the signal amplitude range which is generated. Nevertheless, tests are being carried out to determine the amplification functions (linear or logarithmic) to be used for an eventual adoption of the circuit. If the conditions do not allow us to use it, a classical discriminator will be used. Finally, parameters of the charge integration circuit can then be defined.

To summarize, studies are progressing to define the amplification functions at the output of the PMT and at the input of the discriminators (or the NINO circuit of the FEE) according to the dynamic range of the signal which is 0.65 pC to 650 pC in charge or 3.25 mV to 3.25 V in amplitude at the PMT output. The electronics concept should be finalized by the end of 2004.

3.6 Front-End Electronics (FEE)

3.6.1 ALICE trigger and Data Acquisition Architecture

The ALICE detector is designed to be sufficiently flexible to acquire data during the different run periods and according to the various types of physics and trigger investigated. The heavy-ion runs (calcium, lead) will account for about 10% of LHC running time. Proton-proton interactions will also be collected. Table 3.3 summarizes the luminosities and trigger rates foreseen for the several collision periods.

Table 3.3: Trigger parameters at ALICE.

	Pb–Pb	**Au–Au**	**pp**
Bunch crossing (ns)	125	125	25
Luminosity (cm^2s^{-1})	10^{27}	2.7×10^{27} - 10^{29}	10^{30}
Interaction rates (Hz)	8000	8000 - $3. \times 10^5$	10^5
L0-trigger latency (μs)	1.2		
Max L0-trigger rate (kHz)	1.3	1.3 - 3.0	1.2
L1-trigger latency (μs)	5.5		
Max L1-trigger rate (kHz)	1.1	0.7 - 1.1	1.1
L2-trigger latency (μs)	$\leq$100		
Max L2-trigger rate (Hz)	40	40	$\leq$500
Max V0 event size (Kb)	60	60	$\leq$750

The trigger and the readout systems will therefore be designed with a large bandwidth in order to cope with the very high particle multiplicity produced in ion-ion interactions, as well as with the low-multiplicity events obtained at high rate during the pp running mode.

The ALICE trigger system is subdivided in three levels:

The Level-Zero Trigger (L0) strobes the Front-End Electronics of the ALICE detectors. The trigger latency with respect to the time of the interaction is fixed at $1.2\,\mu$s. The detectors respond to the L0 with 'Detector BUSY' signals. The front-end is held on L0 and the logic waits for a first-level trigger L1 or for a timeout in the case of a missing L1. The trigger is distributed with a fast fan-out to all the front-end cards.

The Level-One Trigger (L1) is issued at a fixed latency of around $6\,\mu$s (still to be precisely specified) with respect to the interaction time. A positive L1 trigger causes the event number to be distributed to the detectors and starts the transfer of the data from the front-end event registers to the multi-event buffers.

The Level-Two Trigger (L2) causes, after data reduction and packing, the data transfer to the ALICE data acquisition. The L2 reject signal (L2r) can be issued at any time before the fixed latency corresponding to a level-2 accept (L2a) trigger at around $90\,\mu$s (that still needs to be precisely specified).

The architecture of the ALICE Data Acquisition (DAQ) system is as follows: event fragments are collected from the Front-End Electronics (FEE) by readout and Local Data Concentrator (LDC) operating in parallel. The connection between the sub-event building system and the Front-End Electronics is

established by the ALICE Detector Data Link (DDL). Each sub-event building system is able to acquire data in stand-alone mode. The event building and distribution system assembles the sub-events into full events and records them onto Permanent Data Storage (PDS). Each Global Data Concentrator (GDC) receives event-fragments from the LDCs via a switch, and sends full events to the PDS through a second switch.

At level 0 the data are held on the front-end registers and, in the case of positive L1 trigger without timeout, are transferred from the Front-End Electronics to the local event memory waiting for the L2 trigger decision. On a positive L2, the data are then transferred to the LDC via the Detector Data Link, a high speed optical fibre. The protocol is common to all sub-detectors.

The aggregate bandwidth is up to 2.5 GByte/s at the level of the GDC. After processing and data compression, the maximum bandwidth is reduced to 1.25 GByte/s towards the PDS.

3.6.2 Overview of the V0 FEE

3.6.2.1 Functional description of the FEE

The readout and data acquisition architecture (Fig. 3.20) is designed to be compatible with the different running modes and to withstand the trigger rates. The system will generate six triggers of level 0 (only five will be sent to the CTP inputs with two centrality triggers selected amongst the three possibilities) and several sets of information listed hereafter:

- A minimum-bias (MB) trigger: this trigger is generated if the number of channels fired during a collision is at least one on V0A and one on V0C. The detection of the fired channels is made by means of two observation windows, one for V0A (named BBA) and the other one for V0C (named BBC).

- Two beam-gas (BG) triggers: one for the beam-gas which occurs on the RB24 side of the ALICE detector, the other one for the beam-gas which occurs on the RB26 side. The detection of these beam-gas events is done by the use of two specific observation windows, BGA and BGC, in partnership with BBC and BBA respectively.

- Three centrality triggers of the collision: these triggers are generated if one or the other, or both of the following conditions are respected:

    1. the integration charge seen by V0A and V0C during a collision is larger than a programmed trigger generation threshold (two such triggers are generated),
    2. the number of channels fired during a collision is larger than a programmed trigger generation (for V0A and for V0C).

- A measure of the multiplicity of MIPs: this measurement is obtained in two different ways:

    1. after an anode charge digitization,
    2. after a pulse length measurement (proportional to the charge of the pulse) if the NINO circuit can be used.

- A measure of the time difference between the detected particles and the beam crossing signal or beam clock (BC).

- A wake-up signal for the TRD: the assigned time to provide this wake-up signal is extremely short. Therefore copies of all PMT anode outputs are sent to the ‘shoebox’ which will perform the wake-up function itself for the TRD.

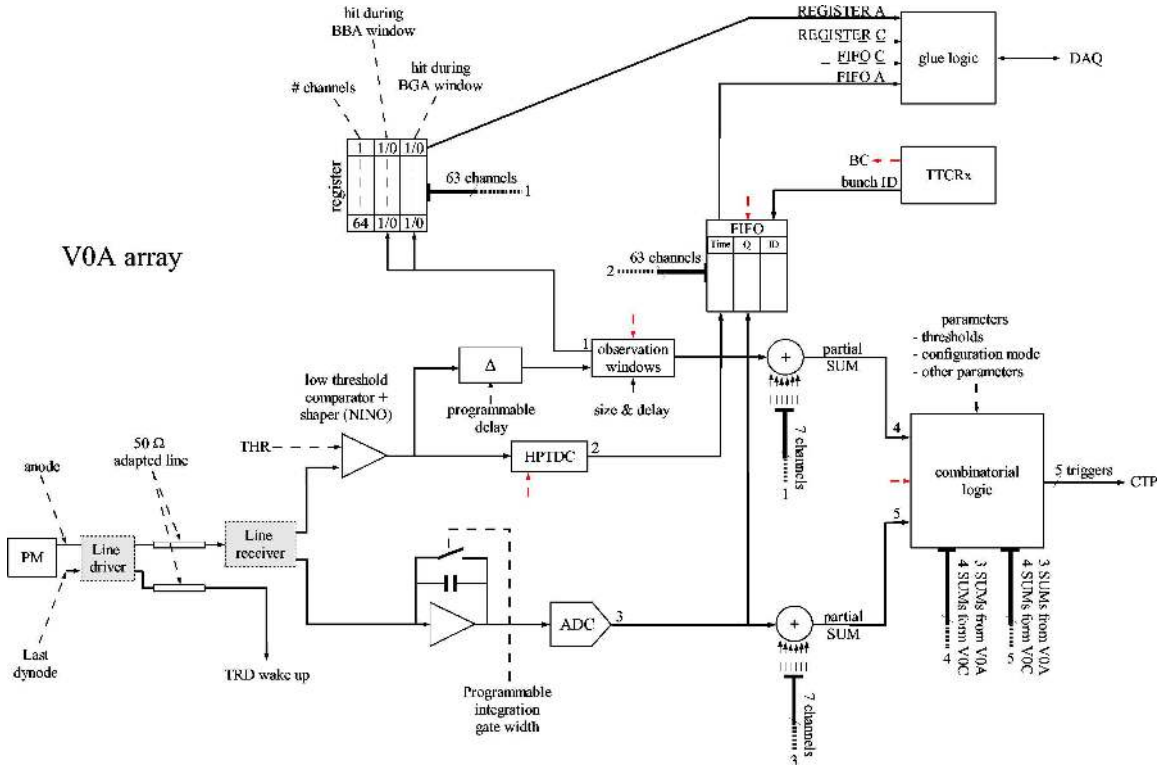

Figure 3.20: V0 Front-End Electronics scheme.

3.6.2.2 Physical description of the FEE

The readout scheme follows the modularity of the detector and the ALICE trigger requirements. In the present design, the segmentation of the V0A/V0C arrays is shown in Fig. 3.1.

The trigger generation, readout, and data acquisition chain of the V0 consists (Fig. 3.21) of the following elements:

TTCIU, Timing, Trigger and Control Interface Unit: it performs the following tasks:

1. Interface between Timing Trigger and Control distribution (TTC) system and V0 FEE,
2. FEE clock and trigger distribution.

The main component of this board is the TTCrx, a custom IC designed by the CERN PH Microelectronics group. The TTCrx acts as an interface between the TTC system for LHC detectors and its receiving users (V0 FEE). The ASIC delivers the clock together with control and synchronization information to the Front-End Electronics controllers in the detector. The TTCrx is programmed by a FPGA, which also performs the interface with the VME back plane, to compensate for the particle times of flight and the propagation delays associated with the detector and the FEE. The IC delivers the 40.08 MHz LHC clock signal, the first-level-trigger decision signal, and its associated bunch and event numbers. All this information is sent to the other boards through the VME back plane. In addition, it provides the transmission of synchronized broadcast commands and individually addressed commands and data. (The integration with the TTC must be studied in detail. The interface between the TTCIU board and the TTCrx must be defined.)

CIU, Channel Interface Unit: it performs the following tasks:

1. measurement of the anode signal amplitude (charge),

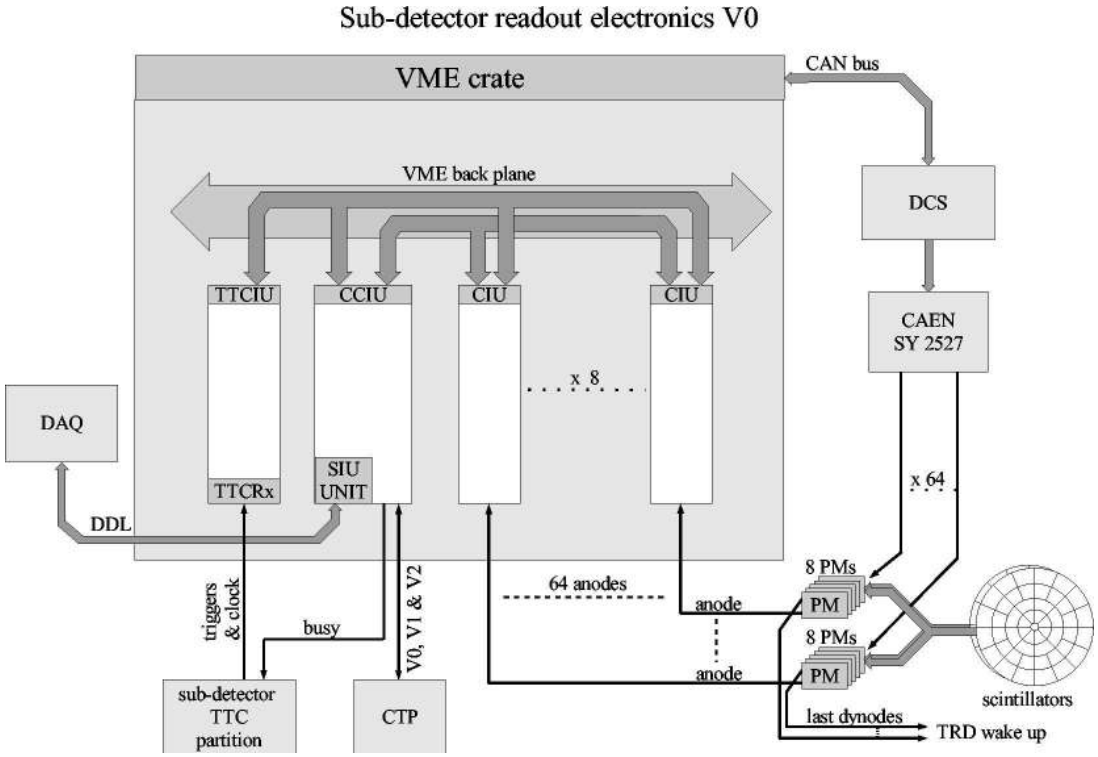

Figure 3.21: V0 Data Acquisition Scheme.

2. digitization of the time for all the hits coming from the ring,
3. pre-processing for the generation of the various triggers,
4. data storage during a L0 and L1 trigger.

The two main components of this board are NINO and HPTDC:

1. NINO [14] is an ultra-fast front-end amplifier discriminator. The use of this component is, however, conditioned by its compatibility with the shape of the V0 signals. In case of non-compatibility, a low threshold discriminator will be used. Moreover, NINO (or any discriminator) must be associated to a buffer in order to preserve the signal integrity, in particular for the charge integration (TBC).
2. HPTDC [15] is a Time-to-Digital Converter.

The CIU board is a 9U format board connected to the rest of the electronics via the specific back plane. Each CIU board processes anode signals from the eight photomultipliers of a V0 ring. There are four CIU boards per detector (four for V0A and four for V0C).

CCIU, Channel Concentrator Interface Unit: it performs the following tasks:

1. processing of the final trigger signal,
2. collection and organization of the data from CIU boards,
3. provision of an interface to the DAQ.

The CCIU board is a 9U format board connected to the rest of its detector electronics via a VME back plane. The CCIU board broadcasts the collected data to the DAQ (Data Acquisition system) via one DDL link. It is connected to the TTC for the five trigger signals and to the LTU for the generation of the 'busy' signal.

The V0 electronics of both array systems (V0A and V0C) is located in one VME crate. This 11U VME crate is used only for its mechanical structure which can accept 9U modules and for its supply voltage. There is no VME controller in the rack. All boards plugged on the VME back plane are full customs and do not use the VME bus but a specific back plane.

3.6.3 Minimum-bias trigger

The minimum-bias trigger makes it possible to identify beam-beam (BB) collisions. For that, it is necessary to verify on each disk (V0A and V0C) the event occurence at the expected time, namely 11 ns after the collision on V0A and 3 ns after the collision on V0C (see Fig. 3.22).

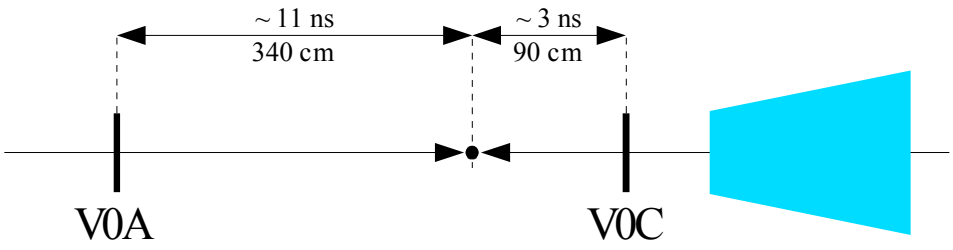

Figure 3.22: Time alignment condition on V0A and V0C.

The hit detection is done through two programmable observation windows (programmable start and stop times in steps of 0.5 ns). These observation windows are named BBA for the V0A and BBC for the V0C. Each hit is then precisely located inside these two windows through delay lines programmable in steps of 20 ps. There is one programmable delay per channel. The generation of the minimum-bias trigger is effective as soon as there is one hit at least simultaneously detected by V0A (BBA = 1) and by V0C (BBC = 1) (Fig. 3.23).

Remarks concerning the minimum-bias trigger circuit:

- The part of the circuit included inside the circle in Fig. 3.23 is entirely integrated in FPGA. It is thus possible to modify the minimum-bias trigger generation logic until the end of the design.
- The control of the selection or the inhibition of channels is possible through an individual ON/OFF command (common command with the other triggers).
- The state of each segment (symbolized by a flag), fired (1) or not (0) by at least one hit in the corresponding observation window, will be sent to the DAQ on the reception of an L2 trigger for an off-line analysis.
- The detection of hits within an observation window is performed in an ultra fast technology (ECLinPS) with a double synchronization to avoid metastability problems.
- The generated trigger is synchronized with the LHC clock.

3.6.4 Beam-gas triggers

The beam-gas (BG) triggers allow one to ensure that a beam-gas collision took place on the RB24 side or on the RB26 side of the detector. The beam-gas detection is done through two observation windows (gates), one applied to V0A counters (called BGA) and the other one applied to V0C counters (called

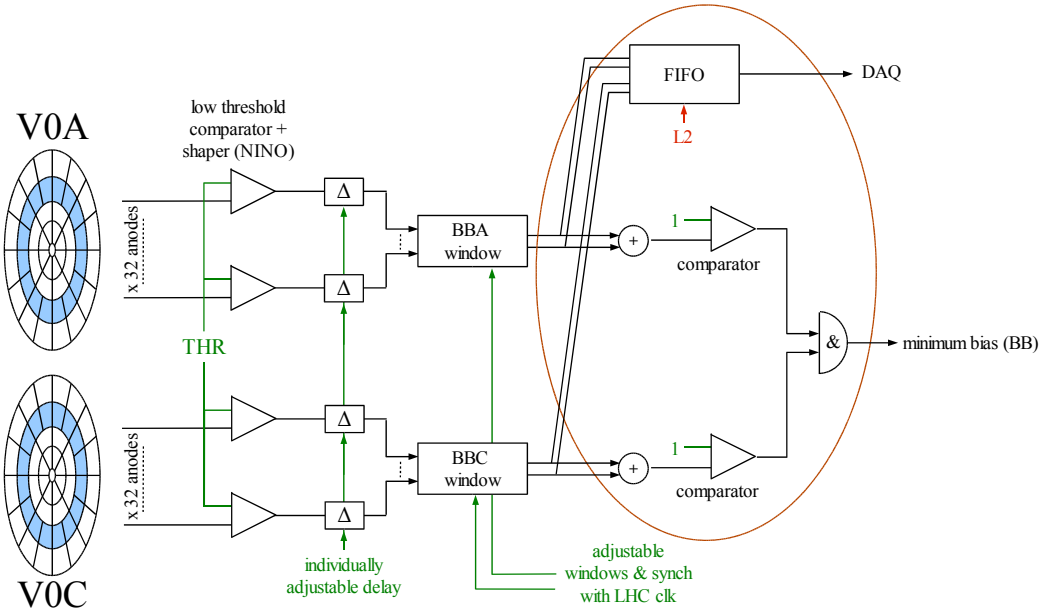

Figure 3.23: Minimum-bias trigger.

BGC). They are also programmable in steps of 20 ps for the start time and in steps of 0.5 ns for the stop time (see Fig. 3.24).

To generate both triggers, it is necessary to detect on each disk (V0A and V0C) an event occurrence at the expected time (Fig. 3.25), namely:

- For BG from RB24: in the same time as an expected hit due to a BB collision on V0C (BBC) and ≈22 ns before the expected hit due to a BB collision on V0A (BBA).
- For BG from RB26: in the same time as an expected hit due to a BB collision on V0A (BBA) and ≈6ns before the expected hit due to a BB collision on V0C (BBC).

The generation of the BG triggers is effective if the following conditions are respected:

- For BG from RB24, if the two following requirements are fulfilled:
  1. for the considered clock period and during the BBC observation window, the number of hits seen by V0C is higher than a programmed threshold TH3 (BBC = 1),
  2. for the previous clock period and during the BGA observation window, the number of hits seen by V0A is higher than a programmed threshold TH4 (BGA = 1).
- For BG from RB26, if the two following requirements are fulfilled:
  1. for the considered clock period and during the BBA observation window, the number of hit seen by V0A is higher than a programmed threshold TH1 (BBA = 1),
  2. for the considered clock period and during the BGC observation window, the number of hit seen by V0C is higher than a programmed threshold TH2 (BGC = 1).

Remarks concerning the beam-gas trigger circuit:

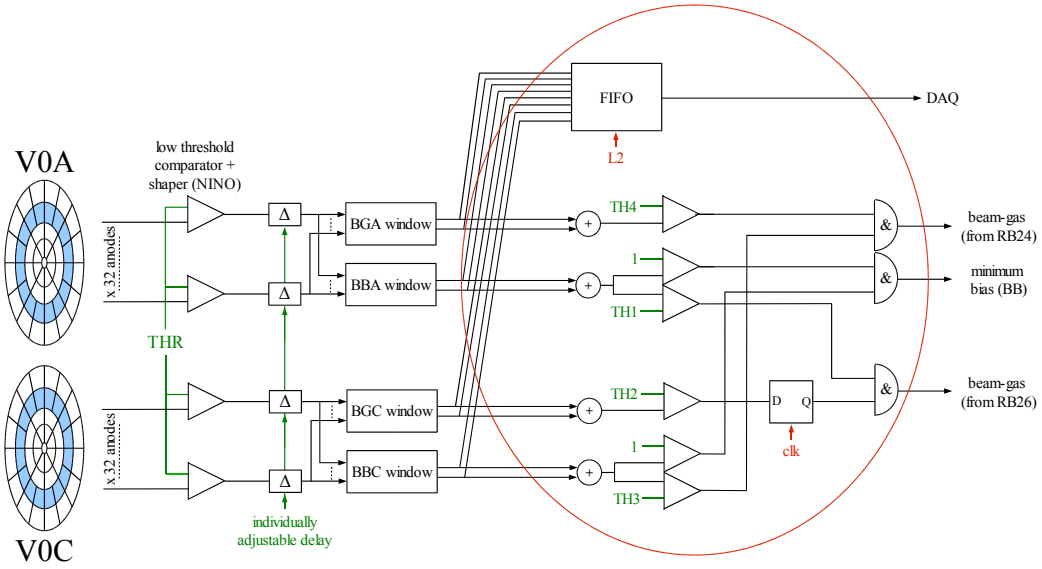

Figure 3.24: Beam-gas triggers.

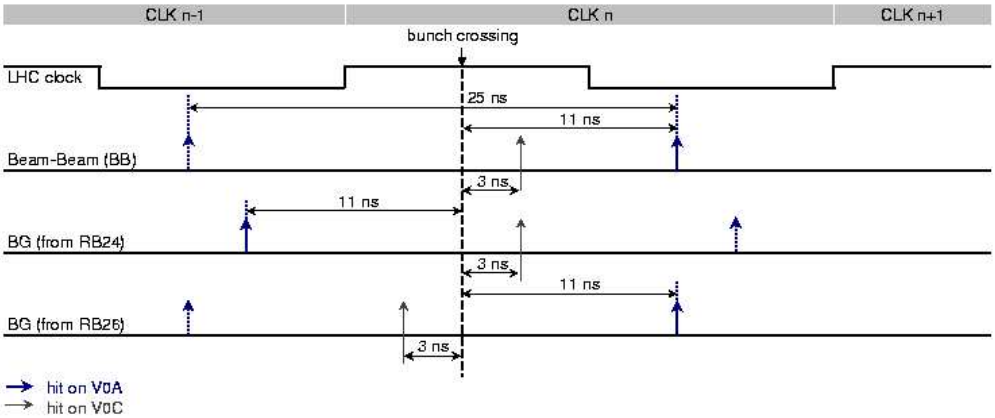

Figure 3.25: Time alignment for BB, BGA and BGC events.

- The part of the circuit included inside the closed line in Fig. 3.24 is entirely integrated in FPGA. It is thus possible to modify the beam-gas trigger generation logic until the end of the design.
- The control of the selection or the inhibition of channels is possible through an individual ON/OFF command (common command with the other triggers).
- The state of each segment (flag) fired (1) or not (0) by at least one hit in the corresponding observation window will be sent to the DAQ on reception of an L2 trigger for an off-line analysis.
- The detection of hits within an observation window is performed in an ultra fast technology (ECLinPS) with a double synchronization to avoid metastability problems.
- The generated trigger is synchronized with the LHC clock.

3.6.5 Centrality triggers and multiplicity measurement

The purpose of these centrality triggers is to give information on the multiplicity for each period of the LHC clock. Electronics must be able to dissociate two consecutive events (e.g. BG after BB) even if the occurrence of such a sequence remains very rare.

Two types of centrality triggers are implemented on the V0 FEE. The first one is able to work for all interaction types (Pb–Pb, Au–Au, pp). It is based on a dual high-speed integrator. It generates a central trigger if a high threshold is exceeded and a semi-central trigger if a moderatly high threshold is exceeded (Section 3.6.5.1). These thresholds will be independently programmable. The second type of trigger, using the observation windows, counts the fired segments on each disk (V0A and V0C) and, generates one trigger if a particular programmable threshold is exceeded (Section 3.6.5.2). The latter will be useful only for events of small multiplicity (like pp) where the probability of having several hits on the same segment is rare.

The CTP has only two inputs dedicated to centrality triggers. The choice of these two ones amongst the three possibilities is selectable by programmable command.

3.6.5.1 Dual high-speed integrator

The multiplicity triggers are in this case based on a charge integration. For each LHC clock the data processing consists in a comparison between the charge seen by the detectors and two programmable thresholds. Two different triggers are thus generated (Fig. 3.26). Central and semi-central collisions in the case of ion-ion physics can be especially selected before the data acquisition.

Remarks concerning the centrality trigger circuit:

- The part of the circuit included inside the circle shown in Fig. 3.26 is entirely integrated in FPGA. It is thus possible to modify the centrality of the trigger generation logic until the end of the design.
- The control of the selection or the inhibition of channels is possible through an individual ON/OFF command (common command with the other triggers).
- The charge seen by each channel will be sent to the DAQ on reception of an L2 trigger for off-line analysis.
- The generated triggers are synchronized with the LHC clock.

In order to perform a charge integration at each clock period, the integrator is made of two integrators working alternately with a programmable gate width and a programmable recovery time. An example is shown in Fig. 3.27.

This dual high-speed integrator allows the performance of a 40 MHz charge digitization on a programmable gate width from 5 ns to 30 ns in steps of 5 ns (TBC). The remaining time period is used for

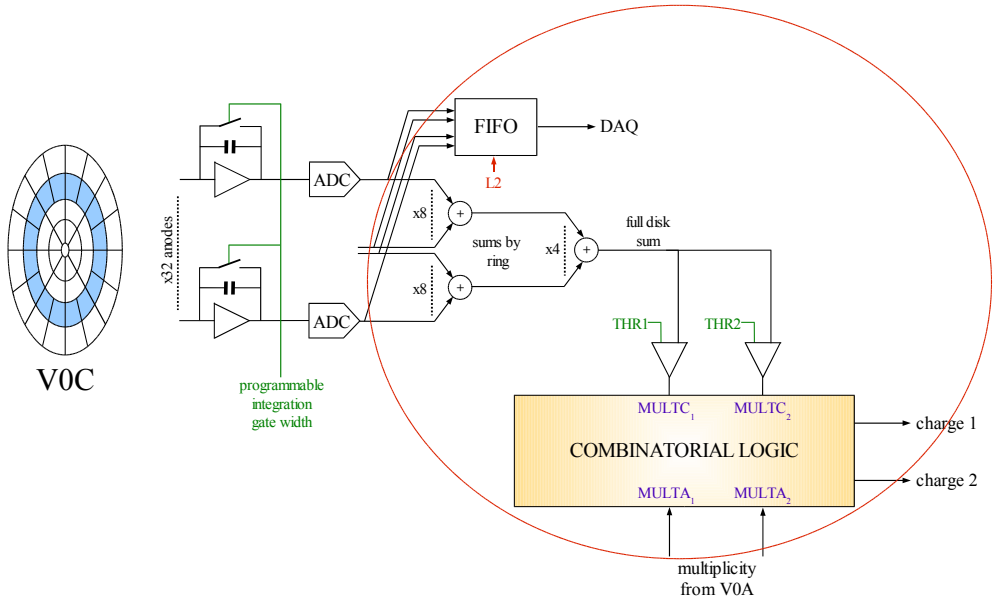

Figure 3.26: Multiplicity triggers.

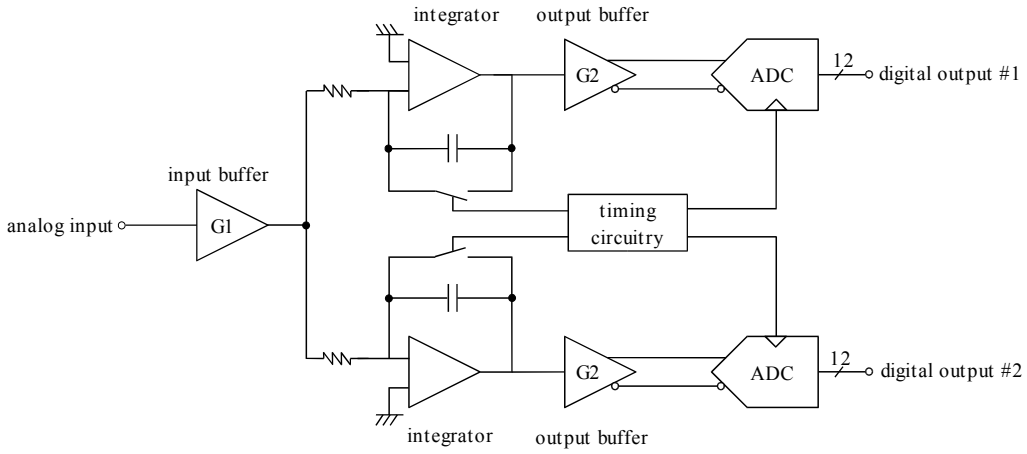

Figure 3.27: Dual high-speed integrator block diagram.

the reset of the integrator. An integrator works on even BC periods while the other one works on odd BC periods. The dead time is used for the capacitor discharge through the switch (Fig. 3.28).

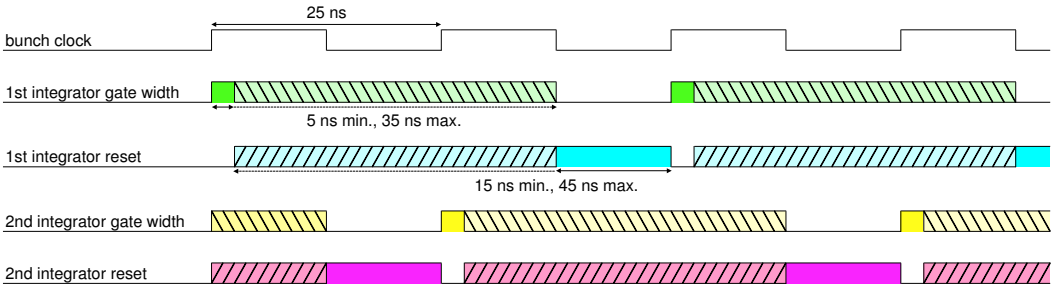

Figure 3.28: Dual high-speed integrator system timing.

For a charge digitization independent (the least dependent possible) of the relative position between the analog signal and the charge digitization command (clock of the ADC), the 64 analog chains of both disks (V0A and V0C) will be individually adjusted with an accuracy of 500 ps maximum (TBC). After this time alignment, the timing fluctuation of the analog signal is mainly due to the location of the hit on the scintillator and the jitter of the used components (≈3 ns to a first estimate). The used clock phase shift will allow 3 ns between the typical analog signal and the delayed command clock (Fig. 3.29).

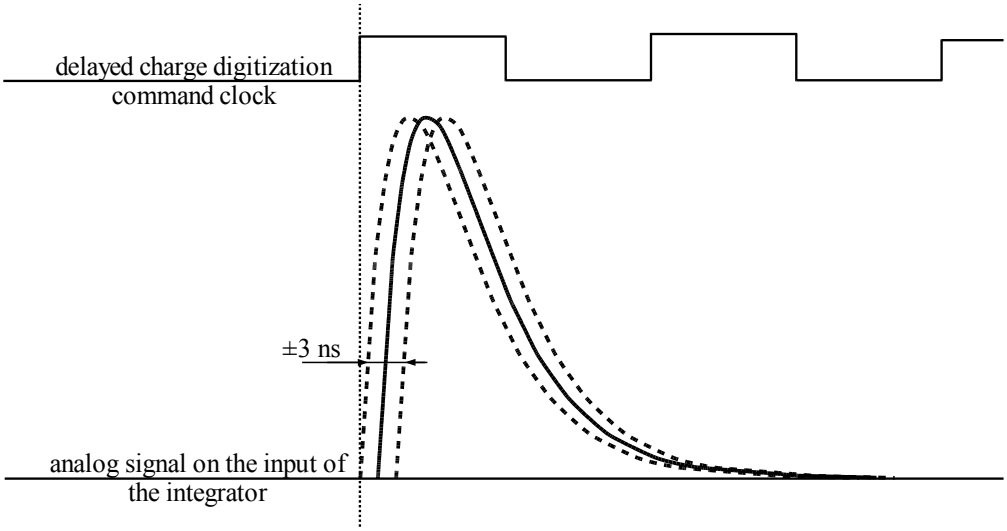

Figure 3.29: Timing between analog input signal and command clock.

The input buffer allows the minimization of the charge fluctuations seen by the adaptation resistor (50 Ω), whereas the output buffer is used to adapt the voltage level and characteristics (differential) to the input stage of the ADC.

For a given ‘n’ BC period, the required data of an eventual trigger are:

- charge digitization corresponding to the ‘n’ BC period,
- charge digitization corresponding to the ‘n+1’ BC period.

In the case of BB interactions, the system will give the charge collected by each V0A and V0C segment in correlation with BBA = BBC = 1. In the case of BG interactions, the system will give the accurate charge collected by the V0C and V0A segments fired from RB24 and RB26 sides respectively. In contrast, it will give erroneous charge values for the V0A and V0C counters due to the slight shift of the hits, +3 ns for V0A and -6 ns for V0C counters relative to the integration gate (Fig. 3.29). In this case, a correction factor can be applied to the measured charge values. In summary:

- When BBA = BBC = 1 (BB), the charge of V0A and V0C segments will be obtained directly.
- When BBC = BGA = 1 (BG from RB24), the charge of V0C elements will be obtained directly, the charge of V0A elements will be obtained after correction.
- When BBA = BGC = 1 (BG from RB26), the charge of V0A elements will be obtained directly, the charge of V0C elements will be obtained after correction.

Before any registration in FIFO, a pedestal value (determined in the calibration phase) is subtracted from the two data corresponding to the output of the ADC (TBC). The rate of the registration in FIFO is 40 MHz. These data are collected by the CCIU board on an L1 trigger request. A 12-bit ADC will be used to digitize the integrated charge (TBC).

3.6.5.2 Multiplicity based on observation window

This centrality trigger is not based on the charge seen by both disks, but only on the number of fired segments. It will thus be useful only for interactions with low-multiplicity events such as pp interactions where the probability of having several hits in the same segment is small.

The detection of the number of fired segments is done by the same observation window system as the one used for the minimum-bias trigger for the hit detection on V0A (BBA) and for the hit detection on the V0C (BBC). The generation of the centrality trigger is effective as soon as the number of events seen by each disk is included between two programmable thresholds. The use of a programmable interval rather than a simple threshold allows events with small and high multiplicity due to BG interactions (Fig. 3.30) to be separated.

Remarks concerning the multiplicity trigger circuit:

- The part of the circuit included inside the circle shown in Fig. 3.30 is entirely integrated in FPGA. It is thus possible to modify the multiplicity trigger generation logic until the end of the design. The rest of the function is common with the minimum-bias function.
- The control of the selection or the inhibition of channels is possible through an individual ON/OFF command (common command with the other triggers).
- The generated triggers are synchronized with the LHC clock.

3.6.6 Time measurement

The main component of this function is the HPTDC [15], a High Performance Time to Digital Converter developed in the microelectronics group at CERN. It allows the measurement of the time intervals between the raising/trailing edges of a PMT signal and the raising edge of the reference clock. Assuming that the pulse width is proportional to the charge of the pulse, the trailing edge is used off-line to estimate the charge of each hit. The hit signal comes from an input buffer (which allows the minimization of the signal distorsion on the charge integration) and then from the NINO [14] output. The data delivered by the HPTDC are registered in FIFO until the arrival of an L2 accept trigger. The possible disparities in time of each V0A and V0C channel will be compensated through the HPTDC which has an offset

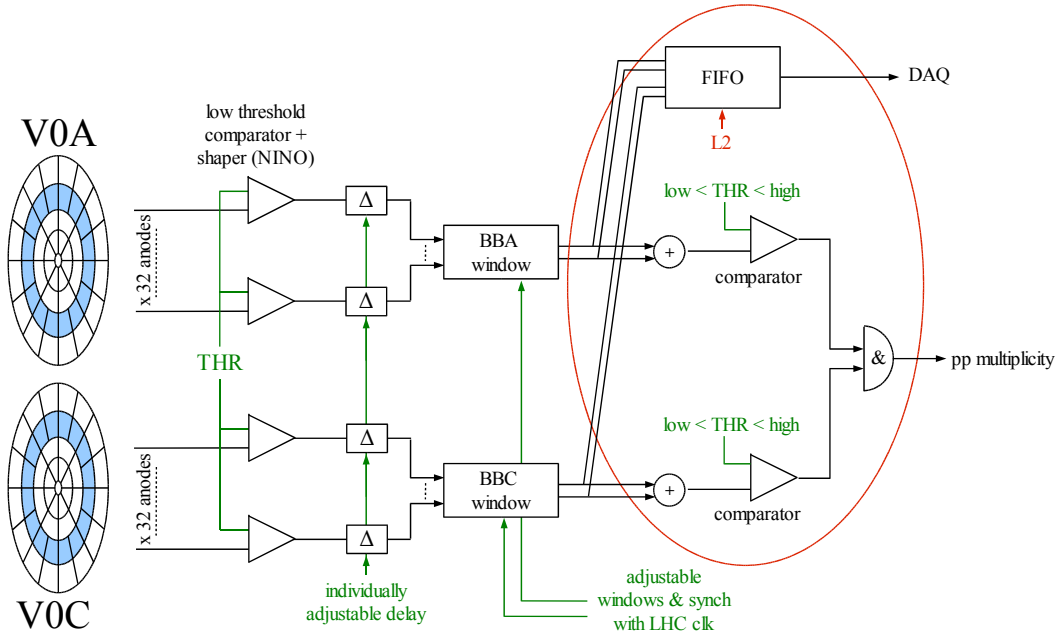

Figure 3.30: Multiplicity based on observation window.

register making possible this alignment. A calibration procedure will allow these values to be adjusted in a simple way (Section 3.6.8).

There is one HPTDC per CIU board. It performs the time digitization of the eight channels of a V0 ring. The complete scheme of the time digitization is shown in Fig. 3.31.

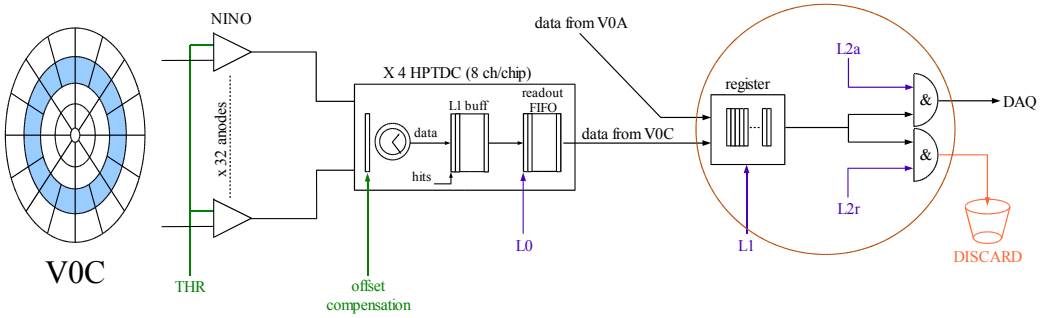

Figure 3.31: Time digitization.

In order to have an access to data which, for some reason, do not generate an L2 trigger, a histogram of the 10 last measurements of each channel will be sent to the DAQ at each L2 trigger instead of the simple ‘useful data’. These data will make it possible to determine off-line the BG event rate versus the BB event rate.

The data-driven architecture of the HPTDC poses limitations which must be taken into account for our application. Several levels of data merging are performed before data are finally read out. Each level of data merging has a related set of de-randomize buffers to minimize the effect of such potential bottlenecks. In addition, sufficient buffering must be available in the ‘HPTDC L1 buffer’ to store data during the trigger latency:

Channel merging The absolute maximum bandwidth which can be used by one channel of the HPTDC is 10 MHz (@40 MHz clocking). When several channels are used the total available bandwidth (40 MHz) is distributed such that each channel gets its fair share (max. 10 MHz or 1/8 of total bandwidth), so 5 MHz min. For the V0, the maximum interaction rate expected in pp is 100 kHz, allowing some margin for the HPTDC one-channel bandwidth.

'HPTDC L1 buffer' The 'HPTDC L1 buffer' must store hit measurements during the latency of the trigger (1.2 μs for the L0 trigger), when the trigger matching function is used. The required buffering is proportional to the product of the average hit rate on eight channels, feeding an L1 buffer, and the trigger latency ($1.2\mu s \times 8 \times 100\,kHz \approx 1$). Knowing that it can in general be considered safe to work under conditions where the average buffer occupancy is less than half the available buffering capability (256/2 = 128), we considered the required buffering as sufficient.

The HPTDC has a large number of programmable features. They allow a very flexible operation under different conditions. A listing of the main programming data is presented in the Table 3.4.

Table 3.4: Main programming HPTDC data.

Enable leading	0	
Enable trailing	0	
Enable pair	1	Pairing of leading and trailing edges
Dead time	00	5 ns dead time to remove potential ringing from analog front-end
Dll clock source	001	40 MHz from PLL
Dll mode	00	40 MHz DLL mode
Leading resolution	001	200 ps
Enable matching	1	Trigger matching enabled
Enable serial	0	Parallel readout
Enable bytewise	0	32 bits readout
Keep token	1	TDC allowed to keep token until no more data
Master	0	All TDC configured as slaves

3.6.7 Readout and Data Acquisition System (DAQ)

All the data collected by the FEE are sent to the DAQ (through the DDL) on an L2 trigger accept.

The integration with the DAQ system must be studied in detail. Interface between the readout card (SIU) and the CCIU board must be defined. For the moment, we assume that one and only one DDL link can be used. The DDL is a standard ALICE DAQ component which connects the Front-End Electronics of the detectors to the main DAQ system. The DDL will be handled by the master processor through a SIU daughter board which will form a part of the CCIU board.

Note: The DDL is also used for initialization, configuration, supervision, and DCS of the FEE (see Sections 3.6.8 and 3.6.9).

The readout is of course used to collect the physics data (through the DDL). It is also necessary to set and monitor several parameters such as configuration modes, thresholds, delays, etc. in data acquisition or in test mode (analog pulses injected at the input of each channel for debugging). The exhaustive list of these data (also transferred through the DDL link) is given below:

- operating mode: such as calibration, operating, init, ON/OFF, debugging,
- observation windows: start and stop time of each window,
- delay: in order to position each hit signal correctly in its observation window,
- offset time: parameter of the HPTDC,
- pedestal value: in order to provide a value pedestal compensated,
- threshold discriminator: threshold of the NINO chip,
- trigger threshold: trigger generation threshold,
- collision mode: Pb–Pb, Au–Au, pp.

The VME crate used for the readout electronics allows several parameters (voltage, current, cooling) to be monitored by means of a Field Bus standard (i.e. CAN).

3.6.8 Calibration and monitoring

The knowledge of the V0 timing and gain response is very important for the generation of different triggers. An initial calibration of the V0 will be done with cosmic rays in laboratories and/or with beam particles (Section 3.7). The response of the detector to the outgoing particles from pp collisions is a good tool for the complete channel gain characterization and for a correct differential timing adjustment between channels.

These operations include:

- alignment of the LHC clock on the hits,
- setting of the observation windows, start and stop times, and the various programmable thresholds,
- gain and pedestal calibration for each channel (also both branches of the dual high-speed integrator) in correlation with the high voltage (PMT supply),
- time alignment of each channel (each one compared to the others):
  1. initially with the lengths of the cables in order to have a time fluctuation of about $\approx$500 ps,
  2. finally using the programmable delays in order to have a time fluctuation of about $\approx$20 ps.
- pulse injection in the FEE for monitoring the proper working of each channel.

3.6.9 Slow Control

The ALICE Detector Control System (DCS) is characterized in Ref. [16]. Two major modes of operation can be distinguished for the DCS:

- In normal operation during physics data taking, a controlled start, operation and shutdown of the different sub-detectors is measured. For this purpose, standard operator commands will be available. Malfunctioning will be signalized through centralized alarms. The DCS will be accessed through the global experiment control system and data exchange with the DAQ will be provided.
- During all other periods, the detectors will be operated in a less coherent manner. It will be necessary to run a detector or parts of it separately. Access to the equipment must nevertheless be guaranteed from remote locations. However, interference between detectors or, between detectors and external services must be screened.

To satisfy the preceding requirements, the architecture will be based on distributed intelligence. The V0 Slow Control System will integrate most of the functions required to monitor and control the subsystem components such as high voltage and readout electronics. Each of these elements is described in Fig. 3.32.

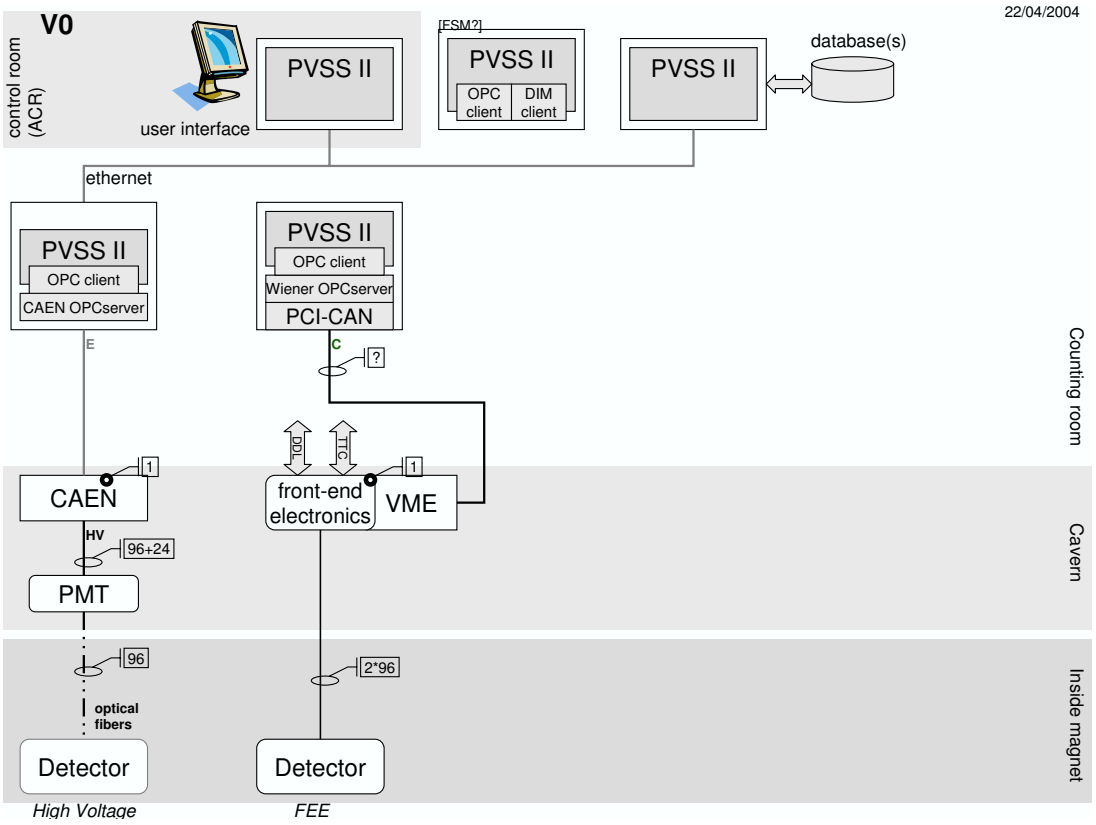

Figure 3.32: V0 Detector Control System.

3.6.10 High-voltage power supply, cabling and racks

The high-voltage power supply will be a commercial unit located in a rack (X02) far from the detector (CR4). The setting of the HV and the monitoring of the voltage and the current will be performed remotely by means of a Field Bus standard (i.e. CAN), which we hope will be adopted by the whole ALICE experiment. The number of channels to be monitored will be 64. The chosen power supply system is the CAEN SY2527 [17], the chosen power supply boards are the A1733P modules (12 channels per module). One cable with 37 conductors will be used to deliver the high voltage to each array. SHV is the standard connector.

The Front-End Electronics will be housed in a rack (B21) of the B group located on the top of the L3 magnet. Less than 25 m of cable are needed to connect the PMTs to the electronics. The chosen 50 Ω cable has an attenuation of 1.7 dB at 100 MHz, namely a power attenuation of about 32% and a voltage attenuation of about 18%. Measurement of the latter quantity gave a value of ≈13%. The transit delay of this cable is about 4 ns per metre. BNC is the standard connector.

3.7 Commissioning

3.7.1 Commissioning in laboratories

The V0 is made of 2×32 channels: 1 channel is made of the counter/PMTij/copper cable/FEE/DAQ ensemble where the counter is the coupling between a V0ij element (V0Aij or V0Cij) and the clear fibres.

The commissioning at the construction site will be carried out as follows:

- With cosmic rays, measurement of the number of p.e. per MIP for each V0ij/clear fibre counter.
- With a LED pulser, calibration of the PMTij:
  1. gain dependence with HV for each PMT starting from the MIP,
  2. linearity at equal gain for each PMT,
  3. dark current at equal gain for each PMT.
- With cosmic rays, digitized value of the MIP for each channel (counter/PMTij/Cu-cable/FEE/DAQ) and for a defined PMT gain.

3.7.2 Commissioning and testing at CERN

If the above measurements are not possible in the laboratory, we foresee to carry out them at CERN with beam: this concerns the calibration of the V0 channel (V0ij/clear fibres/PMTij/copper cable/FEE/DAQ) starting from the MIP.

The equipment will be integrated in due time as indicated in Section 5. Initial rough adjustments will be carried out with short cables in order to align the relative timing of the 32 channels of each V0A and V0C array, then, of the two arrays relatively to each other. The connection and integration of the device to the acquisition and monitoring systems will have to be made. The final fine settings can only be obtained with the help of pp collisions.

3.8 Organization

The following persons have contributed to the work presented in this Technical Design Report:

- IPNL — Institut de Physique Nucléaire de Lyon, Lyon, France;

M. Chartoire	m.chartoire@ipnl.in2p3.fr
B. Cheynis	b.cheynis@ipnl.in2p3.fr
C. Combaret	c.combaret@ipnl.in2p3.fr
L. Ducroux	l.ducroux@ipnl.in2p3.fr
D. Essertaize	d.essertaize@ipnl.in2p3.fr
J.-Y. Grossiord	j-y.grossiord@ipnl.in2p3.fr
A. Guichard	a.guichard@ipnl.in2p3.fr
J.-C. Ianigro	j-c.ianigro@ipnl.in2p3.fr
G. Maurelli	g.maurelli@ipnl.in2p3.fr
M. Miguet	m.miguet@ipnl.in2p3.fr
P. Pillot	p.pillot@ipnl.in2p3.fr
B. Rapp	b.rapp@ipnl.in2p3.fr
R. Tieulent	r.tieulent@ipnl.in2p3.fr
W. Tromeur	w.tromeur@ipnl.in2p3.fr
S. Vanzetto	s.vanzetto@ipnl.in2p3.fr
Y. Zoccarato	y.zoccarato@ipnl.in2p3.fr

- Centro de Investigacion y de Estudios Avanzados del IPN, Universidad Nacional Autonoma de Mexico, Instituto de Ciencias Nucleares, Instituto de Fisica, Mexico City and Merida, Mexico;

Ruben Alfaro	ruben@fisica.unam.mx
Ernesto Belmont	belmont@fisica.unam.mx
Guillermo Contreras	jgcn@amapola.mda.cinvestav.mx
Eleazar Cuautle	ecuautle@nuclecu.unam.mx
Varlen Grabski	grabski@fisica.unam.mx
Gerardo Herrera	gherrera@fis.cinvestav.mx
Luis Manuel Montano	lmontano@fis.cinvestav.mx
Arnulfo Martinez	arnulfo@fisica.unam.mx
Arturo Menchaca	amen@servidor.mx
Guy Paic	guypaic@nuclecu.unam.mx
Sergio Vergara	svergara@nuclecu.unam.mx

There is also serious interest by the Greek group from Athens (Marta Spyropoulu-Stasinakhi) to participate in T0 DAQ. The Greek group would participate both the manpower and the core cost.

3.9 Time-table

The time-table for the V0 project is given in Table 3.5.

Table 3.5: Time–table for the V0 project

Date	V0 project
Fall 2004	Electronics concept finalization
End 2004	CIU design prototype test
March 2005	Sectors ‘0’ of V0A and V0C
	PRR submission
Fall 2005	CCIU and TTCIU design prototype test
	V0C ready for commissioning
End 2005	CIU, CCIU and TTCIU electronical scheme
	V0A ready for commissioning
Spring 2006	Electronics design ready for realization
June 2006	Electronics construction
	V0C ready for installation in ALICE
End 2006	Electronics tests, calibration
	Electronics ready for installation in ALICE
	V0A ready for installation in ALICE

4 Forward Multiplicity Detector (FMD)

4.1 Physics Objectives

The main functionality of the Forward Multiplicity Detector (FMD) system is to provide charged particle multiplicity information in the pseudorapidity range $-3.4 < \eta < -1.7$ and $1.7 < \eta < 5.0$. As shown in Fig. 4.1, the FMD combined with the pixel system of the ITS will provide charged particle multiplicity distributions for collisions of all beam combinations in the range $-3.4 < \eta < 5.0$. Small overlaps between the various rings and with the ITS inner pixel layer provide both redundancy and important checks of analysis procedures. In addition, the segmentation of the detector allows for the study of multiplicity fluctuations on an event-by-event basis, as well as event-by-event determination of the reaction plane.

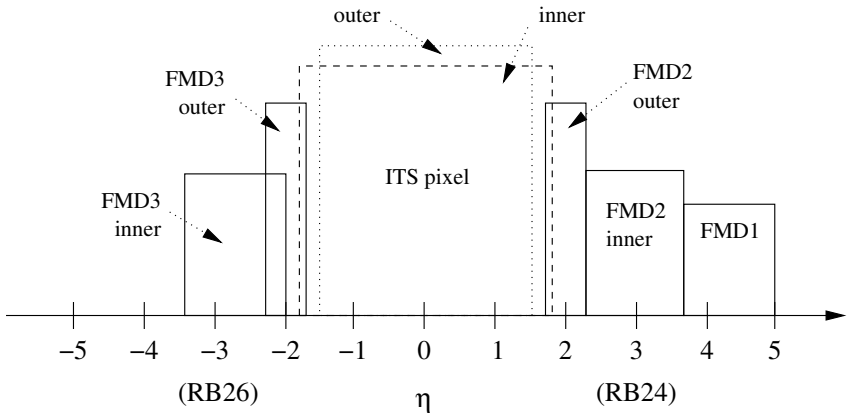

Figure 4.1: Pseudorapidity coverage of the FMD. Also shown (dashed and dotted lines) is the pseudorapidity coverage of the ITS inner and outer pixel system. The vertical axis denotes on an arbitrary scale, the charged particle rapidity density.

The mean number of hits for very central (0–5%) Pb–Pb collisions will be less than three charged particles per detection element. This estimate is based on the standard HIJING generator used as input to AliROOT 3.09 with $dN/d\eta = 8000$ in the midrapidity region. Even for central Pb–Pb collisions, the majority of channels will have, on average, approximately one charged particle including background sources. For peripheral A–A collisions and for pp collisions, the mean number of hits will be substantially lower. Multiplicity information will be obtained in off–line data analysis. The total deposited energy per channel is measured and the number of charged particles determined based on knowledge of the average energy deposition of a single particle. It is also possible to perform a statistical analysis by comparing the number of occupied and empty channels to obtain an independent measure of the multiplicity.

The segmentation chosen for the detector (strips) and the single layer geometry results from a compromise between the desired performance (multiplicity resolution), and the necessity to minimize the overall cost and complexity.

The read–out time of the system allows the detector to participate in the ALICE trigger hierarchy at L2 and higher. A trigger development that would enable the FMD to participate in L0 or L1 triggering has been found not necessary, as the T0 and V0 detectors fulfil the fast trigger functionality required by ALICE.

4.2 General Design Considerations

4.2.1 FMD Geometry

The space available for a Forward Multiplicity Detector in ALICE, and thus its pseudorapidity coverage, is limited by the presence of a number of detector systems (ITS, TPC and muon arm) whose main components, dimensions and locations were decided long before the FMD was conceived.

In the central rapidity region, the ITS and its services (cooling, cables), the V0 detector, the T0 array, and the TPC support structure limit both the distance from the nominal intersection point (IP) and the maximum outer diameter of the complete device. At larger pseudorapidities, the limitations are imposed by the outer diameter (with tolerances and installation clearances) of the ALICE vacuum chamber, including complications arising from the placement of flanges, beam tube support elements, bellows and pumps. It has been agreed that the envelope of the FMD toward the ALICE vacuum chamber will extend inwards to a radius of $R_{min} = 42\,\mathrm{mm}$.

On the RB26 side of the IP, the presence of the muon absorber and the V0 counter limits the maximum distance from the IP to 80 cm while the ITS limits the closest distance from the IP to about 60 cm. In order to accommodate services for the ITS, the outer envelope of the FMD has been defined to stay within an angle of 20.7 degrees relative to the beam direction, as measured from the IP, corresponding to a limit of $\eta = -1.7$.

On the other side (RB24) of the IP, the FMD elements may in principle be placed at any distance $z > 60\,\mathrm{cm}$ from the IP. The limit towards central pseudorapidities imposed by the ITS remains the same as on the RB26 side, but the additional space away from the IP allows for a larger coverage at small angles to the beam direction. For reference, the inside of the door of the L3 magnet return yoke is about 600 cm from the IP.

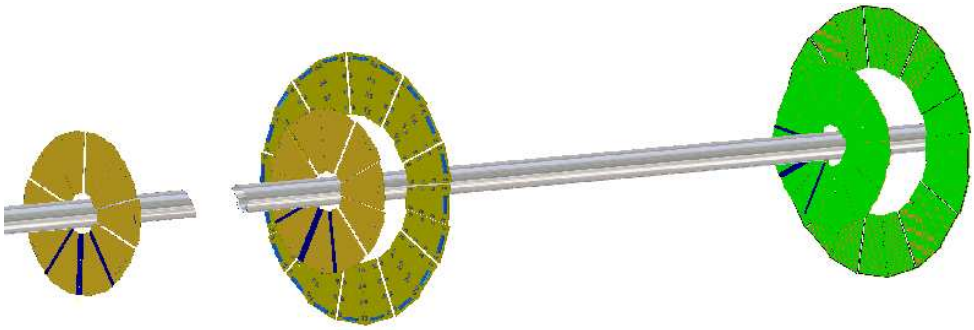

Figure 4.2: Conceptual layout of the FMD detector system showing the five rings placed around the beam pipe. The three sub-detector systems are called FMD1 (left), FMD2 (middle) and FMD3 (right). The muon arm is to the right.

A further important factor that limits the maximum achievable rapidity coverage is the significant background of secondary particles arising from interactions in the vacuum chamber elements at small angles. Simulations indicate that the background from secondary particles increases to more than 200% for the smallest angles covered. This, combined with the desire to enable a common mechanical support for the FMD1 , PMD, V0A and T0-A, limits the maximum forward pseudorapidity to $\eta = 5.0$.

Within these severe geometrical limitations, we have chosen to design a detector based on a ring geometry, conceptually similar to the forward ring system of Phobos [1], but with important technical differences in the strip read-out, which have been imposed by the much more closed geometry of ALICE. A large pseudorapidity coverage may be obtained by placing rings of counters identically designed at different distances on either side of the IP. This use of only two basic modules will thus reduce the overall complexity of the device.

Within these severe geometrical constraints, we have chosen a design for the FMD based on single layers of single–sided silicon strip detectors in a ring geometry, conceptually similar to the forward ring system of Phobos [1], Ring detectors are placed around the beam pipe in each of the two forward regions of ALICE. A large pseudorapidity coverage may be obtained by placing rings of identical design at different distances from the IP. In this way, it has been possible to reduce the overall complexity of the system by using only two basic building blocks.

The detector system consists of five rings of 10 200 Si–strips each, with three "inner" rings divided into 20 azimuthal sectors each, and two "outer" rings of 40 sectors each (see Fig. 4.2). Each sector will be read out independently and comprises 512 and 256 detector strips for inner and outer rings, respectively.

The design of the rings is intimately coupled to the choice of silicon wafer technology. The elements that are combined to build the various rings must be manufactured out of individual circular Si wafers. Currently, a small number of suppliers manufacture 6 inch Si–wafers, permitting the coverage of the desired pseudorapidity range with two designs of counters (one for "inner" rings and one for "outer" rings). Basing the design on wafers of smaller dimensions would require the use of three rings, leading to the system's higher overall cost and complexity.

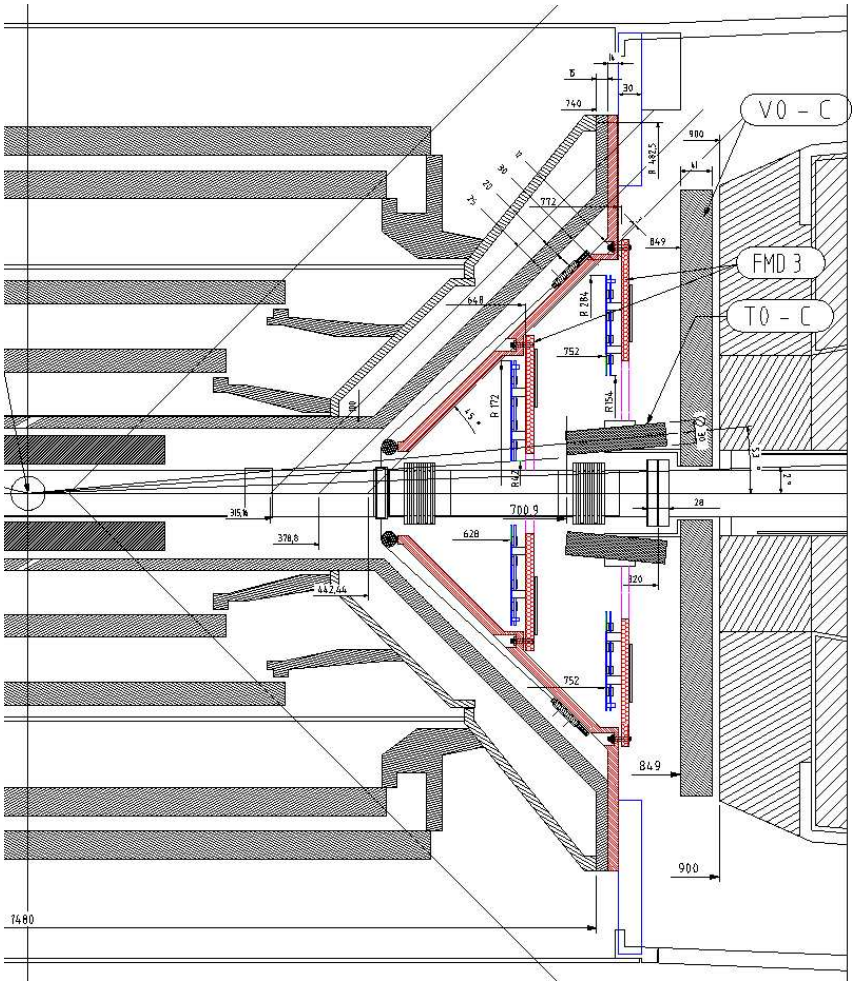

Figure 4.3: Cross section of the forward detector system layout on the RB26 side. The muon absorber is to the right. The two rings of the FMD3 detector are mounted on one support cone. This cone also supports the beam pipe to the left of the indicated bellows. The V0C and T0-C detectors can also be seen.

The positions and sizes of the various Si rings and the corresponding pseudorapidity coverages are listed in Table 4.1. Figures 4.3, 4.4 and, 4.5 show details of the geometry and placement of the FMD

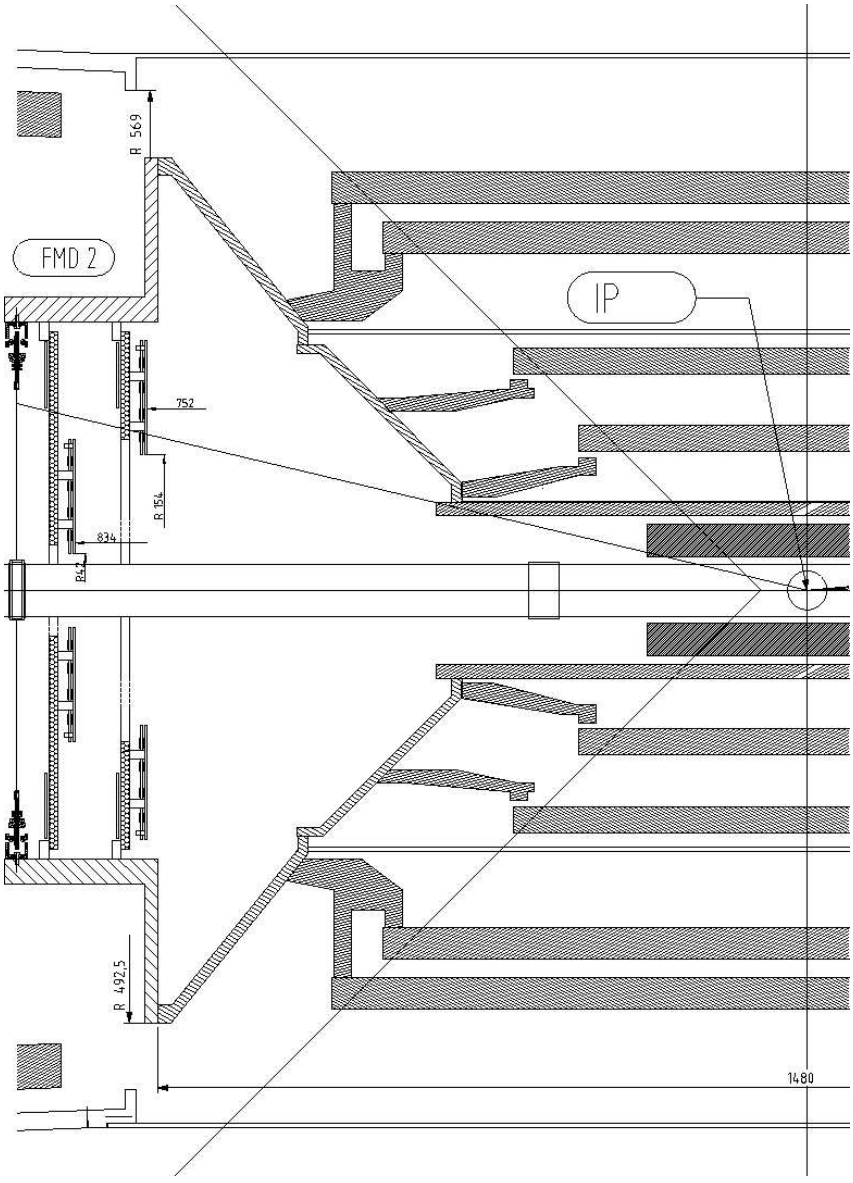

Figure 4.4: Cross section of FMD2 on the RB24 side of the IP. The two FMD2 rings are shown at $z = 752\,\text{mm}$ and $z = 834\,\text{mm}$ from the IP and attached to their cylindrical mechanical support. This support also supports the beam pipe.

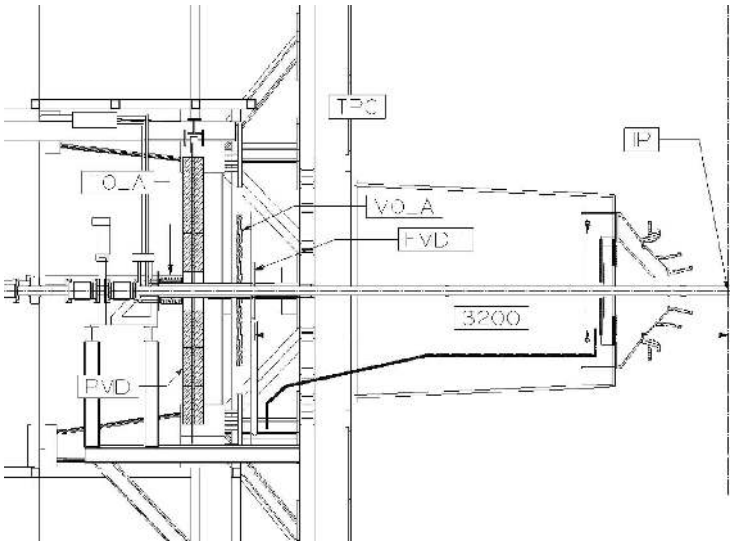

Figure 4.5: Drawing of the placement of the FMD1 and FMD2 rings together with T0-A, V0A and the PMD on the RB24 side. The mechanical support for the three forward detectors near $z = 3.2\,\mathrm{m}$ is attached to a common structure mounted on the TPC service support wheel. This structure will also support the vacuum valve behind T0-A and the central beam pipe. The FMD2 cable path is indicated.

Table 4.1: Geometrical size of each of the five FMD rings. The table lists the nominal distance, z, from the IP to the detector plane, the inner and outer radii, and the corresponding pseudorapidity coverage of each ring.

Ring	z **(cm)**	R_{in} **(cm)**	R_{out} **(cm)**	η **coverage**
FMD1	320.0	4.2	17.2	$3.68 < \eta < 5.03$
FMD2i	83.4	4.2	17.2	$2.28 < \eta < 3.68$
FMD2o	75.2	15.4	28.4	$1.70 < \eta < 2.29$
FMD3o	-75.2	15.4	28.4	$-2.29 < \eta < -1.70$
FMD3i	-62.8	4.2	17.2	$-3.40 < \eta < -2.01$

rings in ALICE.

Together with the ITS inner pixel layer (dashed line in Fig. 4.1), the design ensures a full pseudorapidity coverage in the range $-1.7 < \eta < 5.0$, and an overlap between the FMD and ITS inner pixel layer system of about $\Delta\eta = 0.2$. Note that the placement of the FMD2 and FMD3 rings is not symmetric with respect to the IP. This asymmetry ensures 'seamless' pseudorapidity coverage between FMD1 and FMD2 at the cost of less overlap between the inner and outer ring of FMD2.

4.2.2 FMD Segmentation

The dimensions and the layout of the FMD rings and their segmentation in sensor elements are primarily determined by the size of presently available silicon wafers.

The segmentation of each sensor into strips has been driven by the desire to keep the maximum mean number of hits per strip below a few particles for most strips, even in central Pb–Pb collisions, thereby enabling an accurate multiplicity reconstruction based on total energy deposition in a single strip and possible determination of multiplicity by statistical analysis of empty and filled channels, while respecting the constraints imposed by matching to the front–end (FE) electronics and limiting the number of read–out channels.

We have chosen to sub–divide each Si sensor into two phi sectors, leading to an azimuthal segmentation of 20 for the inner rings and 40 for the outer rings. Due to fluctuations in the mean number of hits and in the energy deposition per particle, each detector must segment to have a linear response for signals, with amplitudes up to 10 times the average signal. It follows that the FE electronics must be able to handle a maximum signal deposition corresponding to about 20 MIPs. The chosen segmentation ensures total strip capacitance of around 10–20 pF, which is well adapted to the solution chosen for the preamplifier chips of the FE electronics.

Based on these considerations, we arrive at the detector segmentation given in Table 4.2.

Table 4.2: Physical dimensions of Si segments and strips, together with the average number of charged particles impinging on each strip in simulated central Pb–Pb collisions.

	Radial coverage (cm)	**Particle flux** (cm^{-2})	**Azimuthal sectors**	**Radial strips**	**Strip area** (cm^2)	**Average number of hits**
FMD1	4.2–17.2	6–27	20	512	0.03–0.14	0.6–1.3
FMD2i	4.2–17.2	8–35	20	512	0.03–0.14	1.5–0.9
FMD2o	15.4–28.4	3–8	40	256	0.12–0.23	1.2–0.7
FMD3i	4.2–17.2	10–65	20	512	0.03–0.14	2.7–1.2
FMD3o	15.4–28.4	3–8	40	256	0.12–0.23	1.0–0.6

4.2.3 Performance Simulations

4.2.3.1 Simulation Package

All simulations of particle densities shown in this document have been carried out using the AliROOT simulation package (version 3.09[1]) using the HIJING generator (which assumes that $dN/d\eta \approx 8000$ around $\eta = 0$ for 0–5% central Pb–Pb collisions at the LHC design energy) as input. The simulation code calculates the energy loss in each FMD strip from all charged particles which hit the strip, including secondary (background) particles, produced in interaction with material in the beam pipe and in ALICE.

4.2.3.2 Charged Particle Densities in the FMD

The FMD is not an isolated detector. Primary particles scattering on material in various other ALICE detectors and support components leads to the copious production of secondary particles. Such secondaries contribute to the measured total energy and the number of hits, hence to the determined multiplicity. The primary sources of this background are:

i) the beam pipe and its various flanges, collars, pumps etc.;
ii) the ITS with its mounting frame and services;
iii) numerous cables, mainly from ITS;
iv) the T0 and V0 detectors with their mounting arrangements; and
v) the absorber for the muon arm.

Figure 4.6 shows the average number of hits per strip as a function of the radial distance from the centre of the beam pipe for the five FMD rings, calculated with AliROOT. A breakdown of the contribution from each of these is shown in Fig. 4.7 and listed in Table 4.3. It is noted that the dominant sources of secondaries are the ALICE beam pipe and the ITS.

[1] In winter 2003/2004, the definition of the ALICE coordinate system was changed so that $\eta \rightarrow -\eta$. However, in AliROOT 3.09 the old definition of η was used, but in the plots in this document, the new definition has been applied.

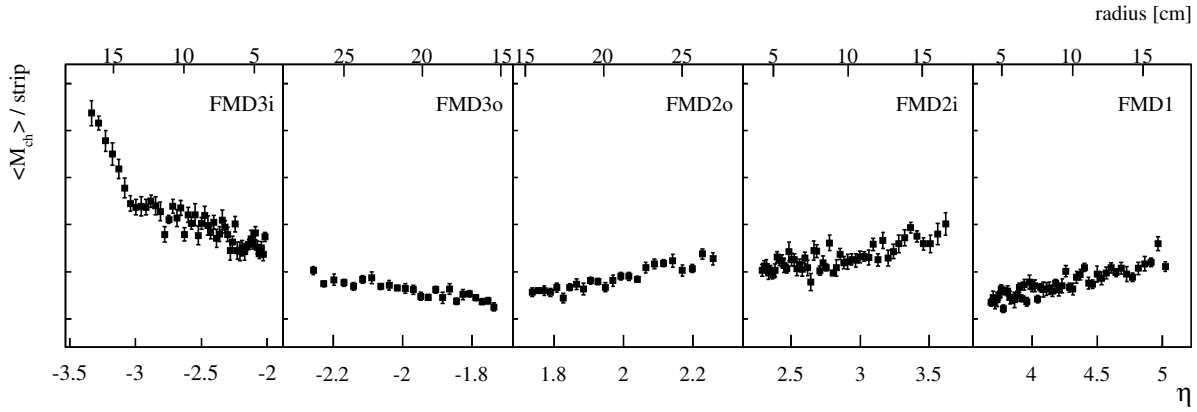

Figure 4.6: Average number of hits per strip as a function of the η and radial distance to the beam pipe centre (top axis), for the five FMD rings. The simulation is for central collisions. The error bars show $RMS/\sqrt{N}$ for the distribution for each collection of strips.

Table 4.3: Number of particles per square centimetre impinging on the FMD detectors. The table lists the total number of particles (primary and secondary) and a breakdown of the secondaries produced in the beam pipe, the ITS, the absorber in the muon arm, and the T0.

Radius	**Total**	**Primary**	**Primary/ total**	**Pipe**	**Pipe/ total**	**ITS**	**ITS/ total**	**Abs**	**Abs/ total**	**T0**	**T0/ total**
FMD1											
5	27.1	13.6	0.50	9.2	0.33	3.8	0.14	0.1	0.00	0.0	0.00
10	13.3	6.1	0.46	3.0	0.22	3.1	0.23	0.0	0.00	0.0	0.00
15	6.9	3.4	0.48	1.5	0.20	1.7	0.24	0.0	0.00	0.1	0.01
FMD2i											
5	33.1	23.5	0.71	5.7	0.17	3.6	0.11	0.0	0.00	0.0	0.00
10	16.7	9.2	0.55	2.6	0.15	3.7	0.22	0.1	0.00	0.0	0.00
15	10.0	4.6	0.46	1.0	0.09	4.0	0.39	0.0	0.00	0.0	0.00
FMD2o											
16	6.2	2.4	0.39	0.6	0.09	3.1	0.49	0.0	0.00	0.0	0.00
21	5.2	2.0	0.38	0.4	0.07	2.7	0.51	0.0	0.00	0.0	0.00
26	4.3	1.8	0.40	0.4	0.08	2.1	0.47	0.0	0.00	0.0	0.00
FMD3o											
16	7.5	2.4	0.32	0.9	0.11	3.2	0.43	0.2	0.02	0.1	0.01
21	6.1	1.8	0.30	0.8	0.12	2.7	0.44	0.2	0.03	0.0	0.00
26	4.0	1.6	0.39	0.3	0.06	1.6	0.40	0.2	0.04	0.1	0.03
FMD3i											
5	62.6	25.7	0.41	33.1	0.52	3.2	0.05	0.0	0.00	0.0	0.00
10	23.1	11.2	0.48	5.0	0.21	6.1	0.26	0.2	0.00	0.1	0.00
15	12.2	4.4	0.36	1.1	0.09	5.9	0.49	0.3	0.02	0.1	0.01

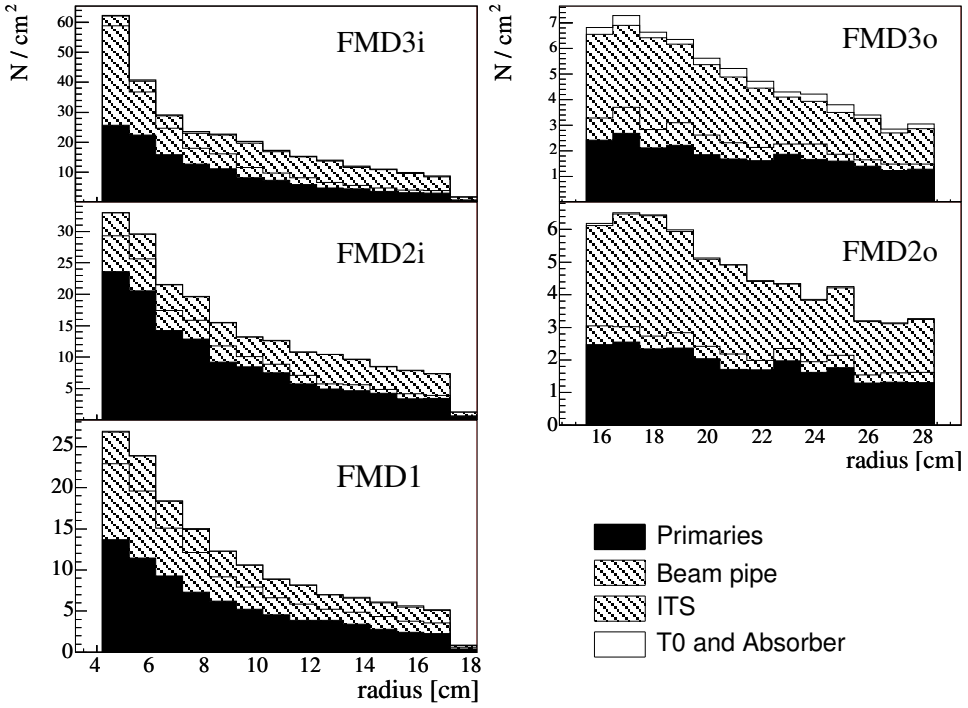

Figure 4.7: Breakdown of the total number of particles (primary and secondary) impinging on each of the five FMD rings. See also Table 4.3.

4.2.3.3 Energy Loss Spectrum

The energy loss spectrum of particles traversing a strip can be described by a Landau distribution. For multiple hits the spectrum is a folding of Landau functions, as displayed in Fig. 4.8(a), resulting in progressively broader energy peaks with increasing multiplicity. Figure 4.8(b) shows a typical energy loss spectrum, both with and without background, for a single strip in FMD3i.

4.2.3.4 Multiplicity Reconstruction

In general, there are two methods to determine the charged particle multiplicity.

- Measuring the total deposited energy, above some appropriate threshold in a strip or a group of strips, and dividing this total energy by the average expected energy deposited by a particle (see Section 4.2.3.5).
- Counting the number of strips in which energy is deposited above threshold and comparing it to the number of empty strips (see Section 4.2.3.6).

Several effects contribute to obscuring the primary multiplicity information.

1. Background from secondary interactions in material extraneous to the Si detectors.
2. Distribution of the energy loss in a detector segment. The average energy loss of a single particle in the detector material (typically 300–400 μm of Si) depends on the particle momentum. The energy loss distribution around the most probable value can be represented by a Landau function.
3. Counting statistics. The distribution of the number of particles that hit a detector segment follows a Poisson distribution.

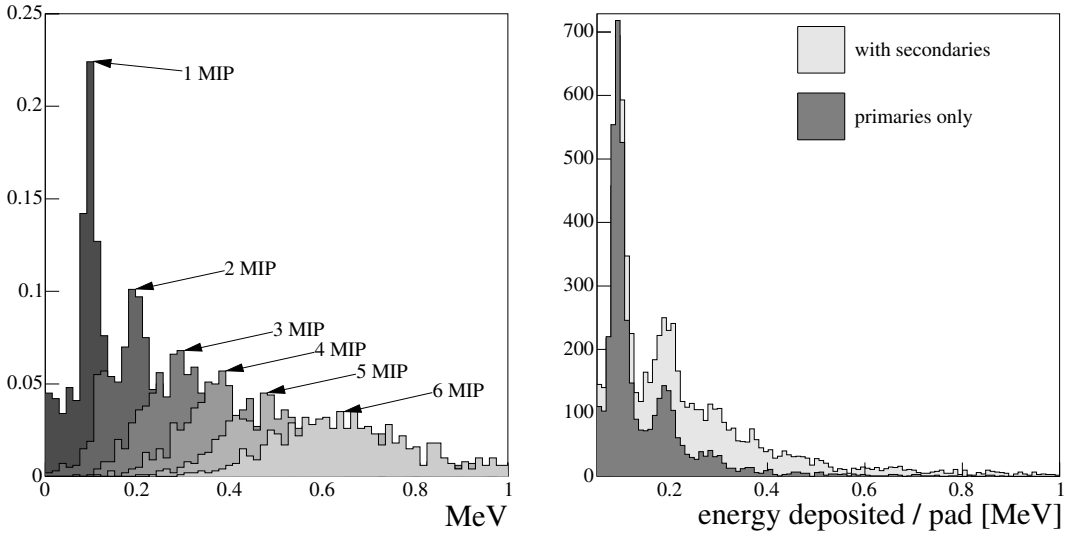

(a) (b)

Figure 4.8: (a) Typical energy loss distributions (Landau) for $1, 2, \ldots, 6$ particles with minimum ionising energy (MIP) impinging on a detector element. Note how the width of the distribution broadens with increasing number of particles.
(b) Typical energy loss spectrum (accumulated over several events) for a strip in FMD3i for 5% central collisions. Simulations are shown with (light grey) and without (dark grey) the contribution from particles from secondary interactions.

4. Accumulated electronics noise.

These factors are addressed in Section 4.2.3.7.

4.2.3.5 Counting Particles using the Deposited Energy

The most direct way to determine the multiplicity of charged particles in the FMD is to divide the total energy signal measured in a strip, or in a group of strips, by the average energy deposited by particles originating from the reaction. The latter number can either be estimated from Monte Carlo calculations (e.g., AliROOT) or deduced from the in–beam measurements of very low multiplicity events themselves for single hits. To arrive at the 'primary' multiplicity, the measured multiplicity must be corrected for the contribution from secondaries as estimated from a Monte Carlo simulation of the experiment.

The relative accuracy of the multiplicity determination can be increased by adding signals from several strips e.g., by summing over strips at different azimuthal angles but at similar rapidities, or integrating over rapidity by grouping strips belonging to a given azimuthal sector.

Figure 4.9 shows the reconstructed multiplicity as a function of the number of generated particles impinging on the detector. The simulations were carried out using a single central HIJING event for Pb–Pb and integrating over strips in the pseudorapidity interval $3.58 < \eta \leq 1.51$. The energy loss spectrum was generated by modelling each detector hit by a Landau distribution. The reconstructed multiplicity was obtained by counting the number of hits in energy intervals ΔE_n up to the n^{th} peak. The iterative procedure was used. In the first step the energy loss corresponding to one particle was required to lie in as the interval from zero to the minimum of the sum of the Landau distributions corresponding to two (ΔE_2). Similarly, two hits were defined as energy deposited in the interval from ΔE_2 to ΔE_3, the latter being the minimum of the sum of three Landau distributions, and so on. In the next step, the set of

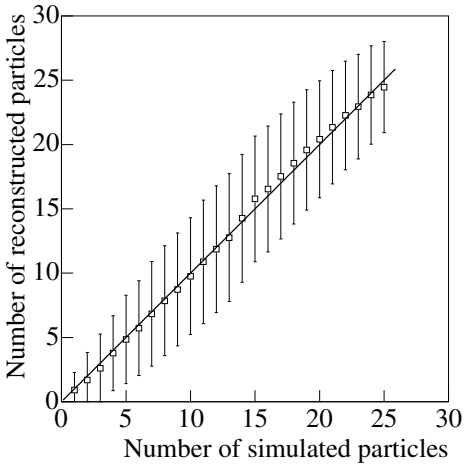

Figure 4.9: Reconstructed multiplicity using the energy method versus generated multiplicity. The error bars show the root–mean–square of the individual reconstructed multiplicity distributions.

interval boundaries $\Delta E_2, \Delta E_3, \ldots$ was adjusted in order to minimize the difference between the generated and reconstructed multiplicity distributions.

The relative accuracy of the multiplicity reconstruction (based on 20 central HIJING events) as a function of pseudorapidity ($\Delta\eta = 0.1$) is shown in the top panel of Fig. 4.10. The lower panel shows the relative accuracy of the multiplicity reconstruction integrating over the pseudorapidity interval $\eta \in [1.9, 3.5]$, corresponding to the pseudorapidity interval covered by the outer rings FMD2 and 3. The distribution is Gaussian with $\sigma = 7\%$ for FMD2+3o. Similarly, the relative reconstruction accuracy for an azimuthal sector of FMD3i is $\sigma = 6\%$ and $\sigma = 12\%$ for a sector of FMD3o.

4.2.3.6 Counting Particles using the Hit Pattern

The average multiplicity can also be determined by studying the pattern of hits across strips, provided that the average multiplicity per strip is small (one hit or less on the average) and that the average multiplicity is uniformly distributed over the considered section of the detector. This will typically be the case for non–central Pb–Pb collisions. For very peripheral collisions or pp collisions the mean number of hits is so low that the multiplicity of particles can be accurately obtained by simply counting the number of pads hit.

The distribution of hits (m) on a strip is the Poisson distribution $P\{m\} = \frac{\lambda^m}{m!}\exp(-\lambda)$, where λ is the mean number of hits. The probability for no hits on a strip is $P(0) = e^{-\lambda}$. Since $P(0) = N_e/N_{tot}$, N_e and N_{tot} being the number of empty strips and the total number of strips in the selected region of the detector, respectively, the average multiplicity λ can be determined.

In the multiplicity reconstruction algorithm it has been assumed that a strip is empty when the ADC signal is below a given threshold. In Fig. 4.11 the reconstructed multiplicity is shown versus the known input. The intrinsic accuracy of this method can be better than 3%, as shown in Fig. 4.12 (circles).

4.2.3.7 Reconstruction of Multiplicity Distribution

To obtain the real (primary) multiplicity, the contribution from secondary particles must be estimated and subtracted. The majority of secondaries originate from interactions in the ITS detector structure and in the beam pipe (see Table 4.3). The correction coefficients as a function of η have been determined using a sample of 200 HIJING events calculated for Pb–Pb collisions with impact parameter in the range $0\,\text{fm} < b < 11.2\,\text{fm}$. These are shown in Fig. 4.13.

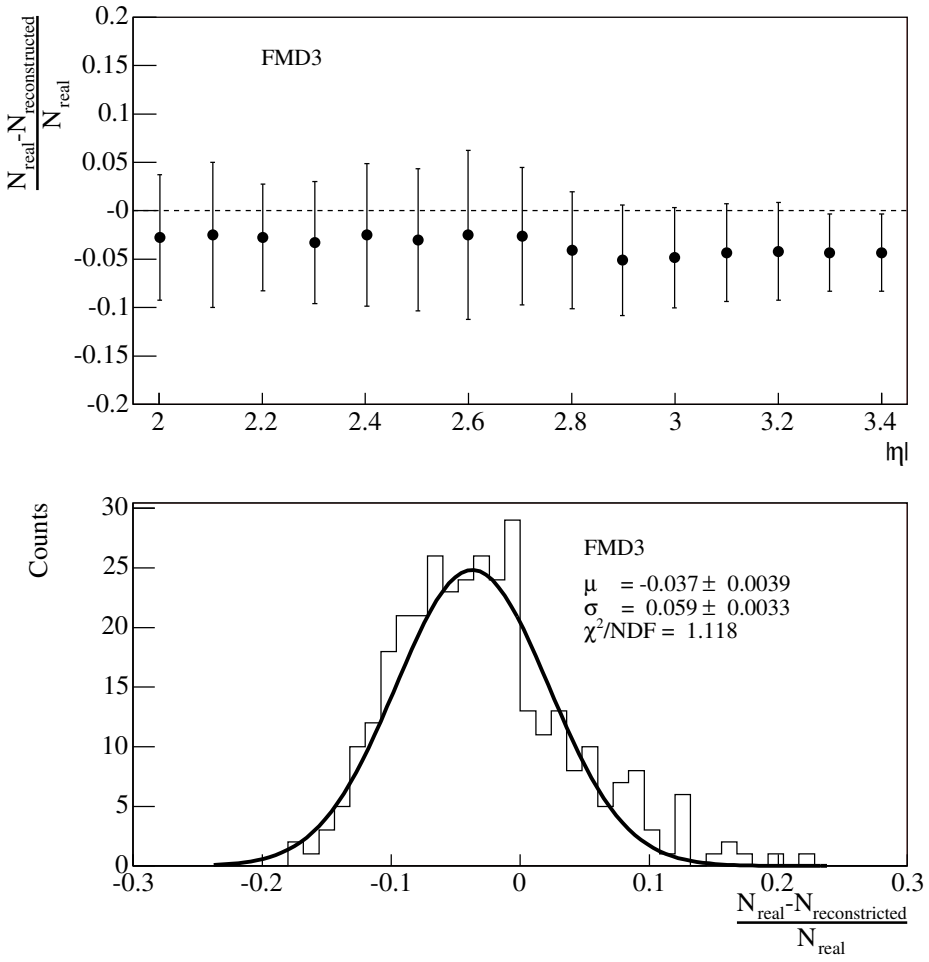

Figure 4.10: Relative accuracy of multiplicity reconstruction. Top panel shows the relative difference between the reconstructed and the input multiplicity in the η range of the inner and outer FMD3 detector. The lower panel shows the distribution of residuals, summed over η ranges.

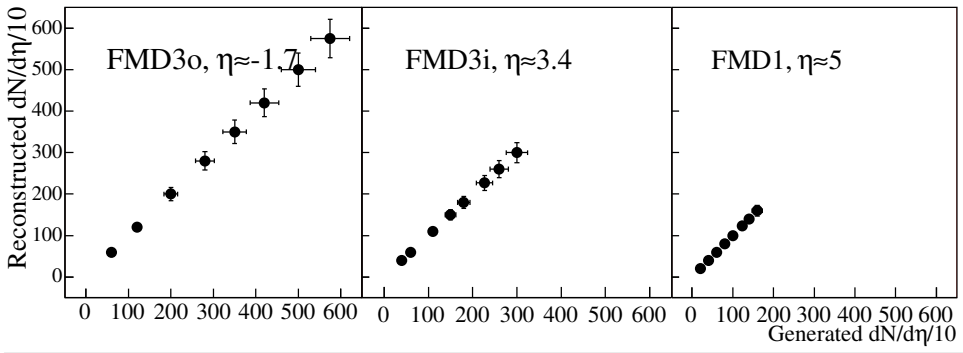

Figure 4.11: Reconstructed multiplicity ($dN/d\eta$) from HIJING, using the Poisson method, as a function of the generated multiplicity for three different pseudorapidity intervals.

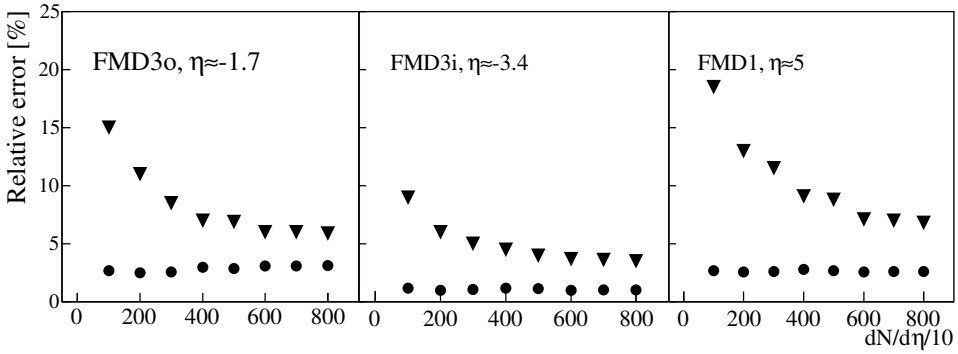

Figure 4.12: Relative error for $\eta = -1.7$ (FMD3o), $\eta = -3.4$ (FMD3i) and $\eta = 5$ (FMD1) using the Poisson method (circles). Triangles show the relative error after subtracting the contribution of secondaries, which are known event by event from the simulations.

The error on the correction coefficients depends on multiplicity. For most central events it is about a factor of 10 smaller than that shown in Fig. 4.13 for minimum bias events.

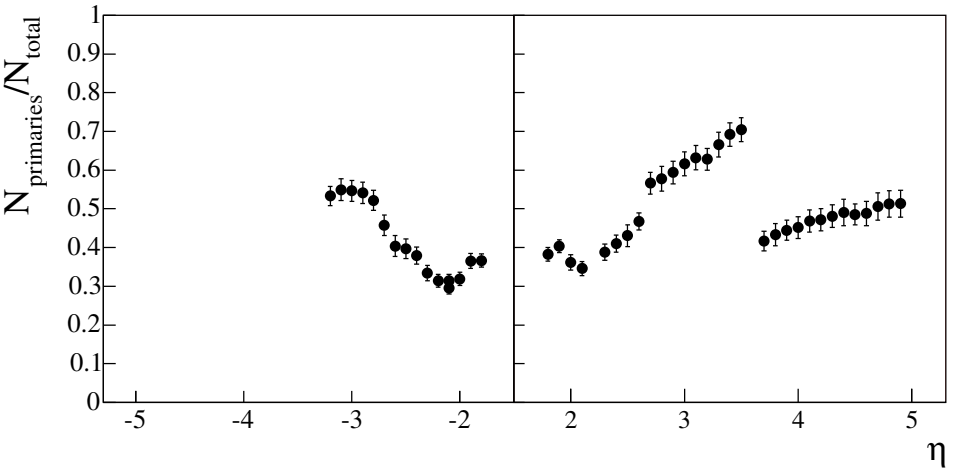

Figure 4.13: Multiplicity correction coefficient (ratio of primaries to total) as a function of η. The discontinuity $\eta = 3.6$ is due to the different background conditions for the FMD2i ($z = 83.4\,\text{cm}$) and FMD1 ($z = 345\,\text{cm}$) detectors.

Figure 4.14 shows the reconstructed multiplicity distribution using the Poisson method (circles and triangles) compared to the input HIJING distribution (80 events). The background correction factors of Fig. 4.13 have been used.

In the general case, where the background correction coefficients are not known because the shape of the primary multiplicity distribution is not that predicted by HIJING, an iterative procedure must be employed. In this method, the first trial for the primary multiplicity distribution is propagated through AliROOT and compared to the measured multiplicity distribution. The ratio of this calculated distribution to the measured distribution is used to scale the trial multiplicity distribution, which again is propagated through AliROOT. This process is repeated until convergence is achieved. In practice, this requires only a few steps. A suitable trial input distribution is the measured multiplicity distribution scaled by the background correction factors calculated by propagating HIJING events through AliROOT.

The reliability of the method is shown in Fig. 4.15. Here, the input distribution is assumed to go to zero outside the interval $\eta = 2, 3.3$. The left panel shows the first iteration, the right panel shows convergence after two iterations. The main distribution is recovered but the 'edges' are smeared. In

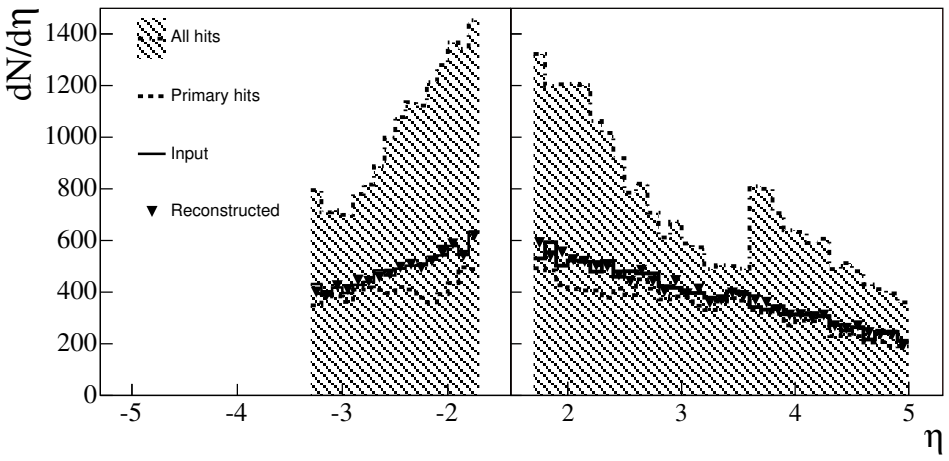

Figure 4.14: Reconstructed $dN/d\eta$ distribution for 80 HIJING events (points) using the background correction factors shown in Fig. 4.13. The full drawn line is the input HIJING distribution. The distribution of primary particles that hit the detector is shown by the short–dashed line (the difference relative to the input distribution is due to absorbed particles). The dashed–dotted line shows all the particle hits registered in the detector (primaries and secondaries).

Fig. 4.16 a flat, wide input distribution is used. The figure shows the three first iterations.

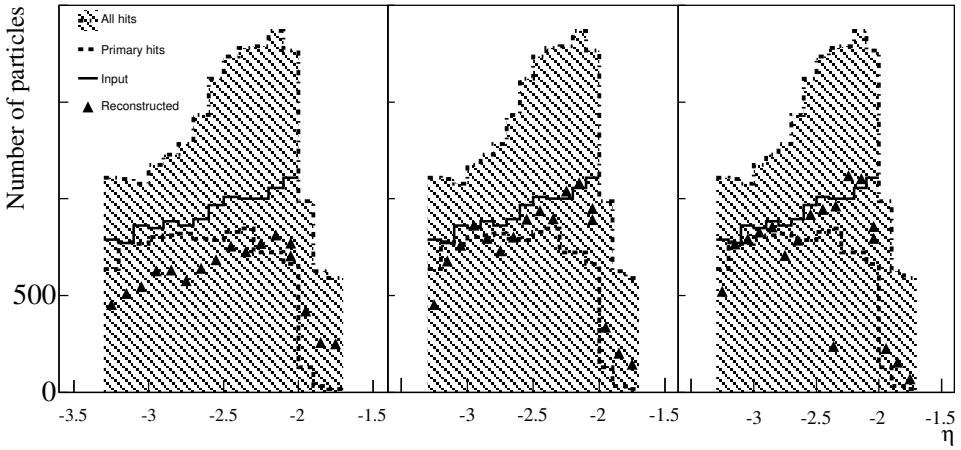

Figure 4.15: Iterative procedure to extract a narrow rapidity distribution with sharp edges (non–HIJING shape). The full drawn line is the input HIJING distribution. The distribution of primary particles that hit the detector is shown with the short–dashed lines. The dotted line shows all the particle hits registered in the detector (primaries and secondaries). The triangles show the reconstructed distribution. The figure shows the first three iterations.

It is possible to give an estimate of the sensitivity to narrow local multiplicity fluctuations using Fig. 4.15. This figure shows how a sharp edge signal is propagated into the detector at $\eta \approx 2$. It is noted that $\approx 70\%$ of the signal survives and that the remaining 30% is 'amplified' and smeared in η, leading to an effective signal-to-noise ratio $\approx 1/1$. This smearing corresponds to an effective $\Delta\eta \approx 0.12$ and $\Delta\phi \approx 2^\circ$. With $dN/d\eta \approx 8000$, such an interval will contain ≈ 5 charged particles and lead to a signal + background of ≈ 9. In this particular example a multiplicity fluctuation in a narrow region e.g., $\Delta\eta \approx 0.12$ and $\Delta\phi \approx 2^\circ$, would need 15–20 particles to give a significant signal. Sensitivity to broader fluctuations follow straightforward statistics, but for each part of the detector the signal-to-background

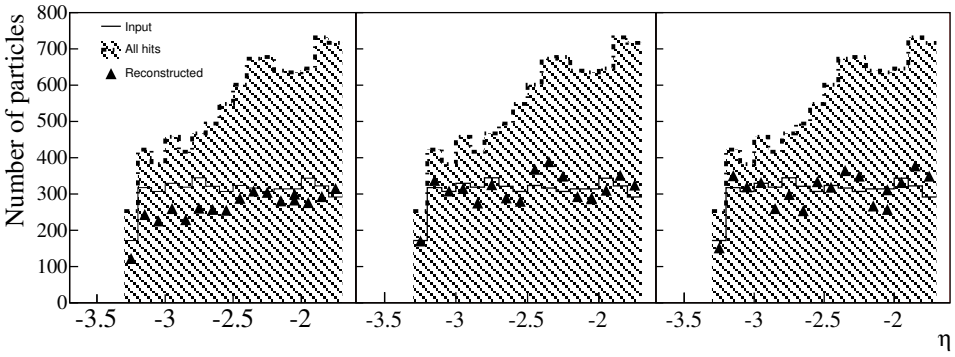

Figure 4.16: As Fig. 4.15, assuming a wide and flat input rapidity distribution. The figure shows the first three iterations.

has to be well known from Monte Carlo calculations.

4.2.3.8 Elliptic Flow

Information provided by the FMD can be used to study the hydrodynamical and thermodynamical properties of the high density and high temperature state produced in the heavy-ion collisions. The azimuthal distribution of produced particles emitted in a nuclear collision is correlated with the orientation of the reaction plane [2]. From measurements of azimuthal asymmetry of the charged particle distribution, it is possible to determine the magnitude of the directed and elliptic flow and their centrality dependence. The FMD studies flow effects via the azimuthal dependence of the multiplicity of charged particles.

A Fourier expansion of the azimuthal distribution of particles reads (with omission of higher order terms):

$$r(\phi) = \frac{1}{2\pi}\left(1 + 2v_1\cos(\phi - \psi_1) + 2v_2\cos(2[\phi - \psi_2])\right) \quad ,$$

where ϕ is the azimuthal angle of the measured particles, ψ_1 and ψ_2 are the angles of the first and second order event planes respectively, and v_1 and v_2 denote the first order and the second order flow coefficients (directed and elliptic flow, respectively). In the simulations we have assumed $\psi_1 = \psi_2 (= \psi_R)$, where ψ_R is the angle of the reaction plane. ψ_R was chosen randomly for each event.

A simulation using 10^4 events with the same impact parameter and fixed values of v_1 , v_2, but different ψ_R was generated using the HIJINGParam + `AfterBurnerFlow`[2] codes. To illustrate the sensitivity to the elliptical flow, we have set $v_1 = 0$ in the simulations.

In the reconstruction, the nth order event plane ψ_n was calculated from

$$\psi_n = \frac{1}{n}\tan^{-1}\left(\frac{\sum_i w_i \sin n\phi_i}{\sum_i w_i \cos n\phi_i}\right) \quad , \tag{4.1}$$

where ϕ_i is the azimuthal angle of the ith outgoing particle. The event plane was determined using the number of hits, where all hits have been assigned equal weights w_i. The event plane can also be determined using energy deposition. In this case the weights are given by the energy deposited. The parameter v_2 was determined as $v_2 = \langle\cos 2(\phi - \psi_R)\rangle$.

The estimated event plane differs from the actual event plane. the calculation gives incorrect v' which should be corrected by a Resolution Correction Factor (RCF) given by [3, 6]:

$$RCF = \langle\cos(n(\psi_n - \psi_R))\rangle = \frac{\sqrt{\pi}}{2\sqrt{2}}\chi_n \exp\left(-\chi_n^2/4\right)\left[I_{\frac{n-1}{2}}\left(\chi_n^2/4\right) + I_{\frac{n+1}{2}}\left(\chi_n^2/4\right)\right] \quad , \tag{4.2}$$

[2]HIJINGParam is a parametrization of HIJING without flow. `AfterBurnerFlow` is an afterburner that generates flow.

where I_v is a Bessel function of order v and χ_n is defined from the sub–event method [4, 5]. In this approach each event is randomly divided into two equally sized sub–events and flow angles ψ_n^a and ψ_n^b for each sub–event are determined. The distribution $\left|\psi_n^a - \psi_n^b\right|$ can be calculated analytically [3, 4]. The fraction of events in the data sample yielding an angle between sub–events of more than $\pi/2n$ is used to calculate χ_n

$$\frac{N_{events}\left(n\left|\psi_n^a - \psi_n^b\right| > \frac{\pi}{2}\right)}{N_{total}} = \frac{e^{-\chi_n^2/4}}{2} \quad . \tag{4.3}$$

The dependence of the v_2 reconstruction error as a function of the v_2 value is shown in Fig. 4.17

The FMD sectors cover azimuthal angular ranges of $\Delta\phi = 18^\circ$ and $\Delta\phi = 9^\circ$, for FMDi and FMDo, respectively. As shown in Fig. 4.17, the uncertainty on v_2 for 40 azimuthal segments is better than $\pm 5\%$, while for 20 azimuthal sectors it is better than $\pm 10\%$.

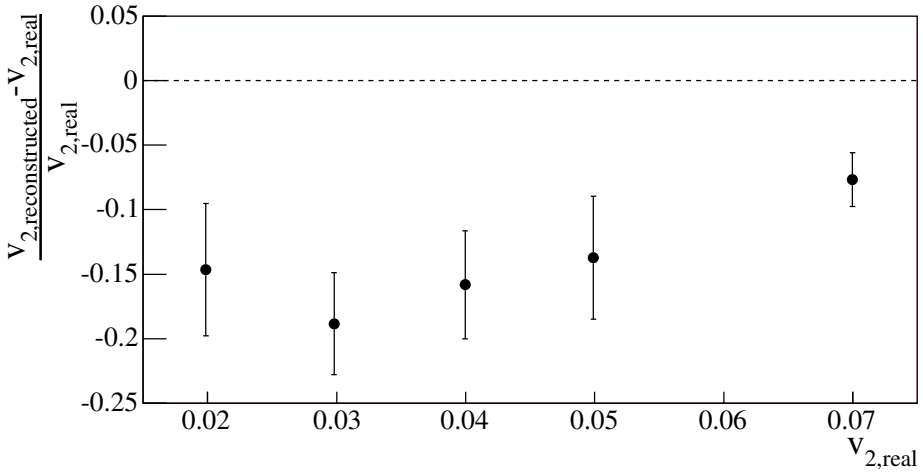

Figure 4.17: Accuracy of v_2 reconstruction as a function of v_2 for 40 azimuthal sectors.

4.3 Silicon Rings

4.3.1 Overview

The Forward Multiplicity Detector is composed as follows (see Figures 4.18–4.20). Each of the two *types* of silicon *sensors* must be cut from 300 μm thick silicon wafers. Each sensor is subdivided into two azimuthal *sectors*, whose active elements, *strips*, are arranged as narrow rings with the nominal beam position as centre. A sensor is glued onto a thin ceramic plate, which is in turn glued to a hybrid PC board containing the preamplifier electronics. Such a unit constitutes a detector *module*. Several modules (5 for the inner type and 10 for the outer type) are mounted on a light support plate to form a *half–ring*. Two half–rings are attached to a support structure and constitute a detector *ring*. The five detector rings (called FMD1, FMD2 inner and outer and FMD1 inner and outer) constitute the full FMD *detector*.

For identification purposes we use the following notation: FMD$\{1,2,3\}\{i,o\}(j,k)$, where the index runs over sector number ($j = (0,19)$ for inner, $j = (0,39)$ for outer) and strip number ($k = (0,511)$ for inner, $k = (0,255)$ for outer). For example, the 137$^{\text{th}}$ strip of the 4$^{\text{th}}$ sector of the inner ring of FMD2 would be denoted FMD2i(4,137). Sectors are labelled counter–clockwise looking down the beam line toward the muon absorber, starting from the horizontal line pointing toward the LHC centre. Strips are numbered from the smallest to the largest radius. See also Fig. 4.18.

Figure 4.19 shows how to assemble the ring detectors from sensor segments cut out of 6 inch silicon wafers. The figure shows how the two chosen ring geometries can be constructed from 10 and 20 sensors, respectively.

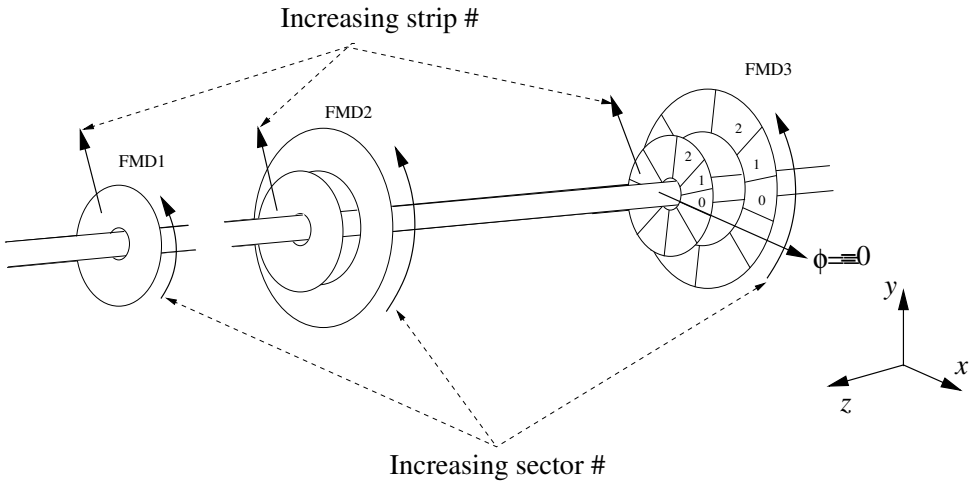

Figure 4.18: Numbering scheme for the FMD strips and sectors in the ALICE coordinate system.

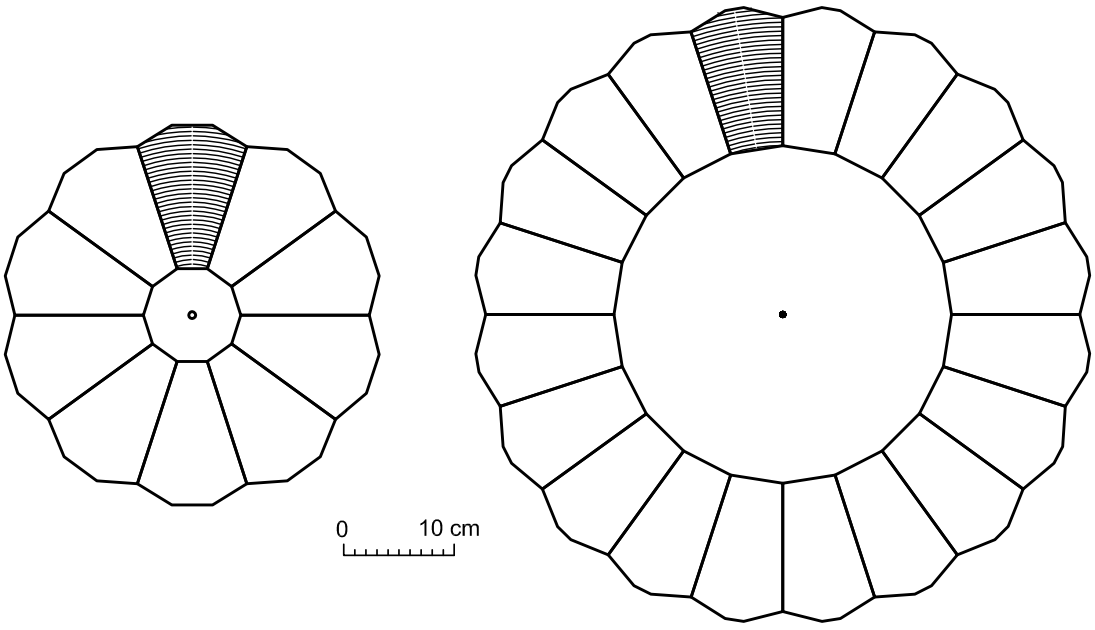

Figure 4.19: Assembly of an inner ring from 10 modules (left) and an outer ring from 20 modules (right). The size and shape of each module is determined by limitations imposed by the fabrication of sensors from 6 inch silicon wafers, see Figures 4.22 and 4.23.

Figure 4.20 shows a photograph of a model of the FMD3 assembly. The silicon sensors (not fully equipped) are mounted on flat support plates, in turn supported by the conical structure.

Figure 4.20: Photograph of model showing the assembly of the FMD3 inner and outer silicon ring (partly equipped in upper half) inside its support cone. The cone and the detector support plates can be split along the horizontal axis.

4.3.2 Silicon Sensors

Figure 4.21 shows a schematic cross–section of a silicon sensor based on bulk n–type silicon with p+ type implants. At the bottom is the aluminium high voltage connection plane (+HV). At the top, p+ type implants are shown for each of the active strips, for a guard ring and for a bias ring. Bias resistors connect the active strips to the aluminium bias ring. Each p+ strip is capacitively coupled to a corresponding aluminium strip, which is terminated by a bonding pad near the edge of the detector, allowing for bonding to the front–end electronics hybrid card. For quality control purposes, a d.c. bonding pad with direct connection to the strip p+ implant is also foreseen. This sensor design follows closely what has recently been produced for the silicon tracker of the CMS experiment [8], with the exception of the use of higher resistivity bulk silicon and changes necessary due to the differences in geometry.

The geometry of the sensors is matched to the effective size available on a 6 inch silicon wafer. The wafers are 300 μm thick with a diameter of 150 mm. Due to details of the manufacturing process, the full area of the silicon wafers cannot be used as an active detector. For the chosen manufacturer (Hamamatsu Photonics K.K.), the active sensor area is limited to lie within a fiducial circle of diameter 134 mm.

Figures 4.22 and 4.23 show the overall sensor geometry for the two types, inner and outer, respectively. The outside radii given in Table 4.1 correspond to the maximum radial dimensions of the sensors. Due to limitations on the useful wafer diameter, the outer corners of the sensors are cut as indicated. This entails a loss in azimuthal coverage of the rings for approximately 10% of the strips at the outermost radii.

The sensors are electrically subdivided into two equal azimuthal sectors with the median as symmetry

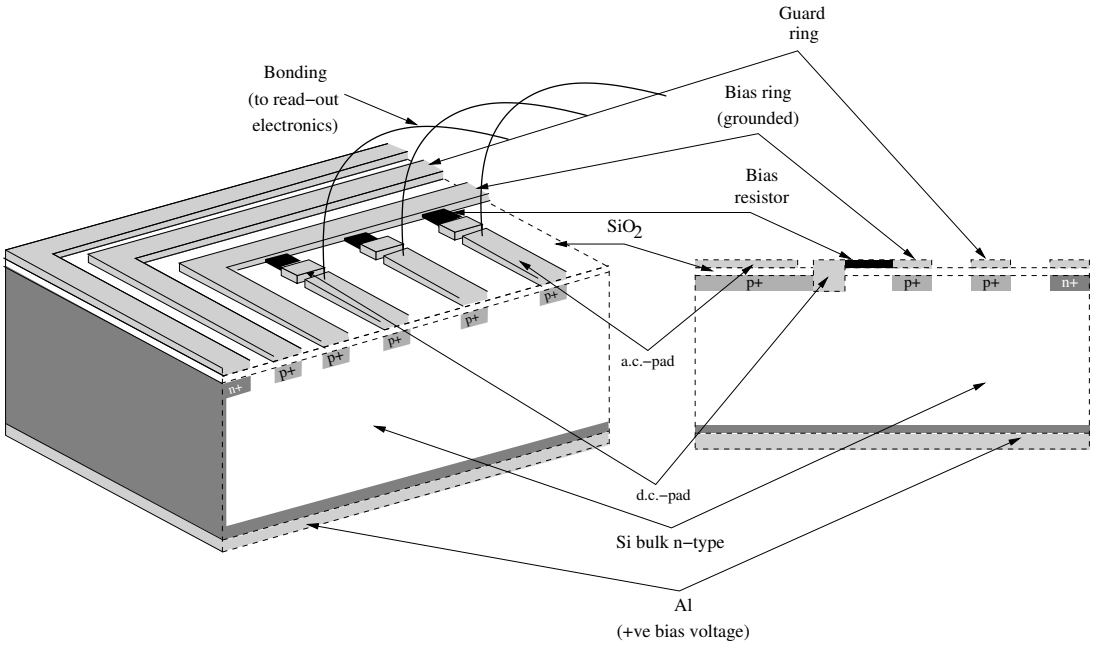

Figure 4.21: Left: a three–dimensional schematic view of the corner of a silicon sensor, showing the placement of guard ring, voltage distribution, etc. Right: a two–dimensional cross–section through the silicon wafer parallel to the direction of the active strips.

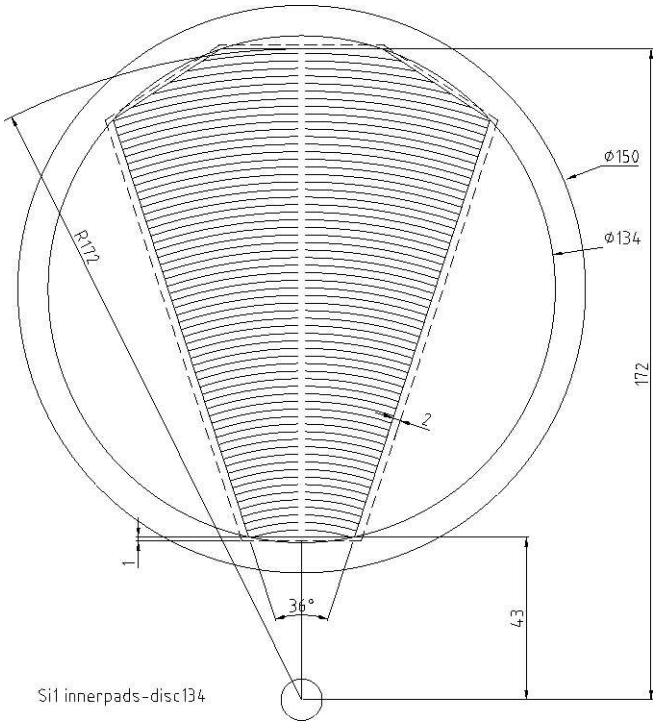

Figure 4.22: Geometry of an inner silicon strip sensor manufactured from a 6 inch Si wafer. The active parts of the detector must stay within the circle of diameter 134 mm for manufacturing reasons. The active area of the wedge–shaped sensor is outlined with full drawn lines, while the slightly larger area indicated with the dashed line represents the physical size of the cut wafer, including bias and guard ring structures. Each sector is subdivided into two azimuthal sectors, each with 512 strips at constant pitch (a smaller number is shown for clarity).

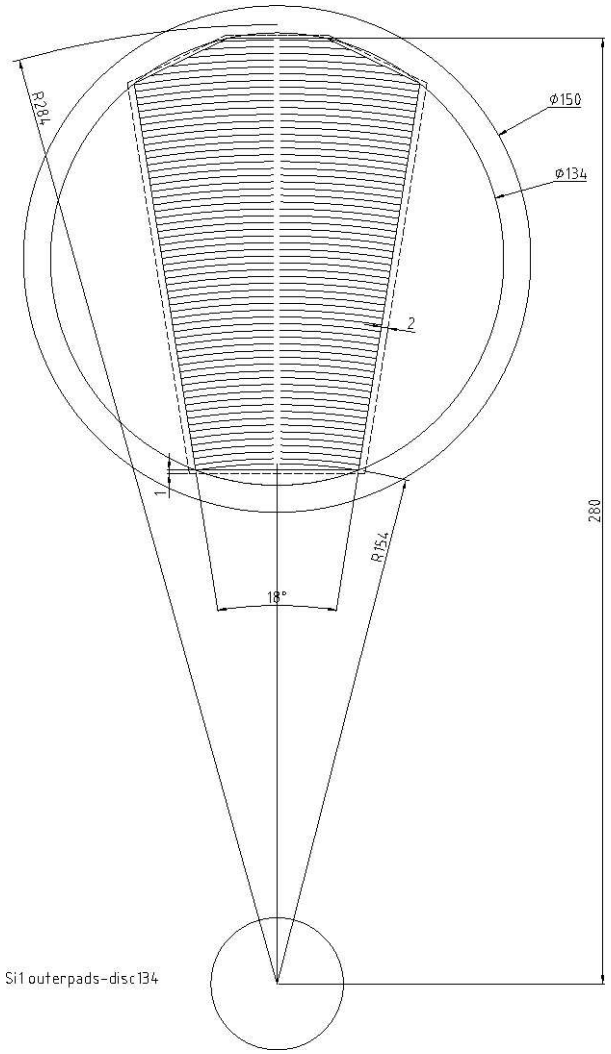

Figure 4.23: Geometry of an outer silicon strip sensor manufactured from a 6 inch Si wafer. The active parts of the detector must stay within the circle of diameter 134 mm for manufacturing reasons. The active area of the wedge–shaped sensor is outlined with full drawn lines, while the slightly larger area indicated with the dashed line represents the physical size of the cut wafer, including bias and guard ring structures. Each sector is subdivided into two azimuthal sectors, each with 256 strips at constant pitch (a smaller number is shown for clarity).

axis. On one side of each sensor (called the back side) a single Al contact covers the full active surface to supply the bias voltage (in the range 50–150 V) to the detector. On the other side (called the implant side) the detector is subdivided into circular strips of equal pitch, centred at the nominal beam position. Sectors of the inner type have 512 strips corresponding to a pitch of approximately 250 μm, while the outer type sectors have 256 strips with a pitch of approximately 500 μm.

Table 4.4 lists some of the specifications for the Si sensors. The higher silicon resistivity of 5 kΩcm compared to the 1.5–3 kΩcm used for the inner CMS detectors was chosen because of the relatively low, yet significant, radiation dose expected for the FMD over a 10–year period [7]. The passivation of the implant side is a protection of this side of the sensor, which will be used as a gluing surface to fix the sensor to its hybrid board, see Section 4.3.3. The Table lists the expected values for initial operational parameters, such as operational voltages and leakage currents.

Figure 4.24 shows a preliminary layout of the strips near the outer edge of an inner type sensor, indicating the geometry of the guard and bias rings, poly–silicon bias resistors, and rectangular bonding pads near the sensor edges which will be used both for the final bonding and near the centre line, which will be used for testing.

Table 4.4: Silicon sensor design parameters.

External parameters	
Radiation dose (10 years)	5 000 Gy
Hadron flux (10 years)	1×10^{13} cm^{-2}
Neutron flux (10 years)	2×10^{12} cm^{-2}
1 MeV n eq. flux (10 years)	3×10^{13} cm^{-2}
Operational temperature	20° C
Geometrical parameters	
Wafer diameter	150 mm
Effective sensor diameter	134 mm
Silicon thickness	$310 \pm 10\,\mu$m
Number of radial strips	512 (inner) or 256 (outer)
Strip pitch	250 μm (inner)or 500 μm (outer)
Strip length	13–50 mm (inner) or 24–42 mm (outer)
Guard and biasing ring width	$\sim$1 mm
Dimension of bonding pads	$\sim 100\,\mu\text{m} \times 300\,\mu$m
Silicon bulk parameters	
Silicon bulk type	n–type
Silicon lattice orientation[3]	$\langle 100 \rangle$
Silicon resistivity	$\sim$ 5 kΩcm
Silicon mask parameters	
Metal strip width	slightly larger than the p+ implant width
Metal strip thickness	1 μm Al
p+ strip width/pitch ratio	0.20–0.25
Metal back side	1 μm Al
Passivation on implant side	1 μm PECVD
Alignment reference	reference mark on implant side mask
Sensor electrical parameters	
Full Depletion voltage	50–100 V
Operational voltage	100–200 V

[3]This is solid–state notation for the lattice orientation relative to the surface $\langle n_x, n_y, n_z \rangle$.

Breakdown voltage	$> 200\,\mathrm{V}$
Total leakage current	$< 3\,\mu\mathrm{A}$
Strip leakage current	$< 5\,\mathrm{nA}$
Strip coupling capacitance	5–25 pF
Polysilicon bias resistors	$\sim 20\,\mathrm{M}\Omega$
Bad strips	$< 1\%$

In addition to the actual sensor, test structures will be placed on the unused part of the wafer for quality control purposes. Examples of such structures are p–n diodes, small MOS devices, a polysilicon resistor chain, a.c. coupling capacitors and, possibly, a mini-sensor.

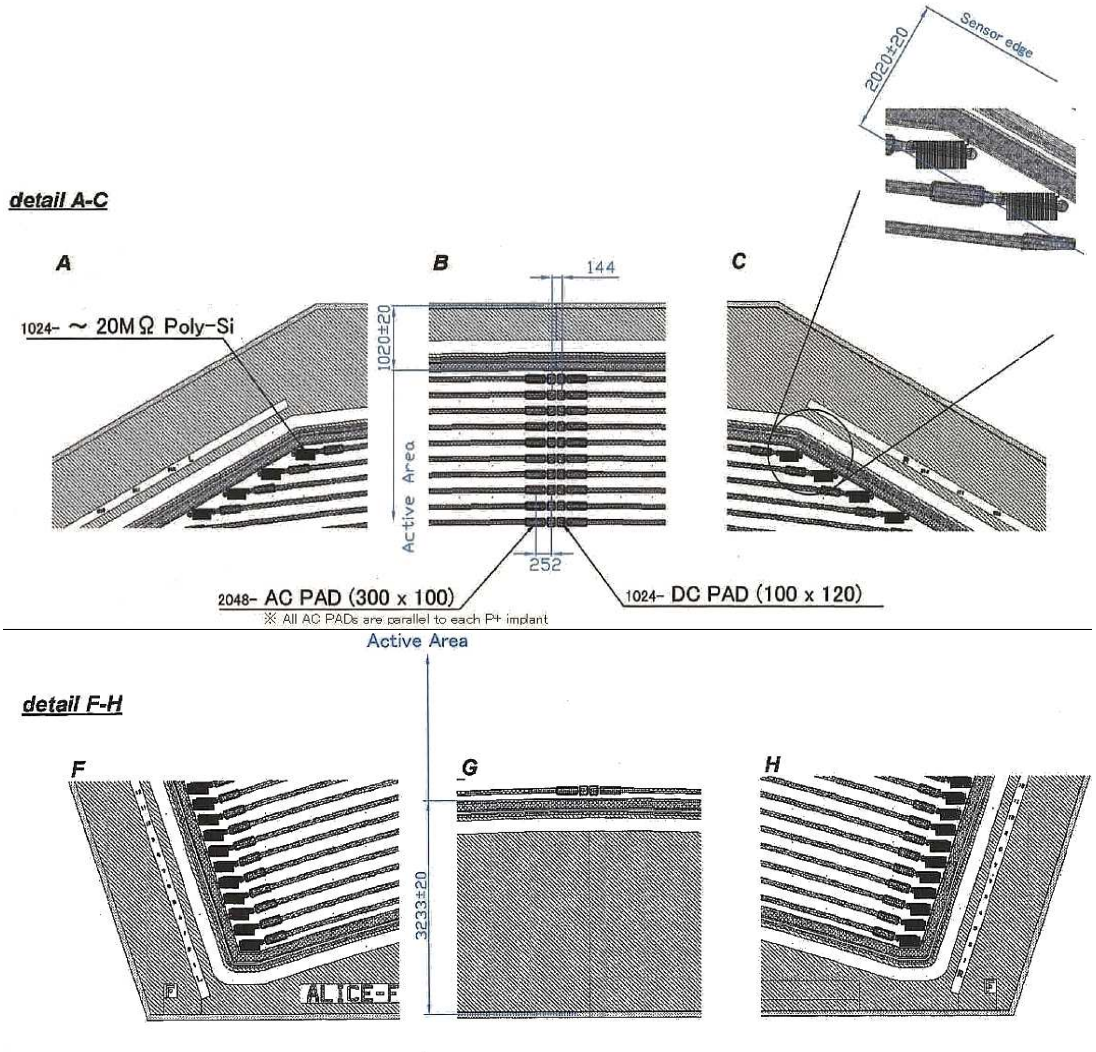

Figure 4.24: Strip layout of the outer (top) and inner (bottom) edge of an inner silicon strip sensor. This preliminary design from Hamamatsu Photonics K.K. shows in addition to the strip structure the guard and bias rings, the polysilicon bias resistors and the rectangular aluminium bonding pads.

4.3.3 Silicon Modules

Each silicon sensor must be held in place by a rigid system, with minimal strain on the very thin Si material, in conditions of varying temperature and humidity. We have chosen to glue the Si sensor (on the implant side of the silicon material) onto a thin (1 mm) ceramic plate. This in turn is glued onto a PCB hybrid card containing the front-end (pre-amplifier) electronics circuitry, to form a silicon module.

Both the ceramics plate and the hybrid PC card will be manufactured with dimensions slightly smaller than the Si sensor so the bonding pads on the sensor are visible beyond the edge of the cards. This will allow for thin wire bonding from the bonding pads on the edge of the sensor (oriented towards the hybrid assembly) to corresponding bonding pads on the hybrid cards. Details of the hybrid card design and the bonding are given in the electronics section (Section 4.4).

Gluing the ceramics and bonding the hybrid card to the Si sensor will be carried out under controlled conditions, allowing for the precise relative adjustment of the two elements. The further alignment of the hybrid card in the assembled detector is secured by three small 'legs', which mount the module on the support plate. The alignment will be made by comparing reference marks on the Si wafer to marks previously laid out on the hybrid card, to a precision better than $50\,\mu$m.

The sensor strip will be electrically bonded to the hybrid card on the modules that have already been glued. This bonding will be carried out at CERN. Bonding pads on sensors and hybrids line up with each other (see Fig. 4.25). The relatively large pitch ($= 250\,\mu$m and $500\,\mu$m) will allow for several bonding wires per strip, thereby avoiding badly bonded strips.

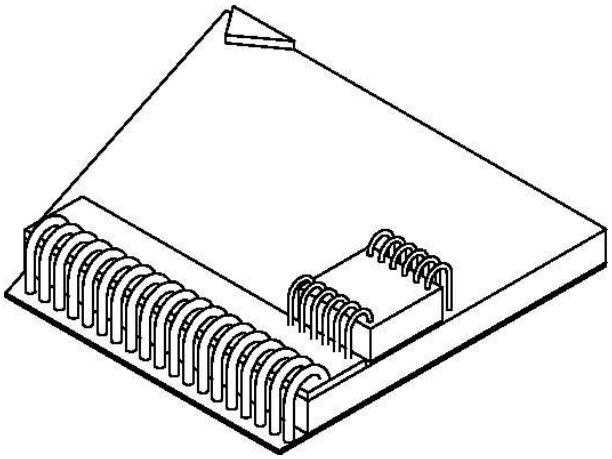

Figure 4.25: Illustration of the bonding of the strips on silicon wafers to the hybrid card. The Si sensor is shown at the bottom with bonding pads along the edge. On top is the slightly smaller hybrid board with a pitch adapter to which thin wires are bonded. Also shown is the bonding of a front-end chip to the pitch adaptor and the hybrid card.

The assembled detector module is an independent unit that can be connected to digitizer and read–out electronics, and fully tested.

4.3.4 Silicon Half–Rings

The wedge–shaped modules consisting of silicon sensors and their hybrid cards are mounted on mechanically stiff half–ring support plates manufactured from 10 mm thick honeycomb plates laminated with 1 mm aluminium on both sides (to provide for precision drilling of holes). Half–rings of the inner and outer types hold 5 and 10 silicon modules, respectively.

Silicon modules are attached to the honeycomb support plate by small supporting legs, see Fig. 4.26. Dead space between the active surfaces of the Si modules in azimuth due to inactive edges on the modules

is avoided by staggering neighbouring modules by about 5 mm in z. To avoid double counting of hits, there is no overlap between the active surfaces.

Cables to and from the hybrid cards are supplied via connectors mounted near the outer rim of the hybrid cards. These connectors pass through cut–outs in the honeycomb plate, where they are connected to the digitizer cards. The digitizer cards will be mounted on the back of the honeycomb support plate, with matching connectors near their outer rim.

The silicon half-ring units constitute independent detector units that can be tested prior to installation.

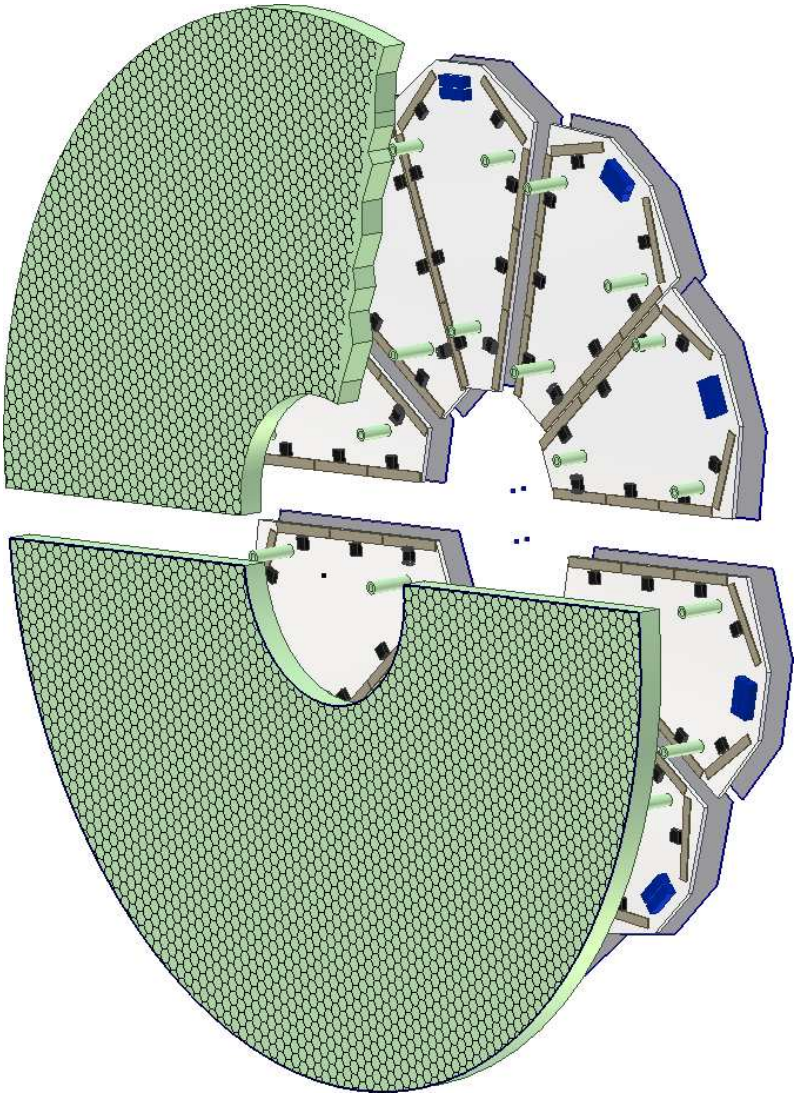

Figure 4.26: Exploded view of the assembly of an inner FMD ring, showing the two honeycomb support plates, the hybrid cards, and Si sensors. On the hybrid cards, the VA front-end chips and their pitch adaptors are visible along the two radial edges, the connectors for the cables are close to the outer rim, and the three support legs attach each module to the support plate. Adjacent hybrids and sensors are staggered slightly to allow for overlaps in azimuth of the inactive part of the sensors.

4.4 Electronics

4.4.1 Overview

In the design of the signal processing electronics for the FMD, existing and proved solutions have been chosen whenever possible. This philosophy has allowed us to use well–proved highly integrated preamplifiers with multiplexed read-out (VA1) [9], adapted to the radiation environment of ALICE and the timing of the ALICE trigger and read–out system. The existence of a fast ADC chip (ALTRO) [10] developed for the ALICE TPC has made it possible to perform analog–to–digital conversion on the detector, consequently avoiding long cables with fast analog signals. Furthermore, the adoption of the TPC analog–to–digital converter allows the use of the back–end TPC read–out electronics (RCU [11]) and results in a significant saving in the development work of both hardware and software related to the read–out system.

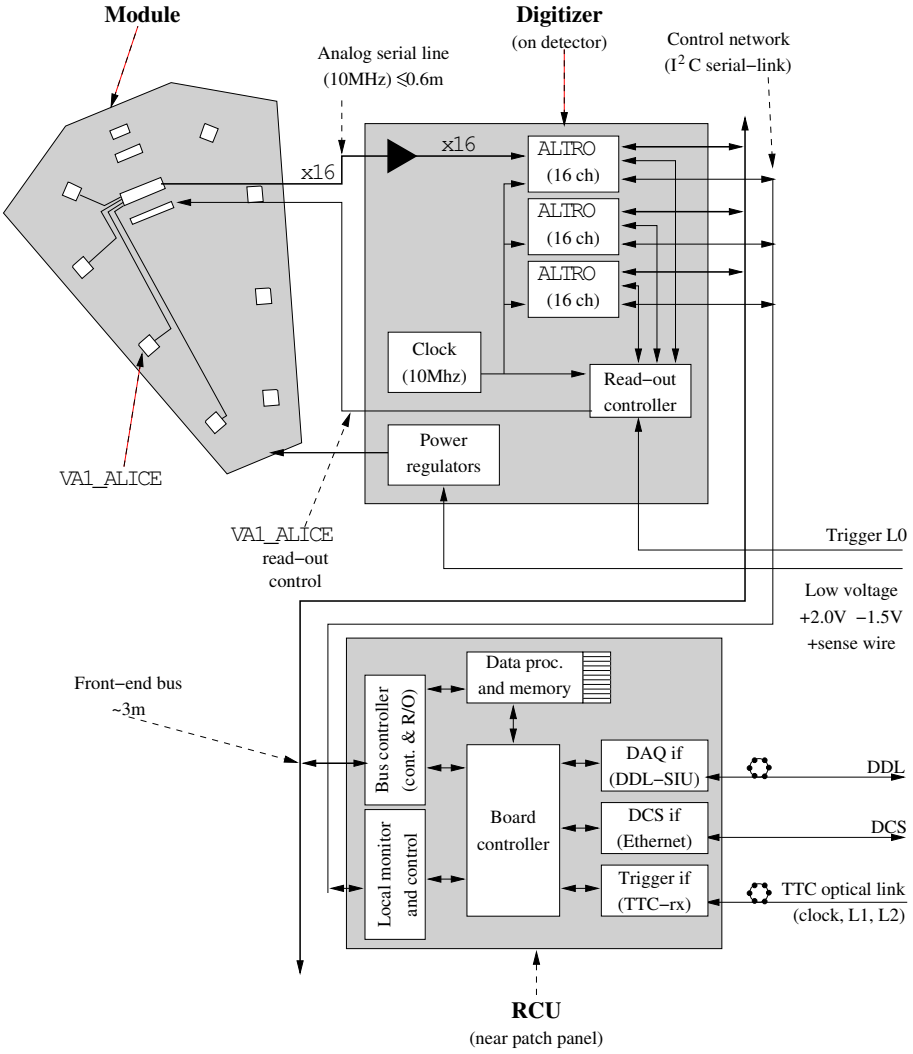

Figure 4.27: Architecture of the FMD read–out electronics. The VA1_ALICE pre-amplifier–shaper chips are placed on the FMD modules with their inputs bonded directly to the silicon sensors. Multiplexed analog signals are digitised and stored by the FMD digitizer cards containing ALTRO analog–to–digital converters. The read–out and control of the ALTRO is achieved by the RCU module developed for the ALICE TPC.

Figure 4.27 shows the architecture of the FMD read–out system starting from the silicon modules

(top left) to the data and control links going to the counting room (bottom right). A module assembly consisting of a silicon sensor and a hybrid card contains the VA1_ALICE pre–amplifier–shaper integrated chips very near to the silicon sensors. The pre–amplifier inputs are bonded directly to the Si strips through pitch adaptors. After analog storage in the VA1_ALICE chips, the data is multiplexed an analog serial link to the FMD digitizer card, where it is digitised in the ALTRO analog–to–digital converter chips and stored in a digital multi–event buffer. The further data transport uses the Read–Out Control Unit (RCU) to deliver the data into another multi-event buffer and onward through the optical DDL link into the ALICE data acquisition system. In addition to the read–out, the FMD digitizer takes care of the distribution of the L0 trigger signal as strobe to the pre–amplifier–shapers and the synchronization of the read–out between the VA1_ALICE and the ALTRO chips. The RCU module is the master of the ALTRO read–out bus and handles all communication upwards to the data acquisition, detector control and trigger systems through the indicated links. The RCU module is identical to the unit developed for the ALICE TPC read–out system.

Each VA1_ALICE chip has 128 independent channels of pre–amplification and shaping circuits, followed by analog storage. The data storage is strobed by the level zero trigger at a fixed time after the beam interaction, common to all channels. During the read–out, the 128 channels are multiplexed onto an analog link and input to a single channel of the ALTRO analog–to–digital converter, which is able to digitise the 128 data values at the same frequency (10 MHz) at which they arrive from the VA1_ALICE chips. Thus, each ALTRO chip with its 16 parallel ADC channels can read out 16 VA1_ALICE chips simultaneously, and store the digitized data for $16 \times 128 = 2048$ strip channels in its digital buffer. A digitizer card with three ALTRO chips and a read–out controller has enough channels to read out the 80 FE chips for one half–ring of the FMD detector.

The remainder of the read–out system, consisting of the ALTRO front–end bus and control network, has sufficient bandwidth to handle the full FMD detector with a single RCU. However, in order to limit the physical length of the front–end bus, three RCU boards and sets of optical links are envisaged, for each of the read–outs of FMD1, FMD2 and FMD3. Table 4.5 summarizes the number of chips and electronics boards needed.

4.4.2 Pre–Amplifier

4.4.2.1 General Considerations

The choice of Front–End Electronics (FEE) and detector characteristics are closely linked. Furthermore, the timing imposed by the ALICE trigger, in particular L0, is important for the internal time constants of the circuit. The major issues related to the matching of the FEE to the silicon sensors and the ALICE environment are:

1. Matching of the strip capacitance and detector leakage current to the pre–amplifier input circuit. This relates to the expected signal–to–noise ratio.

2. The dynamic range of the pre–amplifier must be matched to the signal amplitude of the sensor for the expected range of particle hit densities per strip, and for the energy loss variation due to the particle composition and fluctuations in dE/dx.

3. The shaping time of the amplifier is imposed by the timing of the strobe generated by the ALICE L0 trigger relative to the event time.

4. Matching of the electronics layout and the number of channels to the strip layout.

5. Resistance of the circuitry to radiation.

The signal–to–noise ratio is related to the strip capacitance, the detector leakage current and the pre–amplifier characteristics. For a $300\,\mu m$ thick silicon strip detector, the capacitance presented to the

Table 4.5: The total number of strip channels per ring and the number of front–end pre–amplifier chips (128 channels per chip). Also shown is the number of ALTRO read–out chips for each ring and the number of FMD digitizer cards, assuming three ALTRO chips per card. One Read–out Controller Unit (RCU) is foreseen for each of the three FMD sub-detectors.

	FE Channels	**FE Chips**	ALTRO **chips**	**FMD Digitizers**	**RCU modules**
FMD1	10 240	80	6	2	1
FMD2i	10 240	80	6	2	1
FMD2o	10 240	80	6	2	
FMD3i	10 240	80	6	2	1
FMD3o	10 240	80	6	2	
Total system	51 200	400	30	10	3

pre–amplifier through a 5 cm long and 0.5 mm wide strip is about 25 pf and the number of electron–hole pairs generated on average by a single MIP particle is about 22 400 e^-, corresponding to 3.6 pC charge. The aim is to keep the signal–to–noise ratio well above 10 for a single MIP particle. This requirement means the pre–amplifier noise must be below 2000 e^- for a detector capacitance of 25 pF.

Most existing pre–amplifier circuits for silicon strip detectors have been designed to detect a charge equivalent to a few MIPs. For the FMD the expected maximum number of charged particles hitting a single strip is three, but slow particles (e.g., α) may deposit significantly larger energies. Consequently, the FMD electronics must be able to measure a considerably higher charge deposition. We have chosen to require an effective dynamic range of the pre–amplifier from about 0.1 MIP to about 10 times the expected average energy deposition per strip in central Pb–Pb collisions i.e., about 20–30 MIPs. The lower limit assures a good signal–to–noise ratio even for single particle hits. The higher limit is set in order to accommodate fluctuations both in the number of particles and their energy deposition around their averages, and to keep some safety margin for adverse background or unexpected physics situations.

In the chosen architecture, the shaping time must be such that the amplified signal peaks soon after the arrival of the strobe. In ALICE, this time is 1.2–1.3 μs after the beam crossing. It should be kept in mind that if the shaping time is comparable to the average spacing between events, energy signals will be corrupted by overlapping events. For Pb–Pb running, the expected event rate is about 8×10^3 Hz. Thus, the average time between events is in the range of 100 μs and a shaping time in the microsecond range will not generate many overlapping events. For pp or high luminosity light ion (Ar–Ar) running, however, the luminosity is considerably larger and the event rate expected in ALICE is 2×10^5 Hz, implying an average time between events down to 5 μs. Due to the low multiplicity, the issue of overlapping signals is still not much of a problem in pp, while in Ar–Ar it may be necessary to veto close events to get pulse height measurements.

While each strip channel must be seen directly by a relatively fast pre–amplification and shaping circuit, it is possible to multiplex many channels into the subsequent read–out, provided that the individual analog signals can be stored in an analog buffer on the detector and the read–out does not have excessive dead–time.

Front–end electronics located close to the LHC beam pipe must be radiation hard. Recent estimates made by the ALICE collaboration indicate that the integrated 10–year dose is about 3300 Gy (330 krads) at the inner radius of FMD1, decreasing to below 200 Gy (20 krads) at the outer radius of FMD2 and FMD3 [7].

The specifications for the FE electronics are summarized in Table 4.6.

Table 4.6: Specifications for the FE electronics

Radiation hardness:	$\geq$5000 Gy(500 krad)
Peaking time:	1.2–1.5 μs, adjustable
Noise:	$\leq$ 0.1 MIPs (2,200 e^-)
Capacitance matching:	5–25 pF
Dynamic range:	0–20 MIPs
Test and calibration circuits	yes
Moderate power consumption:	$\leq$1 mW/channel
Early prototype version for detector testing	yes
Affordable cost in relatively small quantities	yes

4.4.2.2 The VA1_ALICE Pre–Amplifier–Shaper

The Viking Architecture (VA) family of pre–amplifiers [9] has a long history as amplifiers for silicon detectors. It is characterized by a high level of integration, low noise and low power requirements. The VA pre–amplifiers exist in a variety of versions based on a common architecture and amplifier design, but with different channel count, shaping times, capacitance matching, chip technology etc. For the FMD, we have based the design on a slightly modified version of the VA1_prime2, a 128–channel chip made in 0.35 μm AMS technology and proved to resist radiation well beyond 1 Mrad [12].

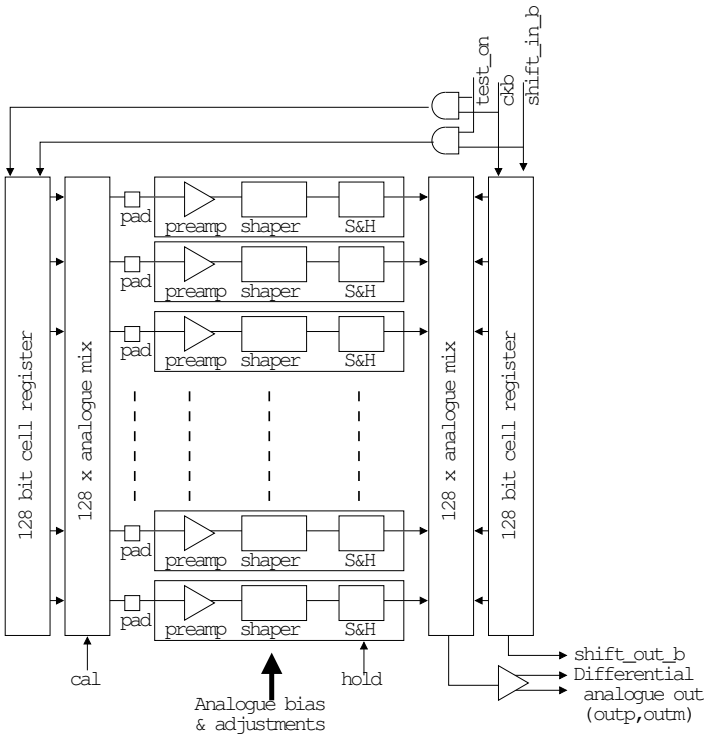

Figure 4.28: The VA1_ALICE architecture.

Figure 4.28 shows the architecture of the VA1_ALICE [13]. The chip consists of 128 identical charge–sensitive amplifiers, each with a pre–amplifier, shaper and sample–hold circuit strobed by a common 'hold' signal. The outputs of all amplifiers enter a 128–channel analog multiplexer controlled by a 128–cell bit register, which is used to direct each of the sample/hold values one at a time to the same differential output buffer. One bit in the register moves through the channels in sequence by clocking the

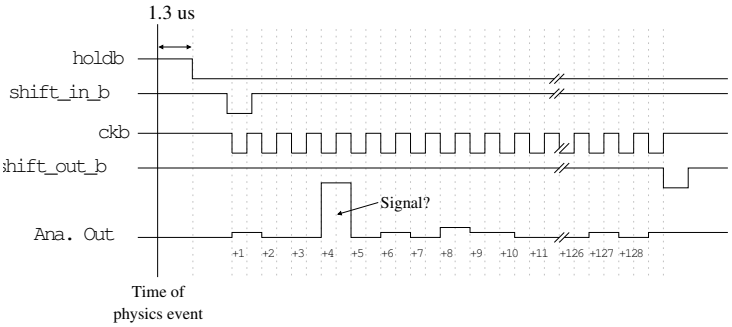

Figure 4.29: The VA1_ALICE normal read–out sequence.

ckb input while the shift_in_b is held up. A normal read–out sequence is displayed in Fig. 4.29. It is seen how each of the 128 analog values are transferred onto the output line (Ana. Out), synchronized by the input clock (ckb). The $5 \times 6\,\mathrm{mm}^2$ chip shown in Fig. 4.30 features a single calibration charge input and external biases to adjust the shaper parameters within a limited range.

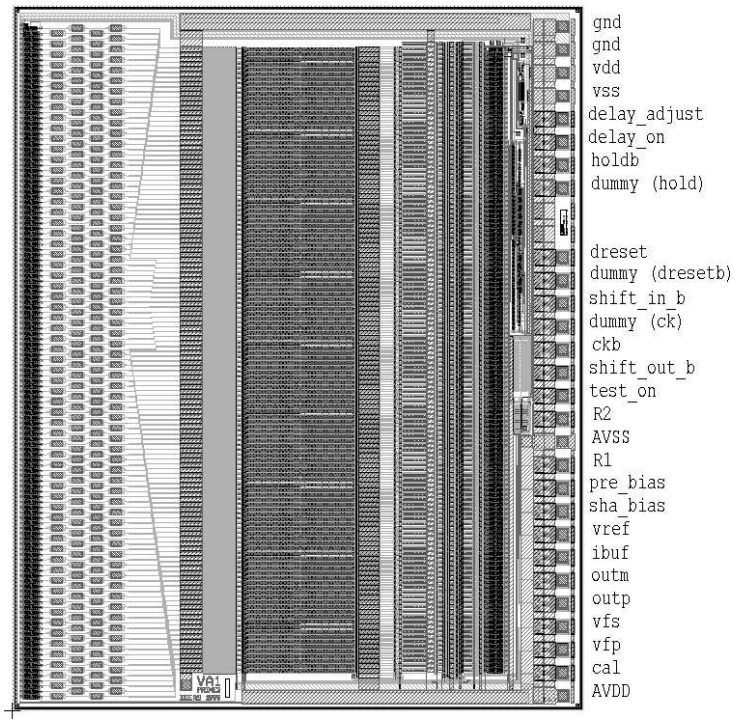

Figure 4.30: The VA1_ALICE pre–amplifier chip. The input pads of the 128 channels are visible along the left side of the chip, while control and output are placed along the right–hand side.

The existing VA1_prime2 fulfils most of the FMD requirements, except for the shaping time, which is too short. For this reason, we have a contract with the IDEAS company to modify the design to our specifications and produce a new VA1_ALICE chip with a peaking time of 1.2–1.5 μs and improved leakage current compensation. Table 4.7 summarizes the specifications of this new amplifier chip, with the expected noise performance and power consumption calculated by IDEAS simulations. Figure 4.31 shows the calculated noise performance with realistic capacitance and leakage currents and Table 4.8 gives a list of the power, control and output pads that must be connected on the VA1_ALICE chips.

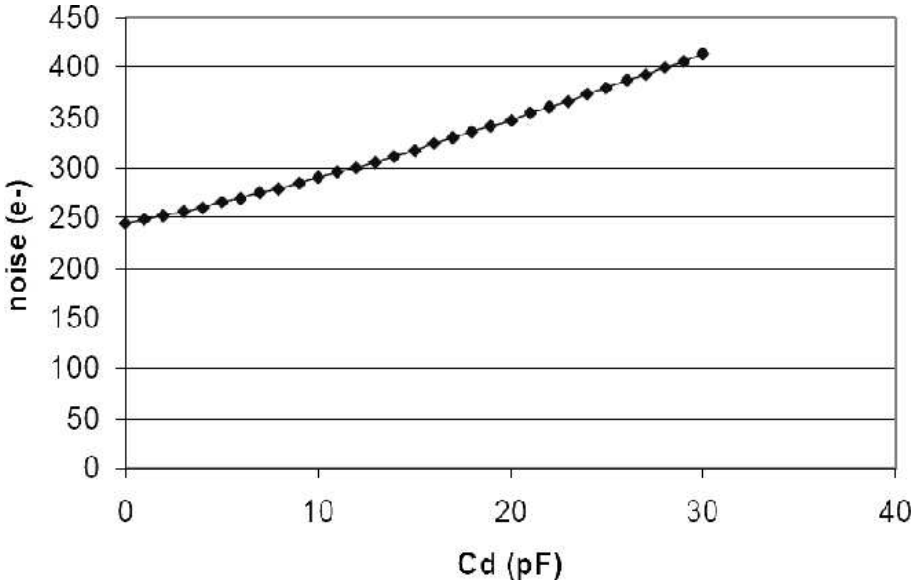

Figure 4.31: ENC noise versus detector load for the VA1_ALICE chip. The leakage current was 3 nA and the peaking time was set at 1.35 μs.

4.4.3 Hybrid Cards

The hybrid cards hold the front–end pre–amplifier chips and serve two purposes: mechanical support for the Si sensors and printed circuit board for the pre–amplifier circuitry.

Locating of the pre–amplifiers as close to the Si sensor as possible is essential to avoid degradation of the signal–to–noise ratio from pickup on the transfer lines. For this reason, the VA1_ALICE chips will be mounted on hybrid boards, to which the silicon sensor itself will be directly attached and the strips bonded. A hybrid board has essentially the same shape but slightly smaller size compared to the Si sensor, and the assembly of sensor and hybrid card constitutes an independent detector unit, an FMD *module*. Figure 4.32 shows an inner and an outer module, seen from the hybrid side with the Si sensors below.

The hybrid substrate will be a "sandwich" of a 0.5-1.0 mm thick ceramic plate on the implant side of the silicon sensor and a multilayer printed circuit board of halogen–free FR4 board. The flatness of the ceramic material assures a good gluing surface for the brittle silicon and allows the back side of the FR4 to be a fully metallized electrical ground plane.

Electrically, the purpose of the hybrid cards is to support the necessary number of pre–amplifier chips and distribute their services (power distribution, bias voltages, test and calibration circuitry, read–out lines and cable connectors). Power regulators, read–out logic, and other electronics components that need not be placed in the immediate neighbourhood of the front-end chips will not be placed on the hybrid card, but rather on the FMD digitizer card. Wherever possible, the electric signal lines are placed on the FR4 circuit of the hybrid card. However, due to the small pitch of the input pads of the VA1_ALICE chip, it will be necessary to have a special pitch adaptor to fan in the signals from the 250 μm (500 μm) pitch of strips in the inner (and outer) sensors to the 45 μm pitch of the VA1_ALICE input pads. This pitch adaptor will be made on a ceramic substrate and glued to the FR4 substrate in front of each VA1_ALICE chip.

The main components to be found on the hybrid card are displayed in Fig. 4.32 and are listed below.

1. VA1_ALICE chips, described in the previous section. Inner modules will hold eight chips along the two edges of the hybrid; outer modules hold only four chips, two on each edge.

2. Pitch adaptors are thin ceramic circuits about 4 mm$\times$32 mm size, used to fan in the signals from a

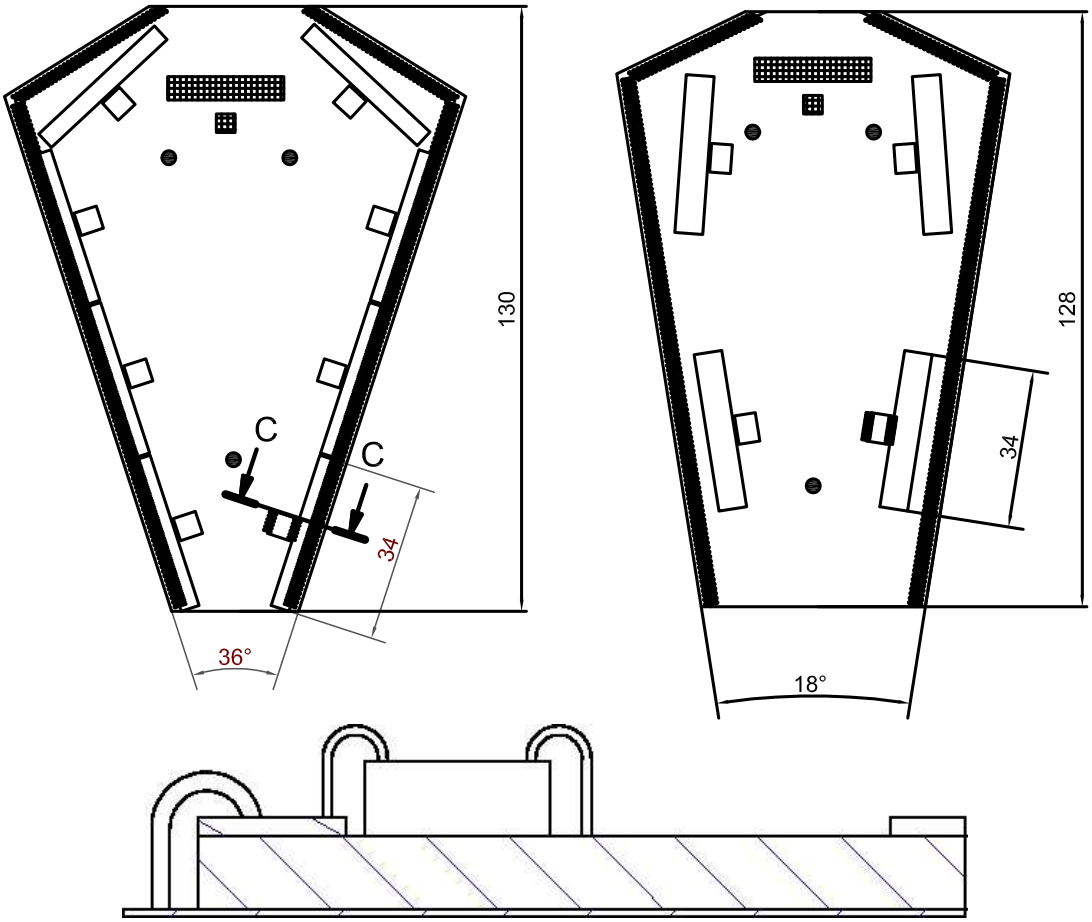

Figure 4.32: Layout of the hybrid cards showing the main components on an inner (left) and an outer module (right). The VA1_ALICE chips and pitch adaptors are placed along the sides of the hybrid, directly opposite the bonding pads of the silicon sensor strips, and the cable connectors, near the upper edge. Also shown (bottom) is the cross sectional view of the inner wafer at C-C. The bonding wires from the pads of the silicon sensor strips to the pitch adaptor are illustrated, and the bonding of the VA1_ALICE chip is also shown.

Table 4.7: Specifications of the VA1_ALICE chip

Process	0.35 μm N–well CMOS, double–poly, triple metal	
Die size	4.95 mm $\times$ 6.12 mm, thickness: $\sim$725 μm	
Input bonding pads	Four rows	
	Pad size:	50 μm $\times$ 90 μm
	Pad pitch:	91.2 μm
	Row pitch:	170 μm
Output pads	Single row	
	Pad size:	90 μm $\times$ 90 μm
	Pad pitch:	200 μm
Channels	128 per chip	
Power rails	Vdd:	+1.3 V
	Vss:	-2.0 V
Currents drawn	dvdd:	$<$10 μA
	dvss:	$<$10 μA
	avdd:	11.5 mA
	avss:	-73 mA
	gnd:	61.5 mA
Peaking time	Nominal:	$\sim$1.35 μs
	Adjustable:	$\sim$1.2 μs–1.5 μs minimum
Power dissipation	Quiescent:	80 mW per chip
		650 μW per channel
Input stage	PMOS referenced to gnd, input potential: $\sim$-1.2 V–-1.3 V	
Gain	Differential current gain about $\pm$10 μA/fC at 1 MIP	
Linear range	minimum $\pm$10 MIP, or 0–20 MIP single polarity	
Noise	$\sim 240 + 6$/pF for 1.35 μs peaking time (calculated)	
Read–out	Controlled via 128–bit shift register	
	Max. read–out speed: 10 MHz	
Calibration/test	Voltage step applied via external 1.8 pF capacitor, 2 mV step represents 1 MIP (=22400 e^- or 3.6 fC)	

pitch of 250 μm to a pitch of 45 μm.

3. Bonds from the pads on the silicon sensors to the pitch adaptors, from the pitch adaptors to the VA1_ALICE input pads, and from the VA1_ALICE output and control pads to the FR4 substrate.

4. Connectors for low voltage power, and control and read–out lines for the VA1_ALICE. Short cables will go from these to the digitizer boards. Figure 4.32 also shows a connector receiving the bias voltage for the silicon sensor which will be connected directly to an individual channel of an HV power supply places outside the L3 magnet. A short cable will connect the bias voltage from the hybrid to the back of the sensor.

5. Circuitry and passive components (not shown in Fig. 4.32) distributing power, control and read-out lines from the VA1_ALICE chips to the connectors. All chips will be read out in parallel and synchronously.

Table 4.8: List of connections on the VA1_ALICE chip.

Signal name	Type	Description	Nominal value
gnd	power	signal ground	0.0 V
dvdd	power	digital vdd	+1.3 V
dvss	power	digital vss	−2.0 V
avss	power	analog vss	−2.0 V
avdd	power	analog vdd	+1.3 V
holdb	digital in	hold analog data	logical
shift_in_b	digital in	start pulse for read–out	logical
ckb	digital in	clock for read–out register	logical
dreset	digital in	reset of digital part	logical
test_on	digital in	turns chip into test mode (calibration)	logical
cal	analog in	test input signal	1 MIP
outm	analog out	negative output signal (current)	varies
outp	analog out	positive output signal (current)	varies
pre_bias	analog in	bias current for pre–amplifiers	500 μA
sha_bias	analog in	bias current for shaper amplifiers	22 μA
ibuf	analog in	bias current for output buffer	140 μA
vfs	analog in	control voltage for shaper	700 V
vfp	analog in	control voltage for pre–amp.	-0.2 V

4.4.4 FMD Digitizer Cards

It has been found that it is advantageous to digitize signals close to the detector and store the digital information in a multi–event buffer before transfer to the DAQ. This digitization of the data synchronously with the read–out from the VA1_ALICE chips is the main function of the FMD Digitizer (FMDD) boards and is done by three ALTRO analog–to–digital converter chips on each board. The boards also contain the power regulation and bias setting for the hybrid cards and their VA1_ALICE chips. Many of the FMDD details, relating to the ALTROs and the communication buses to the RCU module can be taken from the TPC Front End Card (FEC) design, while the VA1_ALICE services are specific to the FMDD.

Each digitizer card will service the detector modules of one half–ring (40 VA1_ALICE chips) and be placed on the rear side of the honeycomb support plate of the half–ring, within a few tens of centimetres of all the hybrid cards. Thus a half–ring becomes a functional unit of the read–out up to and including the multi-event buffers on these cards.

Figure 4.33 shows the functional layout of a FMD digitizer card. The signals are digitized by the ALTRO chips designed for the ALICE TPC read–out in 0.25 μm IBM radiation–hard technology. The ALTRO contains 16 independent channels of 10–bit ADCs, each capable of sampling the input at a rate of 10 MHz, followed by various digital processing capabilities and a multi-event result buffer. For the FMD, only the ADC functionality and digital output buffer is essential, while baseline subtraction and zero–suppression will be optional, possibly depending on the finally observed strip hit rate.

The read-out controller is the same FPGA that will control the initialization and read-out sequence of the ALTROs. On the FMDD, the added functionality is to receive and distribute the L0 trigger signal used to freeze the analog values in the VA1_ALICE chips and, in case of a positive subsequent L1 trigger, to issue a read-out sequence as the one shown in Fig. 4.28 which is synchronized to the same clock as the ALTRO digitization circuit.

Figure 4.34 shows an early prototype set–up to test the synchronization of the VA multiplexing and the ALTRO digitization clocks. An ALTRO test card [14] is used with a synchronization module based on FPGA logic and a Si sensor with a VA1_prime2 chip.

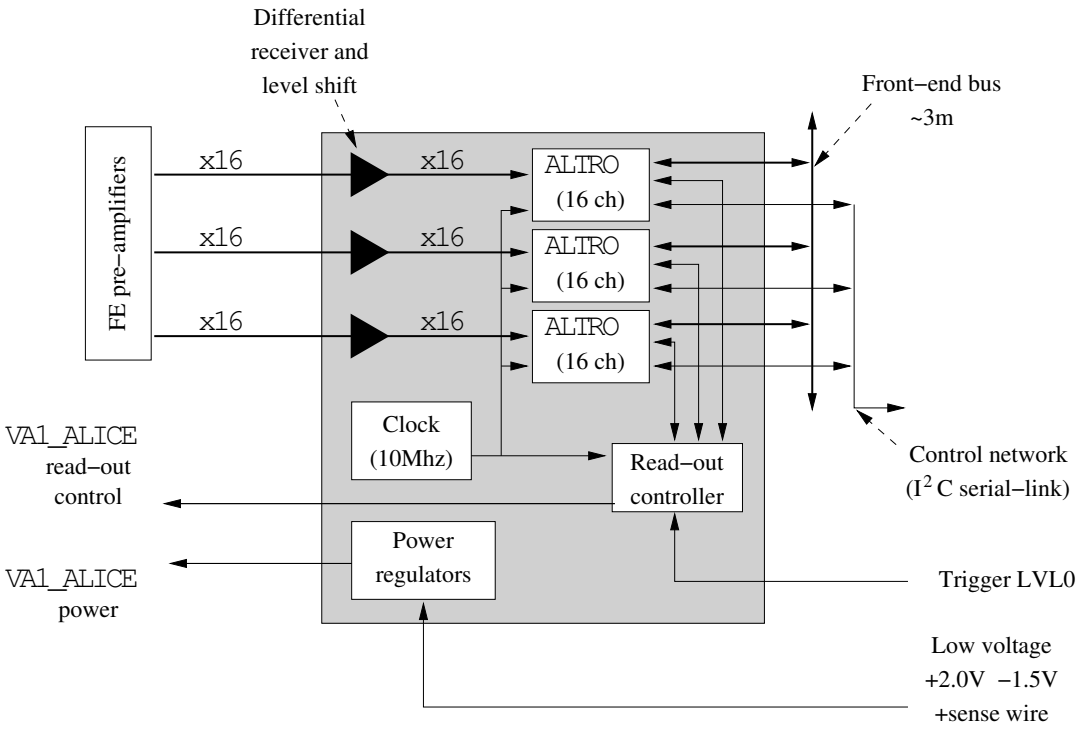

Figure 4.33: Schematic layout of the FMD digitizer card

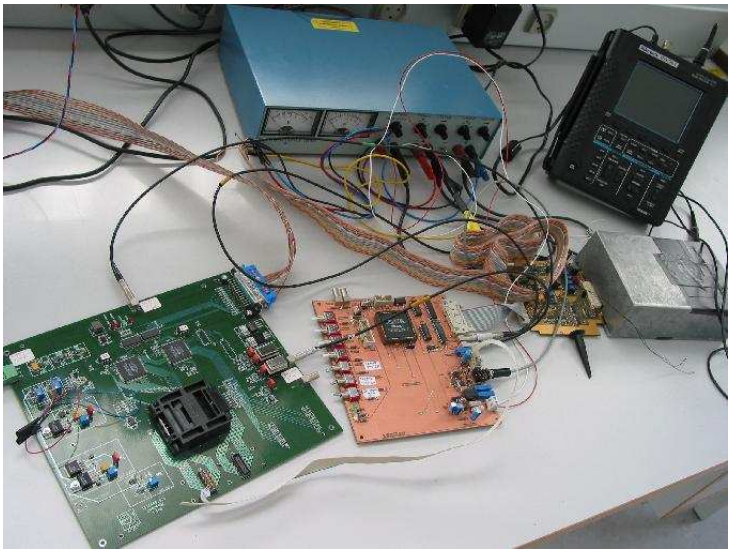

Figure 4.34: Test set–up of ALTRO read–out at NBI. The box on the right contains a Si detector and a VA1_prime2 pre–amplifier chip. The large print–card on the left is an ALTRO test–board. The smaller card in the middle is a custom–built clock and synchronization card. Data is read out into a PC running LabVIEW.

4.4.5 Readout Control Unit (RCU)

The Read–out Control Units (see Fig. 4.35) interface the digitizer cards to the Data Acquisition System (DAQ), the Timing and Trigger System (TTC), and the Detector Control System (DCS). They are responsible for controlling the event data read–out of the FMD and for initializing and monitoring the digitizer cards. The units are identical to those developed for the TPC, and apart from configuration data and custom routines, the software will also be identical. Figure 4.36 shows a photo of the RCU board in a TPC setup.

Three units will be used to interface the 10 digitizer cards. The use of one RCU per FMD ring system guarantees that the length of the buses between the RCU and the corresponding digitizer cards remain below $\sim$3 m. Two separate buses — for data and controls, respectively — provide the interface to the front-end electronics on flat, flexible cables.

The RCU board design is based on a single FPGA containing the logic and on-board memory. It is interfaced to the various links communicating with the external systems. The interfacing to the Trigger and the DAQ systems follows the standard architecture of ALICE, using the optical TTC and Detector Data Links (DDL), respectively. The interface to the DCS system is through an Ethernet connection in the current design, although Profibus is still an option.

L1 and L2 triggers with event number and timing information are received from the TTC interface and used by the RCU to initiate the event read-out. The RCU collects event data from the ALTRO chips on the digitizer cards, assembles a sub-event, reformats the data if necessary, and transfers the event to the DAQ via the optical, full duplex ALICE Detector Data Link (DDL). A multievent buffer is implemented in the FPGA memory.

A dedicated bus between the RCU and the digitizers is used for voltage, current and temperature monitoring of the digitizers. At the same time, the RCU is supervisor for the ALTRO chips and handles the configuration of the ALTRO chips at start-up or in case of errors. Error conditions can be transmitted to the DCS system through the DCS interface.

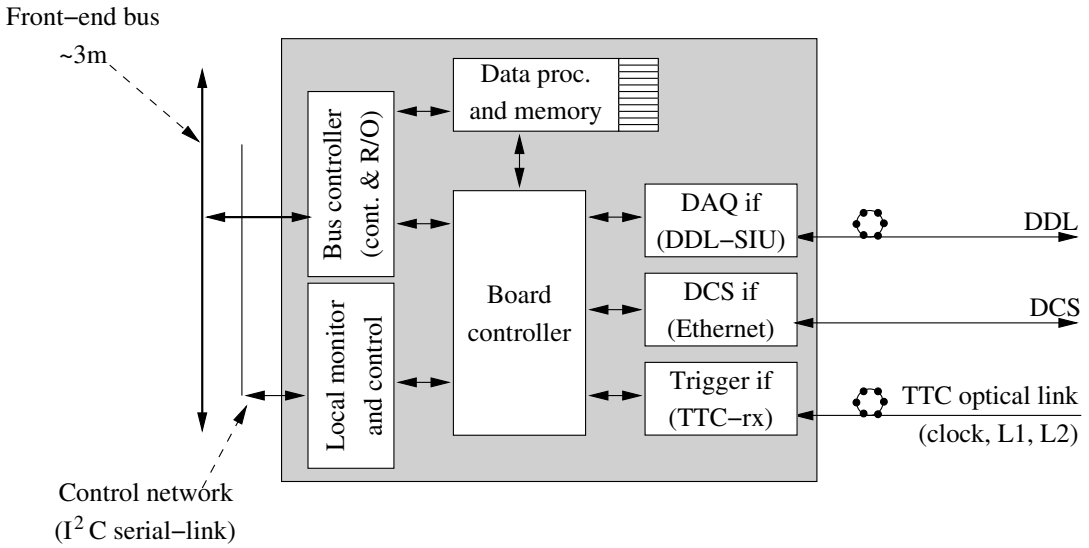

Figure 4.35: Schematic layout of the RCU card. The card is identical to the TPC RCU card. Two buses, for read-out and control purposes respectively, connect to the digitizer cards controlled by the module, and the RCU provides separate interfaces to the DAQ (DDL), DCS (Ethernet or Profibus) and the Trigger and Timing Control (TTC).

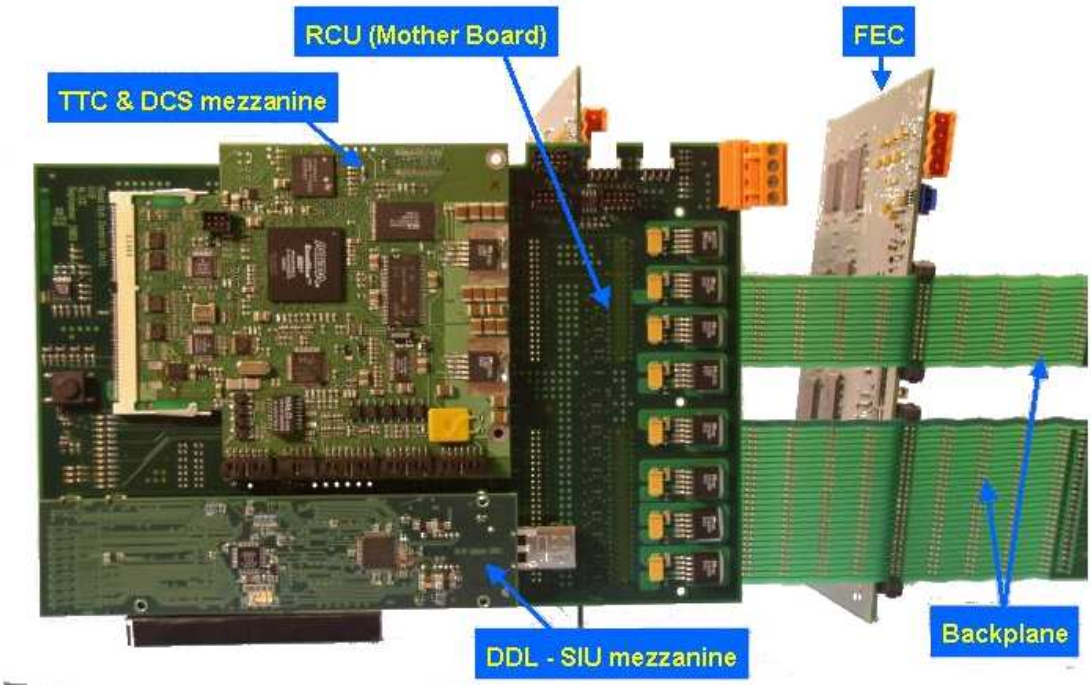

Figure 4.36: Photograph of the TPC RCU card and the two parallel bus connections to a TPC Front-End Card (FEC), used for read-out and control respectively. For the FMD, the FECs are replaced by the digitizer cards and the backplanes by flexible cables. The interfaces to Trigger, DCS and DAQ are placed on mezzanine cards, while the front–end buses and the board controller FPGA are located on the mother board.

4.4.6 Power Consumption

The VA1_ALICE chips consume about 80 mW each. A detector module will thus dissipate about 0.6 W in the inner ring and 0.3 W in the outer ring, which adds up to 6 W for a full ring. To estimate the total power budget, we assume a similar consumption from the rest of the circuitry on the hybrid and digitizer boards, arriving at a total power requirement of 12 W for each fully equipped ring.

4.5 Integration in ALICE

4.5.1 Mechanical Support for FMD

The three FMD sub–detectors require different mechanical support systems.

The most complex support system is on the RB26 side, where the support structure has the form of a cone. This cone must not only support the FMD3 inner and outer detector rings but also the beam pipe, via a wire and collar arrangement. A design study has been performed based on carbon fibre materials. The drawings of the cone are shown in Fig. 4.37.

The weight of each ring, including the honeycomb support plate and cables, is estimated to be at the most 4 kg. The ALICE vacuum chamber group has defined that the four wires holding the beam tube must be tightened with a force of up to 100 N each. The cone will be manufactured from carbon fibre. Based on this, a finite element simulation of stresses and deformations of the proposed support structure has been carried out. The proposed arrangement ensures that the cone does not experience deformations exceeding 20 μm at any point (see Figures 4.38 and 4.39). This is sufficient for the positioning and reproducibility of the FMD.

The design of the support structures for FMD1 and FMD2 has not yes been finalized. A possible layout for the FMD2 is shown in Fig. 4.4. It is based on a cylindrical aluminium cylinder attached to the

ITS/TPC support structure. Apart from holding FMD2, this cylinder also provides the attachment for the four wires holding the vacuum tube behind FMD2.

A preliminary drawing of the support of FMD1 is shown in Fig. 4.5. The FMD1 discs are mounted on a carbon fibre wheel structure supported in a cantilever fashion from the vacuum valve behind T0-A. This support structure will also hold V0A, T0-A and one point of the beam pipe.

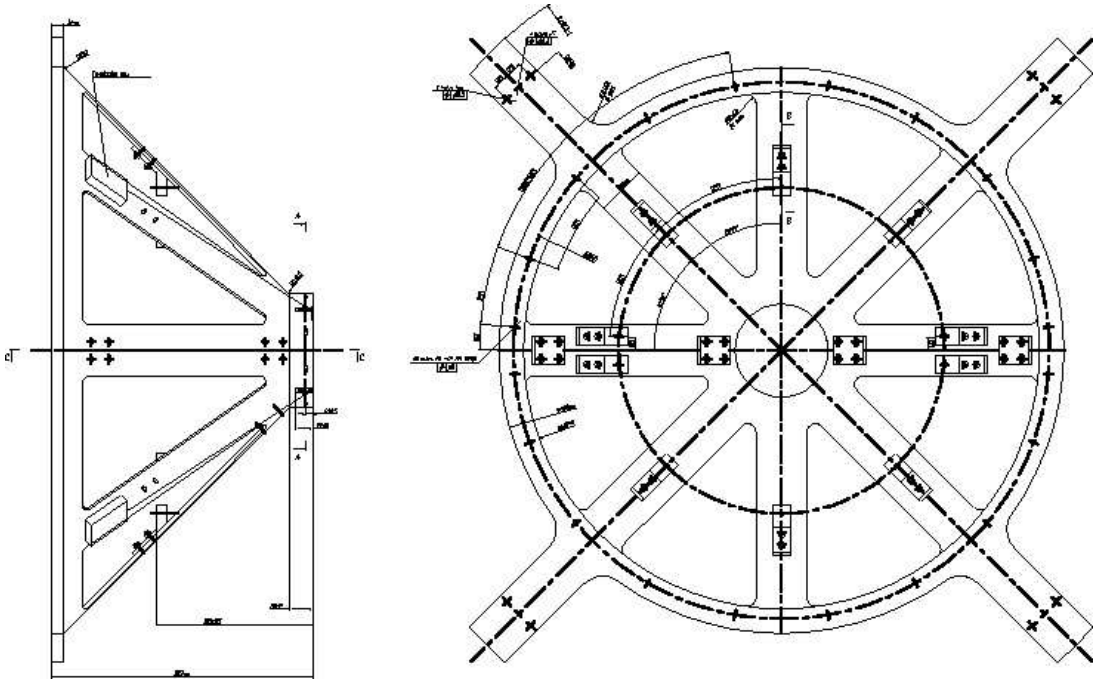

Figure 4.37: Preliminary technical drawing of the FMD3 cone

The sequence of installation steps of the forward detectors and the ITS is complex and will be covered for all FWD in a separate section.

4.5.2 Cabling

Table 4.9 gives an overview of the cables required to power, control and read out the FMD system for each of the five rings, FMD3i, FMD3o, FMD2i, FMD2o and FMD1.

The VA1_ALICE chips on the hybrid cards need a connection to the digitizer card with six electrical lines for controls, plus one differential analog data output connection and four power and ground lines. The control and power lines can be shared between VA chips on the same hybrid card, but the data output lines are individual for each chip. These connections will be assured by short, flexible multiwire cables between each hybrid card and the digitizer card on the half–ring.

Low voltage power to the hybrids is brought in per half–ring through the digitizer card, where it is regulated and distributed to each of the hybrids. In addition each Si sensor will be supplied with a bias voltage input ($\approx$100 V). These will be routed directly from the power supply channels to each sensor through the hybrid card.

Between digitizer cards and the RCUs, separate data and control buses will insure the communication on flexible multiwire flat cables. Up to four digitizer boards (for FMD2 and FMD3) and the corresponding RCU are connected together on one data and one control bus, with the RCU placed about 3 m away (just behind the muon absorber on the FMD3 side). The digitizer cards also need cables for low voltage power, the L0 trigger signals and a separate JTAG connection.

After the RCU, the data stream is optical (DDL), the controls network is based on Ethernet, and the trigger information is carried by the TTC system. The total system contains three RCUs, each with a

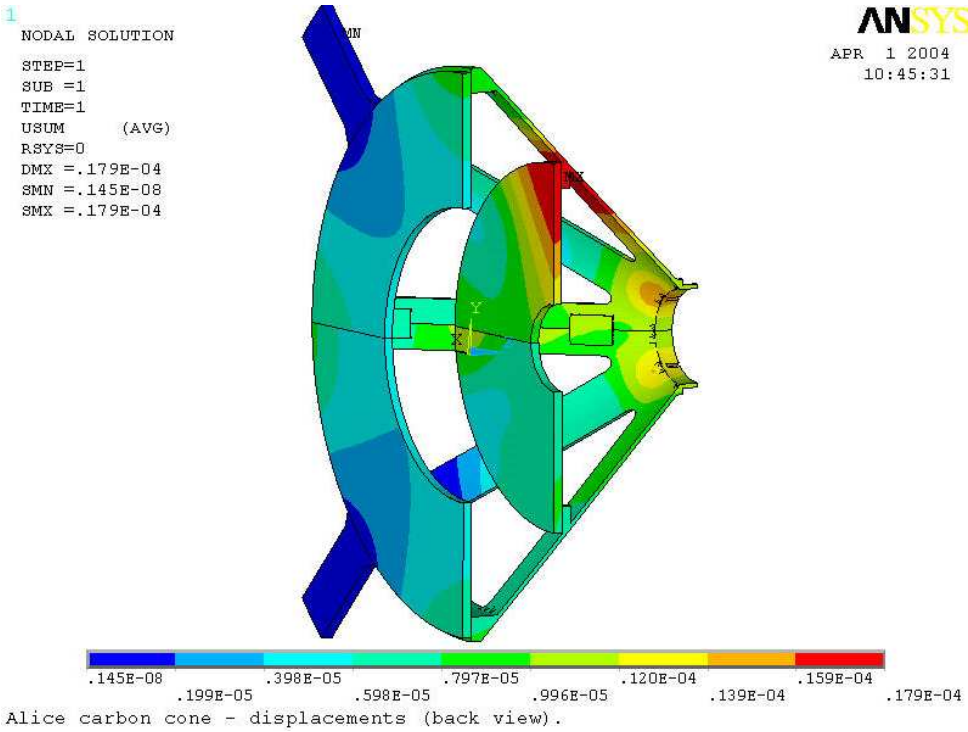

Figure 4.38: Calculated displacement of the FMD3 support cone under the load of the detector and the tension wires of the beam pipe, as seen from the back. The cone is split in two halves horizontally, while the vertical plane is a symmetry plane in the calculation.

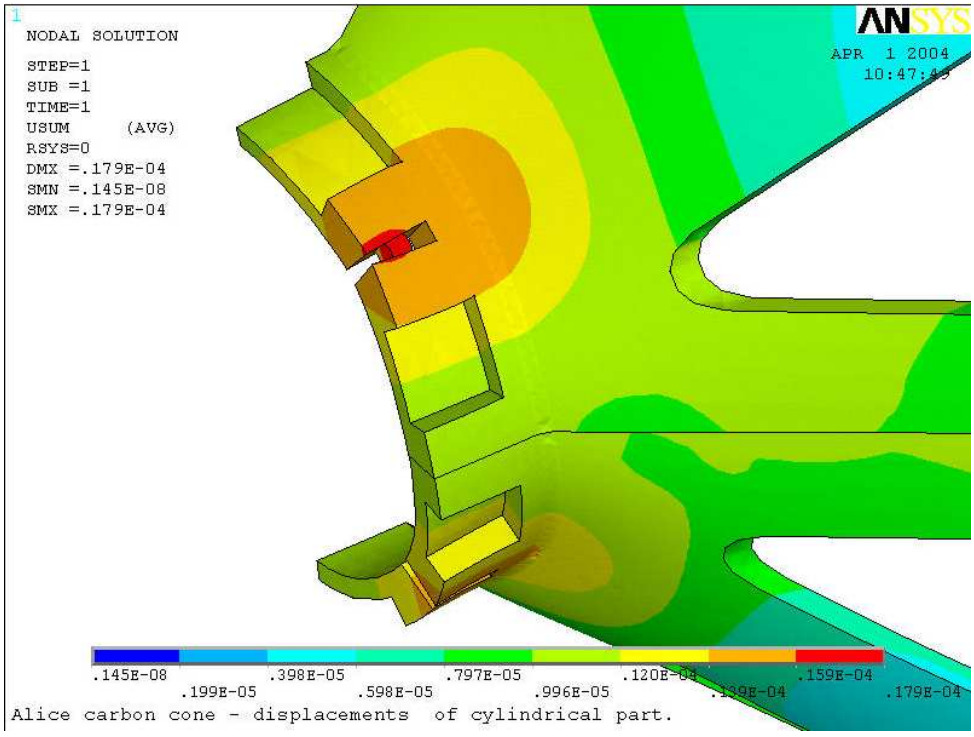

Figure 4.39: Calculated displacement of the nose of the FMD3 support cone. The biggest stress is where the tensioning wires for the beam pipe pull the cylindrical part of the structure.

Table 4.9: List of cables for each of the FMD rings, showing the number of cables with the number of wires in each cable in parentheses.

Cable	FMD3i	FMD3o	FMD2i	FMD2o	FMD1
Between digitizers and hybrids:					
Hybrid power	10(×4)	20(×4)	10(×4)	20(×4)	10(×4)
Hybrid control	10(×6)	20(×6)	10(×6)	20(×6)	10(×6)
Hybrid data	10(×16)	20(×8)	10(×16)	20(×8)	10(×16)
Between digitizers and RCUs:					
Data bus	1(×50)		1(×50)		1(×50)
Control bus	1(×26)		2(×26)		1(×26)
Between detectors and racks in UX25:					
Si bias voltage	10(×1)	20(×1)	10(×1)	20(×1)	10(×1)
Digitizer power	2(×12)	2(×12)	2(×12)	2(×12)	2(×12)
Digitizer control	2(×4)	2(×4)	2(×4)	2(×4)	2(×4)
Digitizer L0	1(×1)	1(×1)	1(×1)	1(×1)	1(×1)
Between RCUs and racks in UX25 or counting rooms:					
RCU power	2(×4)		2(×4)		2(×4)
RCU controls	1(Ethernet)		1(Ethernet)		1(Ethernet)
RCU TTC	1(TTC)		1(TTC)		1(TTC)
RCU DDL	1(DDL)		1(DDL)		1(DDL)

separate DDL link. The RCUs will be powered separately.

The layout of the cable paths from the detector to the outside world is covered in more detail in Section 5. In order to be able to assemble and disassemble ALICE, all cables from the detectors past the muon absorber must be connected through a patch panel at the indicated position. Figure 4.40 shows a photo of a 1:1 scale model of the ITS and FMD3 on the muon absorber side, with some cables mounted in a preliminary configuration. The cable layout on the RB24 side has not yet been studied to the same level of detail. However, in Fig. 4.5 the foreseen cable path from FMD2 to the end of the TPC is indicated. It follows the cable ducts that mainly serve the ITS on the RB24 side.

4.5.3 Cooling

The Front End electronics is cooled by a directed flow of dry air inside the volume of the FMD detector. At present the temperature conditions at the FMD positions have not yet been resolved in detail, but preliminary simulations indicate very elevated temperature in the area ($\approx 75^\circ$), which will require additional work on the air flow system from the part of the ALICE infrastructure group. If necessary the FMD FE electronics boards can be equipped with liquid cooling.

4.5.4 Power Supplies

Each FMD sensor will be supplied with a separate positive bias voltage in the range 70–150 V. Positive and negative low voltages will be supplied to the digitizers and RCU modules while the hybrid cards are supplied through power regulators on the digitizer boards, as described above. Remotely controlled power supplies with current monitoring capabilities for both high and low voltages will be of a standard type, presumably a CAEN 1527 system or similar. The power supplies will be mounted in racks outside the L3 magnet (see Section 4.5.5), and controlled by the DCS system, which already contains samples of code for the desired functionality.

Figure 4.40: Photo of a 1:1 scale model of the ITS and FMD used to study aspects of the mechanical installation and cabling. The space available for patch panels is represented by white blocks.

4.5.5 Racks

Two racks (B2–16 and B2–27) have been reserved for FMD electronics, see Fig. 4.41. These will contain low voltage power supplies and trigger related electronics. High voltage power supplies will presumably be placed in the counting rooms above the cavern.

4.5.6 Detector Control System (DCS)

The FMD Detector Control System will be fully compatible with the ALICE-wide system. As illustrated in Fig. 4.42, it will consist of branches for monitoring and controlling the high voltage and low voltage power supplies, and separate branches for communication with the digitizer and RCU units. All will be common solutions already devised within ALICE.

The CAEN OPCserver connection to the CAEN 1527 or similar system is used in many other ALICE subsystems. It will be used to control and monitor each high and low voltage channel.

Communication with the RCU module is based on Ethernet and the software will be available from the TPC group. With this system it is possible to configure the RCU and digitizer cards, including downloading parameters to the ALTRO and VA chips and monitoring currents and temperatures on both RCU and digitizer cards.

For direct communication to the FPGA chips on the digitizer cards, we foresee the use of dedicated JTAG connections. Other ALICE detectors plan similar connections.

4.5.7 Data Acquisition System (DAQ)

Each of the three RCU boards is connected to a Read-Out Receiver Card (RORC) [12] in the ALICE DAQ system through standard DDL optical communication links. The link is used for event data flowing from the RCU to the RORC and possibly for system configuration in the reverse direction. As the RCU

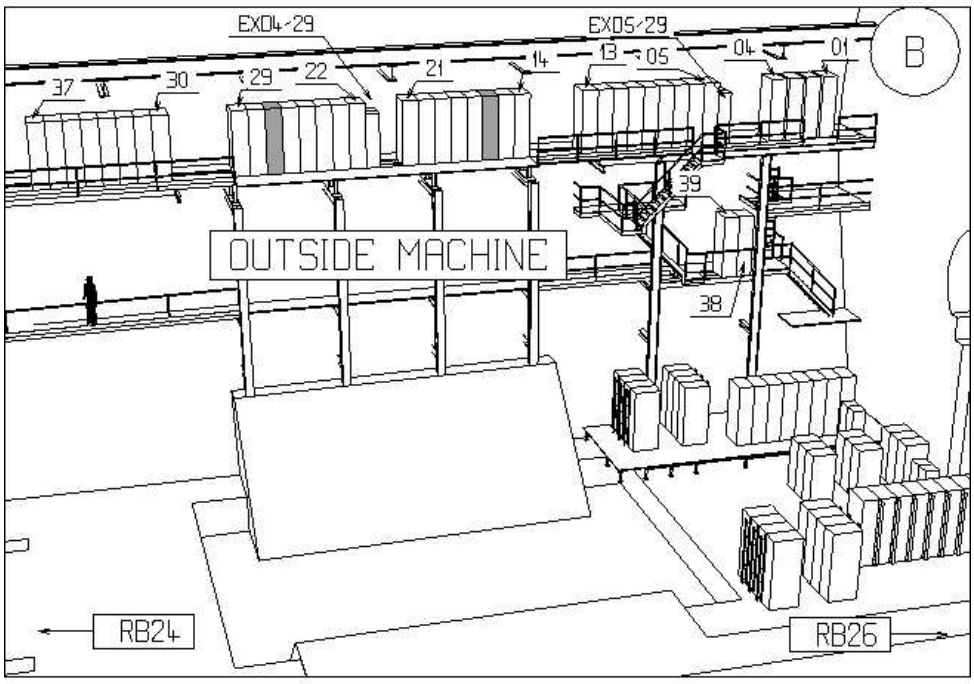

Figure 4.41: Rack placement in the ALICE cavern. Racks reserved for the FMD are marked in grey.

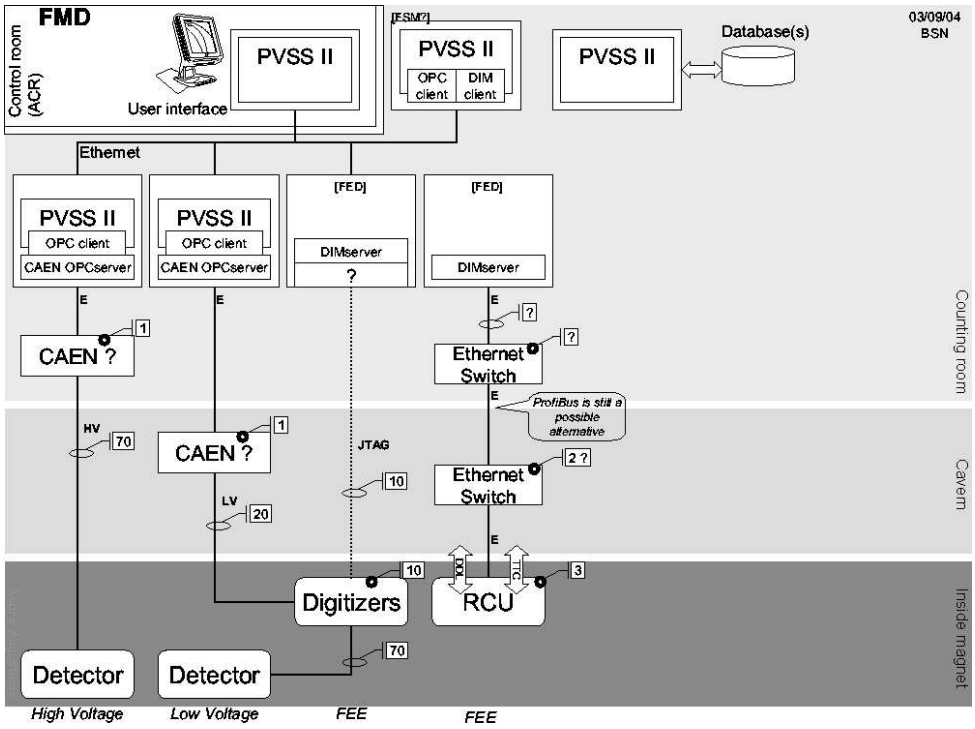

Figure 4.42: FMD Detector Control System.

modules are identical to the ones used in the TPC, the essential communication software will also be copied.

4.6 Commissioning

Currently a commissioning road map is being developed by the ALICE collaboration. It involves three steps:

1. at the production site;
2. at the surface upon arrival at CERN; and
3. in situ after installation in ALICE.

4.6.1 Commissioning and Testing at NBI

The current production plan relies on the delivery of tested Si sensors from the manufacturer accompanied by a specification sheet for each sensor, and for delivery of tested and certified hybrid cards containing the pre–amplifier chips, also by an industrial supplier. The remaining components for the electronics and read–out chain will be developed in collaboration with other ALICE partners.

The delivery plan calls for the delivery of a limited number of prototype elements in late 2004, allowing for detailed testing and debugging. The 70 FMD modules, i.e. sensors glued onto hybrid cards will be tested with pulsers and radioactive sources upon assembly at NBI and CERN.

Prototype detector modules will be tested in beam with 680 MeV electrons and selected modules possibly also in beam at RHIC (BRAHMS experiment [15]).

The digitizer boards will be designed and constructed at NBI and tested there in conjunction with the RCU boards and DAQ or DCL elements. The digitizer board design relies on technology extensively tested by the ALICE TPC, but it will require the modification of a few key elements on the board to match radiation hardness requirements. The RCU is identical to the boards utilized by the ALICE TPC and PHOS systems and has thus undergone extensive testing by other systems.

4.6.2 Commissioning and Testing at Surface at CERN

The FMD and its read–out components will be brought to CERN in February 2006, where the entire system will be tested in the laboratory prior to installation using the charge injection feature of the front–end pre–amplifier chips and radioactive sources.

4.6.3 Commissioning and Testing in Situ in ALICE

After installation in ALICE and before access is prohibited by ITS and TPC installation, the system integrity will tested using the charge injection functionality and the entire read–out chain.

4.6.4 Energy Calibration

The front–end pre–amplifier chips contain a calibration feature that injects a charge into the circuit corresponding to about 1 MIP. Relative calibration of this signal to real minimum ionizing particles will be done in beam tests utilizing 680 MeV electrons from an extracted beam from the ASTRID storage ring at the University of Aarhus. It is planned to test and calibrate all or most of the 70 modules prior to shipment to CERN for installation.

Additional energy calibration will be done in situ with the LHC beam by selecting peripheral or semi–peripheral collisions and pp collisions for which the mean number of hits per strip is far below one, thus allowing the identification of the single MIP response peaks in the spectrum. The measured single

particle peaks from nuclear collisions depend on the momentum distribution of the produced particles and will have to be compared to model calculations. However, at the forward angles covered by the FMD, laboratory momenta of particles are high and most particles have energy depositions in the MIP range.

4.7 Survey

The knowledge of the absolute positioning of the various FMD elements relative to the nominal Interaction Point (IP) is important for the accurate calculation of the pseudorapidity range covered by a given sensor. However, the requirements are moderate as the detector is not directly intended for tracking purposes, although particle track validation may be done between the FMD and, for example, the T0, V0 and PMD.

As an example consider an FMD3 sensor positioned at a distance $z = 62.5\,\mathrm{cm}$ from the IP and with inner radius $R_{in} = 4.2\,\mathrm{cm}$ and outer radius $R_{out} = 17.2\,\mathrm{cm}$. The pseudorapidities corresponding to the inner and outer edges are -3.399 and -2.006, respectively. A longitudinal shift of the detector by 1 mm changes these values by about 0.002 units. A 5 mm shift changes the pseurapidities by 0.008. Similarly, a shift in radius by 1 mm changes the values by -0.023 and -0.006 units, respectively. Likewise, a lateral shift of a ring assembly of 1 mm translates to a change in azimuthal angle at a radius of 4.2 cm of 1.4°, falling to 0.2° at $r = 28\,\mathrm{cm}$.

We thus estimate that the positioning of the various modules on a ring to the precision of a typical strip width ($250\,\mu\mathrm{m}$), and the positioning of the rings in situ in ALICE to a precision of about 1 mm in the transverse dimensions and 5 mm in z, is sufficient. However, the FMD rings must respect the required clearance of 42 mm to the centre of the nominal beam pipe position.

The detector half–rings will be marked with survey points positioned to a precision of about $100\,\mu\mathrm{m}$. The survey equipment must be able to identify the survey marks to a similar precision.

4.8 Safety

In general, the FMD and its support electronics are manufactured using technologies very similar to those employed by the ITS and the TPC. Detector modules are manufactured out of silicon, ceramics and halogen–free FR4 circuit boards. Support systems are manufactured out of carbon fibre or aluminium. Cables and connectors will conform to the required fire standards. Thus we identify no particular safety concerns in the use of materials.

Detectors are supplied with low voltage ($V < \pm 10\,\mathrm{V}$) and high voltage (in the range 50–150 V). The power supplies will be located in the racks in UX25. They will be remotely controllable and will be enabled with an automatic trip mechanism activated by the drawn current; for the HV channels, the limits are in the sub–microampere domain. Monitoring of the currents drawn by the hybrid and digitizer cards will enable these to switch off automatically in case of too high current and report errors to the Detector Control System.

4.9 Time Table

The timetable for the FMD project is given in Table 4.10.

Table 4.10: Timetable for the FMD project

Date	FMD project
Summer 2004	Order Si and FEE hybrid prototypes and pre–amplifier chips.
	Design test–digitizer board (NBI).
Autumn–winter 2004	Construct test–digitizer board.
	Bonding Prototype of Si and hybrids.
	Test Si+hybrid+digitizer+RCU with e^- beam.
Early 2005	Test prototype with heavy–ion beam at RHIC.
Spring 2005	Place production order of Si and hybrids.
June 2005	Delivery of all Si and hybrids.
August 2005	Gluing Si+hybrids at NBI or CERN.
Autumn 2005	Bonding at CERN, system assembly and commission at NBI.
February 2006	Ready to ship to CERN.
June 2006	Ready for installation in ALICE.

4.10 FMD Organization

- NBI — Niels Bohr Institute, University of Copenhagen, Copenhagen, Denmark;

Ian Bearden	bearden@nbi.dk
Henrik Bertelsen	bertelsen@nbi.dk
Hans Bøggild	boggild@nbi.dk
Christian Holm Christensen	cholm@nbi.dk
Jens Jørgen Gaardhøje (Project leader)	gardhoje@nbi.dk
Børge Svane Nielsen (Subproject leader)	borge@nbi.dk
Erik Kaimer Olsen	kaimer@nbi.dk

- INR — Academy of Science, Institute of Nuclear Research, Moscow, Russia;

Alexei Kurepin	akurepin@polynom.ru
Alla Maevskaya	alla@inr.ru
E. V. Karpechev	

The Greek group from Athens (Marta Spyropoulu-Stasinakhi) has also expressed strong interest in participating in the FMD DAQ. The Greek group would contribute both in terms of manpower and CORE costs.

5 Forward Detector integration in ALICE

The Forward Detector integration and installation procedure is driven by the consideration that in ALICE, in contrast with other LHC experiments, the bake-out of the central part of the beam pipe will not be possible once the Inner Tracking System (ITS) and Forward Detectors (FWD) are installed. The beam pipe bake-out will in fact most probably be needed not only at the installation of the experiment but also rather regularly in the long shut-downs, in order to guarantee high vacuum quality during the whole operation period. Furthermore, access to the ITS and many of the FWD and their services will be impossible once the TPC is in place (standard position). This is particularly the case on the RB26 side, where the detectors are completely hidden between the ITS and the muon arm.

Consequently, it must be foreseen that the ITS and FWD will be removed from the operating position and re-installed at regular intervals both for their maintenance and for beam pipe bake-out. This requires not only appropriate design, but also the definition of a detailed and precise sequence in their installation and removal. ITS and FWD are parts of the same mechanical complex; therefore some reference will be made to the ITS and its services, although they are, strictly, outside the scope of this TDR.

Another particularity of ALICE is the presence of the Muon Arm on one side of the Interaction Point (IP) and the resulting asymmetry of the experimental set–up. Consequently, the FWD situated at the RB24 (shaft) side are different in position and configuration to the corresponding detectors on the RB26 (muon arm) side.

One of the essential technical targets of ALICE is a high level of thermal protection of the TPC from heat sources in its environment. Particular care must therefore be taken in the design of the cooling and ventilation system in the volume inside the TPC inner cylinder. No liquid cooling is, however, currently foreseen for the FWD because the heat dissipation of these detectors is small compared to the dissipation from the ITS cables, for which a solution based on a general ventilation of the full volume inside the TPC is being sought.

None of the FWD are gas detectors. Services described here thus comprise only cables, optical fibres and possibly air ventilation ducts.

5.1 Common Design Features

Needing to be able to bake out the beam pipe without the presence of the FWD means that these detectors will have to be mounted and remounted while the central beam pipe is installed. Thus, all the Forward Detectors and their support structures will be divided in half and assembled around the beam pipe. A radial clearance to the beam pipe must be respected according to following criteria:

- In those cases where the beam pipe and a detector are supported by the same mechanical structure, a radial clearance of 5 mm will be respected between them, with due consideration of all the design and fabrication tolerances.
- Where the beam pipe and a detector are supported by different mechanical structures, a radial clearance of 10 mm will be observed between them, again considering all design and fabrication tolerances.

5.2 Mechanical support

5.2.1 RB24 Side

As shown in Figures 5.1 and 5.2, both halves of T0-A, V0A, and the FMD1 are mounted on a cantilevered carbon fibre structure fixed to the vacuum valve support. The valve, its support and the central vacuum

pipe are all held by a mechanical structure bolted to the Service Support Wheel (SSW) of the TPC. Although the deflection of the cantilevered support under the weight of the three detectors is calculated to be below 1 mm, two arms will connect the free edge of the support to the structure to compensate the deflection and avoid dangerous vibrations.

FMD2 is mounted inside two half-cylinders fixed to the ITS mechanical structure. The second support of the central beam pipe is attached to the same cylinder by four stretched wires behind FMD2.

Both support systems secure the detectors in a fixed position with respect to the beam pipe.

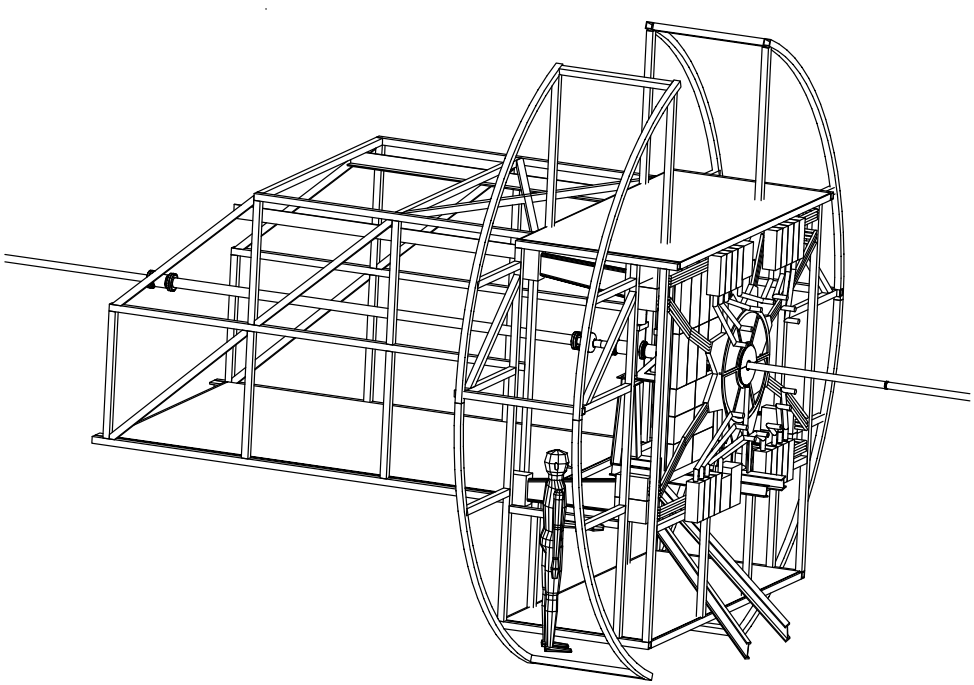

Figure 5.1: Three–dimensional drawing of the Mini Frame and Baby Frame structures that support the T0-A (hidden behind the PMD), V0A, and FMD1 detectors and their services. The cables and optical fibres exit the detectors radially and connect to shoeboxes mounted on the periphery of the Mini Frame.

5.2.2 RB26 Side

V0C is directly fixed to the front face of the muon absorber while T0-C is mounted on a short cantilevered carbon fibre cylindrical structure bolted to the front face of the muon absorber and protruding through the inner circumference of V0C.

FMD3 is mounted inside the two halves of the same carbon fibre conical structure to which the first support of the central beam pipe is also fixed by four stretched wires. The half-cones are mounted on the ITS support structure.

While the muon absorber supports the beam pipe inside its own volume, bellows allow small movements relative to the vacuum pipe at the ITS and FMD3 positions. The fixture of the beam pipe to the FMD cone and the ITS allows for smaller tolerances between these objects and a fixed relative alignment.

5.3 Services

The services (power cables, signal cables, and optical fibres) are identical for the Forward Detectors installed on either side of the IP. However, the routing of these services are significantly different.

5.3.1 RB24 Side

Apart from FMD2, all services on the RB24 side are concentrated on the Mini Frame (MF) structure of ALICE, which also supports the PMD detector, as shown in Fig. 5.2. The cables for FMD2 follow the channels of the ITS services until they also connect to the MF.

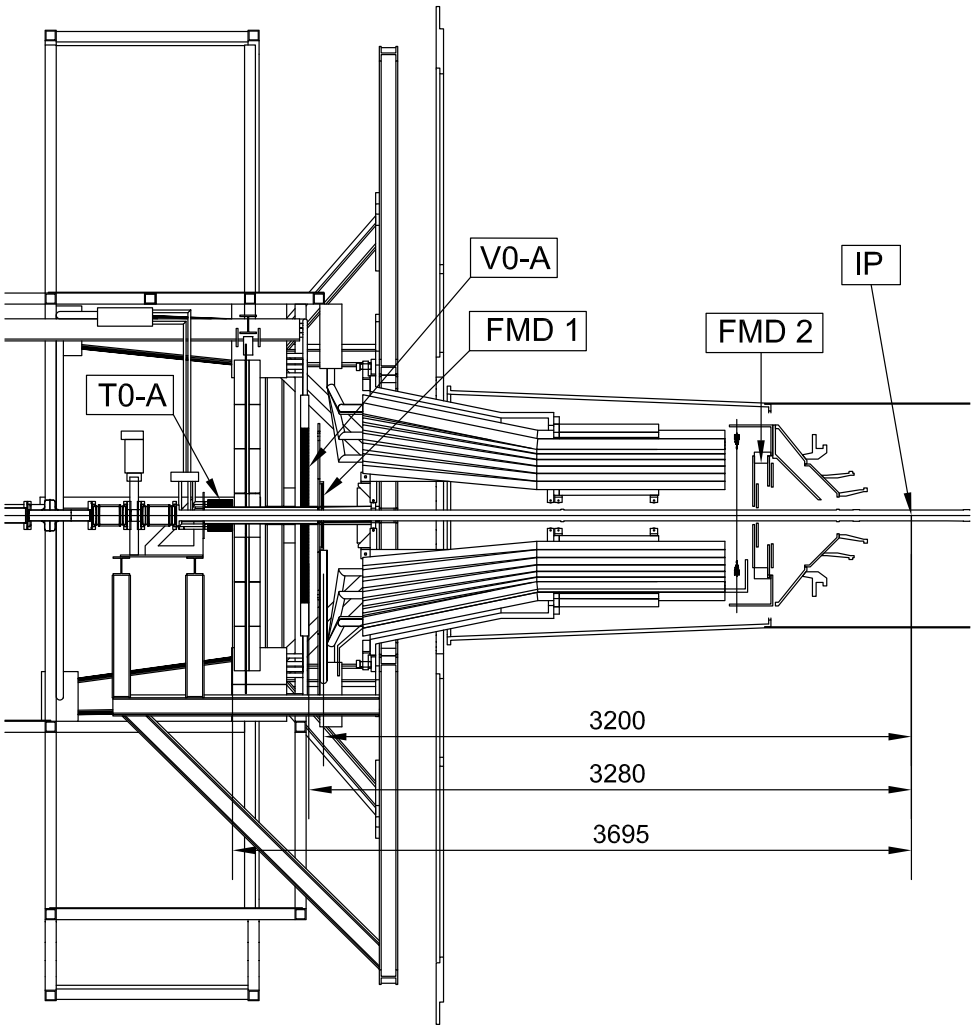

Figure 5.2: Details of the cabling for the Forward Detectors on the RB24 side. Together with the ITS services, the cables from FMD2 follow in the cylindrical and conical channels and connect to shoeboxes on the Mini Frame structure. Cables and optical fibres from FMD1, V0A and T0-A exit radially towards their shoeboxes near the periphery of the Mini Frame.

T0-A

The power and signal cables from the 12 photomultipliers of V0A are connected first to a patch panel mounted above the detector on the Mini Frame and subsequently to the TRD shoebox. Here, the signals are split and sent to both the proper T0-A electronics placed outside the L3 magnet, and to the TRD electronics to provide its wake–up signal.

V0A

For V0A, the optical fibres connected to the 32 scintillating sections are grouped in eight units of four bundles, each following the octagonal structure of the detector. Each bundle is connected to one of the 32 photomultipliers, themselves grouped into eight units of four and mounted to the Mini Frame structure. All fibres are adjusted to have an identical length, and kept shorter than 5 m to minimize signal attenuation. The power and signal cables for the photomultipliers are similarly routed in four groups of eight to four shoeboxes mounted on the Mini Frame. As for T0-A, the signals are split in the shoeboxes and sent to two different electronic systems: the proper V0A electronics placed outside the L3 Magnet and the TRD detector shoebox to provide its wake–up signal.

FMD1

Cables connect the FMD1 detector to a shoebox containing the RCU circuit and the patch panel for power and signal cables. The shoebox is fixed to the Mini Frame below FMD1 at a distance less than 3 m from the digitizer circuits on the detector. From the shoebox, cables connect to a patch panel mounted on the outer part of the Mini Frame. Cables connecting from this patch panel to the FMD electronics outside the L3 magnet are attached to the Baby Space Frame (BSF), from where they hang as flexible and short pigtails.

FMD2

FMD2 uses the ITS service support. The cables are grouped at the bottom of the detector support and connected to the patch panel mounted on the ITS structure as flexible and short pigtails. From the patch panel, the cables are routed through the FMD duct and emerge as flexible and short pigtails, to be connected to the FMD2 shoebox mounted on the Mini Frame. A new section of cables connects this shoebox to a patch panel on the outer part of the Mini Frame. The final cabling that reaches the outside electronics is attached to BSF, from where they will again hang as flexible and short pigtails.

5.3.2 RB26 Side

On the RB26 side, all services have to pass through narrow ducts positioned along the conical surface of the muon absorber. On the tip of the absorber, near the FWD and ITS detectors, patch panels allow (dis)connection of the cables and pipes at this point during detector installation. Fig. 5.3 shows the layout of the patch panels and ducts on the circumference of the absorber.

V0C

V0C has a total of 96 fibre bundles, distributed in four groups of 24 each, coming out of the detector at 45 $^\circ$ with respect to the x and y axes (see Fig. 5.3). The four groups are channelled directly into four ducts mounted on the muon absorber (see Fig. 5.4) and reserved exclusively for the V0C; they reach four boxes placed at the end of the ducts, containing eight PMs each. All the fibres have an identical length of less than 5 m. The power and signal cables are connected to the PMTs of each box, whose services are routed to four shoeboxes mounted on the muon absorber support. In analogy to the V0A, the signals are split and sent both to the V0C electronics outside the L3 magnet and to the TRD.

T0-C

The T0-C services coming from the 12 photomultipliers are connected to a patch panel mounted almost on top of the muon absorber, then to the shoebox, where the signals are split and sent to the T0-C electronics placed outside the L3 magnet and to the TRD electronics to provide its wake–up. Fig. 5.5 shows the position of the patch panels and shoebox on the muon absorber.

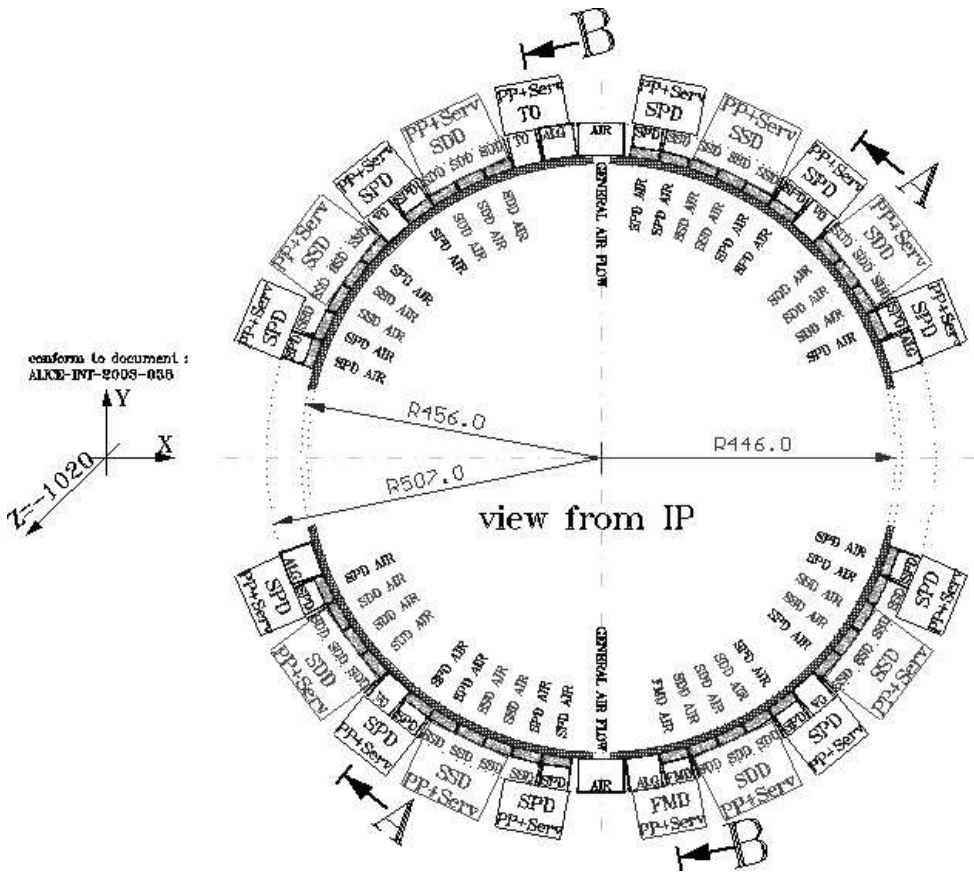

Figure 5.3: Overview of the patch panel and cable duct distribution on the surface of the muon absorber near its front face.

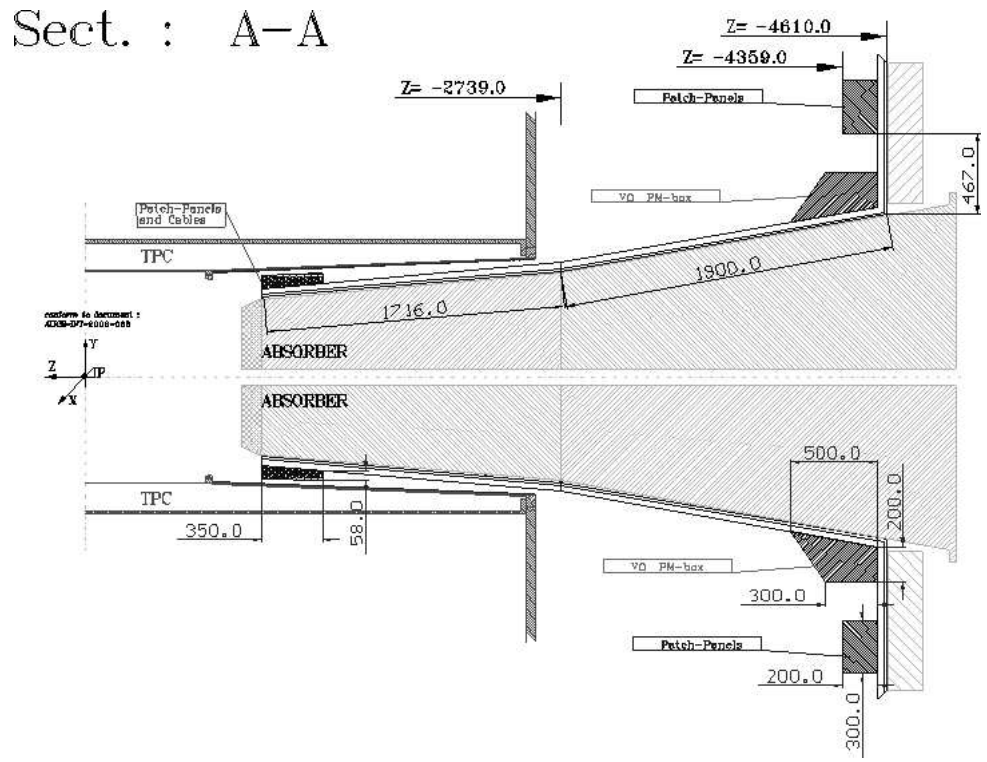

Figure 5.4: Muon absorber on the RB26 side, showing the placement of the V0C services patch panels near the detector, the PM boxes and the patch panels for connection outside the L3 magnet.

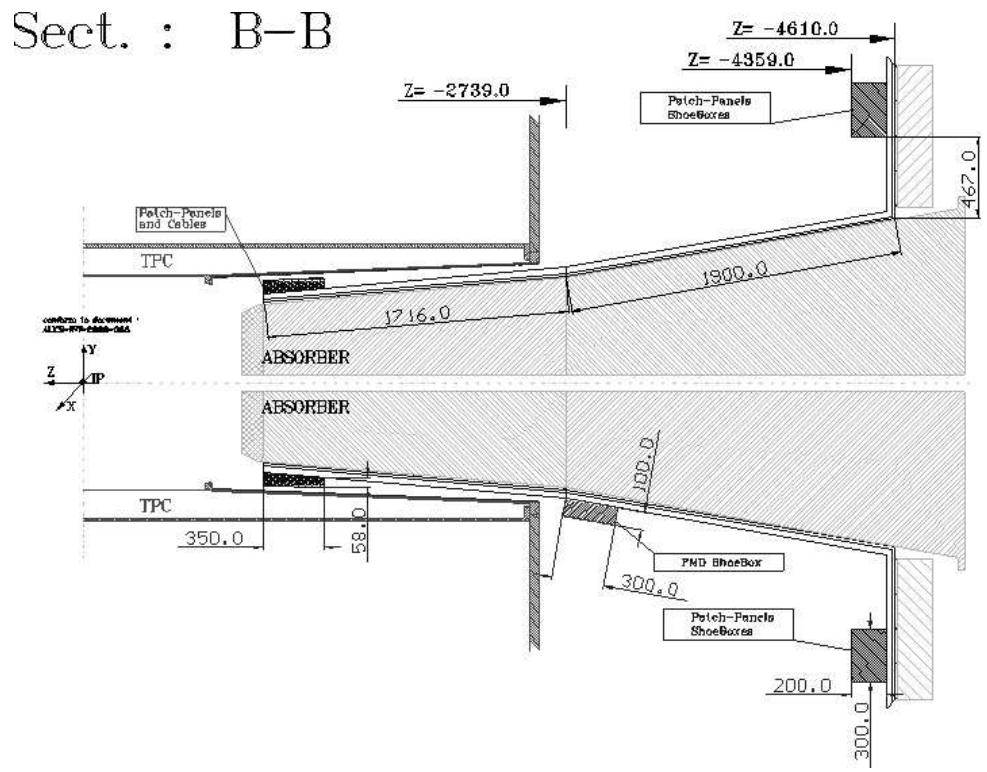

Figure 5.5: Muon absorber on the RB26 side, showing the placement of the T0-C patch panel near the detector and the shoebox with a patch panel for the connection to the outside of the L3 magnet. Also shown is the position of the FMD3 patch panel and the shoebox containing the RCU module.

FMD

The cabling scheme of FMD3 is constrained by several parameters, including:

- the only available place for the FMD patch panel and duct is near the bottom of the muon absorber;
- the maximum length of the cables carrying the signals from the FMD digitizers to the RCU is 3 m; and
- each of the FMD halves must be mounted in its half conical carbon fibre support and completely pre–cabled before its installation in the set–up.

For these reasons, the cables coming from the two halves of FMD3 first merge together at the horizontal edge of their junction, and are then routed around the border of their conical support to the FMD patch panel and duct. From the patch panel, the cables follow their duct up to the FMD shoebox placed at the end of the duct, just outside the TPC (see Fig. 5.5), in order to keep the signal cable lengths close to the desired 3 m (see Fig. 5.5). From the shoebox, power and signal cables continue their path to the FMD electronics outside the L3 magnet.

5.4 Installation Sequence

The sequence of installation steps of the forward detectors and the ITS is complex and has been explored in detail through a series of 3D installation drawings and in full-scale mock-ups. Figure 5.6 and 5.7 show selected steps of the installation procedure of those Forward Detectors that are situated inside the TPC inner cylinder, i.e. V0C, T0-C, FMD3 and FMD2. Some details follow below.

5.4.1 RB26 Side

First, the beam pipe is installed with a temporary support structure and equipment for bake–out. Then V0C and T0-C are mounted on the absorber nose and a temporary holder of the beam pipe is installed. This allows the lower half of the FMD3 cone, already equipped with detectors, to be installed and attached to the temporary beam support structure. When the upper half of the cone and FMD3 is in place, the wire mechanism for the beam pipe support can be attached and the beam pipe position fine adjusted. The ITS is now pushed in (first the two pixel layers and then the two drift and strip layers) and the temporary beam support structure is removed.

These are the details of the installation sequence of the services:

1. Install the four sectors of the ITS and FWD services with pre–cabled ducts, patch panels, PM supports and shoeboxes on the muon absorber and its support structure.
2. Connect detector shoeboxes to the electronics outside the L3 magnet.
3. Install the central beam pipe on a temporary support and bake–out. Remove the bake–out jackets.
4. Assemble the two halves of the T0-C support around the beam pipe and fix the cylindrical structure to the front face of the muon absorber.
5. Assemble the two halves of the V0C detector around the T0-C support and fix the combined structure to the front face of the muon absorber.
6. Assemble the two halves of the T0-C detector around its support and fix it to this support.
7. Connect the optical fibre bundles to the feed-through fixed around the V0C. Assemble the fibre bundles in four groups at 45 $^\circ$ with respect to the x and y axes. Pass each group of fibres into the dedicated duct mounted below the SPD patch panels. Connect the fibre bundles to the photomultipliers mounted in the PM boxes.

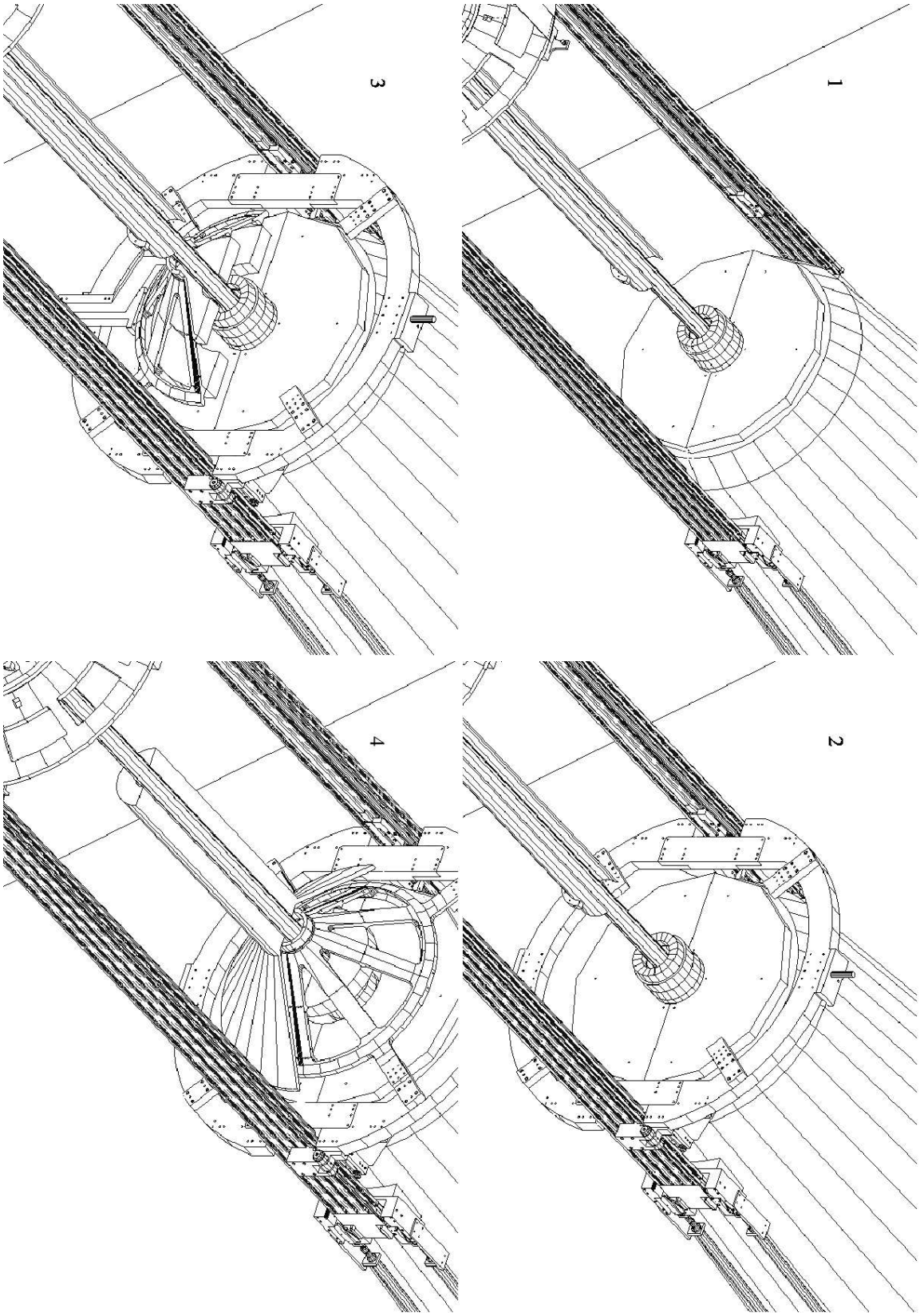

Figure 5.6: Installation sequence, left to right, top to bottom order. Continued on Fig. 5.7.

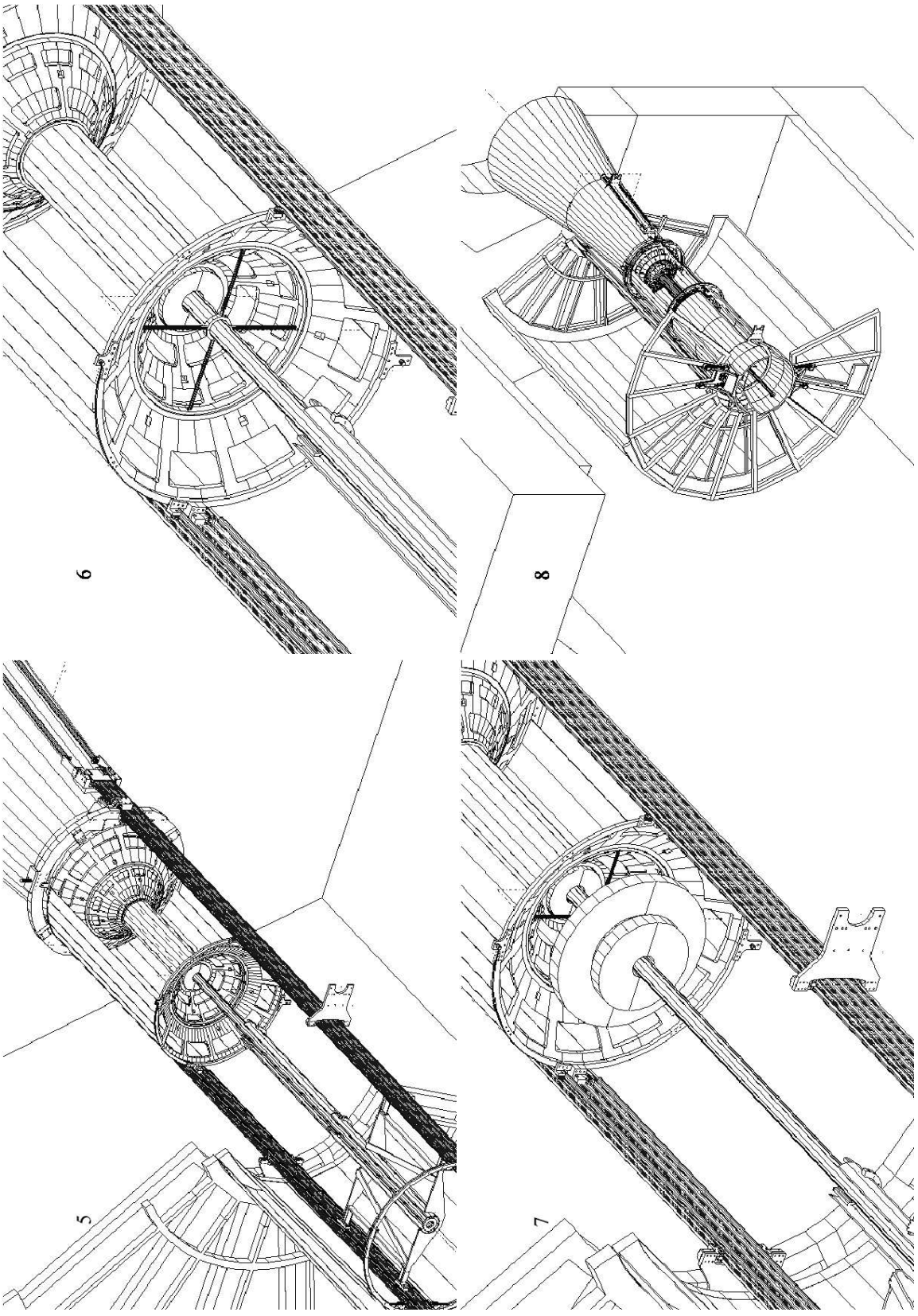

Figure 5.7: Installation sequence, left to right, top to bottom order. Continued from Fig. 5.6.

8. Connect the T0-C services to their patch panel.
9. Install the two halves of FMD3 with its conical support structure.
10. Regroup and connect the two bundles of services to the FMD patch panel.
11. Connect and adjust the four wires for the beam pipe support on the conical support.

5.4.2 RB24 Side

After the ITS installation, the support structure for FMD2 and the beam pipe support on the RB24 side can be installed. Finally, a support cover for the ITS cables is installed and the TPC can be rolled in, enclosing V0C, T0-C, FMD3, ITS and FMD2. FMD1 will be mounted together with PMD, T0-A and V0A on the Mini Frame structure.

1. After the installation of the ITS on its provisional support, mount the FMD2 on the cylinder to which the second beam pipe support is fixed.
2. After the introduction of the pre-cabled ITS service support, the FMD2 services are connected to their patch panel on this support.
3. After the final installation of TPC, its Service Support Wheel (SSW), and the ITS, the fixation of the ITS services to the SSW, and the connection of the central beam pipe to the vacuum valve support, the two halves of the T0-A, V0A, and FMD1 will be mounted on a common support structure.
4. Next, the Mini Frame is equipped with ITS and FWD shoeboxes, patch panels and pre-cabled services is introduced.
5. The FMD2 services (pigtails), emerging from their duct (near the bottom of the conical service support structure), are now connected to their shoebox on the Mini Frame (together with the ITS services).
6. Finally, the FMD1, V0A and T0-A services are connected to the respective shoeboxes on the Mini Frame.

6 Editorial Committee

The TDR editorial committee was composed of:

- Ian G. Bearden
- Hans Bøggild
- Christian Holm Christensen
- Jens Jørgen Gaardhøje (chair)
- Jean–Yves Grossiord
- Tomasz Malkiewicz
- Børge Svane Nielsen
- Guy Paic
- Wladyslaw Trzaska

References

Chapter 1

[1] N. Ahmad *et al.*, ALICE: Technical proposal for A Large Ion Collider Experiment at the CERN LHC, CERN/LHCC-95-71 LHCC/P-3, (1995).

[2] L. Betev and P. Chochula, Definition of the ALICE Coordinate System and Basic Rules for Subdetector Components Numbering ALICE note ALICE-INT-2003-038, (2003).

[3] S. Beolè *et al.* [ALICE Collaboration], ALICE technical design report of the detector for high momentum PID, CERN-LHCC-98-19, ALICE TDR 1, (1998).

[4] G. Dellacasa *et al.* [ALICE Collaboration], ALICE technical design report of the photon spectrometer (PHOS), CERN-LHCC-99-4, ALICE TDR 2, (1999).

[5] G. Dellacasa *et al.* [ALICE Collaboration], ALICE technical design report of the zero degree calorimeter (ZDC), CERN-LHCC-99-5, ALICE TDR 3, (1999).

[6] G. Dellacasa *et al.* [ALICE Collaboration], ALICE technical design report of the inner tracking system (ITS), CERN-LHCC-99-12, ALICE TDR 4, (1999).

[7] G. Dellacasa *et al.* [ALICE Collaboration], ALICE technical design report of the dimuon forward spectrometer, CERN-LHCC-99-22, ALICE TDR 5, (1999).

[8] G. Dellacasa *et al.* [ALICE Collaboration], ALICE technical design report: Photon multiplicity detector (PMD), CERN-LHCC-99-32, ALICE TDR 6, (1999).

[9] G. Dellacasa *et al.* [ALICE Collaboration], ALICE technical design report: Time projection chamber (TPC), CERN-LHCC-2000-01, ALICE TDR 7, (2000).

[10] G. Dellacasa *et al.* [ALICE Collaboration], ALICE technical design report of the time of flight system (TOF), CERN-LHCC-2000-12, ALICE TDR 8, (2000).

[11] P. Cortese *et al.* [ALICE Collaboration], ALICE technical design report of the transition radiator detector (TRD), CERN-LHCC-2001-21, ALICE TDR 9, (2001).

[12] P. Cortese *et al.* [ALICE Collaboration], ALICE technical design report: Trigger, Data Acquisition, High Level Trigger, Control System, CERN-LHCC-2003-062, ALICE TDR 010, (2004).

[13] P. Cortese *et al.* [ALICE Collaboration], ALICE Physics Performance Report, Volume I CERN-LHCC-2003-049, (2003).

Chapter 2

[1] ALICE Collaboration, Technical Proposal CERN/LHCC/95-71.

[2] L. Betev *et al.*, Internal note, ALICE-INT-2003-038.

[3] L. Betev *et al.*, Internal note, ALICE-INT-2003-039.

[4] A.E. Antropov *et al.*, Nucl. Phys. **B78** (1999) 416.

[5] M. Bondila *et al.*, Nucl. Instrum. Methods Phys. Res. **A478** (2002) 220.

[6] K. Ikematsu, *et al.*, Nucl. Instrum. Methods Phys. Res. **A411** (1998),238.

[7] S. Ahmad, *et al.*, Nucl. Instrum. and Methods Phys. Res. **A387** (1997), p. 43.

[8] S. Ahmad, *et al.*, Nucl. Instrum. and Methods Phys. Res. **A400** (1997),149.

[9] V.A. Kaplin, *et al.*, Beam tests of the first prototype of a Cherenkov counter for ALICE T0 detector. ALICE INT 2000 05.

[10] V.A. Kaplin, *et al.*, Status of the ALICE T0 detector based on Cherenkov counters. ALICE/01–07/ Internal note/T0/ 16 January 2001.

[11] V.A. Grigorev, *et al.*, Nuclear Experimental Techniques, **43 6** (2000), 28.

[12] `http://www.ozoptics.com/` .

[13] http://www.phillipsscientific.com/phisci1.htm .

Chapter 3

[1] B. Rapp, thesis, Production de Dimuons en reactions p–p et Pb–Pb avec ALICE : le detecteur V0 et les resonances de basse masse, Lyon University, June 2004.
[2] B. Cheynis *et al.*, Internal note, ALICE/2000-29 (2000).
[3] ALICE Physics Performance Report, CERN/LHCC 2003-049, ALICE PPR Volume 1 (2003).
[4] B. Cheynis *et al.*, Internal note, ALICE/2003-40 (2003).
[5] T. Sjöstrand *et al.*, Comput. Phys. Commun. **135** (2001) 238 (LU TP 00-30, hep-ph/0010017).
[6] X. Wang and M. Gyulassy, Phys. Rev. **D44** (1991) 3501.
[7] I. Azhgirey *et al.*, LHC Project Note 258 (2001); LHC Project Note 273.
[8] E. Cuautle, G.Paic, and R. Alfaro, Internal note, ALICE-INT-2004-021 (2004).
[9] S. Kim *et al.*, Nucl. Instrum. Methods Phys. Res. **A306** (1995) 206.
[10] STAR collaboration IUCF, Proposal to construct an endcap electromagnetic calorimeter for spin physics at STAR, Internal Report (2002).
[11] BICRON, Saint-Gobain Industrial Ceramics, P.O. Box 3093, 3760 DB Soest, The Netherlands.
[12] KURARAY Corp., 3-10, 2-Chome, Nihonbashi, Chuo-ku, Tokyo, Japan.
[13] HAMAMATSU Photonics, 360 Foothill Rd Bridgewater, NJ 08807, USA.
[14] F. Anghinolfi *et al.*, NINO, an ultra-fast, low power, front-end amplifier discriminator for the time-of-line detector in ALICE experiment.
[15] M. Mota, J. Christiansen, HPTDC, High Performance Time to Digital Converter, version 2.2, for HPTDC 1.3, Proc. ICECS98, Lisbon, 1998, IEEE, Vol 1, p 409.
[16] O. Villalobos Baillie, D. Swoboda and P. VandeVyre, ALICE/98-23, Internal Note. Data Acquisition, Control and trigger: Common report for the preparation of the ALICE technical Design reports.
[17] CAEN, Via Vetraia, 11, 55043 Viareggio, Italy.

Chapter 4

[1] B.B. Back *et al.* [PHOBOS Collaboration], Nucl. Instrum. Methods Phys. Res. **A499** (2003) 603.
[2] H.A. Gustafsson *et al.*, Phys. Rev. Lett. **52** (1984) 1590.
[3] M. Poskanzer and S. A. Voloshin, Phys. Rev. C**58** (1998) 1671.
[4] J.Y. Ollitrault, Phys. Rev. D**46** (1992) 229.
[5] J.Y. Ollitrault, Phys. Rev. D**48** (1993) 1132.
[6] R. Raniwala, S. Raniwala, and Y.P.Viyogi, ALICE-INT-1999-32.
[7] A. Morsch and B. Pastirčák, Internal Note, ALICE-INT-2002-28 version 1.0, (2004).
[8] J.-L. Agram *et al.*, Nucl. Instrum. Methods Phys. Res. **A517** (2004) 77.
[9] Ideas ASA, VA1_prime2,
http://www.ideas.no/products/ASICs/VAfamily.html .
[10] R. Esteve Bosch, A. Jimenez de Parga, B. Mota and L. Musa, IEEE Trans. Nucl. Sci. **50** (2003) 2460.
[11] R. Esteve Bosch *et al.*, Proc. 8th Workshop on Electronics for LHC Experiments, Colmar 9–13 September 2002.
[12] A. Yokoyama *et al.*, IEEE Trans. Nucl. Sci. **48** (2001) 440.
[13] Ideas ASA, "VA1_ALICE",
Draft document, see http://fmd.nbi.dk/fmd/VA1-ALICE-draft-v1r2.pdf .
[14] http://ep-ed-alice-tpc.web.cern.ch/ep-ed-alice-tpc/testing.htm .

[15] M. Adamczyk *et al.* [BRAHMS Collaboration], Nucl. Instrum. Methods Phys. Res. **A499** (2003) 437.